University of California
Santa Barbara

Cold Atoms in Dynamic Quasiperiodic Optical Lattices

A dissertation submitted in partial satisfaction
of the requirements for the degree

Doctor of Philosophy
in
Physics

by

Peter Dotti

Committee in charge:

Professor David Weld, Chair
Professor David Patterson
Professor Chetan Nayak

June 2024

The Dissertation of Peter Dotti is approved.

Professor David Patterson

Professor Chetan Nayak

Professor David Weld, Committee Chair

March 2024

Cold Atoms in Dynamic Quasiperiodic Optical Lattices

by

Peter Dotti

To my uncle, Dr. Steven Wallis,

for sparking my interest in physics,

while encouraging a 7 year old to shout

maniacally, "The fools at the academy!"

Acknowledgements

The value of attending graduate school is perhaps less so in the undertaking of research and study itself than in learning from the company and camaraderie of a talented community of individuals engaged in the scientific process. I would like to acknowledge the many individuals who enriched my graduate school experience through good times and challenges. They have made this endeavor possible.

Foremost, I would like to acknowledge my advisor David Weld for his expert guidance regarding the many theoretical and technical questions whose resolutions have enabled the results presented in this thesis as well as for the invaluable personal and professional guidance he has offered throughout my time as a graduate student. I have greatly benefited from and sought to emulate David's gift for distilling complex ideas into a basis of simple ideas that can be understood intuitively in the generally unintuitive landscape of quantum science, which has been immensely helpful as a graduate student learning how to operate at the cutting edge of science. I am also very grateful for the empathy and consideration that he shows his students and post docs that have made graduate school endurable for me when it might otherwise not have been.

I would like to acknowledge the support of my one-time post-doc and current project scientist Toshihiko Shimasaki on the strontium machine, who I have to thank for an enormous component of my technical knowledge regarding the hardware and software of an atomic, molecular, and optical physics laboratory. He has been a stalwart presence and source of knowledge during the entirety of my time as a graduate student, and this is incredibly fortuitous for me. There are innumerable practical considerations and troubleshooting procedures that abound in an AMO physics laboratory, and Toshi has taught me the intricate procedure of identifying and solving each problem that has arisen. I have appreciated his ceaseless dedication, as well as the many conversations we have had that have ranged from serious discussions of current events

as well as frequent jovial banter that has lightened the burden of experimental challenges over the years.

I would further like to express my great appreciation for the current graduate students on strontium machine, Yifei Bai and Anna Dardia, with whom I have had the pleasure to working, learn, and teach. Since joining the lab, they have each been instrumental in data taking, data analysis, and trouble shooting of the strontium machine, and I have the fullest confidence in their skills and talents. They each bring a determination, a creativity, and their own brand of richly humorous conversation that have made for many productive and enjoyable hours spent in the lab.

Yifei has brought into the lab a stunning encyclopedic knowledge of scientific publications that a can not say I have encountered in another graduate student, along with a keen reasoning and an aptitude for producing high quality numerical simulations of quantum systems. Each of these abilities has been an incredible asset to our research efforts that have transcended the boundaries of the strontium machine to other experiments in the Weld lab. My numerous discussions with Yifei have substantially enhanced my theoretical understanding of the AAH model and greatly increased my appreciation of scientific literature, most relevantly pertaining to studies of bichromatic lattices, but also to myriad related works as well. I also have him to thank for contributions to the numerical studies presented in this thesis that dwarf my own and that have enhanced our understanding of experimental results in important ways.

Anna has an exceptional insight for discourse and discussion regarding science and other topics too great in number to recount here. Her flawless reasoning coupled with her exceptional work ethic, understanding, and dutiful record keeping have made her an invaluable experimentalist already in her relatively short time as a graduate student. Working with her has markedly improved my skills, and her unrivaled appreciation for a great many topics has vastly increased my appreciation of philosophy, society, management, music, cinema, visual art, and more. She has also rapidly developed the skills necessary to operate and troubleshoot the strontium ma-

chine which has increased productivity greatly and her contributions are displayed here in our recent experiments. I expect she will be better than me at my zenith in her operation of the strontium machine before long.

I further acknowledge the founding graduate students of the strontium machine, Ruwan Senaratne and Shankari Rajagopal, as well as the other founding graduate members of the Weld Lab, Zach Geiger, Cora Fujiwara, and Kevin Singh. Together they accomplished the extremely challenging and time consuming tasks of designing and constructing the Weld lab Bose-Einstein condensate machines, and I am grateful for having been able to learn from them and benefit from their wealth of knowledge and experience. I am also grateful for their establishing the Weld lab as a genuine community of graduate students, not just coworkers, and I had the good fortune of being welcomed and supported among them.

To Shankari I owe a debt of gratitude for her mentorship during my first several years in the Weld lab. I hope that I have at least partly replicated her successful mentorship in the subtler day-to-day rituals of the strontium machine that can only be gotten "into your bones" by practice and experience. Her PhD thesis also stands as an enduring, invaluable, and detailed recorded of the intricate components and design principles of the strontium machine. I have often referred for technical records as well as guidance. It was also a great benefit to work with someone with shared taste in memes, movies, actors like Shia LaBouf and Kristianne Baille, and music, and her recommendations in these subjects remain many of my favorite.

I would also like to acknowledge Esat Kondakci who served as a post-doc on the strontium machine and made many valuable contributions to the analysis and presentation of our recent works. I gained significant knowledge from him regarding optics procedures and equipment. I must also thank him for his work in the installation of the continuous wave titanium sapphire laser (Yggdrasil) that we use now in our experiments.

I have also benefitted from the fact that the strontium machine is collocated in the lab space of the lithium machine by the extensive interaction with its operators. Quinn Simmons and

Roshan Sajjad have notably been my companions for the entirety of their time as graduate students and for the majority of mine. In addition to stimulating scientific discussion, I must thank Quinn for his adept management of all things computers and software, that my limited knowledge of networking and computer architectures only enables me to appreciate in the fact that when there is a computer issue, he makes it go away. I must also thank Quinn and Roshan for their recent acceptance of the often thankless responsibility of managing the shared water cooling system of the strontium and lithium machine that was recently in desperate need of redress before upgraded it. More valuable than this to me though has been time we've spent together outside of the lab, where I've had the pleasure of friendly discussion with sentences enhancers in the form of references to shows of my youth, and a number of other fascinating, enjoyable, and cathartic conversations.

Likewise, I have enjoyed my frequent interactions with Jeremy Tanlimco and Eber Nolasco-Martinez, the newer generation of graduate students on the lithium machine. I have gained a fair bit of insight from our casual conversations in which I have learned about their solutions to complex problems that I had not personally considered. I have, on a more personal level, appreciated their dedication to the tradition of lab game, to which I am perhaps a distant third in attendance, but not for lesser enjoyment.

The lithium team has also hosted the post-docs Hector Mas and Xiao Chai whose tenures in the lab did not overlap, but who share similar easy-going and amicable natures that have made them very approachable and freely giving from their wealths of AMO and related technical knowledge.

I would further like to acknowledge the young potassium team, Jared Pagett, Jeremy Estes, and Madeleine Bow Jun Leibovitch. The barrier of a doorway between our experiments does little to limit our interaction, and I have appreciated the many treasured, fruitful, and entertaining discussions that have come out of their shared willingness to discuss all manner of experiments, AMO theory, and anything else that's going. I have been enlightened to learn the

various solutions they have implemented in the course of construction of the potassium machine, and I have enjoyed the occasions that I have been able to partake in the distinct and rich culture of the potassium machine (and I'm very glad that my offhand suggestion of decorative clouds was made real with flying colors.) I would also like to add that as a former member of the strontium team, Jared contributed in several critical ways to a number of the experiments discussed below through data taking and analysis as well as through the benefit of his exactingly precise yet creative implementations of a number of valuable upgrades to the strontium machine.

Special acknowledgment need also be given to Alec Cao, whose quick wit, astounding work ethic, and belief in what is possible for science made him uncommon among undergraduates for his many hours in the lab throughout his four years of undergraduate study at UCSB. He extensively and meaningfully impacted numerous scientific efforts in the Weld lab, and his contributions are subtly on display in various works of this thesis, from his early work with optical lattice setups, to his contributions regarding the kicked AAH model. His positive attitude made him pleasure to mentor, to the extent that I mentored him, since towards the end of his undergraduate degree, I would estimate he had accumulated the skills rivaling or exceeding those of third year graduate student. Perhaps more personally enduring, I cherish the daily, delightfully absurd, and jolly interactions that for a couple years defined the interactions between Alec, Toshi, and myself in the late hours of the day.

Max Prichard has also earned special acknowledgement as the most accomplished undergraduate strontium machine operator. I am grateful to him for collecting several data sets presented in parts of this thesis. He also implemented several very useful hardware and software features to the strontium machine that have become valuable for daily use, which he provided with an incredibly considerate politeness along with a motivated excitement that made it a pleasure to work with him.

I would also like to acknowledge several current undergrads, Xuanwei Liang, Samyuktha

Ramanan, Siddharth Mukherjee, and Jack Kingdon, who I have had the pleasure of mentoring on occasion with various projects. They have each at various times run into subtle and interesting questions of AMO physics and electronics development, and working through the various problems with them has enhanced my understanding of these topics as well. It has been a joy to see them develop into competent and promising scientists, and I look forward to hearing of the future accomplishments that I am certain are in store for them.

I would like to share, too, an acknowledgement of the wealth of collaborators, mentees, and lab mates with whom I have had the pleasure of discussing science and engineering. I will surely not be able to recount them all here and this appreciation is woefully inadequate given the benefits and joys I have received for having known and worked with them. Nevertheless, I offer this recognition of Kimberlee Keithley, Zak Espley, Katya Weiss, James Chow, Shuo Ma, Yi Zeng, Chisondi Warioba, Addison Hartman, Brian Bauer, Eila Neuroth, Morgan Brubaker, Sean Frazier, Jacob Hines, and countless others.

Additionally, I would like to acknowledge Professor Tengiz Bibilashvili with whom I had the great pleasure of serving as a teaching assistant for the College of Creative Studies (CCS) introductory series and a number of classes in later quarters. His unwavering dedication and compassion for all of his students has been inspiring to me. He teaches physics classes of incredible caliber in their effectiveness of learning outcomes and ability to engage students with interesting and challenging problems. Much of my ability as a mentor and teacher are merely attempts to recreate his teaching style. It has been a joy to see how unanimously beloved he is by his students through my time as a graduate student, and he creates a truly supportive extended family of students and mentors through his leadership in the CCS physics program. I was grateful to have a part in the important work that he does, and I am grateful to the many CCS students I have gotten to teach and learn from, who welcomed me open-heartedly into the CCS community.

And finally, I would like to acknowledge the extensive network of family and friends out-

side of the lab with whom I shared many fond memories, and who have supported me throughout my time graduate school. I have not the space nor words here to adequately express my gratitude, but if you are reading this, know that you sustained me through this challenge-filled chapter of my life.

Curriculum Vitæ

Peter Dotti

Education

2024	Ph.D. in Physics (Expected), University of California, Santa Barbara.
2018	M.A. in Physics, University of California, Santa Barbara.
2015	B.A. in Physics, University of California, Berkeley
2015	B.A. in Applied Mathematics, University of California, Berkeley

Publications

Stainless steel microcapillary array nozzle for in vacuo high temperature atomic sources. P. Dotti, X. Chai, D. M. Weld. *In Preparation*

Localization phase diagram controlled by the interplay of disorder and driving. P. Dotti, T. Shimasaki, Y. Bai, A. R. Dardia, D. M. Weld. *In Preparation*

Reversible phasonic control of a quantum phase transition in a quasicrystal. T. Shimasaki, Y. Bai, H. E. Kondakci, P. Dotti, J. E. Pagett, A. R. Dardia, M. Prichard, A. Eckardt, and D. M. Weld, arXiv:2312.00976 (2023).

Anomalous localization in a kicked quasicrystal. T. Shimasaki, M. Prichard, H. E. Kondakci, J. E. Pagett, Y. Bai, P. Dotti, A. Cao, T.-C. Lu, T. Grover, and D. M. Weld, *Nature Physics* (2024).

Phasonic Spectroscopy of a Quantum Gas in a Quasicrystalline Lattice. S. V. Rajagopal, T. Shimasaki, P. Dotti, M. Raciunas, R. Senaratne, E. Anisimovas, A. Eckardt, and D. M. Weld. *Physical Review Letters* **123**, 223021 (2019).

Quantifying and controlling prethermal nonergodicity in interacting Floquet matter. K. Singh, K. M. Fujiwara, Z. A. Geiger, E. Q. Simmons, M. Lipatov, A. Cao, P. Dotti, S. V. Rajagopal, R. Senaratne, T. Shimasaki, M. Heyl, A. Eckardt, and D. M. Weld. *Physical Review X* **9**, 041021 (2019).

Quantum simulation of ultrafast dynamics using trapped ultracold atoms. R. Senaratne, S. V. Rajagopal, T. Shimasaki, P. E. Dotti, K. M. Fujiwara, K. Singh, Z. A. Geiger, and D. M. Weld. *Nature Communications* **9**, 2065 (2018).

Abstract

Cold Atoms in Dynamic Quasiperiodic Optical Lattices

by

Peter Dotti

It is well known that quasiperiodicity in the Aubry-André-Harper (AAH) model produces a localized phase of the system when the on-site potential term is sufficiently large. It is also the generic experience of an experimentalist that externally applied time-periodic potentials will add energy to a quantum system, resulting in heating. However, contrary to this intuition, dynamic localization occurs in lattice potentials of particles exposed to a time-periodic force of appropriate amplitude. The drive in this case reduces the rate of spreading and at certain amplitudes arrests the spread of the particles entirely. This is well established theoretically and has been observed experimentally.

In this thesis, we present results of experimental and theoretical investigation into the effects of a number of dynamic generalizations of the AAH model. We explore the effect of applying a time-periodic external potential (chapter 5), as well as the effect of making the potential term in the AAH model periodically pulsed, referred to as the kicked AAH model (chapter 4), and the effect of periodically translating the potential in the AAH model relative to the underlying tight-binding lattice in two different frequency regimes (chapter 4). We describe the not obvious consequences of this incorporation of dynamics into experimental systems of ultracold atoms in quasiperiodic potentials.

Contents

A Musing

The world is imbued with inexhaustible richness by the fact that elemental entities ubiquitously coalesce into unfathomably permutable formations. Elements of nature, mathematics, society, art, literature, technology, and thought itself are everywhere assembled into assemblies that are elements themselves in assemblies of greater complexity. Atoms aggregate into molecules, molecules into the biochemistry of life, cells into beings, beings into communities; this is but one branch of an incomprehensible tree illustrated in these words less deftly than a painting of Monet might be illustrated with a stick in wave-muddied sand by a child before the tide comes in.

Yet, humanity appears graced with understanding, some capacity to find order in the vastness. Logic and mathematics, informed by investigation, seem to enable a grasp of the patterned relationships between elements, time, and space. This process of making hypotheses and finding evidence for them is the central procedure of science.

The atomic, molecular, and optical physicist artificially, but productively, conceptualizes three isolated elements, namely, electrons, nuclei, and a rather wide band of electromagnetic radiation. The behavior of these elements in time and space is contextualized most often in the mathematics of the Schrödinger equation and the postulates of quantum mechanics to provide an impressively accurate description of these elements' behavior. Historically, study has centered on spectroscopic measurements of the electronic structure that naturally arise in atoms and molecules, but more recently there has risen an exciting venture to precisely control ensembles of atoms in time and space to demonstrate what manifestations of quantum mechanics may exist, proven by direct fabrication. What follows is the presentation of a small set of efforts in this vein.

Chapter 1

Introduction

As an introduction, we will present information on the concept of dynamic quantum systems and the Aubry-André-Harper model. We have included a fair degree of historical connection between problems and technical details that can be safely skimmed or ignored on a first read, but we feel its inclusion in this thesis is important to give context for the work that is later presented.

An Overview of Driven Systems

In this thesis, we will focus on quantum particles under the influence of an explicitly time-varying potential, which will referred to as an "applied drive" to emphasize their controlled external application. The time evolution of the particle state is described by the Schrödinger equation, containing time dependent potential terms. In our study, the quantum particles are ^{84}Sr atoms that have been cooled to extremely low temperatures so as to begin in the state of a Bose-Einstein condensate when introduced into these time varying systems.

In the specific cases we consider, the time dependent potentials will be periodic in time. We will observe in subsequent sections that previous theoretical analyses using Floquet theory well describe these driven systems when the period of these potentials is appropriately small,

i.e., when the frequency is quite high. When we say the frequency is "high" we are comparing it to the width of the energy spectrum of the model Hamiltonian, i.e., the difference in energy between the highest $E_{\max}$ and lowest energy state $E_{\min}$. To be precise then, the drive frequency ν is high if $h\nu \gg E_{\max} - E_{\min}$. Of course, it is often the case that there is no maximum energy state of a quantum system, and that will technically be our case, but our approximate descriptions of the system will have a well defined $E_{\max}$. When higher energy states are physically occupied, we will be able to disregard them as lost, but we will aspire to operate in regimes where these states are not occupied on the time scale of our experiment. Our explorations will at times extend beyond the relative familiarity of these high frequency regimes into the regime where $h\nu \approx E_{\max} - E_{\min}$, which reveal novel and previously unpredicted responses.

The details and concepts of Floquet theory are quite complicated and the models are interesting to consider. However, we will not spend much time introducing them here. Instead, we recommend the excellent resources in references [1, 2, 3, 4, 5] that already serve as introduction to the subject and that are particularly well matched to the scope of this thesis.

The Aubry-André-Harper Model and the Hofstadter Butterfly

The focus of this thesis will be on time varying-versions of the Aubry-André-Harper model, which, in the original static case, is given by the tight-binding Hamiltonian

$$H_{\text{AAH}} = -J \sum_l \Big[|l+1\rangle\langle l| + |l\rangle\langle l+1| \Big] + \Delta \sum_l \cos\left(2\pi\beta(l-\delta)\right) |l\rangle\langle l| \tag{1.1}$$

where J, Δ, β, and δ are constant parameters of the system. A specific form of this Hamiltonian was studied by Harper [6] and Hofstadter [7] in the context of crystals subject to magnetic fields and later by Aubry and André [8] for different values of Δ. This model is directly realized in our cold atom experiments using optical lattices, which is the context in which we will discuss it for the most part. As is typical in tight-binding models, state $|l\rangle$ represents the state localized

on site number l, which has neighboring states $|l+1\rangle$ and $|l-1\rangle$.

The Aubry-André-Harper model gives rise to a striking dependence on the value of β. If β is a rational number written as p/q, where p and q are integers, then the system is periodic in space with period q. One can apply Bloch's theorem and solve for the eigenstates and energies to discover that there are q separate energy bands. The exact range of energies included in each band and the gaps between will depend on J and Δ, or just Δ/J if we work in energy units of J. In the limit $J \gg \Delta$ the gaps are small and grow as Δ increases until ultimately, the potential energy $\Delta\cos(2\pi\beta(l-\delta))$ on site l dominates to determine q very narrow energy bands that look more like energy levels.

This consideration then begs the question, what occurs when β cannot be written as p/q, that is to say, when β is irrational? Naturally, there will no longer be any continuous bands, rather as originally pointed out by Hofstadter [7], the energy spectrum will be like the Cantor set, having infinitely many points but measure zero. (In fact, Hofstadter calls this "a Cantor set.") However, as with the Cantor set, there is still structure. Typically, there will be energy gaps of varying widths. In these cases, the largest gaps will look like band gaps at some resolution, and the distribution and scale of these gaps are related to the rational approximations of β. This leads to a hierarchical structure of energy regions. (See for example, reference [9] and the references therein.)

As alluded to before, there is a close relationship between the AAH model and crystals subject to magnetic fields. We will set our goal here to describe the mathematical connection between these two models. In short, the studies of Harper and Hofstadter find equation (1.1) to arise in a process of separation of variables when solving the 2D tight-binding Hamiltonian of a single particle in a square lattice in a uniform magnetic field B perpendicular to the lattice. Toward a fuller illumination of this statement, let us describe the tight-binding basis on a square

lattice with lattice spacing a as the set of states

$$\{\, |l,m\rangle \mid l,m \in \mathbb{Z} \,\}.$$

Here, $|l,m\rangle$ is taken to be the state localized on the lattice site at coordinates $x = la$, $y = ma$. We will describe the magnetic field as $B\hat{\mathbf{z}} = \nabla \times \mathbf{A}$, taking $\mathbf{A} = Bx\hat{\mathbf{y}}$ after making a choice of gauge for the magnetic vector potential $\mathbf{A}$. With this model, Hofstadter describes the system with the Hamiltonian

$$\begin{aligned} H_{\text{Hof}} = -J \sum_{l,m} \Big[\; |l+1,m\rangle\langle l,m| \; + \; |l-1,m\rangle\langle l,m| \; + \\ e^{-i2\pi\alpha l} |l,m+1\rangle\langle l,m| \; + \; e^{i2\pi\alpha l} |l,m-1\rangle\langle l,m| \; \Big] \end{aligned} \tag{1.2}$$

where $\alpha \equiv Ba^2/(hc/Q)$ for a particle with charge Q. In solid state systems, one is usually concerned with the case of electrons in the lattice so that $Q = -|e|$, where e is the charge of the electron.

We will not rigorously prove here how Hamiltonian (1.2) is derived from the consideration of a 2D square lattice potential of charge particles in a magnetic field perpendicular to the lattice. Instead, we offer motivation in parallel to Hofstadter's explanation [7, 10]. Consider that another way to write the 2D square lattice tight-binding Hamiltonian when $\mathbf{B} = 0$ is

$$H_{\text{Square,TB}} = -J \left[\; e^{ip_x a/\hbar} + e^{-ip_x a/\hbar} + e^{ip_y a/\hbar} + e^{-ip_y a/\hbar} \; \right] \tag{1.3}$$

where $p_x = -i\hbar\partial/\partial x$ and $p_y = -i\hbar\partial/\partial y$ are the x and y momentum operators. $e^{ip_x a/\hbar}$ is the translation operator that translates a state one lattice site in the positive x direction, and one can see that in this model that $e^{ip_x a/\hbar} = \sum_{l,m} |l+1,m\rangle\langle l,m|$ since it satisfies $e^{ip_x a/\hbar}|l,m\rangle = |l+1,m\rangle$. The other terms in equation (1.3) behave in an analogous manner. Thus, it is clear that, for the

case $\mathbf{A} = 0$, $H_{\text{Square,TB}} |l, m\rangle = H_{\text{Hof}} |l, m\rangle$ for any l, m, hence, $H_{\text{Square,TB}} = H_{\text{Hof}}$.

We can then argue that a magnetic field applied to the 2D square lattice should amount to altering $H_{\text{Square,TB}}$ by replacing $\mathbf{p}$ with $\mathbf{p} - Q\mathbf{A}$, as is done in the free space Hamiltonian when a magnetic field is present. Making such a replacement in the case $Q\mathbf{A} = QBx\hat{\mathbf{y}}$ transforms $H_{\text{Square,TB}}$ into H_{Hof}.

To see how considering the AAH Hamiltonian (1.1) follows from the model (1.2), Hofstadter supposes as an ansatz that the eigenfunctions $|\psi\rangle$ of the Hamiltonian take the form

$$|\psi\rangle = \sum_l e^{i2\pi\nu m} c_l |l, m\rangle$$

and concludes that the eigenvalue problem is equivalent to solving for the coefficients c_l. This is a valid approach, but we prefer to present a slightly different perspective to reach an equivalent conclusion. That is, we would rather re-express Hamiltonian (1.2) in terms of a different basis of states denoted $|l\,;\nu\rangle$ related to the basis $|l, m\rangle$ by the Fourier transform

$$|l, m\rangle = \int_{-1/2}^{1/2} \mathrm{d}\nu\; e^{i2\pi\nu m} |l\,;\nu\rangle$$

The new basis $|l\,;\nu\rangle$ has the orthonormal property $\langle l\,;\nu\,|\,l'\,;\nu'\rangle = \delta_{l,l'}\delta(\nu - \nu')$, where the first delta is the Kronecker delta and the second is the Dirac delta. By substitution of this expression (and its hermitian conjugate) into (1.2), we can show that

$$\begin{aligned} H_{\text{Hof}} &= \int_{-1/2}^{1/2} \mathrm{d}\nu\; (-J) \sum_l \Big[\; |l+1;\nu\rangle\langle l\,;\nu| \;+\; |l-1;\nu\rangle\langle l\,;\nu| \;+\; 2\cos\left(2\pi(\alpha l - \nu)\right)\; |l\,;\nu\rangle\langle l\,;\nu| \;\Big] \\ &= \int_{-1/2}^{1/2} \mathrm{d}\nu\; H_{\text{Hof},\nu} \end{aligned} \tag{1.4}$$

where we have introduced the notation $H_{\text{Hof},\nu}$ for the expression in the integral and will discuss its relation to the AAH Hamiltonian momentarily.

From the form of equation (1.4), we conclude that the eigenstates are of the form

$$|\psi\rangle = \sum_l c_l \, |l\,;\nu\rangle$$

One can then venture to solve for the energy spectrum, indexing the states with a new index μ along with the index ν from the Fourier transform. This implies solving the equation

$$H_{\text{Hof}} \, |\psi\rangle_{\mu,\nu} = H_{\text{Hof},\nu} \sum_l c_l^{(\mu,\nu)} \, |l\,;\nu\rangle = E_{\mu,\nu} \sum_l c_l^{(\mu,\nu)} \, |l\,;\nu\rangle = E_{\mu,\nu} \, |\psi\rangle_{\mu,\nu}$$

which, is an eigenvalue problem to find eigenvalues $E_{\mu,\nu}$ and coefficients $c_l^{(\mu,\nu)}$ that define the eigenvectors in the $|l\,;\nu\rangle$ basis. We note that the newly introduced μ must index an uncountably infinite set, and we will discuss this more in a moment.

At this point, we can achieve our original goal and recognize how the Hofstadter energy spectrum is related to the AAH Hamiltonian (1.1). Let us consider the AAH Hamiltonian for the case

$$\Delta = 2J, \; \beta = \alpha, \; \text{and} \; \delta = \nu/\beta$$

Solving for the eigenstates $|\psi\rangle_\mu = \sum_l c_l^{(\mu)} \, |l\rangle$, that satisfy

$$H_{\text{AAH}} \, |\psi\rangle_\mu = E_\mu \, |\psi\rangle_\mu$$

is equivalent in this case to solving for the eigenenergies of H_{Hof} for eigenstates of the form $|\psi\rangle_{\mu,\nu} = \sum_l c_l^{(\mu)} \, |l\,;\nu\rangle$

$$H_{\text{Hof}} \, |\psi\rangle_{\mu,\nu} = H_{\text{Hof},\nu} \, |\psi\rangle_{\mu,\nu} = E_{\mu,\nu} \, |\psi\rangle_{\mu,\nu}$$

Therefore, the whole spectrum of H_{Hof} is obtained by finding the spectra of the AAH Hamil-

tonian for all of the possible distinct values of δ, when $\Delta = 2J$. It is this mapping between the problems that underlies the close relationship between the H_{Hof} and H_{AAH} Hamiltonians.

As mentioned, we note that newly introduced μ must index an uncountably infinite set of energies E_μ for the solution of the eigenvalue problems above. In the case that α is a rational number, the H_{AAH} (and $H_{\text{Hof},\nu}$) take the form of a periodic 1D lattice, and μ is quite naturally substituted with a discrete band index n and a continuous quasimomentum q, i.e., we can make the replacement $\mu \to n, q$. The fact that quasimomentum is continuous preserves the cardinality of the set of μ values. However, when α is irrational, which is the more relevant situation in this thesis, there is not such an obvious labeling of states. The problem is similar to that of indexing the Cantor set, but we will not present here a way to index the set of energies that arise.

The Aubry-André-Harper Model More Generally

The AAH Hamiltonian has been studied more generally in the case that $\Delta \neq 2J$. This was first explored by Aubry and André [8], and it was later more technically shown that when β is an irrational number and $\Delta/J > 2$, it typically arises (with exceptions to be discussed momentarily) that the eigenstates will exponentially decay away from a lattice site $|l\rangle$ with some length scale [11]. In other words, in this case, the eigenstates will be localized at site $|l\rangle$. In contrast, when $\Delta/J < 2$, all of the eigenstates are delocalized in that they have significant occupation at points across the whole lattice.

The reason that $\Delta/J = 2$ is the special value was originally given by Aubry and André [8]. They argued that when β is irrational, we can define a dual basis of states denoted by $|k_{\text{d}}\rangle$, related to the original basis by

$$|l\rangle = \frac{1}{\sqrt{\Gamma}} \sum_k e^{-i2\pi\beta(kl - k\delta - l\delta)} |k_{\text{d}}\rangle \tag{1.5}$$

and likewise

$$|k_{\mathrm{d}}\rangle = \frac{1}{\sqrt{\Gamma}} \sum_{l} e^{i2\pi\beta(kl - k\delta - l\delta)} |l\rangle \tag{1.6}$$

where $1/\sqrt{\Gamma}$ gives a normalization factor. In the case that the lattice size is infinite the sums in equations (1.5) and (1.6) are over all integers and there is no numerical value of Γ that satisfies the normalization condition on $|l\rangle$. However, this case is not dissimilar from what arise one considers the unnormalized momentum basis in continuous space, and Aubry and André take $\Gamma = 1$. Note that it is critical to the argument that β be irrational for an infinite number of lattice sites. Otherwise, the relationship in equation (1.5) does not work, for if $\beta = p/q$ for integers p and q, then it would imply that the state $|l = 0\rangle$ is the same state as $|l = q\rangle$, and we cannot consider equation (1.5) to be a proper basis transformation.

One can also consider cases in which the model is finite with N lattice sites with periodic boundary conditions. This is important in numerical studies of the AAH model in finite systems. In these cases, the sums in equations (1.5) and (1.6) are from 1 to N, and we can take $\Gamma = N$, to save the considerations of infinities in normalization. However, in this case we do not want β to be irrational, but instead, we want β expressed as the irreducible fraction p/N. Equivalently, we want integers p and N to be coprime. This should be sufficient to ensure that a proper basis is defined. It is also worth noting that this transformation is very much like a Fourier transformation on discretized space, and the normal Fourier transformation arises for the special case $\beta = 1/N$. When $\beta = p/N$, the set of $|k_{\mathrm{d}}\rangle$ basis vectors is still the Fourier basis, but "reorganized" (except when $p = 1$,) which is relevant to the meaning of the tunneling terms $|(k+1)_{\mathrm{d}}\rangle\langle k_{\mathrm{d}}|$ that we will see in a moment.

In either case, we can make the substitution (1.5) and express the AAH Hamiltonian (1.1) in this dual basis to find

$$H_{\mathrm{AAH}} = \frac{\Delta}{2}\left[-\sum_{k} \Big(|(k+1)_{\mathrm{d}}\rangle\langle k_{\mathrm{d}}| + |k_{\mathrm{d}}\rangle\langle (k+1)_{\mathrm{d}}| \Big) + \frac{4J}{\Delta} \sum_{k} \cos(2\pi\beta(k-\delta)) |k_{\mathrm{d}}\rangle\langle k_{\mathrm{d}}| \right] \tag{1.7}$$

We see that the AAH Hamiltonian in this dual basis has the exact same form as in the position basis (1.1), but with the replacements $J \to \Delta/2$ and $\Delta \to 2J$. When $\Delta/J = 2$, we have the special case that the Hamiltonian in the position basis and the dual basis are exactly equivalent.

A point made by Aubry and André is that, for an infinite lattice, if an eigenstate for a specific pair of values J and Δ in the basis dual basis $|\psi\rangle = \sum_k f_k |k_\mathrm{d}\rangle$ is localized in the sense that $\sum_k |f_k|^2 < \infty$ then it will be delocalized in the position basis so that writing $|\psi\rangle = \sum_l c_l |l\rangle$ gives $\sum_l |c_l|^2 = \infty$, and vice versa. This fact suggests that if all states are localized in the position basis when $\Delta/J > 2$, then they will all be delocalized in the dual basis where the corresponding $4J/\Delta < 2$, and if the opposite case of $\Delta/J < 2$ is considered, then all of the states should be localized in the dual basis and delocalized in the position basis. This reasoning implies that if a transition between a localized and delocalized phase exists, it should occur at $\Delta = 2J$. (See discussion near equation 79 in reference [8].)

The exact nature of the eigenspectrum and corresponding localization properties of the eigenfunctions were proven by Jitomirskaya [11]. The resulting statement is the following theorem, which we rephrase slightly for the current context:

THEOREM: *For all but an infinitesimal fraction of irrational values $\beta \in \mathbb{R}$ and $\delta \in \mathbb{R}$, the Hamiltonian H_AAH* (1.1) *has*

1. *For $\Delta/J > 2$, a pure point spectrum with exponentially decaying eigenfunctions,*

2. *For $\Delta/J = 2$, a purely singularly-continuous spectrum, and*

3. *For $\Delta/J < 2$, a purely absolutely continuous spectrum.*

Jitomirskaya further states a belief that point 2 is true for all irrational values of β and all values of δ, and a belief that point 3 of the theorem is true for every value of β (including rational values) and every value of δ, which suggests to us a very "Bloch wave-like" nature to the resulting spectrum and solutions when $\Delta/J < 2$ in all cases.

The Aubry-André-Harper Model in Relation to the Anderson Model

The localized states of the AAH model are often compared to the localized states that occur in the Anderson model [12] given by

$$H_{\text{Anderson}} = -J \sum_l \left[|l+1\rangle\langle l| + |l\rangle\langle l+1| \right] + \Delta \sum_l w_l |l\rangle\langle l| \tag{1.8}$$

where w_l is a random variable sampled uniformly from the range $[-0.5, 0.5]$ as a function of l. There are of course many realizations of Hamiltonian (1.8) depending on which random values of w_l you consider, but it is generically the case that all of the eigenstates are localized for every value of $|\Delta| > 0$. The scale over which the eigenstates are localized naturally depends on the magnitude of Δ, but they are localized nonetheless. And it perhaps goes without saying that, given the random sampling of w_l, the localization occurs for all but an infinitesimal fraction of special cases, such as when $w_l = 0$ for all values of l, but it is safe to ignore these improbable cases.

Aubry and André took an interest in their namesake model because there is a transition between a phase of localized eigenstates and delocalized eigenstates in the space of Δ and J values. The localization behavior is in many ways similar to the localization that occurs in Anderson localization, and one can heuristically consider the AAH model with irrational β to look somewhat like a random on-site potential. However, as is already apparent by the phase transition at finite values of Δ, the fact that the on-site potential preserves a long scale order realizes different behavior than truly random potentials in certain ways.

The Structure of This Thesis

In chapter 2, we discuss the design of "the strontium machine," the apparatus that was used to conduct the later discussed experiments. In chapter 3, we present a review on the mathematical description of light and optical lattices along with a review of the mechanism

of the optical dipole trap that underlies the optical lattice. In chapters 4 and 5, we present recent research on dynamic versions of the AAH model. In chapter 6, we present designs for optical lattice control schemes that could be used for novel study of time varying 2D optical lattice potentials and bichromatic lattice potentials with relative phase control. We also include a selection of technical appendices regarding machine designs and computational resources.

Chapter 2

Machine Design

The majority of the design of the strontium machine has been well documented in the PhD theses of Shankari Rajagopal [13] and Ruwan Seneratne [14]. However, a number of upgrades and changes have taken place in the meantime, which we aspire to illuminate in this section.

2.1 461 nm and 403 nm Laser System

Given their shared laser table and since the 403 nm laser frequency is referenced to the 461 nm laser, we will provide information regarding the 461 nm and 403 nm laser systems together. A number of changes have been made to the setup over the years, and we will use this section to provide a record of the changes. Section 5.1.4 of Shankari's thesis [13] should be referenced for complementary details.

A diagram of the optics in figure 2.1 serves as a visual overview of the laser optics. We also present a laser frequency diagram for the 461 nm laser beams in figure 2.2 as an aid in understanding the functions of the acousto-optic modulators (AOMs) depicted in figure 2.1.

The 461 nm laser is used for the first stages of optical cooling and trapping, as well as absorption imaging in our experiments. The light is sourced from a commercial laser system

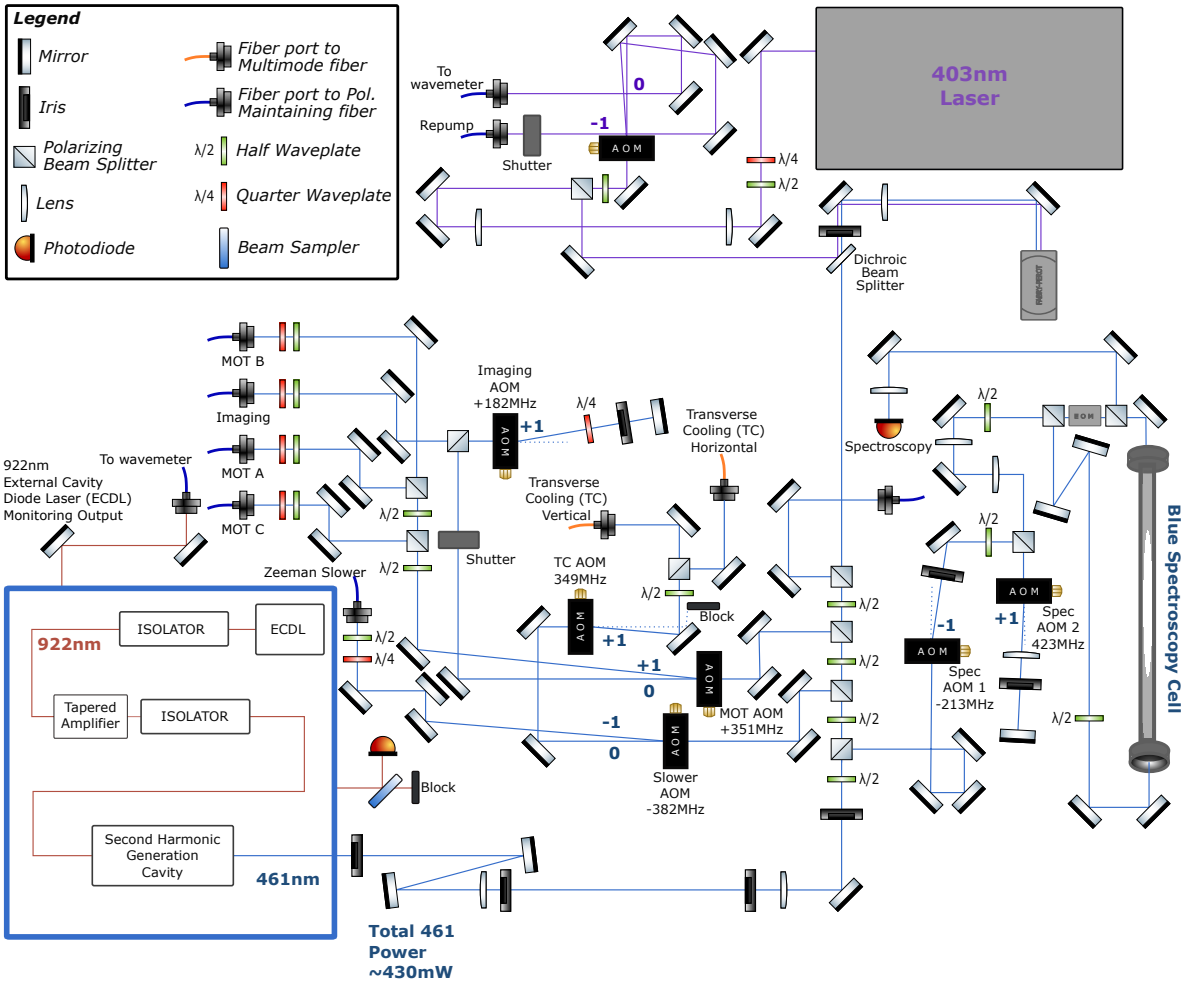

Figure 2.1: Diagram of the the optics used for the 461 nm laser and the 403 nm (repump) laser. Bold numbers after the AOMs indicate which diffraction orders are used.
Diagram Credit: Anna Dardia

(TOPTICA, Product ID: TA-SHG pro_14085) that utilizes second harmonic generation of an amplified 922 nm laser beam. All 461 nm laser beams are near resonance with the broad (30.5 MHz) linewidth $5s^2\,{}^1S_0$ to the $5s5p\,{}^1P_1$ atomic transition of strontium. The laser's frequency is stabilized ("locked") to a spectroscopy cell that is used as a reference, and one of the main technical changes to the report in this thesis is the upgrade to the method of error signal generation and an associated change to the electronics. This upgrade allowed for a dramatic reduction in the amount of laser power required to generate a robust spectroscopy signal. In fact, one is able to produce a robust error signal for locking even though the Doppler free absorption signal appears to have poor signal-to-noise ratio by eye at these low laser powers. The details of this new setup are documented separately in appendix B.

The Zeeman slower [15, 16], utilizing a spin flip design, is the first stage of cooling. The atomic source is an oven held at 510°C with an effusive nozzle [17] held at 560°C. Effective slowing of the atomic beam exiting the oven requires the largest fraction of the 461 nm laser power. The choice of frequency shifts depicted in figure 2.2 reflects this requirement; only one AOM is needed to shift the frequency from the laser output to the desired frequency of the Zeeman slower laser beam. If more AOMs were used to produced this beam from the laser, it would lead to a large amount of wasted power due to finite AOM diffraction efficiency. A 10 m long polarization maintaining (PM) optical fiber with protective end-caps for handling the high power (Coastal Connections Model: P-FAnskFAnsk-3.8/125/3-10) carries the Zeeman slower light from the laser table to the other optical table ("the machine table") on which the vacuum chamber sits near the Zeeman slower window. We input a beam of about 200mW into this fiber with a coupling efficiency in the range 60-72% to produce a laser beam of about 120mW in Zeeman slower. We allow the beam to diverge from the fiber before it is roughly collimated by a 1 inch diameter lens with a 50mm focal length that is mounted in a translation stage. We adjust the position of this collimating lens to optimize capture of atoms in our magneto-optical trap (MOT), which occurs when the beam converges slightly as it travels through the chamber,

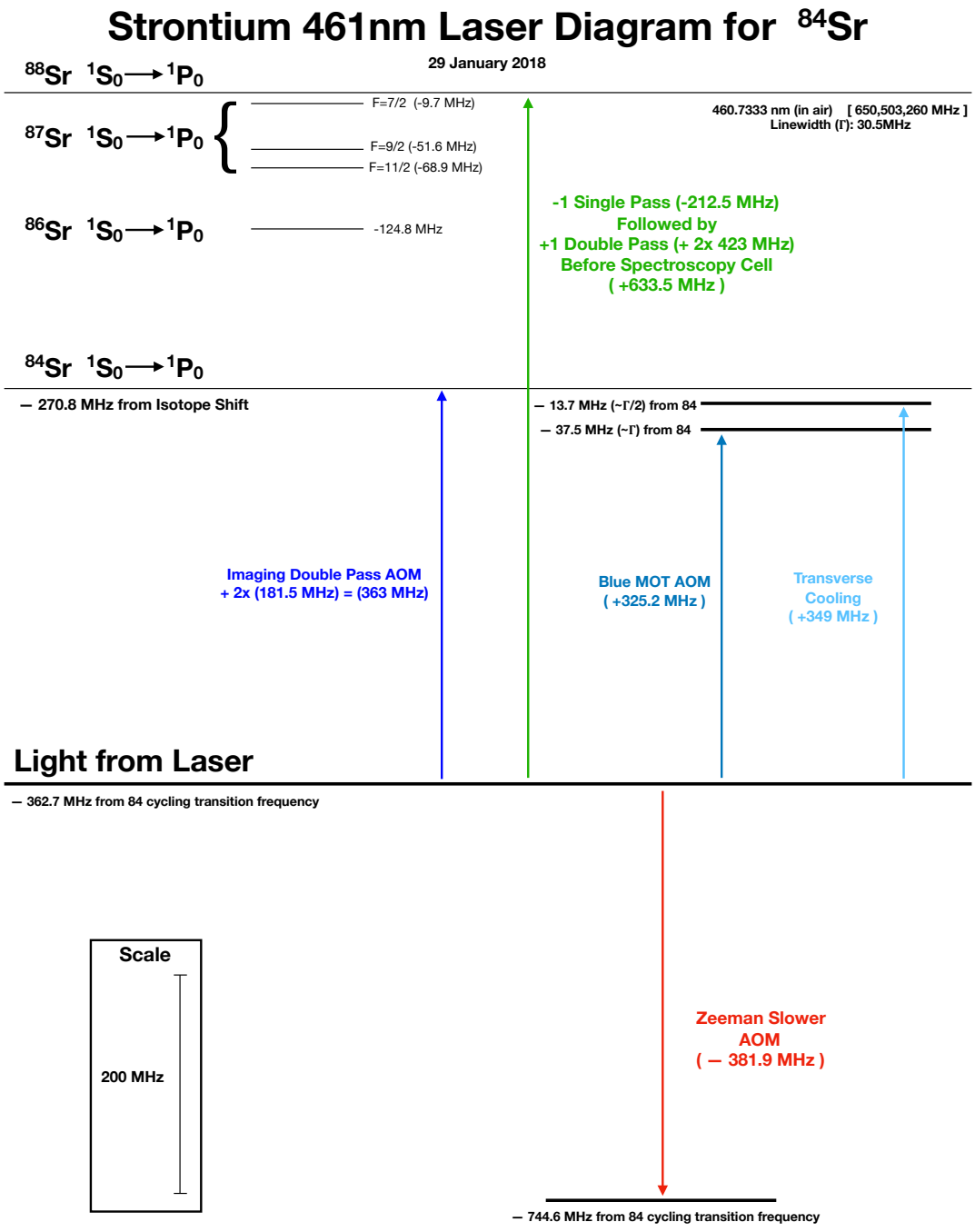

Figure 2.2: 461 nm laser frequency diagram laser beams generated on the laser table.

slower section, and differential pumping tubes towards the oven. After this lens are two quarter waveplates that are used to optimize the polarization of the slower for atom capture in the MOT, which occurs for appropriate circular polarization in the Zeeman slower. The beam is finally directed through the chamber with two 2 inch diameter mirrors.

The names MOT A, MOT B, and MOT C are used to denote the three laser beams of the magneto-optical trap that operates on the 461 nm transition (the "blue MOT"). MOT A and MOT B are directed through the chamber at 16 degrees relative to horizontal and are approximately, but not exactly, perpendicular to each other, a consequence of the cylindrical symmetry of the chamber windows. MOT C is directed at 11 degrees relative to vertical (See [14], section 4.4.3). Each of the beams is retro-reflected through a quarter waveplate, and considering these reflected beams as new beams, we have the six MOT beams. The MOT A and B beams are attached to the chamber using a mounting scheme described in figure 5.8 of [13]. We note that a practical drawback of this design is that adjusting the position of the collimating lens with the lens tube rotates the fiber, and so necessitates rotating the quarter waveplate at the same time. We would also comment that the arrangement of these MOT beams deviates quite substantially from the prototypical MOT configuration. In particular, the laser beams are not directed parallel to the magnetic field lines. This is a minor effect for the vertical beam, but is considerable for the horizontal beams. Fortunately, the MOT still functions for these angles and an analysis following, for example, reference [18] and the references therein, shows that the MOT beams will still predominantly excite the appropriately trapping σ^- transition with a lesser amount exciting the π transition (which cools but does not trap the atoms) and a very small ($\sim$1%) excitation of the anti-trapping σ^+ transition. On the laser table, the light for each of the blue MOT beams is coupled into its own fiber, and at the atoms, there are approximately 6mW in MOT A, 6mW in MOT B, and 8mW in MOT C. MOT A and MOT B are limited to a beam diameter of 0.5 inch due to the clear aperture size of the 1.33 inch CF flanges. MOT C is approximately 1 inch in diameter.

In a cooling procedure very similar to that described by Stellmer [19], the blue MOT is operated continuously to cool and capture atoms from the Zeeman slower. The blue MOT is operated without repump light so that a fraction of atoms decays to the long lived $5s5p\,^3P_2$ state where they accumulate and remain magnetically trapped in the magnetic field of the blue MOT. After operating the blue MOT for about 10 seconds, the trap is close to saturated by which we mean that the loading rate is matched by the loss rate. It is at this point in the sequence that the 403 nm laser is flashed on with a power between 1mW and 2mW to transfer atoms from the $5s5p\,^3P_2$ back to the ground state, where they can be further cooled in the "red MOT," which is the MOT operating on the narrow 7.4kHz linewidth $5s^2\,^1S_0$ to $5s5p\,^3P_1$ transition with wavelength 689 nm.

The 403 nm laser is a commercial ECDL (Sacher Lasertechnik Group, Model: TEC 150, SN: L-403-1115-01939), which repumps atoms from the long lived, magnetically trapped $5s5p\,^3P_2$ population using the transition between the $5s5p\,^3P_2$ and $5s6d\,^3D_2$ states. The 403 nm laser is stabilized relative to the 461 nm laser using the detected transmission through a commercial Fabry-Perot cavity (Thorlabs, Model: SA200-3B), whose length is repeatedly scanned with a piezo. The transmission signal as a function of cavity length is detected, and the scan range is set so that only one transmission peak for each of the lasers is observed. A program written in LabVIEW (1) plots this transmission data as a function of the piezo voltage that controls the cavity length, (2) detects the transmission peaks, and (3) implements a PID controller with feedback to the 403 nm ECDL to maintain the peak separation as a function of the cavity length over each scan. The PID setpoint for the transmission peak separation is adjusted to maximize the fluorescence of a repumped blue MOT. This is lock is typically well maintained over the course of a day except for the occasional need to adjust the scan range so that both peaks are visible on the scan. However, the 403 nm laser mode hops somewhat frequently, particularly at the start of the day, and we recover a useable mode with a wavemeter as we change the 403 nm laser diode temperature, ECDL grating piezo control voltage, and diode current to

bring the laser back near resonance with the repump transition.

2.2 Application of Intercombination Light ("Shielding") During Magnetic Trap Loading

In June 2023, we implemented the method described in reference [20] to increase the number of atoms loaded into the combined populations of the blue MOT and magnetic trap. As discussed in the reference, applying light that is near resonant with the 689 nm transition between the $5s^2\,{}^1S_0$ ($|g\rangle$) state and $5s5p\,{}^3P_1$ ($|s\rangle$) state results in a fraction of the atoms populating the $5s5p\,{}^3P_1$ ($|s\rangle$) state at any one time where they are invulnerable to loss mechanisms associated with the $5s5p\,{}^1P_1$ ($|e\rangle$) state. To achieve enhancement, we simply left the red MOT beams (see section 2.3) on during the magnetic trap loading stage, discussed previously in section 2.1, during which the blue MOT is continuously run to allow atoms to decay from the $5s5p\,{}^1P_1$ ($|e\rangle$) state into the long lived and magnetically trapped $5s5p\,{}^3P_2$ state. This impressively enhanced the number of atoms in subsequent cooling stages by 10-20%. We found this enhancement to be generally insensitive to the exact frequency of the 689 nm red MOT beams which is not so surprising given the Doppler broadening that is a consequence of the relatively high temperature of the atoms at this stage.

We note one open question for us regarding the mechanism involved here. In our machine, we are intentionally populating the metastable $5s5p\,{}^3P_2$ state for holding in the magnetic trap, and our understanding of reference [20] is that they consider this to be a loss mechanism for their purposes. In contrast to their discussion, it would seem beneficial to maximally populate the $5s5p\,{}^1P_1$ ($|e\rangle$) state, so as to most rapidly populate the metastable $5s5p\,{}^3P_2$; running the 689 nm laser for shielding would seem contrary to this purpose. Nonetheless, we do indeed observe this beneficial 10-20% enhancement in our system when we run the 689 nm laser. We

posit then that there is some other loss mechanism at play here that is partially mitigated by populating the $5s5p\,^3P_1$ ($|s\rangle$) state. One possibility is that some population of the $5s5p\,^3P_1$ ($|s\rangle$) state reduces the optical density of the blue MOT, thereby increasing the maximum number of atoms that can be held in the blue MOT. Another possibility is that some population of the atoms are being captured by their interaction with the 689 nm beams and the magnetic fields in a way that leaves them invulnerable to the loss mechanisms that typically limit the blue MOT population. We are not sure which, if either, is a good explanation for the cause of our enhancement. We emphasize that we are not refuting any of the claims in reference [20]. We are just expressing our incomplete understanding of the exact mechanism of the enhancement in our case.

2.3 689 nm Laser System

In this section, we discuss the production of 689 nm laser light for the narrow line red MOT that operates on the $5s^2\,^1S_0$ to $5s5p\,^3P_1$ transition with 7.4kHz linewidth. This is also the same system for the light used in the shielding method previously described in section 2.2. A diagram of the current laser table setup is shown in figure 2.3, and an associated frequency diagram for the produced laser beams is given in figure 2.4

Our 689 nm laser is a commercial ECDL system (TOPTICA, Product ID: DL pro_020098). We stabilize the laser's frequency against slow drift using a spectroscopy cell, however, we believe that our laser cooling is limited by the laser linewidth, as we have only ever been able to cool to several μK and more typically we only reach higher than 10 μK, limited by the trap depth of the optical dipole traps (ODTs) that we load into at the end of the red MOT, in a manner similar to [19]. Narrowing the linewidth of the laser with fast feedback to a stable cavity, as has been implemented previously by other groups, is a planned upgrade to improve this. In any case, these temperatures are sufficient to create large BECs in our machine.

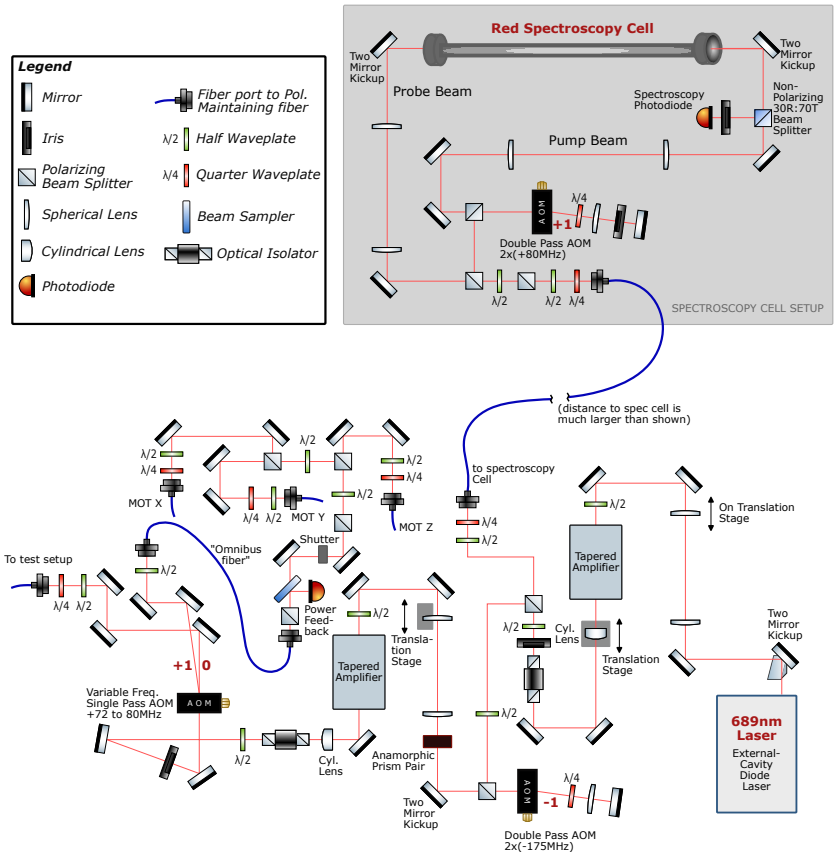

Figure 2.3: Diagram of the optics used for the 689 nm laser. Bold numbers after the AOMs indicate which diffraction orders are used.
Diagram Credit: Anna Dardia.

Our laser light undergoes two stages of amplification with tapered amplifiers (TAs) as shown in figure 2.3. We use 690 nm TA chips produced by Eagleyard, and purchased from the supplier XSoptix in a C-Mount package (XSoptix Product number: EYP-TPA-0690-00250-2003-CMT02-0000). We currently use TA mounts constructed from designs presented in the thesis of John F. Barry [21]. We have found that these tapered amplifiers seem to deteriorate over the time scale of months, which we suspect is due to the challenges of fabricating gain media at this wavelength. We try to limit the laser power out of the TAs to about 95mW each to extend the lifetime, and as we observe the output power to nonetheless deteriorate over time, we increase the TA current to compensate. This necessitates replacing a TA chip about every

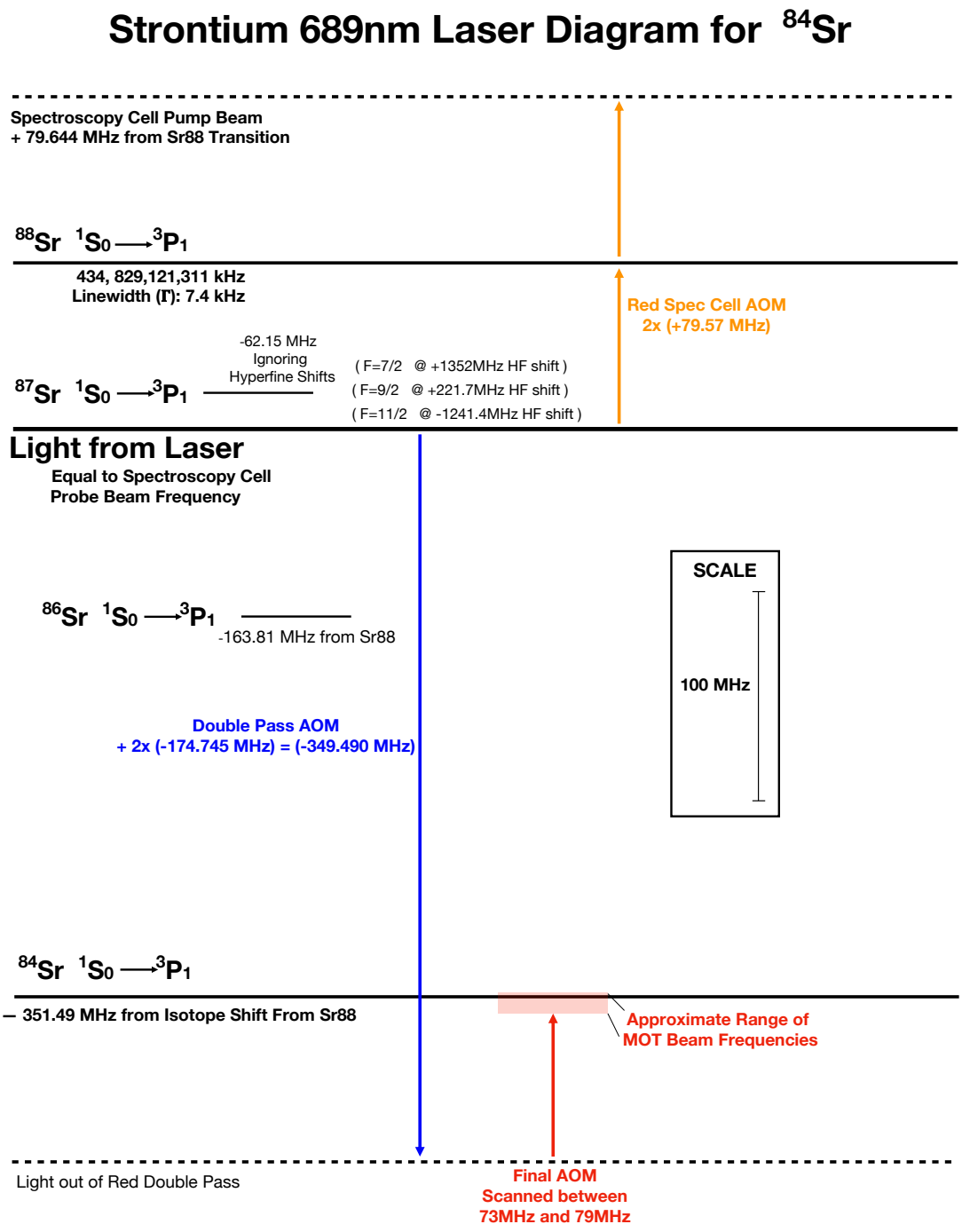

Figure 2.4: 689 nm laser frequency diagram.

two years.

After the TAs and a double pass AOM (shown in figure 2.3) that is driven with constant RF drive frequency and power, the beam passes through a single pass AOM and a fiber (the "omnibus fiber") used to clean up the laser mode and provide a static output laser mode. Use of this fiber makes it so that only the single omnibus fiber instead of the three MOT beam fibers needs to be recoupled when the TA mode changes or beam direction drift before the omnibus fiber, which are a relatively common occurrences. The power of the beam exiting the omnibus fiber is monitored with a photodiode, which is used to stabilize the power with feedback to the single pass AOM's radio frequency (RF) drive power. We do find that the feedback is unable to keep up perfectly when the frequency of the single pass is modulated with high amplitude during the first stages of the red MOT, but it does successfully stabilize as the frequency modulation tapers off. This might be improved by modulating the double pass AOM frequency instead, but we do not believe this is feasible in the current setup due to the subsequent TA that would be sensitive to beam changes during the modulation.

The beam after the omnibus fiber is then split into the three MOT beams, denoted MOT X, MOT Y, and MOT Z. These are brought to the chamber with PM fibers and are arranged in a very similar manner as the blue MOT beams, where MOT X and MOT Y are approximately in the horizontal plane, and MOT Z is approximately vertical. MOT X and MOT Y are operated with approximate equal max powers of 3mW. MOT Z is operated with a max power of approximately 6.5mW.

The red MOT is operated in three stages that are roughly the same as those described by Stellmer [19]. During the first stage ("RedMOT1"), to contain the relatively hot atoms in the MOT, we intentionally broaden the frequency spectrum of the MOT beams. We do this by modulating the frequency of the final single pass between approximately 73 MHz and 79 MHz. This is accomplished by sending a control voltage signal to the frequency modulation input of the RF driver (MOGLabs, Model: XRF421.) In the second stage ("RedMOT2"), the amplitude

of the frequency modulation is tapered down nearer to resonance with the 689 nm transition. Concurrently, the intensities of the MOT beams are reduced to mitigate power broadening of the 689 nm transition that would limit the temperature, and the optical dipole traps are partially ramped up. In the final stage ("RedMOT3"), the MOT beams' frequency is held at roughly half a linewidth detuning from the atomic transition. At the same time, the optical dipole traps are ramped to final power and the red MOT beam powers are ramped to zero. Note that MOT beam frequency is shifted in the RedMOT2 and RedMOT3 stages from the natural transition frequency due to the A.C. Stark effect (see section 3.3) in the presence of the ODTs. We experimentally adjust the final frequency to get atom count and temperature that optimizes phase space density in the optical dipole trap.

Lastly, a beam with power between 6mW and 10mW is brought to the spectroscopy setup with a PM fiber. The designs for the red spectroscopy cell used to stabilize the 689 nm laser are discussed in section 2.5. The electronics and frequency stabilization scheme are discussed in appendix C.

2.3.1 AOM Drivers

One important upgrade regarding the red MOT was made to the RF drivers that provide radio frequency (RF) power to the AOMs. Previously, the sources of RF were open loop voltage controlled oscillators (VCOs) from Mini-Circuits (Models: ZX95-100, ZX95-200+, or ZX95-535). This RF signal was then sent through an RF switch (Mini-Circuits, Model: ZX80-DR230+) and a variable voltage attenuator (VVA) (Mini-Circuits, Model: ZX73-2500+). And finally, the signal was sent through an amplifier (Mini-Circuits, Model: ZHL-3A or ZHL-2010+) sometimes also with a preamp before it (Mini-Circuits, ZX60-8008E). We used very similar designs for the RF drivers in our 461 nm laser system and for power control of the optical dipole traps (with additional amplification in that case), where they work quite robustly

and are easy to tune.

The issue with this design in the red laser system is that the VCOs are typically not quite stable to within a few kilohertz, which is necessary for laser cooling consistently on the 7.4 kHz linewidth atomic transition linewidth. We identified that drift in the frequency results from changes in the VCO temperature, and we attribute the issue predominantly to this.

Fortunately, RF stability to within 1 kHz is easily achieved when the frequency is referenced to a standard temperature compensated crystal oscillator (TCXO). This is the frequency reference in most commercial products, such as arbitrary waveform generators. For our purposes, we replaced the RF source for the spectroscopy AOM and for the 175 MHz double pass with commercial signal generators (RF-Consultant Robert Yarbrough, Model: TPI-1002-A). The details for the RF driver used for the spectroscopy AOM are discussed in appendix C. The final single pass AOM required a different RF source because, while the TPI-1002-A allows for modulation of the frequency with an AC signal, it does not allow for DC shifts of the frequency with the control voltage as we desired. In our case, we use a commercial RF driver from MOG Laboratories (MOGLabs, Model: XRF421,) which allowed for easy implementation of the modulation sequence.

2.4 Optical Dipole Traps and Optical Lattices

Recently, we changed how we generate the 1064 nm light for our experiments. We use a fraction of the power from a new narrow linewidth seed laser (Coherent Model: Mephisto 200FC Laser System) that is amplified using a 50 W constant current amplifier (Toptica/Azurlight Model: ALS-IR-1064-50-A-CC-SF.) Another general change is that we now use optical fibers (Coastal Connection Model: P-FAknsFAkns-6c/125/3-5) designed for powers greater than 1 W to transfer all of our 1064 nm laser beams from the surface of the laser table to the elevated breadboard that is at the level of the vacuum chamber. All of the waveplates and polarizing

beam splitting cubes used to divide up the 1064 nm laser power as well as the AOMs for power and frequency control of the 1064 nm light are on the laser table surface before the fibers bring them up to the chamber level breadboard. This is helpful for ensuring beam mode quality and minimizing drift.

We considered before this implementation that thermal lensing might potentially cause distorted beam modes at the output fiber collimators. For this reason, we tested fiber collimators from Schäfter+Kirchhoff (Model: 60SMS-1-4-12-37) and from Thorlabs (Model: PAF2-7C) that we planned to use. We found no detectable beam mode change as a function of power using either collimation package by measuring the collimated beam on a beam profiler (Cinogy Technologies Model: CinCam CMOS 1201.) In these tests, we measured the beam at a distance of roughly 20 cm away from each output collimator and observed the output beam mode at output beam powers up to 5 W. The only change seen were small and due to sensor effects when the profiler was set to different exposure times. From this, we concluded that any thermal lensing using these types of collimators is negligible for our experiment. We note this to be in contrast to significant thermal lensing observed with an isolator we tried from Thorlabs (Model: IO-5-1064-VHP,) and on recommendation from Azurlight, we now use one from Coherent (PAVOS series 5 mm aperture 1045-1080 nm) that does not produce significant thermal lensing.

2.5 Spectroscopy Cell for Red MOT 2022

We now discuss updated designs to the red spectroscopy cell. Our previous spectroscopy cell designs are documented in Shankari Rajagopal's thesis (Section 5.1.6, page 127, and figure I.7, page 272 of reference [13].) The designs were based on those from Simon Stellmer's thesis [19] with similar design principles, namely, making the spectroscopy cell long to reduce the flux of strontium that reaches the viewports, using a buffer gas, and using large diameter pump

and probe beams. Both viewports in our previous design were mounted with their surfaces perpendicular to the axis of the roughly cylindrical spectroscopy cell. This made the windows perpendicular to the beam path, which resulted in some undesirable interference between the reflections from the viewports and the primary beams, but otherwise did not hinder function greatly.

Over time, the functionality of the previous spectroscopy cell deteriorated. Some issues were already discussed in [13]. Two major causes were definitively identified: (1) The buildup of strontium on the viewports, and (2) the migration of strontium away from the center cup and associated formation of an annular buildup that limited the usable beam size. Before redesigning the spectroscopy cell, we reduced some of strontium layer that had deposited on the windows using 532 nm laser pulses from a Continuum Minilite Q-switched Nd:YAG laser. This technique was able to increase measured laser transmission from roughly 40% to roughly 70%.

The peak-to-peak width of our spectroscopy error signal was roughly 3 MHz. This was determined by converting the ECDL piezo voltage (x-axis of our error signal) to laser frequency of the 689 nm laser. One check of this conversion is given by Toptica's test data that states a 466 MHz shift in laser frequency per volt change in piezo voltage in the ECDL (i.e., 466 MHz/V conversion factor.) Another check was done by measuring the piezo voltage of the ^{88}Sr Doppler free spectroscopy signal peak and the Doppler limited profile minimum. The voltage difference was 0.213 V. The difference in laser frequency between these two features correspond to 79.710 MHz, the frequency of the RF drive to our spectroscopy AOM. Together, this implies 374 MHz/V, which is in good enough agreement with the quoted 466 MHz/V for our estimates. Since the error signal width was large compared to the 7.4 kHz linewidth transition, we decided that designing and ordering a new spectroscopy cell was warranted.

We ordered a custom design from ANCORP. Technical drawings provided to ANCORP are shown in figures 2.5 and 2.6. There are a couple notable changes from the previous designs.

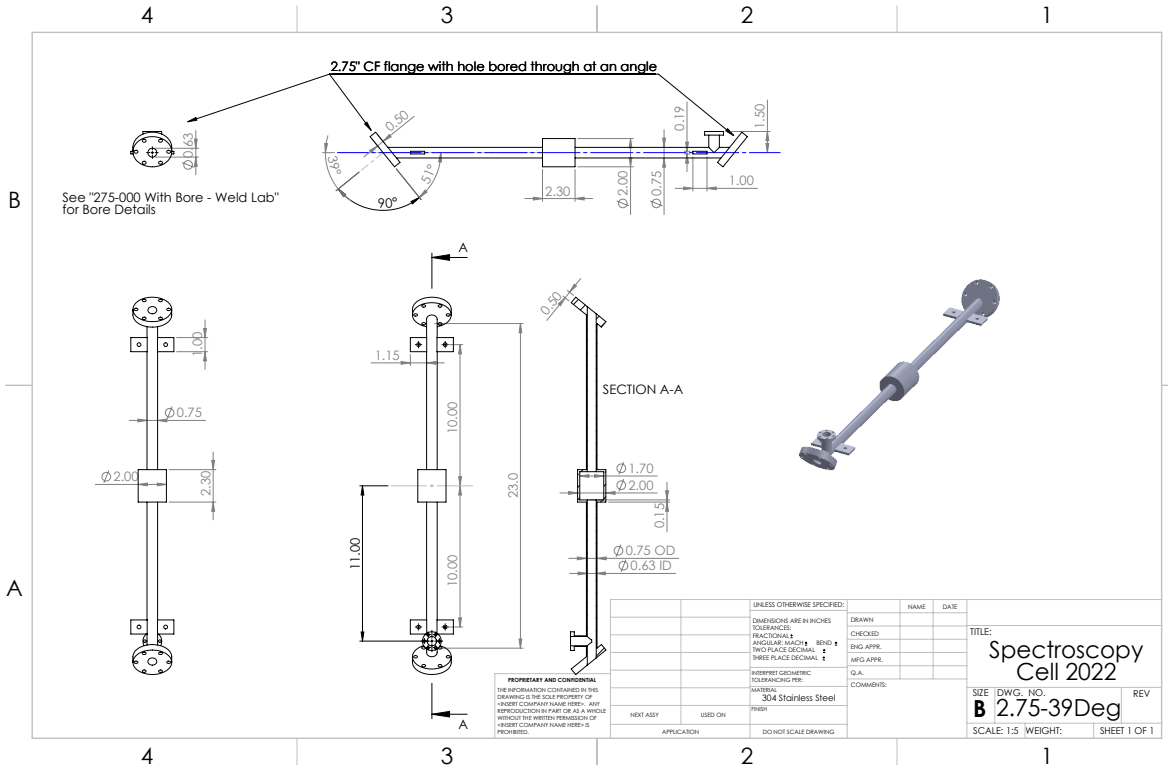

Figure 2.5: Designs of spectroscopy cell. More complete designs provided by ANCORP during the ordering process are presented in Appendix D.

Firstly, the strontium is held in a larger diameter central region, rather than a cup. This allows for easier wrapping of the source with heater tape and eliminates potential accumulation of strontium on a relatively cold upper surface. The diameter and length of the center region holds 20g of strontium. The other main change was the use of standard 2.75" CF flanges welded at a 39° angle from normal to be used for the viewports. Having the windows at an angle avoids multiple reflections causing interference effects to appear in the spectroscopy signal, which were present previously if care was not taken to misalign and separate stray reflections. Stellmer [19] used viewports mounted at the brewster angle near 56°. However, this angle cannot be achieved using 2.75" CF flanges without obstructing the beam for the standard 0.75" diameter vacuum chamber section, hence our use of the maximum 39° angle. Assuming an index of refraction of 1.487, as quoted by Corning Inc. for alkali borosilicate

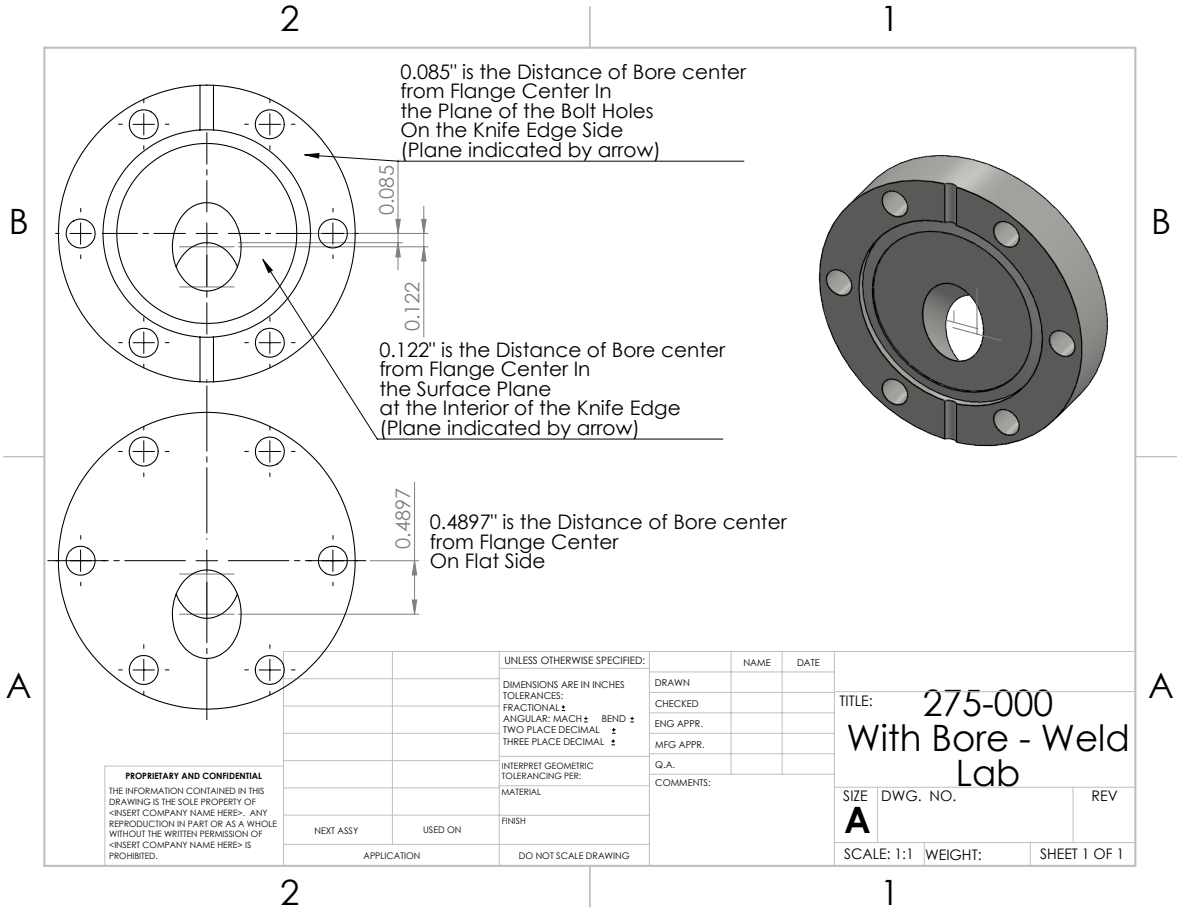

Figure 2.6: Details of CF2.75” bore location.

7056 [22], this angle reduces the reflection losses for P polarized light to about 1.5% from each viewport surface, down from 3.8% for normally incident light. This was acceptable to us to avoid the added challenges of sourcing proper brewster angle windows, since it sufficiently reduced reflection losses and eliminates interference effects.

Additionally, since we were concerned that part of the spectroscopy signal deterioration was due to pressure broadening from some form of outgassing or a slow leak in the vacuum chamber, we decided to attach a pressure gauge to the spectroscopy cell. We settled on the use of a convection enhanced Pirani gauge from Kurt J. Lesker Company (Model: KJL275803LL). Because the pressure is near the lower limit of the gauge, the readings change dramatically

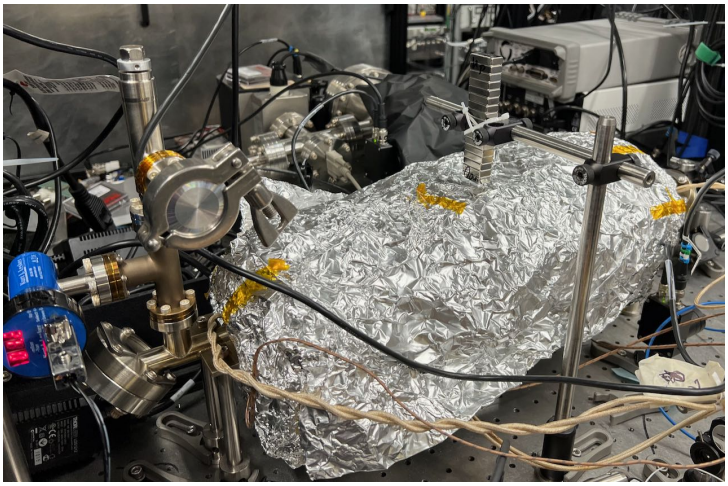

Figure 2.7: Spectroscopy cell installed on the strontium laser table. On the left side is the Pirani gauge, tee, and angle valve. Centered is the bulky foil wrapped insulation.

(usually reading 0.0 mTorr) each time the unit is disconnected and then reconnected to power, and there are also reading variations with temperature. Nonetheless, we use it to assess whether or not the pressure in the spectroscopy cell is rising significantly.

To enable attachment of the gauge to the spectroscopy cell, we attached a standard 1.33" CF tee to the spectroscopy cell as can be seen in figure 2.7. We connect the Pirani gauge to one flange of the tee and an all-metal angle valve to the other. This angle valve was purchased from Kurt J. Lesker Company (Part number: VZCR20R,) and is used to pump on, flow argon into, and seal the spectroscopy cell.

Figure 2.7 shows the fully assembled and installed spectroscopy cell. Visible are magnets above the spectroscopy cell, and there are other magnets hidden below. This adds a magnetic field that induces a Zeeman shift that ensures only π transitions are possible when the laser is on resonance. This minimizes broadening of the spectroscopy error signal from background magnetic fields as discussed by Stellmer [19].

To heat the spectroscopy cell, we used heater tape controlled by variacs. We used the Omega Engineering Super-High Temperature Samox-insulated resistive heating tape [13]. Similar products are sold by McMaster if one does not need specific dimensions (e.g., McMaster

Figure 2.8: Heater tape wrapped around the spectroscopy cell before insulation was added. The central component of the heater tape was bleached white from being raised to high temperatures in a previous bake.

Part number: 4550T113.) The placement of the heater tape is shown in figure 2.8. We wrapped it in three sections to allow heating the source separately from the adjacent sections of the spectroscopy cell. This allows either heating evenly or heating the sections to the left and right of the source to a higher temperature to avoid accumulation of strontium in that region.

To monitor the temperature of the spectroscopy cell, we put thermocouples (McMaster Part number: 9251T92) in contact with the spectroscopy cell. They were tied to the cell with stainless steel wire. These were then wrapped in a couple layers of aluminum foil. The foil layer was then wrapped with heater tape as seen in figure 2.8. Each thermocouple was placed under one of the strips of heater tape to monitor the temperature beneath it. One might consider using a shielded thermocouple (e.g., McMaster Part number: 3860K53), but we have found that when wrapped in aluminum foil in usual operating fashion, these can read 50°C or lower near 400°C compared with the unshielded ones, presumably because of reduced heat conductance to the thermocouple through the shielding. This can be an issue if one desires accurate readings, which is quite valuable in this case where the equilibrium strontium vapor pressure grows

exponentially with temperature.

We found in heating the spectroscopy cell that the insulation was sufficient to keep the exterior of the windows, gauge, and 1.33" CF flanges below 35°C as measured with an IR thermometer, so we were not concerned about thermal stresses on any of the CF flanges or exceeding the maximum operating temperature of 40°C for the Pirani gauge.

2.5.1 Recommended Cell Assembly Procedure

As will be discussed in the section 2.5.2, in our first assembly of this spectroscopy cell, we opted to incorporate several steps that seem unnecessary after the fact or that would be unnecessary under different conditions. In light of this experience, we suggest the following minimal procedure.

1. Assemble most of the spectroscopy cell and load strontium under argon.

2. If you are concerned that there are some oils or other contaminants in the cell, bake about 180°C for a couple days. This will also drive off water, but water should be reacted away by the strontium in any case.

3. If you opted to bake, attach the vacuum gauge under argon at this point. If not, the vacuum gauge could have been attached initially.

4. Wrap the spectroscopy cell source with heating tape and insulation. Heat it to about 330°C for a couple days while pumping on it with a turbo pump to drive out any gases from the strontium itself. Cool back to room temperature afterwards.

5. Calibrate the gauge and fill the spectroscopy cell to roughly 2 mTorr of argon (accounting for any gas dependent reading of the gauge).

6. Seal the spectroscopy cell and monitor its pressure to ensure that it is not leaking or outgassing substantially. If there is a low level of outgassing, one might try operating the spectroscopy cell anyway and rely on strontium's getter effect to remove it.

7. Install the spectroscopy cell on the optical table.

2.5.2 Spectroscopy Cell Assembly and Issues that Arose

Below is a description of the assembly process for the first spectroscopy cell of this design. We took extra precautions for the first version, and in particular, we did not wish to rely on strontium's getter property to remove gases. As described in reference [23], the reactiveness of strontium makes it an effective pump for gases in the atmosphere, with the exception of the noble gases. This should enable it to remove the initial water present on the chamber walls and to absorb hydrogen that diffuses out of the stainless steel of the chamber. One might also expect it to help with the majority of small leaks, with the exception being the 1% of argon present in the atmosphere.

Hydrogen Bake

We began with a hydrogen bake in air. That is, we heated the spectroscopy cell using heater tape without any CF flanges attached. The components wrapped around the spectroscopy cell from the surface of the spectroscopy cell outwards are as follows: 1. Thermocouples, 2. Foil, 3. Heater tape, 4. Sheets of insulation wrapped in foil, 5. An extra foil layer. Wrapped in with the spectroscopy cell was the 1.33" CF tee, so that it would also be baked. This whole setup was placed in an oven (Despatch model LAC2-18-8), mostly because it was a safe place to do so to prevent fire hazards or burns, but we did operate the oven at 200°C partway through the bake in an attempt to limit thermal gradients. The oven could not be used alone unfortunately because its maximum operating temperature is 260°C.

The motivation for this was the consideration that the slow release of absorbed hydrogen from the stainless steel could raise pressure in the spec cell over time. The *Handbook of Vacuum Technology* [24] suggests an initial hydrogen concentration in stainless steel of 40 Pa·l/cm^3, which for the dimensions of our spectroscopy cell would cause the pressure to rise 10s of Torr if a more than about 20% of the hydrogen in the stainless steel accumulated in the interior of the spectroscopy cell. Given that we wished to operate with a buffer gas of roughly 3×10^{-3}Torr, this seemed like a potential issue. However, it seems likely in retrospect that the strontium in the spectroscopy cell would react with the hydrogen and remove this gas.

We held the cell at above 400°C for 4 days. For this bake, we used one J-type thermocouple that was shielded in stainless steel (similar to McMaster part number 3860K53) and two unshielded J-type thermocouples. We found that the unshielded thermocouples both read close to 485°C when the shielded thermocouple read roughly 400°C. It seems likely that this is due to the shielding limiting thermal conductance to the thermocouple and causing it to read consistently low. In any case, this is sufficient to remove the majority of the hydrogen from the stainless steel.

Aluminum Deposit Removal

A detrimental outcome of the hydrogen bake was that the heated aluminum foil deposited on the steel chamber in some areas. The deposits were in the form of millimeter to centimeter scale strips in several locations on the spectroscopy cell surface. Unfortunately, two such locations were the 1.33” CF flange and one of the 2.75” CF flanges, likely because the foil was wrapped tightly in these regions with heating tape directly on top.

Fortunately, we were able to chemically remove these deposits by sonicating the flanges for several hours in a pH 12.5 aqueous solution of NaOH (0.2% by weight made with 2 g of NaOH in 1 L of water).

Baking the Strontium

After an incident in which a Buna-N rubber KF flange was unintentionally used and heated to the point of leaking in a bake, we successfully loaded strontium into the spectroscopy cell. Loading of 20 g of strontium was carried out in the argon atmosphere of a glovebag. All components of the spec cell were assembled after loading except for the gauge, whose port was sealed off with a 1.33" CF blank for the bake. This was necessary because max bakeout temperature of the gauge is a very low 70°C, and it would not have survived the bake.

One particular issue for us was that the strontium that we were supplied from Plasmamaterials seems to have been contaminated with some type of soil. We encountered a previous issue in which this substance condensed on the viewports of a vacuum chamber. Fortunately, it was possible to bake away this mysterious deposit at temperatures near 100°C. We were able to see similar condensation in a test in which a sample of the this strontium was heated. Plasmamaterials insists that there was no oil in the production process of the strontium, and to their credit, they offered to have us send the strontium back for analysis. We did not have them analyze it. In any case, the primary purpose of the bake was to remove this unknown substance, rather than the usual objective of removing water from the vacuum chamber.

In an effort to protect our turbo pump from contamination, we used a liquid nitrogen cold trap from Kurt J. Lesker (Model: TLR4XI100QF,) which we filled with liquid nitrogen every 10 hours. In using this, we found that close to when the liquid nitrogen finished evaporating, the gas load on the turbo would increase significantly as condensed vapors were released from the trap surface.

The bake proceeded like a typical water bake. We used the aforementioned oven (Despatch Model: LAC2-18-8) to bake the spectroscopy cell. We ramped the temperature at 40°C/hour to 180°C. We then held it at 180°C for 72 hours. Afterwards, we ramped back down to room temperature at 40°C/hour. The peak turbo pump pressure reading was 2.3×10^{-6} mbar (low in

part because of the LN2 trap), and it reached the minimum pressure that the turbo pump could sustain by the end of the bake, which was 1.1×10^{-7}mbar.

After the bake, the Pirani gauge was attached under argon and its zero was calibrated after pumping out the spectroscopy cell.

Outgassing Issues

We tried leaving the spectroscopy cell at room temperature while monitoring the increase in the Pirani gauge reading. We found that the pressure was rising at about 1.3 mTorr per hour initially. After a few days of monitoring and careful leak checking with a helium leak checker, we determined that this pressure was entirely due to outgassing, likely from the addition of the pirani gauge. A "bake" at 64°C for five days was insufficient to eliminate the outgassing.

We eventually wrapped the strontium source heating tape as shown in Figure 2.8 and insulated it. We heated the source to 330°C and pumped on it for three days. As the temperature was ramped, the turbo pump pressure reading reached a high of 2.0×10^{-4} mbar when the source was roughly 295°C. Fortunately, the pressure dropped quickly after this, otherwise, we would have aborted the procedure for fear of overloading and damaging the turbo pump. This seems to strongly suggest that some substance in the strontium was outgassing. Whether this substance was evaporating from the surface of the strontium or escaping from gases trapped in pockets in the interior of the strontium is unclear. After this, we heated the source to 450°C for a few hours while pumping. There was no large pressure spike this time, but the pressure did increase. Heating the cell to 450°C proved a major mistake because it coated one of the windows with strontium. Why only one of the windows, rather than both was coated is not clear to us, but we speculated the possibilities of some asymmetry in temperatures somewhere, some difference in line-of-sight between the windows to the strontium granules, or some vapor dynamics within the spectroscopy cell. The outgassing was no longer an issue when the spectroscopy cell was brought back to room temperature. We subsequently replace the strontium

coated window under an argon environment.

Adding Buffer Gas

After this, we added enough argon to the cell that the Pirani gauge read 1.8 mTorr, but, because of the gas dependence of the gauge, the actual pressure was 2.6 mTorr. This is a factor of 3 higher than Stellmer's suggestion of roughly 10^{-3}mbar, but we opted to fill a bit higher to ensure no rapid window coating occurred as we set up the spectroscopy cell with the expectation that even the increased pressure broadening would be small compared to saturation broadening and transit time broadening effects [25].

Installation

We installed the spectroscopy cell on the strontium machine laser table and ramped up the temperature until a spectroscopy signal was seen. Because we were replacing a previous version of the spectroscopy cell, no realignment was necessary. We had an operable signal at when the spectroscopy cell reached 350°C.

Also notable in this process was the observation of a pressure increase in the spectroscopy cell that was clearly present when the cell was about 80°C. This pressure continued to rise until the peak pressure of about 30 mTorr around 260°C. As the strontium was heated beyond this, we believe it rapidly reacted with and absorbed the gases that were evidently being released in the heating process. The pressure returned to a reading of 1.1 mTorr (uncorrected for the gas dependence of the gauge) when the temperature had reached 400°C. The discrepancy from the 1.8 mTorr reading that it was filled to is because of the change in gauge pressure reading when the Pirani gauge is power cycled.

2.6 New Oven Design

2.6.1 Previous Design

To generate a collimated beam of strontium atoms, we use an oven nozzle design based on our group's 2015 paper [17]. As discussed in that publication, the nozzle is essentially a hexagonal lattice of stacked microcapillaries assembled into a double-sided 2.75" CF blank. This has been an effective design for the most part, but we attempted to improve on this design because of certain non-ideal features.

The most critical of these non-ideal features is that heating the nozzle heats two CF vacuum flanges that are on each side of the nozzle. As alluded to in the original publication, we have heated our nozzle to as much as 650°C, which is far above the specified 450°C temperature rating of the flange. Impressively, the flange handles this reasonably well, and can go without leaking for an extended period of time at these temperatures. In our experience, this time period is about 2.5 years. In the most recent oven change of March 2022, the nozzle leaked soon after replacement at a substantially lower temperature of about 570°C, but the leak went away after cooling the nozzle, and retightening the bolts to a torque of 165 in·lb, which is above the initially used manufacturer specified value of 144 in·lb. In that case, we suspect the heating deformed the nickel gaskets that we used, and retightening the bolts was able to improve the seal. However, after roughly two years of constant elevated temperature, we find that the bolts of the CF flange themselves degrade and fail, presumably because of some slow chemical process with the air, given the dark gray corroded look of the bolts. The bolts also warped and snapped under the torque of a wrench when we tried to unscrew them, and they needed to be cut free with a Dremel to open the oven. The state of the flange after two years of heating is shown in figure 2.9. The white patches are strontium oxide. Also shown is a pair of 1/4"-28 silverplated bolts fused into a platenut that were used at the flange. The one broken in the middle snapped when we tried to unscrew the bolt. The other one needed to be removed

Figure 2.9: Components of the oven installed in July 2019 after the strontium source had been depleted and the flange had leaked in February 2022.

by cutting off the head of the bolt.

For comparison, we show images of the state of the oven when installed in February 2019 in figure 2.10.

In contrast, the same design used for our lithium oven has not leaked, and we suspect this to be due to operating temperature being within specifications for the CF flange, and the benefit of using copper gaskets instead of nickel.

We also note that we no longer lower the temperature of the oven regularly to prevent temperature cycling induce degradation of the flange seal. When the oven leaked in February 2019, we believe it was temperature cycling that caused it. In 2021, a leak was present in the oven in spite of no temperature cycling, it should be noted that the actual reason the oven needed to be changed was because the strontium source had been nearly fully evaporated, so being able to turn down the temperature confidently might have helped the lifetime.

Beyond this, there were some features that made manufacturing and assembly less convenient than it might be. First, because the microcapillaries have a nominal outer diameter of 8.3 thou (0.21mm), using wire electrical discharge machining (wire EMD) requires use of a wire

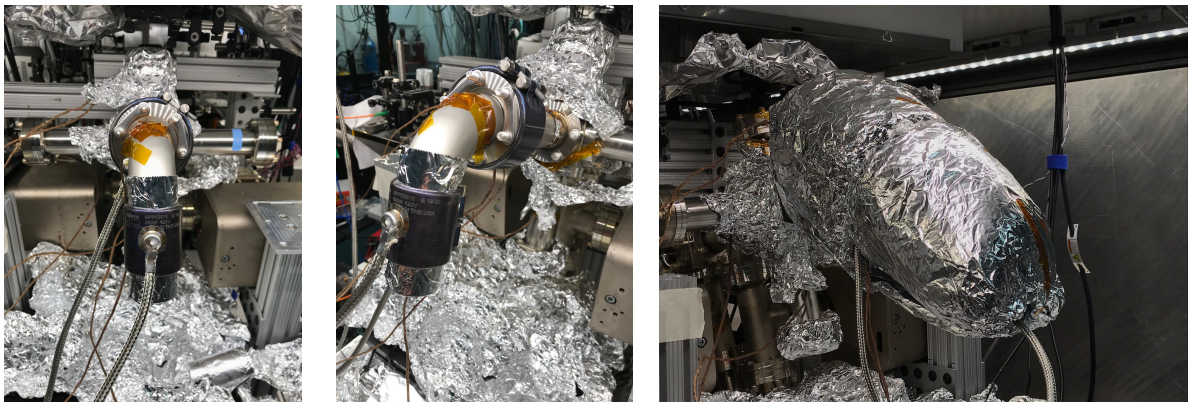

Figure 2.10: Components of the oven of July 2019 when they were being installed. The left two images depict the vacuum chamber components of the oven section and the right image depicts the same section insulated with "Superwool" ceramic insulation. The fibrous insulation sheets are wrapped in aluminum foil before installing them around the oven to mitigate the fibers from shedding around the experiment and protect. The wrapped insulation sheets are held onto the oven using Kapton tape on the exterior surface of the insulation.

with a radius of approximately 4 thou or less. More commonly available are wires of radius 5 thou. In fact, this is what our on-campus machine shop used. Second, the sloped edges of the channel for the microcapillary made clamping the capillaries difficult, and required a nearly exact number of rows of microcapillaries. And finally, because the capillaries are recessed into the blank, a tapped hole cannot be used as part of the clamp. Instead bolts and nuts must be used to create the clamp, reducing the reliability of the clamp and necessitating care and dexterity to assemble the clamp without spilling microcapillaries.

2.6.2 New Multiple Piece Design

In an attempt to improve upon the previous design, we opted to use a nozzle made of multiple pieces. Firstly, intending to reduce the risk of vacuum chamber leaks, we redesigned the oven section to no longer contain any flanges as shown in figure 2.11. By including interior mounting holes, it is designed to be loaded with strontium through the 2.75" CF flange and 0.77" diameter hole into the cup section and then attach the nozzle over the 0.77" hole. This mildly complicates loading of strontium by requiring funneling of reasonably small strontium

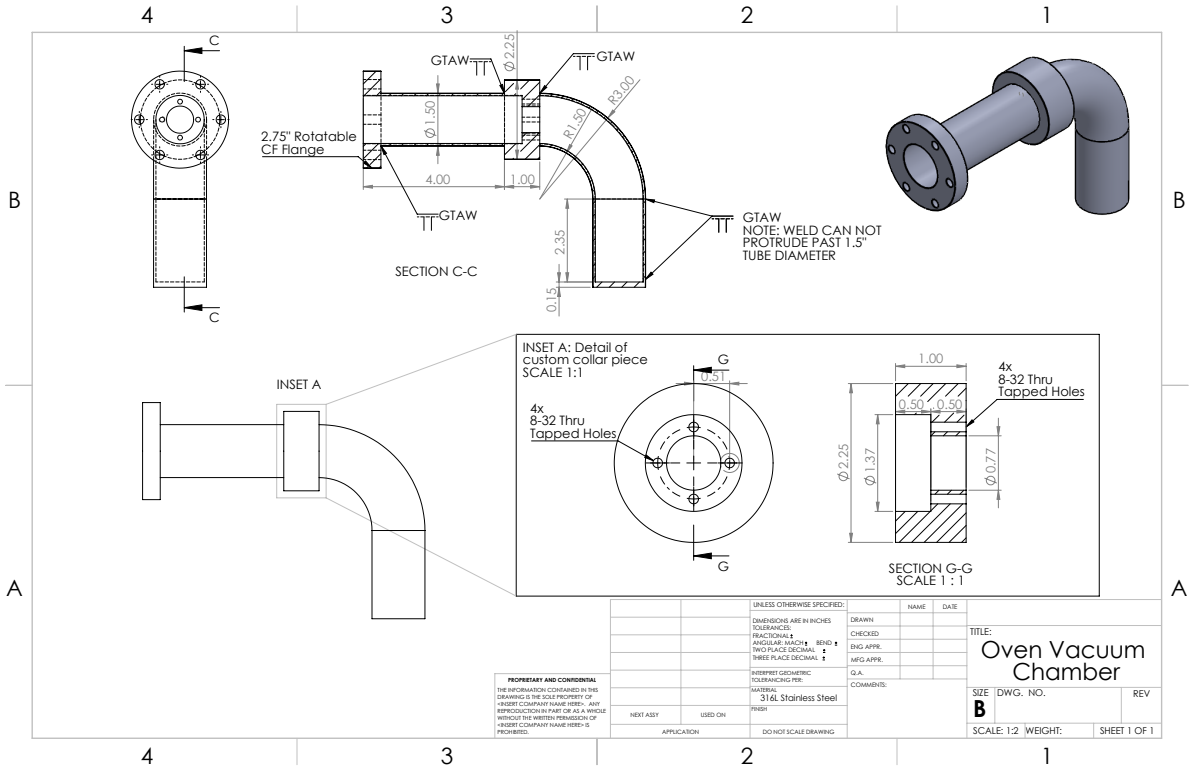

Figure 2.11: New oven design. The details of the 2.75” CF flange are not shown.

pieces into the cup.

We custom ordered this part to be assembled by ANCORP. The one part that they did not provide is the piece shown in “Inset A” of figure 2.11. They would have machined this part for us in and this is recommended, but because of lead time concerns at the time of ordering, we had this component made by Xometry and shipped it to them.

The heating elements of the oven section and nozzle are similar to the previous design. We use custom sized Mi-Plus® mineral insulated band heaters from Tempco. One heater with ID 2.25” and length 1” is used to heat the nozzle mounting collar (the piece in Inset A), and another heater with ID 1.5” and length 2.5” is used to heat the straight section of the cup where the strontium sits. The whole oven is externally insulated with ceramic fiber insulation wrapped in aluminum foil.

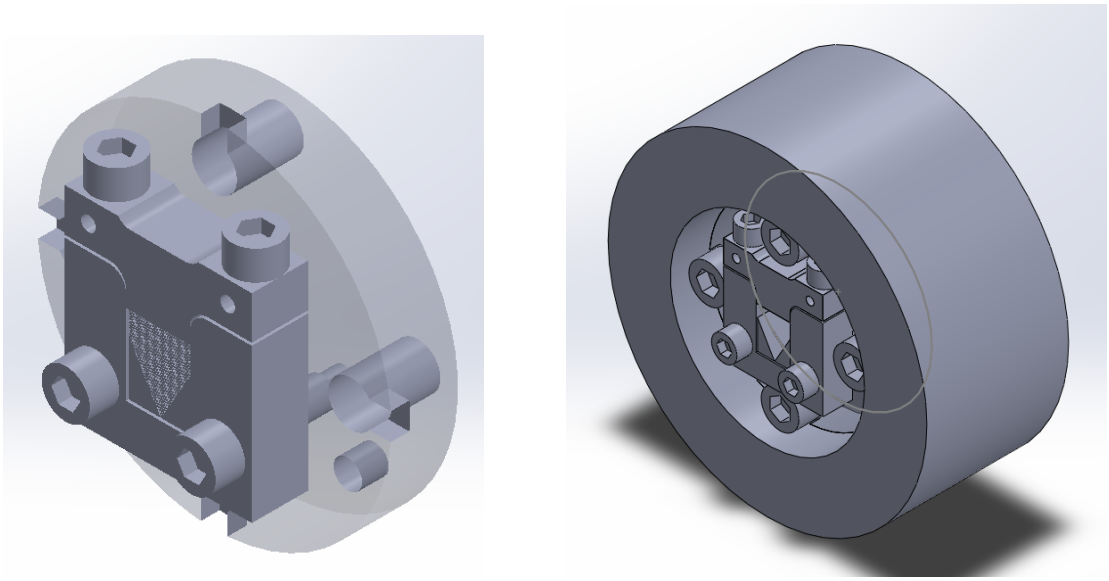

Figure 2.12: Left: Nozzle assembly with microcapillaries. Note that the screws on the top side are for clamping the capillaries in place, and must be used first, while the screws on the front face just ensure that there is no gap for strontium to get around the nozzle between the two pieces. Right: Nozzle assembly attached with 8-32 bolts into the collar piece of the oven section shown in figure 2.11

The nozzle itself is made up of 4 custom pieces. Full technical drawings and a few additional details are provided in Appendix E. Computer-aided design (CAD) renderings of its final form are shown in figure 2.12. Most notably, instead of cutting the triangular channel with wire EDM from a single piece, the channel is made by setting sharp cornered triangular wedges into a rectangular channel. These wedges and channel can be easily cut by a CNC machine, provided specification of 1 thou precision on a few key features and sharp unbroken edges in a few places. The primary benefits of this approach are fourfold: (1) the bottom corner of the channel accommodates only one tube in contact with the sloped edges of the triangular pieces, ensuring ideal stacking of the tubes, (2) the CNC machines needed to create the parts are more readily available and typically require less lead time, (3) clamping the microcapillaries is accomplished using tapped holes, and (4) the exact number of microcapillary rows can be varied.

There is a downside in that the loose triangle pieces during assembly can jostle out of place

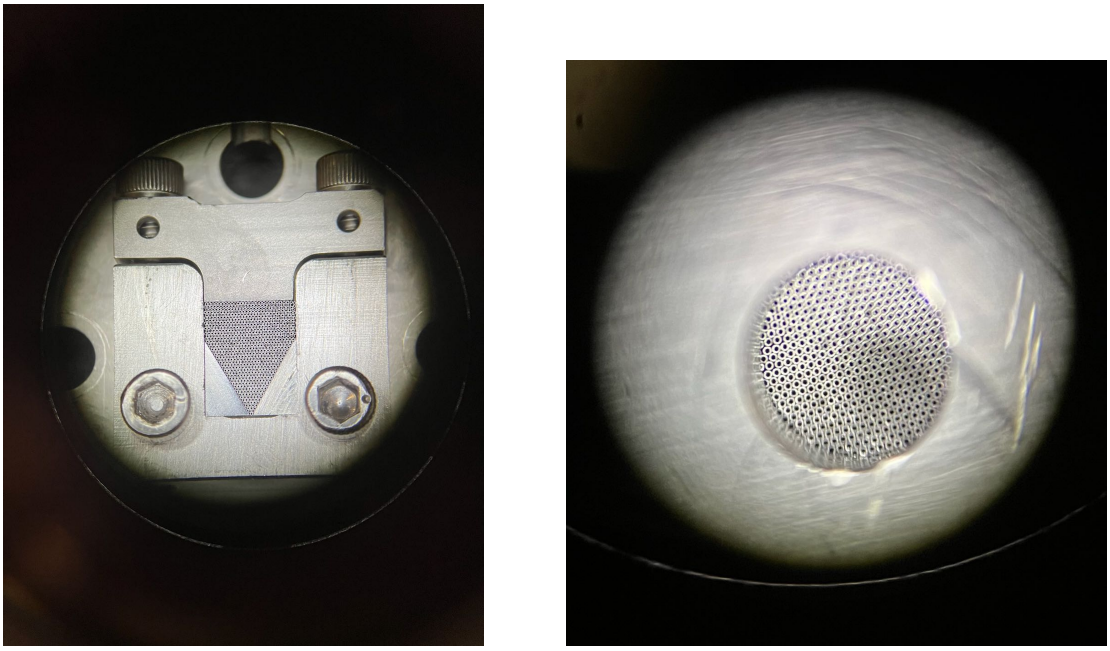

Figure 2.13: Images of the nozzle taken through a microscope. Left: The side of the nozzle that faces away from the oven. The total number of microcapillaries used in this nozzle was 798. Right: The masked side of the oven that faces the oven.

requiring some attention to this when assembling, but I personally found this not to be too difficult to avoid. Nonetheless, I would recommend using a wire EDM if available rather than the wedge pieces, even if the stacking is imperfect. Stacking imperfections seem somewhat unavoidable in my experience, and the easier assembly is likely worth it. Also, an improvement could be made by widening the rectangular channel and making the triangular wedges larger so that fewer tubes need to be stacked with straight sides. This was possible to do and still preserve packing, but stacking more than 3 or 4 rows with straight sides occasionally caused imperfect packing because the tubes would try to stack in a straight row against the vertical sides.

We successfully assembled the nozzle and an image of the front and back of the assembled nozzle are shown in figure 2.13. There are a few locations where imperfect packing can be identified, mostly near the edges of the vertical wall section. These do not appear to affect functionality, but would likely go away if the triangular wedges were widened.

2.6.3 Tips for Assembly

Assembly can be rather challenging, and we offer the following advice.

First, we suggest keeping the capillaries on a large conducting surface during assembly to remove any static charge from the microcapillaries. We believe that static charge can cause them to interact, but it is not entirely clear whether or not we mistook some magnetic interactions (which are also present) for electrostatic ones.

We recommend sonicating all of the parts, bolts, tools, and capillaries in isopropanol before assembly for cleanliness.

For assembly, we designed a sort of "scaffolding " for the rectangular channel and triangles to sit on during assembly. A CAD rendering of the part is shown in figure 2.14, and technical drawings are in Appendix E. During assembly, the rectangular channel part can be taped to the scaffolding and the nozzles can be loaded into it while taped together. A short extrusion is on the scaffolding to keep the channel in place and to make sure that the microcapillaries and triangle are flush with the front face of the channel. I should note that the extrusion was a bit shorter than it probably should have been which causes the capillaries to extend a couple of rows above the extrusion before they can be clamped. Ideally, the extrusion would match the final height of the stacked capillaries. When construction is near completion, the clamping portion of the assembly can be loosely clamped into place from above before the scaffolding is removed. After the scaffolding is removed, the clamp can be tightened much more securely, and the bolts that hold to channel piece flat against the face of the clamp can be added. At this point, one should try poking the capillaries a bit to make sure that they are securely clamped, and tighten the clamp a bit more if they move. A few extra rows of capillaries than the bare minimum is necessary before clamping here to ensure that a tight clamping can be achieved when the microcapillary array compresses slightly under the force of the clamp.

I also highly recommend the assembly technique pioneered by Quinn Simmons. He found

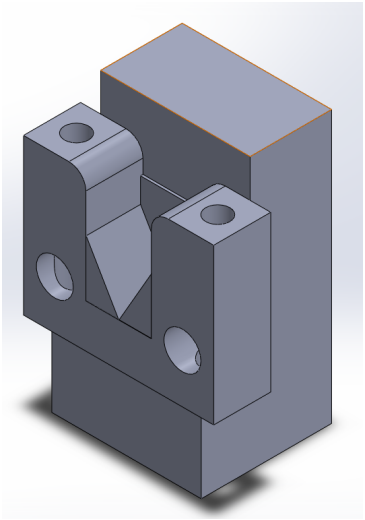

Figure 2.14: A CAD rendering of the component to be used as a temporary scaffolding to assemble the nozzle.

that it is not necessary to perfectly stack the tubes one by one. Instead, 10s of microcapillaries can be loosely set in the channel and then agitated into a perfect lattice structure. My preferred method of agitation is holding the whole nozzle assembly on the scaffolding and tap it against the table. Quinn prefers to tap the scaffolding with tweezers. One can also poke the nozzles with tweezers, but this is somehow worse, unless there is a missing nozzle near the bottom of the stack and one needs to force a nozzle into place there before the remainder will file in. This is very effective until the last one or two rows, at which point it is necessary to place tubes one at a time to get a flat top row. Much of the time, the tubes can be seen with the unaided eye, which is sufficient for agitating the capillaries into a perfect lattice. However, an optical microscope is necessary to check for defects and to make sure that there is a complete final row. One should have fine point tweezers for manipulation of the microtubes. Tweezers with a curved nose are very helpful as well, especially when a microscope is in the way. Flat large tweezers can also be used to place large numbers of tubes loosely in the channel at once.

Chapter 3

Primer on Optical Dipole Traps

In this chapter, we discuss the mathematical representation of laser beams that are used throughout this thesis, and the concept of the optical dipole trap (ODT), which is the underlying mechanism by which our optical lattices are created. We hope this will be a valuable primer to understand the experimental setups in chapters 4 and 5. At times, we delve into theoretical details that can be safely skimmed over on a first pass, namely the details of section 3.3, but we include these to potentially serve as a helpful introduction to the technical resources regarding the analysis of ODTs.

3.1 Complex Representation of Laser Light

We use standard complex notation to represent an electromagnetic plane wave with

$$\mathbf{E} = \mathbf{E}_0 e^{i(\mathbf{k}\cdot\mathbf{r}-\phi)} \tag{3.1}$$

Here, $\mathbf{E}_0$ is a three-dimensional complex vector

$$\mathbf{E}_0 \;=\; \sum_i E_{0,i}\hat{\mathbf{x}}_i \;=\; E_{0,1}\hat{\mathbf{x}} + E_{0,2}\hat{\mathbf{y}} + E_{0,3}\hat{\mathbf{z}}$$

where $\hat{\mathbf{x}}_1 = \hat{\mathbf{x}}$, $\hat{\mathbf{x}}_2 = \hat{\mathbf{y}}$, and $\hat{\mathbf{x}}_3 = \hat{\mathbf{z}}$ are the unit vectors in cartesian coordinates and $E_{0,i}$ is a complex number. We will also write

$$E_{0,i} = \left|E_{0,i}\right| e^{i\phi_i}$$

Equation (3.1) describes the physical time varying electric field $\mathbf{E}_{\text{real}}$ of the plane wave described equally well by the following equivalent expressions

$$\mathbf{E}_{\text{real}} \quad = \quad \text{Re}(\mathbf{E}\, e^{-i\omega t}) \quad = \quad \frac{1}{2}\mathbf{E}\, e^{-i\omega t} + \frac{1}{2}\mathbf{E}^*\, e^{i\omega t} \quad = \quad \sum_i \left|E_{0,i}\right| \hat{\mathbf{x}}_i \cos(\mathbf{k}\cdot\mathbf{r} - \omega t - \phi + \phi_i)$$

More generally, we can consider non-plane waves, which we represent by a complex valued vector function of space by

$$\mathbf{E}(\mathbf{r}) = \begin{bmatrix} E_x(\mathbf{r}) \\ E_y(\mathbf{r}) \\ E_z(\mathbf{r}) \end{bmatrix}$$

This represents the physical field given by

$$\mathbf{E}_{\text{real}}(\mathbf{r}) = \text{Re}\left(\mathbf{E}(\mathbf{r})e^{-i\omega t}\right)$$

Lastly, it will be useful at some points to express $\mathbf{E}$ as

$$\mathbf{E} = E\hat{\mathbf{u}} \tag{3.2}$$

where E is a complex scalar and $\hat{\mathbf{u}}$ is a complex vector that is normalized to satisfy $\hat{\mathbf{u}}^* \cdot \hat{\mathbf{u}} = 1$

Using complex numbers in this way to represent electric fields has a few primary benefits:

- The superposition of two electric fields is made relatively easy to compute as the sum of two complex representations $\mathbf{E}_1 + \mathbf{E}_2$. One can confirm this by observing

$$\mathrm{Re}((\mathbf{E}_1 + \mathbf{E}_2)e^{-i\omega t}) = \mathrm{Re}(\mathbf{E}_1 e^{-i\omega t}) + \mathrm{Re}(\mathbf{E}_2 e^{-i\omega t})$$

  This is helpful since computing $\mathbf{E}_1 + \mathbf{E}_2$ is much simpler than the alternative manipulation of trigonometric functions.

- The notation is more compact.

- Both the polarization and phase of the light is encoded in the single complex vector $\mathbf{E}$.

- The time averaged intensity of the electric fields is made simpler to compute with the help of the theorem in section 3.1.1.

Take care though that not every mathematical operation carries trivially to the complex representation. Most importantly, the product $\mathbf{E}_1 \cdot \mathbf{E}_2$ *does not* correspond to the product of two electric fields as can be seen by comparing $\mathrm{Re}(\mathbf{E}_1 e^{-i\omega t}) \cdot \mathrm{Re}(\mathbf{E}_2 e^{-i\omega t})$ and $\mathrm{Re}(\mathbf{E}_1 \cdot \mathbf{E}_2 e^{-i\omega t})$

3.1.1 Time Averaging Theorem

We will now consider a valuable theorem for our purposes that a simple extension of the theorem given in Zangwill's *Modern Electrodynamics* [26] section (1.6.3):

Consider two complex representations $\mathbf{a}(\mathbf{r})$ and $\mathbf{b}(\mathbf{r})$ as defined above. Let $T = 2\pi/\omega$ be

the period of one cycle. Then the time averaged product of the two fields is given by

$$\begin{aligned} \langle \operatorname{Re}\left[\mathbf{a}(\mathbf{r})e^{-i\omega t}\right] \cdot \operatorname{Re}\left[\mathbf{b}(\mathbf{r})e^{-i\omega t}\right] \rangle &= \frac{1}{T}\int_0^T dt \operatorname{Re}\left[\mathbf{a}(\mathbf{r})e^{-i\omega t}\right] \cdot \operatorname{Re}\left[\mathbf{b}(\mathbf{r})e^{-i\omega t}\right] \\ &= \frac{1}{2}\operatorname{Re}\left[\mathbf{a}^*(\mathbf{r}) \cdot \mathbf{b}(\mathbf{r})\right] \end{aligned} \tag{3.3}$$

where "$\cdot$" represents the usual dot product between vectors and "$\langle\rangle$" represents taking the time average.

3.2 Optical Dipole Traps

Optical dipole traps are a flexible tool in atomic physics that enable the creation of broad classes of hamiltonian potentials. Most relevant to this thesis, optical dipole traps can be used to create harmonic traps and optical lattices. We discuss first the physical mechanism behind this technique in this section and then briefly describe optical lattices at the end.

General Introduction to the Optical Dipole Potential

When an atom is irradiated with laser light of a frequency that is very different from the atom's resonant frequencies, it will negligibly absorb photons from the laser beam. Instead, the energy of the atom's internal states will shift in proportion to the square of the laser beam's electric field, an effect known as the A.C. Stark shift. For an intuitive sense of the consequence of this statement, suppose the atom is in a nondegenerate ground state. The laser beam will induce a change in the energy[1] of this ground state, $\delta\epsilon$, given by the formula

$$\delta\epsilon = \alpha(\omega)\left(\frac{1}{4}|E|^2\right) \tag{3.4}$$

[1] If considered in the floquet formalism, this is actually a shift of the quasienergy.

where $\alpha(\omega)$ is a constant of proportionality that depends on the laser's frequency ω and the polarization of the laser light. Here, we are also assuming that the laser beam is well approximated by a plane wave and that we have

$$|E|^2 = \mathbf{E}^* \cdot \mathbf{E}$$

where $\mathbf{E}$ is the complex vector representing the laser beam per the description in section 3.1.

However, if the electric field amplitude varies with its position in space $\mathbf{r}$, then this change in the atom's internal energy state can be considered as a spatially varying potential energy $V(\mathbf{r})$, which is referred to as the optical dipole potential,

$$V(\mathbf{r}) = \delta\epsilon = \alpha(\omega)\left(\frac{1}{4}|E|^2\right) \tag{3.5}$$

This potential enters into the hamiltonian $\hat{H}$ in the usual way:

$$\hat{H} = -\frac{\hbar^2}{2m}\nabla^2 + V(\mathbf{r}) = -\frac{\hbar^2}{2m}\nabla^2 + \alpha(\omega)\left(\frac{1}{2}|E(\mathbf{r})|\right)^2$$

Often, one can also say that the potential $V(\mathbf{r})$ is proportional to the intensity of the laser beam, $I(\mathbf{r})$, but this is only precisely true if one defines intensity to be proportional to E^2, which does not exactly match the textbook definition of intensity. This becomes apparent in the case of a standing wave of light formed by two counter-propagating laser beams, and this is in fact the important scenario of an optical lattice as we will later discuss. If one calculates the intensity for this standing wave using the time average of the Poynting vector, one finds zero intensity everywhere. But, E^2 is not zero everywhere, and so an optical dipole trap is present. Nevertheless, the optical dipole force is often described in terms of intensity, and it is nice as an experimentalist to operate with the rough notion that the potential depth is proportional to the easily measured intensity of a laser beam, which is often the case in practice.

A key feature of $\alpha(\omega)$ is that it can be negative or positive depending whether the laser light is a lower frequency ("red detuned") or higher frequency ("blue detuned") than the most relevant atomic transition(s). The most relevant transitions are typically the ones with the largest linewidths, but sometimes smaller linewidth transitions are important if the laser is near resonant with them as we will see from equation (3.16).

The force associated with this potential is referred to as the optical dipole force, and a simplified introduction can be found reference [27] where a two level atom is analyzed. In the case of a two level atom where the energy difference between the two levels is $\hbar\omega_0$ and the linewidth of the transition between these levels is Γ, the optical dipole potential can be found to good approximation to be [27][2]

$$V(\mathbf{r}) = \frac{3\pi c^2}{2\omega_0^3}\frac{\Gamma}{\Delta} I(\mathbf{r}) \tag{3.6}$$

assuming that $I = \frac{1}{2}\epsilon_0 c\,|E|^2$ and where $\Delta \equiv \omega - \omega_0$. This formula gives good intuition for how the potential scales with the detuning Δ and transition linewidth Γ, which is approximately applicable even with a real multilevel atom in the common case when only two levels are important.

Also helpful to know is the rate at which the atoms scatter photons from the laser in this two level approximation, which is given by [27]

$$\Gamma_{\mathrm{sc}}(\mathbf{r}) = \frac{3\pi c^2}{2\hbar\omega_0^3}\left(\frac{\Gamma}{\Delta}\right)^2 I(\mathbf{r}) \tag{3.7}$$

The quadratic scaling with detuning Δ suggests that heating caused by scattering photons from the laser beam can be made negligible if Δ is sufficiently large, and this fact is frequently utilized.

[2]Note that our convention differs by a factor of 2 from that of [27] for the complex representation of the electric field, so that our relationship between I and $|E|$ differs by a factor of 4. We follow the convention of [26].

In section 3.3, we will offer a more formal discussion of the dipole potential with references.

Utility of Optical Dipole Traps

The optical dipole trap is a very versatile tool in atomic physics, since it is completely controlled by adjusting the spatial intensity of a laser beam. The potential can be applied or removed very rapidly by turning a laser beam on or off with an acousto-optic modulator. Lattice potentials can be formed from standing waves of light, which are referred to as optical lattices and enable the study of certain theoretical problems in solid state physics. The potential can be translated in space by redirecting the laser beam, and the depth of a trap can be varied by adjusting the intensities of laser beams.

3.3 A.C. Stark Effect: Formal Theory of the ODT

The effect of an oscillating electric-magnetic field on an atom is known as the A.C. Stark effect, and it is the origin of the optical dipole force felt by an atom in a far detuned laser beam. We will discuss the theory of this effect, drawing on resources [28, 29, 30].

We begin with the semiclassical description of the Hamiltonian where the atom is described quantum mechanically and the field is described classically. This gives the Schrödinger equation

$$i\hbar\frac{\partial\Psi}{\partial t} = (H_0 + V_{\text{real}})\Psi$$

where H_0 is the hamiltonian system in the absence of the externally applied potential (e.g. the system of the isolated atomic nucleus and atoms) and V is the applied fields (e.g. the electric field of a light wave.)

The operator for the field can then written as[3]

$$V_{\text{real}}(t) = \frac{1}{2} V e^{-i\omega t} + \frac{1}{2} V^{\dagger} e^{i\omega t} = \text{Re}(V e^{-i\omega t})$$

V is further conveniently expressed in the multipole expansion

$$V = V_d + V_\mu + V_Q + \cdots$$

where V_d is the electric dipole interaction term, V_μ is the magnetic dipole interaction term, V_Q is the quadrupole interaction term, and so on, where

$$V_d = -\mathbf{d} \cdot \mathbf{E} \qquad V_\mu = -\boldsymbol{\mu} \cdot [\mathbf{n} \times \mathbf{E}] \qquad - \frac{i}{3} \sum_{\alpha,\beta} Q_{\alpha\beta} k_\alpha E_\beta$$

$\mathbf{d}$ and $\boldsymbol{\mu}$ are the electric and magnetic dipole moment operators, $Q_{\alpha\beta} = \frac{1}{2} e \sum (3 r_\alpha r_\beta - r^2 \delta_{\alpha\beta})$ is the quadrupole moment tensor of the atom, e is the electron charge ($e < 0$), $\mathbf{n}$ is proportional to the wavevector according to $\mathbf{k} = \frac{\omega}{c}\mathbf{n}$, and the sum in the expression $Q_{\alpha\beta}$ means the sum over all electrons in the atom. V_μ accounts for the magentic field of the wave $\mathbf{H} = \mathbf{n} \times \mathbf{E}$. V_Q takes into account spatial inhomogeneity of the field.

For an off resonance laser interacting with an atom, we are usually well justified in approximating the interaction by only the electric dipole interaction. For the AC stark analysis, we will do this by setting

$$V \approx V_d$$

yielding

$$V_{\text{real}} = -\text{Re}(\mathbf{d} \cdot \mathbf{E} e^{-i\omega t}) \tag{3.8}$$

[3]We opt to differ by a factor of 2 from reference [29] so that the convention matches that used for the electric field in equation (3.1). Strange to us is that reference [29] shares our convention for $\mathbf{E}$, but then chooses a slightly different definition for V.

The details of the theory of this interaction are rather involved, and a full treatment requires a perturbation theory discussion as treated in [29]. Here we will only sketch out the details and highlight the results that are relevant to an experimentalist.

First, let us consider the basis of relevant atomic states. We consider an atom with hamiltonian H_0. We will consider atomic state with quantum number γ, the total atom spin quantum number f, and spin along a given axis M. We will denote these states by $|\gamma f M\rangle$ and we will have

$$H_0 |\gamma f M\rangle = \varepsilon_{\gamma f} |\gamma f M\rangle$$

where $\varepsilon_{\gamma f}$ are the energies of H_0. If one would like to be more concrete, one can consider γ to indicate both the principle quantum number n and the fine structure J quantum number, in which case f would be the total spin quantum number F and M would be the associated z component spin quantum number m_F. However, we opt to use γ, f, and M to allow for more general cases, such as when we wish to only consider the fine structure states, in which case γ represents the principle quantum number n, and f represents the combined spin-orbit coupled spin J with M the associated z component of spin m_J.

We will then consider the full hamiltonian to be

$$H(t) = H_0 + V_{\text{real}}(t)$$

where V_{real} is the dipole interaction from equation (3.8).

Because $V_{\text{real}}(t) = V_{\text{real}}(t + (2\pi/\omega))$ is time-periodic, it is then appropriate to work in the Floquet formalism to the time-periodic total hamiltonian and develop a perturbation theory approach as in [29]. Let us denote the Floquet states associated with $|\gamma f M\rangle$ in Floquet space by $|\gamma f M\rangle\!\rangle$ [1]. Then, finding the perturbed quasienergies becomes a problem of finding the

eigenvalues of the matrix

$$T_{M,M'} = \langle\langle \gamma f M \,|\, V_{\text{real}} \mathcal{G}^{(\gamma f)} V_{\text{real}} \,|\, \gamma f M' \rangle\rangle \tag{3.9}$$

where $\mathcal{G}^{(\gamma f)}$ is a modified version of the quasienergy state Green's function. Note that, as is typically the case for floquet states, $\langle\langle \cdots \rangle\rangle$ denotes an integration over time along with taking the usual inner product of the regular Hilbert space $\langle \cdots \rangle$. The quasienergies $\tilde{\varepsilon}$ are then given by solutions to the eigenvalue problem

$$\det |\tilde{\varepsilon} I - T| = 0 \tag{3.10}$$

where I is the identity matrix.

Fortunately, the time integration implicit in equation (3.9) can be carried out analytically, leaving a relatively simple expression in terms of matrix elements of the usual eigenstates $|\gamma f M\rangle$. This time integration can be thought of as taking a sort of time average of the energy shift over each cycle of the laser. The resulting equation given in equation (5.3) of [29] is

$$T_{M,M'} = \frac{1}{4} |E|^2 \langle \gamma f M \,|\, (\hat{\mathbf{u}}^* \cdot \mathbf{d}) G_{\varepsilon_{\gamma f} + \hbar\omega + i0} (\hat{\mathbf{u}} \cdot \mathbf{d}) + (\hat{\mathbf{u}} \cdot \mathbf{d}) G_{\varepsilon_{\gamma f} + \hbar\omega} (\hat{\mathbf{u}}^* \cdot \mathbf{d}) \,|\, \gamma f M' \rangle \tag{3.11}$$

where G_ε is the green's function for the static hamiltonian H_0, and E and $\hat{\mathbf{u}}$ represent the electric field of the laser as defined in equation (3.2).

Le Kien et al. [28] consider a slightly different version of (3.11). This expression suggests to them an operator V^{EE} for the A.C. Stark effect. Using their approach, we consider the effective Hamiltonian for atoms in the presence of the laser beam to be

$$H = H_0 + H_{\text{HFS}} + V^{EE} \tag{3.12}$$

where H_0 is the atom hamiltonian approximated up to fine structure, H_{HFS} is the hyperfine interaction, and

$$V^{EE} = \frac{1}{4}|E|^2 \left[(\hat{\mathbf{u}}^* \cdot \mathbf{d})\mathcal{R}_+(\hat{\mathbf{u}} \cdot \mathbf{d}) + (\hat{\mathbf{u}} \cdot \mathbf{d})\mathcal{R}_-(\hat{\mathbf{u}}^* \cdot \mathbf{d})\right]$$

With this perspective, if we assume that the hyperfine states are well separated in energy, T from perturbation theory is then simply

$$T_{M,M'} = \langle \gamma f M \,|\, V^{EE} \,|\, \gamma f M' \rangle$$

in agreement with equation (3.11), except that $\mathcal{R}_+$ and $\mathcal{R}_-$ are slightly different operators than G_ε. We consider a discussion of these operators, their derivations, and their differences beyond the scope of this section and typically not so critical to the work of an experimentalist.

Following Le Kien et al [28], let us use the hamiltonian in equation (3.12). We consider the case that the H_{HFS} possibly induces small energy splittings comparable or smaller than those created by V^{EE}. In this case, we need to consider matrix elements for different total spin F (setting $f = F$), in addition to the already considered m_F (setting $M = m_F$). Thus, our perturbation theory now involves considering the matrix

$$T_{F,m_F,F',m'_F} = V^{EE}_{Fm_FF'm'_F} \equiv \langle nJFm_F \,|\, V^{EE} \,|\, nJF'm'_F \rangle$$

in the eigenvalue problem (3.10).[4] Here, we use n to denote the principle quantum number and J to denote the combined spin-orbit angular momentum quantum number, and we have that

$$H_0 \,|nJFm_F\rangle = \varepsilon_{nJ} \,|nJFm_F\rangle$$

[4] Of course, one may wish to consider H_{HFS} as part of the perturbation in which case we should have

$$T_{F,m_F,F',m'_F} = \langle nJFm_F \,|\, H_{\text{HFS}} + V^{EE} \,|\, nJF'm'_F \rangle = \langle nJFm_F \,|\, H_{\text{HFS}} \,|\, nJF'm'_F \rangle + \langle nJFm_F \,|\, V^{EE} \,|\, nJF'm'_F \rangle$$

The actual theoretical calculation of $V^{EE}_{Fm_F F' m'_F}$ for an atom using the formulas derived so far is a rather challenging task. Fortunately, there are some steps that can be taken to express it more simply in terms of relatively few constants. This procedure is discussed in detail in appendix B of [28]. Here we will provide an abridged overview.

The main procedure in this simplification is to operate in the spherical basis for both vectors and operators. For a review of scalar, vector, and tensor operators along with a derivation of the Wigner-Eckart theorem that we will soon apply, we recommend the Notes 20 on the Wigner-Eckart theorem in reference [31]. In brief, we use the spherical basis vectors defined by

$$\hat{\mathbf{e}}_{-1} = \frac{\hat{\mathbf{x}} - i\hat{\mathbf{y}}}{\sqrt{2}} \qquad \hat{\mathbf{e}}_0 = \hat{\mathbf{z}} \qquad \hat{\mathbf{e}}_1 = -\frac{\hat{\mathbf{x}} + i\hat{\mathbf{y}}}{\sqrt{2}} \tag{3.13}$$

A vector operator, a.k.a. a rank 1 tensor operator, $\mathbf{A}$ can then be expanded in this basis by

$$A_q = \hat{\mathbf{e}}_q \cdot \mathbf{A} \qquad \text{and} \qquad \mathbf{A} = \sum_q A_q \hat{\mathbf{e}}^*_q$$

where * is used to denote the complex conjugate.

It benefits us to operate in the spherical because it allows us to apply the Wigner-Eckart theorem[5] to the dipole operator $\mathbf{d}$ to write

$$\langle nJFm_F|d_q|n'J'F'm'_F\rangle = (-1)^{F-m_F} \begin{pmatrix} F & 1 & F' \\ -m_F & q & m'_F \end{pmatrix} \langle nJF\|\mathbf{d}\|n'J'F'\rangle \tag{3.14}$$

where the 2×3 array in parentheses denotes the Wigner 3-j symbol. $\langle nJF\|\mathbf{d}\|n'J'F'\rangle$ denotes the reduced density matrix, which is essentially just a constant that depends only on the n, J, and F quantum numbers (but not m_F) and the total operator $\mathbf{d}$ (but not the component q).

[5]Be aware that sometimes the reduced matrix operators are defined differently so that a factor of $1/\sqrt{2j+1}$ appears on the right side of the equation (3.14). In fact, reference [29] opts to use this alternative version of the theorem, while [28] uses the convention given in equation (3.14) so there are some differences in the formulas for the conventional dynamical polarizability equations as a result.

The power of using the Wigner-Eckart theorem here is that we only need the reduced matrix elements to easily determine the substantially larger number of matrix elements.

Moreover, because the operator $\mathbf{d}$ does not act on the nuclear spin, one is able to further relate $\langle nJF||\mathbf{d}||n'J'F'\rangle$ to the reduced density matrix $\langle nJ||\mathbf{d}||n'J'\rangle$ with the relation given in equation (B.27) of reference [28].

$$\langle nJF||\mathbf{d}||n'J'F'\rangle = (-1)^{J+I+F'+1}\sqrt{(2F+1)(2F'+1)}\begin{Bmatrix} F & 1 & F' \\ J' & I & J \end{Bmatrix}\langle nJ||\mathbf{d}||n'J'\rangle$$

where the 2×3 array in braces denotes the Wigner 6-j symbol, and I is the nuclear spin of the atom.

Thus, we have greatly reduced the number of values needed to define the matrix T or V^{EE} from the total number of matrix elements to the relatively small number of reduced matrix elements $\langle nJ||\mathbf{d}||n'J'\rangle$. It is further noted in reference [28] that the values of $\langle nJ||\mathbf{d}||n'J'\rangle$ can be gotten from the oscillator strengths or transition probability coefficients, which are measurable by experiment.

Similar operations can be carried out utilizing the properties of the spherical basis and the decomposition of the combined $\mathcal{R}_+$ and $\mathcal{R}_-$ operator into irreducible tensor operators. The net result is equation (1) in reference [28], which states

$$\begin{aligned} V^{EE}_{Fm_F F'm'_F} = \frac{1}{4}|E|^2 \sum_{\substack{K=0,1,2 \\ q=-K,\ldots,K}} \alpha^{(K)}_{nJ}\{\hat{\mathbf{u}}^*\otimes\hat{\mathbf{u}}\}_{Kq}(-1)^{J+I+K+q-m_F}\sqrt{(2F+1)(2F'+1)} \\ \times\begin{pmatrix} F & K & F' \\ m_F & q & -m'_F \end{pmatrix}\begin{Bmatrix} F & K & F' \\ J & I & J \end{Bmatrix} \end{aligned} \tag{3.15}$$

Here, $\alpha^{(K)}_{nJ}$ denotes the reduced dynamical scalar polarizability (for $K=0$), the reduced dynamical vector polarizability (for $K=1$), and the reduced dynamical tensor polarizability (for $K=2$.) These quantities are given by formula (11) in reference [28], which we reproduce

here:

$$\begin{aligned}\alpha_{nJ}^{(K)} =&(-1)^{K+J+1}\sqrt{2K+1}\sum_{n'J'}(-1)^{J'}\left\{\begin{array}{ccc}1 & K & 1\\ J & J' & J\end{array}\right\}|\langle n'J'\|\mathbf{d}\|nJ\rangle|^2\\ &\times\frac{1}{\hbar}\mathrm{Re}\left(\frac{1}{\omega_{n'J'}-\omega_{nJ}-\omega-i\gamma_{n'J'nJ}/2}+\frac{(-1)^K}{\omega_{n'J'}-\omega_{nJ}+\omega+i\gamma_{n'J'nJ}/2}\right)\end{aligned} \tag{3.16}$$

where $\omega_{nJ} = \varepsilon_{nJ}/\hbar$ and $\gamma_{n'J'nJ}$ is the linewidth of the transition between $|nJ\rangle$ and $|n'J'\rangle$, and where the sum is taken over all n' and J' such that $|nJ\rangle \neq |n'J'\rangle$. Be warned however, that there are also the *conventional* dynamical polarizabilities that differ from the *reduced* dynamical polarizabilities. They are also referred to as the scalar α_{nJ}^{s}, vector α_{nJ}^{v}, and tensor α_{nJ}^{T} polarizabilities and they are related to their reduced polarizability counterparts by the formulas

$$\alpha_{nJ}^{s} = \frac{1}{\sqrt{3(2J+1)}}\,\alpha_{nJ}^{(0)} \tag{3.17}$$

$$\alpha_{nJ}^{v} = -\sqrt{\frac{2J}{(J+1)(2J+1)}}\,\alpha_{nJ}^{(1)} \tag{3.18}$$

$$\alpha_{nJ}^{T} = -\sqrt{\frac{2J(2J-1)}{3(J+1)(2J+1)(2J+3)}}\,\alpha_{nJ}^{(2)} \tag{3.19}$$

And lastly, $\{\hat{\mathbf{u}}^*\otimes\hat{\mathbf{u}}\}_{Kq}$ denotes the compound tensor components given by

$$\{\hat{\mathbf{u}}^*\otimes\hat{\mathbf{u}}\}_{Kq} = \sum_{\mu,\mu'=0,\pm1}(-1)^{q+\mu'}\sqrt{2K+1}\begin{pmatrix}1 & K & 1\\ \mu & -q & \mu'\end{pmatrix}\hat{u}_{\mu}\hat{u}^*_{-\mu'}$$

where $\hat{u}_\mu = \hat{\mathbf{u}}\cdot\hat{\mathbf{e}}_\mu$ are the spherical components, defined in equation (3.13), of the polarization vector, defined in equation (3.2).

The overall benefit of this exercise is the realization that the only values we need in order to quantify the A.C.Stark shift (and the associated optical dipole forces) are the reduced matrix elements $\langle n'J'\|\mathbf{d}\|nJ\rangle$, the transition frequencies $(\omega_{n'J'}-\omega_{nJ})$, and the linewidths for the most

relevant transitions, along with the frequency ω, polarization $\hat{\mathbf{u}}$, and electric field amplitude $|E|$ of the laser light.

For the purposes of cooling and conducting experiments with ^{84}Sr, we are interested in the A.C. stark shift for a couple reasons. Most critical for experimental design is for determination of the optical dipole potential in the presence of a far detuned laser. This is relatively simple for ^{84}Sr atoms in the ground state because $J = 0$, $F = 0$, and $I = 0$. The consequence of this is that the Wigner 3-j and Wigner 6-j in equation (3.15) symbols both evaluate to 1, $\{\hat{\mathbf{u}}^* \otimes \hat{\mathbf{u}}\}_{00} = \frac{1}{\sqrt{3}}\hat{\mathbf{u}} \cdot \hat{\mathbf{u}}^* = \frac{1}{\sqrt{3}}$, and $\alpha^{(K)}_{n0} = 0$ for $K \in \{1, 2\}$ because of the Wigner 6-j symbol in equation (3.16). After plugging these values into equation (3.15) and using n to indicate the ground state, the net result of this is that the ground state energy shift is simply

$$\langle n0|V^{EE}|n0\rangle = V^{EE}_{0000} = \frac{1}{4}|E|^2\left(\frac{1}{\sqrt{3}}\alpha^{(0)}_{n0}\right) = \alpha^s_{n0}\left(\frac{1}{4}|E|^2\right) \tag{3.20}$$

and we recover exactly the energy shift given in equation (3.4) that gives rise to the very simple form of the optical dipole potential given in equation (3.5). In practice, one can look up the reduced dipole matrix elements, transition frequencies, and linewidths for strontium's atomic transitions and use it to accurately determine α^s_{n0} for a given laser frequency to then calculate the optical dipole potential (see for example, table 3.2 and surrounding text of reference [32].) In the case of atomic states where $J = 1/2$, as frequently occurs for alkali atoms, there is a similar simplification when the laser light is linearly polarized. In this case, $\alpha^{(2)}_{n0} = 0$ because $J = 1/2$ and $\{\hat{\mathbf{u}}^* \otimes \hat{\mathbf{u}}\}_{1q} = 0$ when $\hat{\mathbf{u}}$ corresponds to linear polarization, thus only a scalar light shift remains for this case.

Another reason we have considered the A.C.Stark shift is because it is relevant to the cooling effectiveness of our red MOT (the magneto-optical trap operating on the 689nm strontium transition.) While the red MOT is cooling, we introduce an optical dipole trap composed of strong 1064 nm laser beams so that the atoms are loaded into the optical dipole trap as they

are cooled by the red MOT. However, the dipole trap laser beams will shift both the upper and lower atomic energy levels of the 689nm transition, which potentially requires tuning of the 689nm laser beam frequency as the dipole trap is ramped up so that the red MOT continues to operate properly.

As a final note on the A.C. Stark shift, we note that it is possible to consider a polarizability operator $\hat{\boldsymbol{\alpha}}$ and write the optical dipole potential as [33]

$$V(\mathbf{r}) = -\mathbf{E}^*(\mathbf{r}) \cdot \hat{\boldsymbol{\alpha}} \cdot \mathbf{E}(\mathbf{r})$$

This gives a nice sense of connection to polarization induced by a light field in the classical case.

Optical lattices are generally a special case of the optical dipole trap in the case that laser beams are arranged to interfere with each other. When such interference occurs, the electric field amplitude (and possibly polarization) varies periodically in space. A detailed introduction and discussion of optical lattices formed with a generic number of interfering laser beams is presented in chapter 6. We will simply note here the most relevant case for the experiments discussed in the subsequent section. In these cases, two counterpropagating Gaussian laser beams are set to interfere. Supposing that the beams are traveling in the $+\hat{\mathbf{x}}$ and $-\hat{\mathbf{x}}$ directions and further supposing that we can ignore the finite Rayleigh ranges of the beams in our approximation, the beams will interfere with each other to form a potential of the form

$$V(x, y, z) = V_0(y, z) \sin^2(k(x - \delta))$$

that results from the optical dipole force. Here, the form of $V_0(y, z)$ depends on the beam waist. This can be an important consideration, since $V_0(y, z)$ determines how the atoms are supported against gravity (assuming gravity is in the z direction, as in our experiments,) and the form

of $V_0(y,z)$ suggests the possibility of excitation of transverse modes. We note that in certain circumstances, the finite Rayleigh ranges of the beams that we have ignored are also important to consider, and typically this is dealt with by modeling it as a superimposed harmonic trap along the x direction.

Chapter 4

Dynamic Realizations of the Aubry-André Model

In this chapter, we will briefly survey three recent experiments, conducted with the strontium machine described in chapter 2, and based on techniques using optical lattices. Then in the subsequent chapter 5, we will discuss in greater detail our most recent work on experiments exploring the competition and mutual enhancement of Aubry-André localization and dynamic localization in a class of systems where both are at play.

In all of these experiments, we create a bichromatic lattice, formed by superimposing two optical lattices. The two optical lattices will be generated with laser beams of differing wavelengths (hence, the term bichromatic.) We can approximate these systems as 1D and describe them by the Hamiltonian

$$H = -\frac{\hbar^2}{2m}\frac{\mathrm{d}^2}{\mathrm{d}x^2} + V_p(t)\sin^2\left(k_p(x-\delta_p(t))\right) + V_s(t)\sin^2\left(k_s(x-\delta_s(t))\right) \tag{4.1}$$

$V_p(t)$ and $V_s(t)$ denote the (possibly time dependent) lattice potential depths of the primary and secondary lattice, respectively. Likewise, $\delta_p(t)$ and $\delta_s(t)$ denote the position of the lattice

potential. Also, $k_p = 2\pi/\lambda_p$ and $k_s = 2\pi/\lambda_s$ where λ_p and λ_s are the wavelengths of the lasers used to generate the primary and secondary optical lattices, respectively. For the experiments in this section, λ_p is approximately 1064 nm and λ_s is approximately 915 nm. The secondary wavelength was changed for the experiment discussed in chapter 5.

4.1 Phasonic Spectroscopy

The structure of a quasicrystal is in part determined by a set of phasonic degrees of freedom [34]. The underlying geometry of a regular crystal is defined by its Bravais lattice. In contrast, quasicrystals require more information than this. One relatively simple definition for defining a broad and relevant class of quasicrystals is provided by the "cut-and-project" (or sometimes "projection") method for constructing a quasicrystal geometry [35]. To carry out this theoretical construction of a quasicrystal in N dimensions (with $N \leq 3$ for physical quasicrystals), one must specify (A) a *true* crystal Bravais lattice in an M-dimensional space of higher dimension than the space of the quasicrystal (i.e., $M > N$), and (B) a subspace of dimension N within the M-dimensional space onto which one can "project" nearby vertices of the M-dimensional lattice according to the procedures described in reference [35]. The quasicrystal is constructed by this projection procedure.

One can consider the concrete example case of an $N = 2$ dimensional quasicrystal constructed from a projection procedure in an $M = 3$ dimensional space. Here, the subspace is a 2D plane that "cuts" through the 3D crystal, and quasicrystal is found by "projecting" points of the 3D crystal onto the 2D plane. Note that for some orientations of the N-dimensional subspace, the cut-and-project method will produce an actual periodic crystal instead of a quasicrystal, and we will assume that the orientation was chosen so that this is not the case.

The phasonic degrees of freedom can be understood as a quasicrystal construction parameter within the framework of this cut-and-project method. In total, we see that the quasicrystal

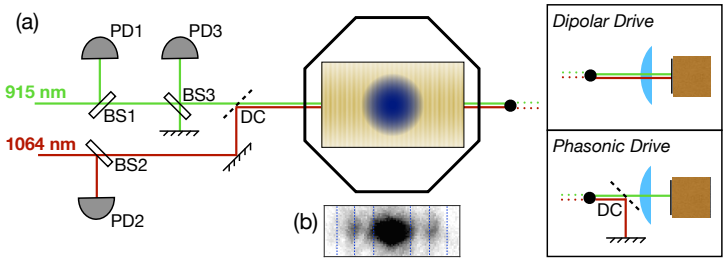

Figure 4.1: Experimental schematic. (a)BEC (blue) in a bichromatic lattice (yellow). Photodiodes (PD), beam samplers (BS), and dichroic mirrors (DC) are indicated, as is the configuration for both dipolar and phasonic driving using a piezo-driven mirror (solid block). (b) Sample band-mapped data. Dotted lines indicate zone edges of the primary lattice. *Reproduced from reference* [36].

can be completely described by the following: (A) the geometry of the M-dimensional space lattice, (B) the dimension N of the projection subspace within the higher M-dimensional space, (C) the orientation of the N-dimensional subspace as defined by its basis vectors in the M-dimensional space, and (D) the location of the N-dimensional subspace in the M-dimensional subspace.[1] The phasonic degree of freedom is the degree of freedom determined in step (D); tuning this phasonic degree of freedom is achieved by translating the N-dimensional subspace perpendicular to itself (i.e. in a direction perpendicular to all of its basis vectors) within the M-dimensional subspace.

A bichromatic lattice formed from incommensurate lattices (i.e., when k_s/k_p is irrational) also has a phasonic degree of freedom that it inherits from a mapping to a 1D quasicrystal [37]. In this case, the phasonic degree of freedom corresponds to the difference in position of the primary and secondary lattice, given by $\tilde{\delta} \equiv \delta_s - \delta_p$. In reference [36], we explored how a cloud of ultracold strontium atoms loaded into a bichromatic optical lattice reacts to rapid modulation of the phasonic degree of freedom by driving $\tilde{\delta}$ as a function of time.

Figure 4.1 shows the two configurations of the experimental apparatus that were used in reference [36]. In the dipolar drive configuration, the entire bichromatic lattice was translated

[1] Note that two different sets of parameters potentially describe the same quasicrystal, so while these parameters completely describe the quasicrystal, it is not necessarily a unique description.

to produce a dipolar drive. In the phasonic drive configuration, only the secondary lattice was translated, resulting in a modulation of the phasonic degree of freedom. To determine what excitations this induced, we performed a band-mapping procedure in which the potential was ramped down on the 100us time scale after which the atoms were allowed to freely expand for some time before imagining. The atom position after imaging indicates which bands were populated.

In the experiment, the dipolar drive is described in terms of equation (4.1) by

$$\delta_p(t) = \delta_s(t) = A_{\text{dip}} \sin(\omega_{\text{dip}} t)$$

The force perceived in the non-inertial reference frame in which the potential is stationary is then given by

$$F(t) = K \sin(\omega_{\text{dip}} t) = m\omega_{\text{dip}}^2 A_{\text{dip}} \sin(\omega_{\text{dip}} t)$$

We then define the dimensionless drive parameter α_{dip} according to

$$\alpha_{\text{dip}} = \frac{K\lambda_p}{2\hbar\omega_{\text{dip}}} = \frac{\lambda_p}{2}\frac{m\omega_{\text{dip}} A_{\text{dip}}}{\hbar}$$

which is equivalent to K_0 used in chapter 5 and elsewhere, but we use α_{dip} here to remain consistent with the notation of reference [36]. We also define $f_{\text{dip}} = \omega_{\text{dip}}/(2\pi)$.

Phasonic driving is instead defined by the case

$$\delta_s(t) = A_{\text{phason}} \sin(\omega_{\text{phason}} t), \qquad \delta_p(t) = 0$$

In this case too, we introduce a dimensionless amplitude α_{phason} given according to

$$A_{\text{phason}} = (1000 \text{ nm} \cdot \text{kHz}) \frac{\alpha_{\text{phason}}}{f_{\text{phason}}}$$

where $f_{\text{phason}} = \omega_{\text{phason}}/(2\pi)$.

Figure 4.2 explores excitation to higher bands as a function of primary lattice depth and drive frequency, and Figure 4.3 explores excitation to higher bands as a function of drive strength and drive frequency. A comparison is made in both figures between dipolar driving and phasonic driving. We observe in particular that excitations arise strongly for harmonics of the drive frequency in the phasonic drive case that are not present when compared to dipolar driving. Lastly, in figure 4.4, we observe the change in excitation spectrum as a function of secondary lattice depth, which allows us to observe the coarse features of the energy structure that result from the introduction of a secondary lattice of increasing strength.

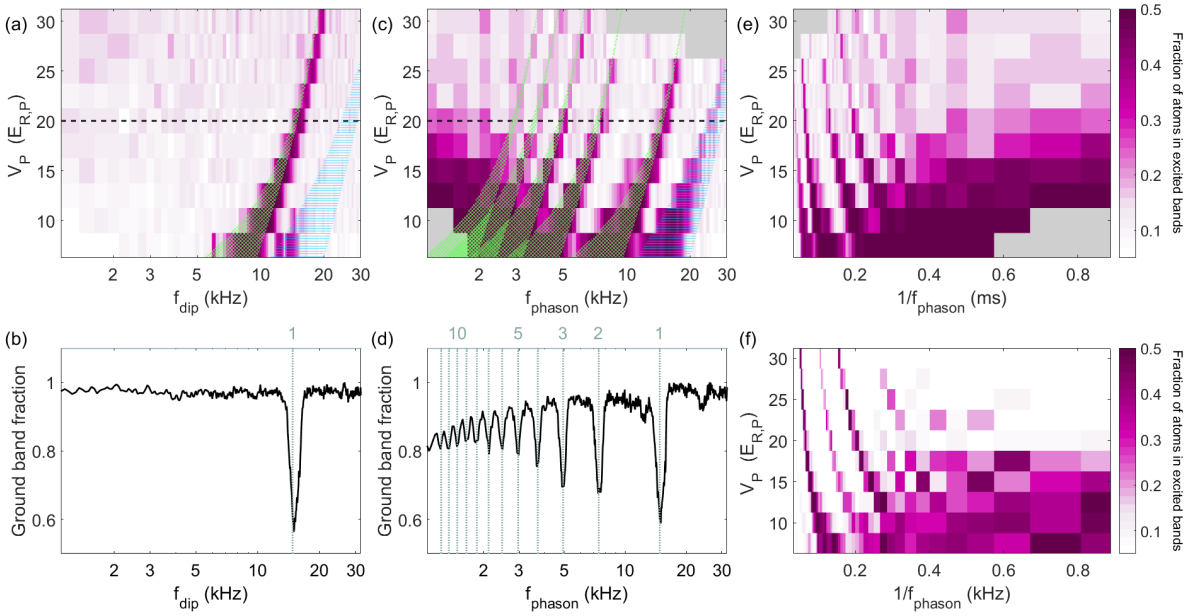

Figure 4.2: Comparison of dipolar and phasonic spectroscopy; areas where no data was taken are marked in gray. **(a)** Excitation due to dipolar driving as a function of drive frequency f_{dip} and primary lattice depth V_p with $\alpha_{\text{dip}} = 3.2 \times V_s/V_p$ and $V_s = 1.35E_{R,p}$. Green hatched (Blue horizontal) overlay shows calculated first (second) interband transition. We note that this value of α_{dip} differs from that presented in reference [36] because post-publication, it was realized that a factor of 20 amplifier gain was neglected in relating a control voltage to the displacement of the mirror on a piezo. This did neglected factor did not affect values of α_{phason}. **(b)** High-resolution dipolar spectrum at $V_p = 20E_{R,p}$. Line shows the calculated center of the first interband transition. **(c)** Excitation due to phasonic driving as a function of drive frequency f_{phason} and primary lattice depth V_P. α_{phason} is set to ≈ 1. Green hatched (Blue horizontal) overlays show calculated first (second) interband transition, with multiphoton subharmonics also indicated for the first transition. **(d)** High-resolution phasonic spectrum at $V_p = 20E_{R,p}$. Lines show the calculated center of the first twelve multiphoton transitions corresponding to the lowest interband transition. **(e)** Data from (c) plotted versus drive period $1/f_{\text{phason}}$, showing a broad low-frequency absorption feature. **(f)** Theoretical prediction for (e). *Reproduced from reference* [36] *with further detail therein.*

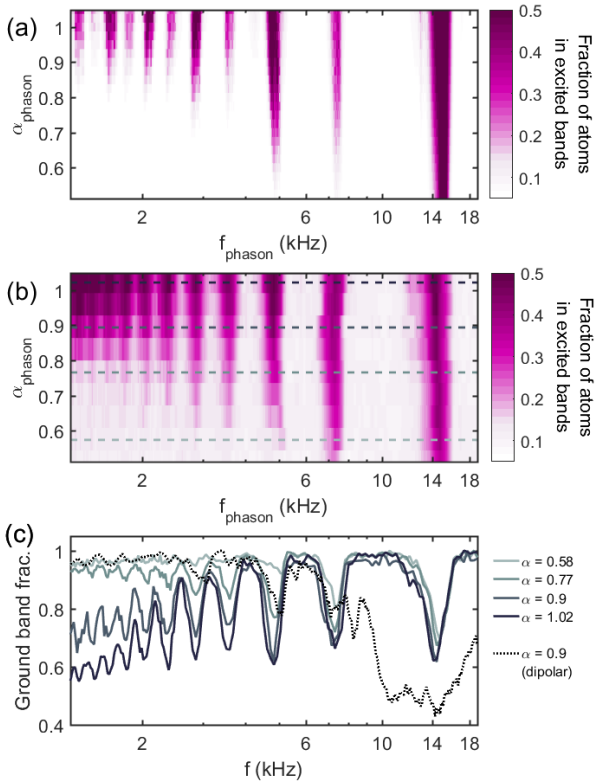

Figure 4.3: Amplitude dependence of multiphoton resonances. (a) Theoretical simulation of phasonic spectra for varying drive amplitude α_{phason}. (b) Experimentally measured phasonic spectra for $V_p = 20E_{R,p}$ and varying α_{phason}. Both experiment and theory show the onset of a non-perturbative regime near $\alpha_{\text{th}} = 0.9$. (c) Line cuts of experimental phasonic (solid) and dipolar (dashed) spectra at various α values. Note the extreme power broadening in the dipolar spectrum. *Reproduced from reference* [36].

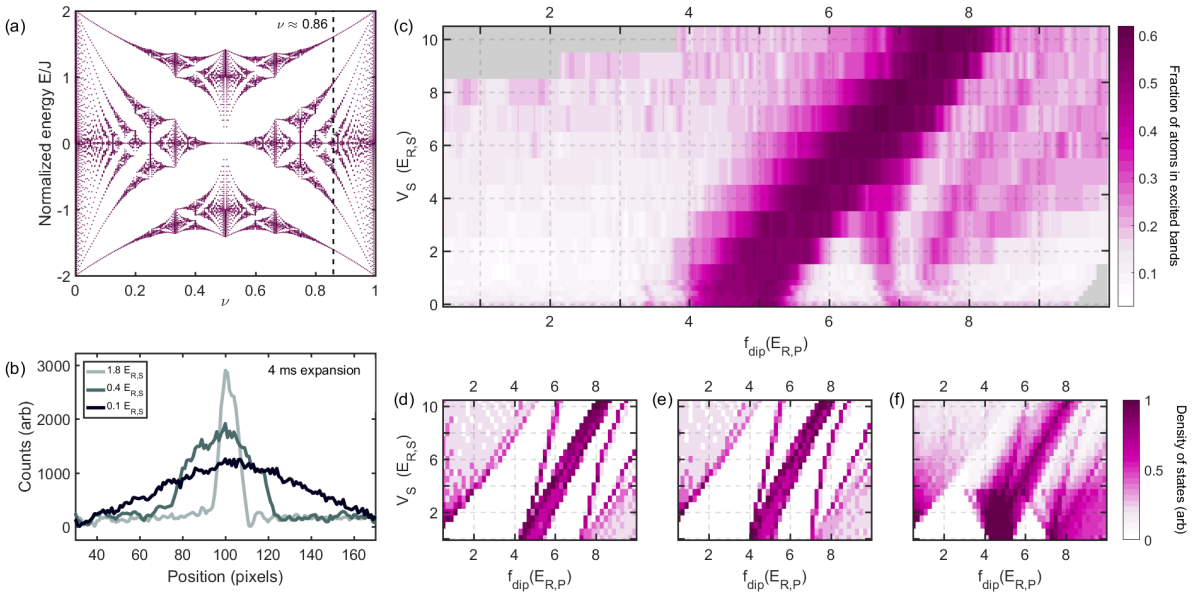

Figure 4.4: Spectroscopy of an interacting quasicrystal. (a) Calculated energy spectrum vs. $\nu = \lambda_s/\lambda_p$. Dashed line shows the slice corresponding to the quasicrystal used in this experiment. (b) Post-expansion atomic density distribution at varying disorder strengths V_S, showing the effects of crossing the localization transition. We note here again the difference in α_{dip} from reference [36] for the reason described in the caption of figure 4.2 (c) Experimentally measured dipolar excitation spectra for varying V_s/V_p at $\alpha_{\text{dip}} = 0.44$, showing spectral minigaps. No data were taken for the gray areas in the upper-left and lower-right. (d) Calculated density of final states for a non-interacting system, starting from a BEC. (e) Calculated density of final states for an interacting BEC; a shift of the resonance line to lower frequencies from Fig. 4.4(d) is observed. (f) Calculated non-interacting transition density assuming all single-particle orbitals below $1.5E_{R,s}$ are initially populated. *Reproduced from reference* [36].

4.2 Kicked Aubry-André-Harper Model

The kicked Aubry-André-Harper (kAAH) model is given by the tight-binding Hamiltonian

$$H_{\mathrm{kAAH}}(t) = -J \sum_l \Big[|l+1\rangle\langle l| + |l\rangle\langle l+1| \Big] + F(t)\Delta \sum_l \cos(2\pi\beta(l-\delta))\, |l\rangle\langle l| \tag{4.2}$$

which differs from the AAH model described in equation (1.1) of the introduction by the time dependent factor $F(t)$. We will consider $F(t)$ to be a somewhat generic pulse train that has short intervals of relatively high value with zero or very low magnitude between these intervals. In theoretical study of the kAAH model, $F(t)$ is typically taken to be a delta function pulse train defined by

$$F(t) = \sum_n \delta(t/T_{\mathrm{p}} - n)$$

where δ is the Dirac delta. Thus, equation (4.2) represents a tight-binding model where the on-site potential of the AAH model is pulsed (or "kicked on") intermittently in time.

In the recent work of reference [38], we experimentally realize this kicked version of the AAH model. A schematic of the experiment is shown in Figure 4.5(c) and (d). The experiment is conducted with a time dependent bichromatic optical lattice Hamiltonian of form (4.1) in the case that $V_s(t)$ is pulsed periodically with period T_{p} according to

$$V_s(t) = V_{s,0} \sum_{n=1}^{N} f_\tau(t/T_{\mathrm{p}} - n) \tag{4.3}$$

where $f_\tau(t/T_{\mathrm{p}})$ represents the functional form of the pulse shape that is non-negative and defined such that $\max f_\tau(t/T_{\mathrm{p}}) = 1$. We will further define an "effective pulse time"

$$\tau \equiv \int_0^{T_{\mathrm{p}}} f_\tau(t/T_{\mathrm{p}})\, \mathrm{d}t$$

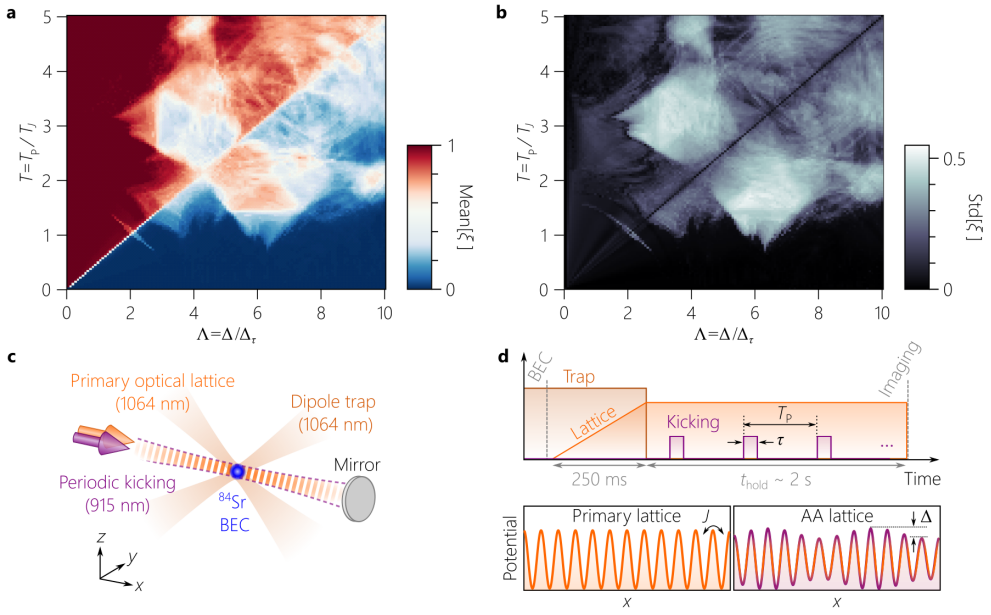

Figure 4.5: **Kicked Aubry-André-Harper model phase diagram and experimental approach.** **a**, Average IPR scaling exponent $\bar{\xi}$ as a function of Λ and T, for $\alpha = 1.162842$. **b**, Standard deviation of IPR scaling exponents. Along the diagonal ($\Lambda/T = 2$), scaling exponents for all eigenvectors take a single value. **c**, Experimental schematic. **d**, Experimental sequence. *Reproduced from reference* [38].

Here, τ corresponds to the pulse duration in the case of square pulses given by

$$f_\tau(t/T_\mathrm{p}) = \begin{cases} 1 & t \in (0,\tau) \\ 0 & \text{otherwise} \end{cases}$$

We will arrange such that the duration of the pulse[2] is small compared to the pulse period T_p. In these experiments, $V_p = 10E_{R,p}$ was constant in time, where $E_{R,p} = h^2/2m\lambda_p^2$ is the recoil energy of the primary lattice, and δ_p and δ_s were constant for the expansion of an individual atom cloud, but may have drifted slowly between experimental runs.

We introduce a couple other definitions at this point as well. It will be helpful to define the kick strength Λ as

$$\Lambda = \frac{\Delta}{\Delta_\tau} = \frac{\Delta\tau}{\hbar}$$

[2]We define the pulse duration as when $f_\tau(t/T_\mathrm{p})$ is not approximately 0.

and the pulse period in units of tunneling time T_J by

$$T = \frac{T_{\mathrm{p}}}{T_J} = \frac{T_{\mathrm{p}} J}{\hbar}$$

In Figure 4.5(a) and (b), we present some theoretical predictions for the scaling behavior of the IPR of the single-particle position-space eigenstates. The IPR for each eigenstate

$$|\psi\rangle = \sum_l \psi_l |l\rangle$$

for written in terms of the tight-binding basis states $|j\rangle$ is calculated for a system of L sites, and the scaling exponent of the IPR is defined as the value ξ that satisfies

$$\sum_{l=1}^{L} |\psi_l|^4 \sim L^{-\xi}$$

The average of ξ calculated over the set of eigenstates is presented in Figure 4.5(a) in terms of Λ and T, and the standard deviation of the set of ξ values for the eigenstates is shown in Figure 4.5(b). These suggest an extended range of kicked strengths Λ and dimensionless pulse times T that are theoretically predicted to create multifractal states.

To best match the theoretical delta pulses, one might wish to have pulses of very short duration compared to the time scale of the dynamics in the bichromatic lattice. This is achievable in many cases, but a practical issue arises in that a pulse train can excite atoms out of the ground band of the primary optical lattice. The theoretical tight-binding model (4.2) implies a lattice system with only a single (ground) band, and so does not capture the possibility that kicks will excite atoms to the higher energy bands that exist for a bichromatic lattice. Experimentally, these excitations also result in destructive loss of atoms from the trap. If the time between pulses is sufficiently small (i.e., high frequency) we can explore this experimentally without issue as shown in the results presented in figure 4.6. In figure 4.6, we depict the width σ_x,

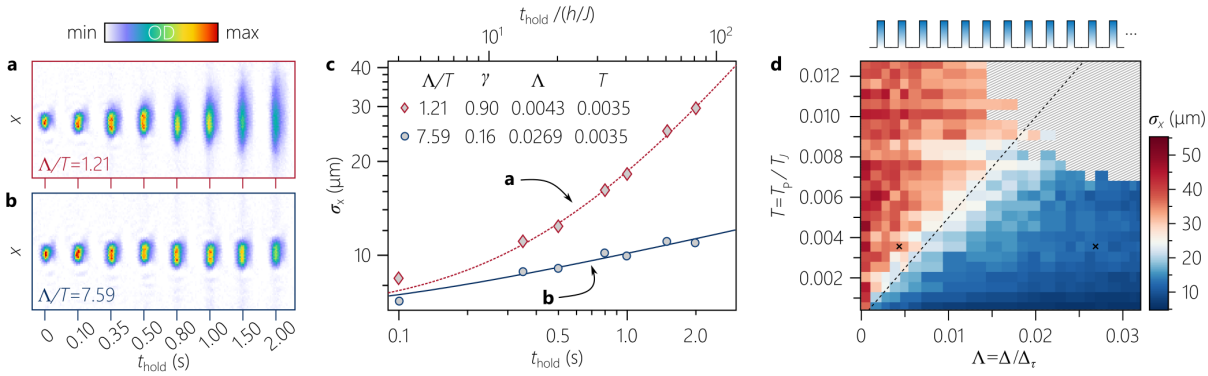

Figure 4.6: **Realizing the kicked Aubry-André-Harper model in the high-frequency regime.** **a**,**b**, Time sequence of density profiles in the kicked lattice for Λ/T below (**a**) or above (**b**) the localization transition. **c**, Fitting expansion curves to a form which captures both short and long-time behavior at various (Λ, T) allows for measurement of the exponent γ. The extracted widths were fit to $\sigma_x(t) = \sigma_0(1+t/t_0)^\gamma$, the solution to a generalized diffusion equation. **d**, Measured localization phase diagram of the kAAH model for small Λ and T, using a simple rectangular form for the pulse shape $f_\tau(t)$ with $\tau = 1$ μs. Colormap depicts fitted width of the density distribution σ_x as a function of Λ and T at $t_{\text{hold}} = 2$ s. Dashed line indicates the time-averaged static AA transition at $\Lambda/T = 2$. The center point (white) of the colormap is set to the σ_x observed at the same hold time when the expansion exponent is in the center of its transition from localized to delocalized values. Black crosses indicate (Λ, T) values of the data in **a**, **b**, and **c**. Cross-hatched pixels indicate data which failed cuts of the fitting procedure due to heating via interband transitions. Without mitigative measures, such heating prevents exploration of the phase diagram much beyond the region shown here; see Fig. 4.7 for details on characterization and suppression of this effect. *Reproduced from reference* [38].

which is the standard deviation of a gaussian fit to the 1D atomic cloud density distribution along the lattice direction (details in reference [38].)

These destructive excitations, which are the reason for the cross-hatched pixels of figure 4.6(c), generically occur when the frequency power spectrum of the pulse train has sufficient power in the range of frequencies resonant with transitions from the ground band to higher bands. This can arise in some cases because the frequency of the pulses $f = 1/T_{\text{p}}$ matches the excitation frequency to higher band. Data exhibiting this excitation and the corresponding decay (loss) rate is presented in figure 4.7(a). However, for the more interesting regions of T and Λ in figures 4.5(a) and 4.5(b), the period T between pulses is in fact much

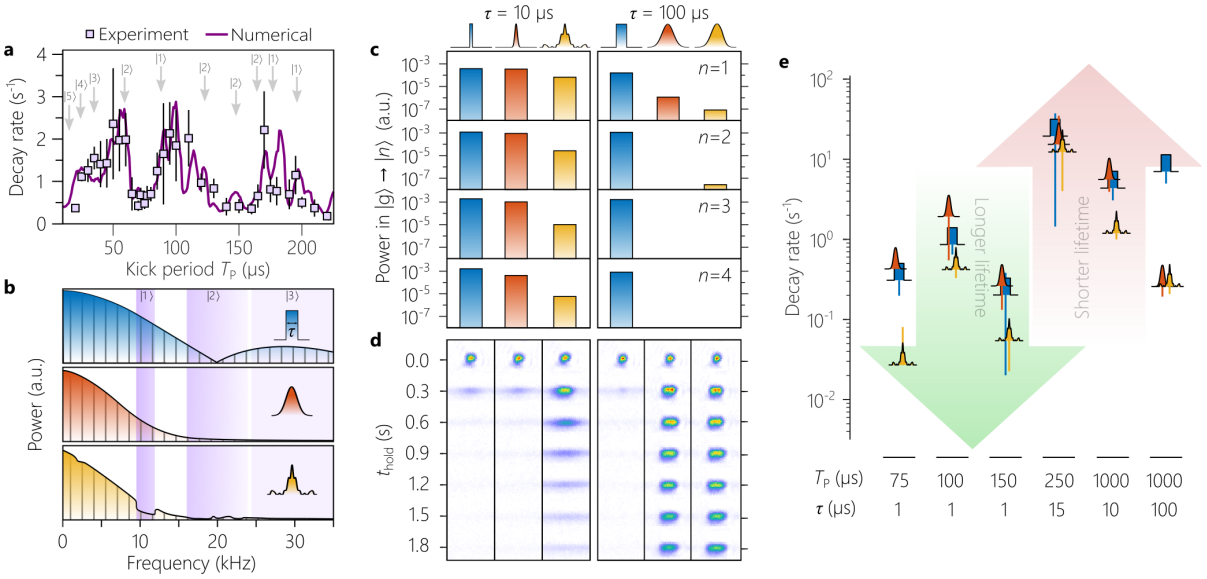

Figure 4.7: **Apodized Floquet engineering. a**, Decay rate of atoms kicked by square pulses with a pulse duration of $\tau = 1$ μs and a kick strength of $\Lambda = 0.018$ for $t_{\text{hold}} = 2$ s as a function of kick period T_P. Solid curve is the result of a numerical calculation (see Supplementary Information section IV A of reference [38]). Arrows indicate dominant transitions from ground band $|n = 0\rangle$ to excited bands $|n = 1, 2, ...\rangle$. Error bars represent 95 % confidence intervals from an exponential fit to 20 measurements. **b**, Form of the power spectrum of square (top), Gaussian (middle) and filtered (bottom) pulses. Shaded areas represent interband transitions. Note that the frequency comb spacing is not drawn to scale for visibility. **c**, Net power in frequency ranges corresponding to interband transitions, for square, Gaussian, and filtered pulses of two pulse widths, each with period $T_P = 1$ms. For longer pulses, the gaussian pulse already has little power in the interband transition frequencies, and so filtering has little additional effect. **d**, Measured density profile at various times for each pulse shape. **e**, Measured decay rates from the ground band for different pulse shapes at various values of T_P and τ. The baseline of each symbol corresponds to the measured decay rate. Error bars represent 95% confidence bounds from an exponential fit. *Reproduced from reference* [38].

longer than those that would excite from the ground band to the first excited band in our system. Nonetheless, operating with short square pulses with these longer pulse periods results in dramatic atom loss because the power spectrum for this square pulse train still contains substantial resonant excitation frequencies, but in this case, changing the pulse shape can avoid such excitation as we now explain.

Let us consider the Fourier transform of (4.3). To simplify, we ignore the effect of the finite duration of the pulse train by approximating $V_s(t) = V_{s,0} \sum_{n=-\infty}^{\infty} f_\tau(t/T_p - n)$. Given the

periodicity of the pulse train, a simple approach is to write its Fourier series according to

$$V_s(t) = \sum_n A_n \, e^{i2\pi nt/T_\mathrm{p}}$$

and solve for A_n in the usual way. However, we feel that an application of the convolution theorem gives more insight. To this end, consider that we can write

$$V_s(t) = V_{s,0} \sum_{n=-\infty}^{\infty} f_\tau(t/T_\mathrm{p} - n) = V_{s,0} \sum_{n=-\infty}^{\infty} \int f_\tau(t'/T_\mathrm{p}) \delta((t-t')/T_\mathrm{p} - n) \mathrm{d}t'$$

The last expression is a convolution between the function f_τ and a pulse train of Dirac delta functions, so we can apply the convolution theorem to write the Fourier transform as

$$\tilde{V}_s(\nu) = \tilde{f}_\tau(\nu) T_\mathrm{p} \sum_n e^{-i2\pi n\nu T_\mathrm{p}} = \tilde{f}_\tau(\nu) \left[\frac{1}{T_\mathrm{p}} \sum_n \delta(\nu T_\mathrm{p} - m) \right] \tag{4.4}$$

where we have denoted the Fourier transform of a function $g(t)$ by $\tilde{g}(\nu)$. Thus, we see from equation (4.4) that when $1/T_\mathrm{p}$ is small compared to the excitation frequency to higher bands, the delta function comb factor will be finely spaced and the factor $\tilde{f}_\tau(\nu)$ predominantly determines the relevant features of the energy spectrum of the drive. This is shown for a number of sample pulse shapes in f_τ in figure 4.7(b). Figure 4.7 generally depicts the critical requirement of pulse shaping for this experiment, which in this case is referred to as "apodization." We conclude that we can suppress excitations to higher bands by shaping the pulse so that $\left|\tilde{f}_\tau(\nu)\right|$ is small when ν corresponds to a resonant excitation frequency between the ground band and excited bands.

Figure 4.8 details the measured expansion at longer T_p that was enabled by this apodization procedure. In particular, we observe features of reentrant localization in which increasing kick strength initially increases localization, then *decreases* localization before continuing to increase localization, which deviates quite dramatically from the simple time averaged expec-

tation. This is a rather unintuitive effect as it is contrary to the naive expectation that as the disorder kick strength increases, the degree of localization would increase.

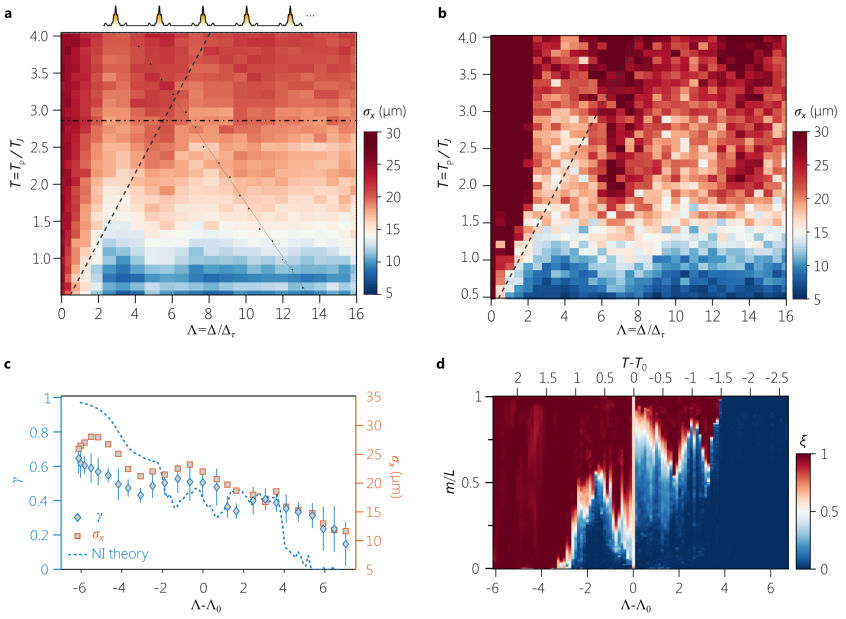

Figure 4.8: **Experimental signatures of anomalous localization in the kAAH model.** **a**, Measured phase diagram of the kAAH model for large T and Λ using apodized kicking waveforms in the form of a Gaussian pulse with $\tau = 319.3$ μs. Colormap shows fitted width of density distribution σ_x for $t_{\text{hold}} = 2$ s. Dashed line indicates the time-averaged static AAH transition at $\Lambda/T = 2$. The colormap center (white) is chosen at this transition point as in Fig. 4.6(d). **b**, Calculated phase diagram of the kAAH model for parameters and observable chosen to match the experiment. Numerically calculated time-evolved density distributions were convolved with the estimated point spread function of our imaging system and fitted with a Gaussian; colorbar shows the fitted width and has the same limits as panel a. **c**, Expansion exponent γ versus $\Lambda - \Lambda_0$ (diamonds), for parameter values indicated by points in panel **a**, extracted by fitting the late-time width evolution to $\sigma_x(t) \propto t^\gamma$. Error bars show 95 % confidence bounds from such a fit to 16 measurements Measured σ_x is also plotted (squares), indicating that this single measurement tracks well with fits of the full time series. Equivalent expansion exponent data for the horizontal dot-dashed line in (a) appears in extended figure 5 of [38]. **d**, Scaling exponent ξ of inverse participation ratio for single-particle states as a function of disorder strength Λ for the same parameter range. m/L denotes the normalized index of eigenstates. *Reproduced from reference* [38].

4.3 Coherent Control of Localization

We will now introduce recent work on coherently controlling localization of atoms in a driven version of the AAH model that is presented in reference [39] and is in the process of review for publication. The form of the drive is very similar to that used in the experiments of section 4.1, but at a much lower frequency. As before, δ_s in equation (4.1) is modulated in time, where V_p, V_s, and δ_p are constant for each cloud. The modulation is given according to the form $\delta_s(t) = -2k_s A \sin(\omega t)/(2\pi\beta)$, where A is adjusted in the experiment and $k_s \equiv 2\pi/\lambda_s$ for a secondary lattice of wavelength $\lambda_s = 914.4$ nm.

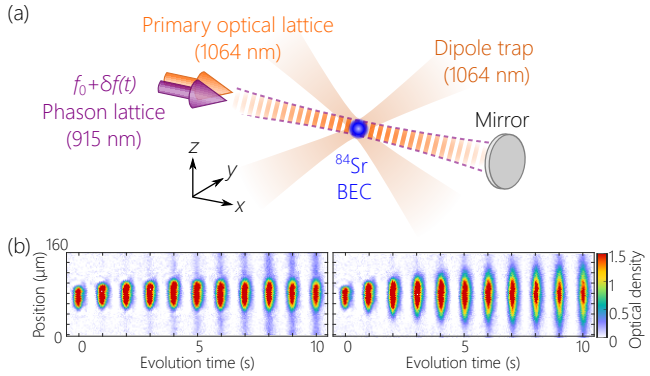

Figure 4.9: Experimental schematic and typical data. **(a)** An optically trapped BEC is loaded into a bichromatic lattice and allowed to evolve. A time-varying phasonic displacement between the two sublattices is controlled by varying the frequency of the secondary lattice laser ($\lambda_S = 915$ nm). **(b)** Absorption images of the atoms taken after various evolution times in the phasonically modulated bichromatic lattice, in the localized regime (left panel) and delocalized regime (right panel). *Reproduced from reference* [39].

A diagram of the experimental setup is shown in figure 4.9(a). δ_s is controlled by changing the frequency of the laser beam that is retro-reflected to form the secondary lattice. This work is not the first usage of this technique, but it is not so widely used lately, and could use an introduction for those first encountering it. For this reason, we will supplement some detail here.

The lattice in this case is formed by retro-reflecting a laser beam from a mirror. The mirror implies a boundary condition on the light wave that sets a fixed phase condition on the lattice.

To describe the lattice with this boundary condition in mind, let us take the origin ($x = 0$) to be centered on the atomic cloud and the retro-reflecting mirror to be a distance L away from the origin at $x = L$. The contribution to the potential from the secondary lattice is then described by

$$V_{s,\text{latt}}(x,t) = V_s \sin^2\left(k_s(t)\cdot(x-L)+\pi/2\right)$$

This satisfies the boundary condition requirement at the mirror ($x = L$) that the laser field amplitude be zero, which corresponds to a maximum in the lattice potential. If we write $k_s(t) = k_{s,0} + \delta k_s(t) = k_{s,0} + 2\pi\cdot\delta f(t)/c$, where c is the speed of light and $\delta f(t)$ is the change in the laser frequency from the nominal frequency $f_0 \equiv c/\lambda_s = ck_{s,0}/(2\pi)$, then we can equivalently express the potential as

$$V_{s,\text{latt}}(x,t) = V_s \sin^2\left(k_s(t)\cdot x - 2\pi\cdot\delta f(t)L/c+\phi_0\right)$$

where $\phi_0 \equiv k_{s,0}L + \pi/2$ is a constant phase. Lastly, we must consider that $L \sim 1\text{m}$ is about 10^4 times larger than maximum width of the atomic cloud in our experiment. Furthermore, the changes in laser frequency $\delta f(t)$ away from f_0 will amount to translating the secondary lattice near the atoms by a few lattice sites at most, which corresponds to the condition $2\pi\cdot\delta f(t)L/c \lesssim 10$. This implies that $2\pi\cdot\delta f(t)x/c \lesssim 10^{-3}$, and we use this small value to justify the approximation $k_s(t)x \approx k_{s,0}x$ in the region of x values that the atomic cloud will explore during our experiment. Using this approximation implies

$$V_{s,\text{latt}}(x,t) \approx V_s \sin^2\left(k_{s,0}x - 2\pi\cdot\delta f(t)L/c+\phi_0\right),$$

This expression reveals how the frequency modulation $\delta f(t)$ effectively gives rise to translation of the lattice at the atoms.

One may find it helpful to envision the lattice sites as being like the pleats on an accordion

(or the loops on a spring). If one end of the accordion (spring) is fixed to a wall and one watches it some distance away from the wall, the expansion and compression of the accordion (spring) will be seen predominantly as a translation of the pleats (loops) at small length scales away from the wall.

The experiment explores drive frequencies ω with corresponding drive energy quanta $\hbar\omega$ (analogous to "photon energy") that are greater than the energy width of the ground band, but much less than the energy band gap. This is in contrast to the experiment discussed in section 4.1, where $\hbar\omega$ was at a scale comparable to the band gap to explore frequencies that induce transitions to higher bands. Figure 4.10 summarizes our initial experimental observation of how the system reacts as a function of phasonic drive amplitude A at frequencies in this range. We observe that the system behave under these drive conditions according to the effective Hamiltonian

$$H^F_{\mathrm{CC}} = -J \sum_l \Big[|l+1\rangle\langle l| + |l\rangle\langle l+1| \Big] + \Delta_{\mathrm{eff}} \sum_l \cos(2\pi\beta(l-\delta)) \, |l\rangle\langle l| \tag{4.5}$$

where

$$\Delta_{\mathrm{eff}} = \Delta \, \mathcal{J}_0(2k_{\mathrm{s}}A)$$

$\mathcal{J}_0$ denotes the zeroth Bessel function. We recognize that effective Hamiltonian (4.5) has the same form as the AAH Hamiltonian, and so we expect localization to occur when $|\Delta_{\mathrm{eff}}|/J > 2$ and delocalization to occur if $|\Delta_{\mathrm{eff}}|/J < 2$. The data in figures 4.10(a) and (b) shows agreement with this model, and we see that we can induce dynamic delocalization by adjusting the phason amplitude A. The data in figure 4.10(c) further demonstrates behavior in agreement with this model in the case that $\Delta/J < 2$. In this regime the cloud width σ after a fixed expansion time is expected to behave according to $\sigma = \alpha(2 - \Delta_{\mathrm{eff}}/J)$ where α is a constant of proportionality.

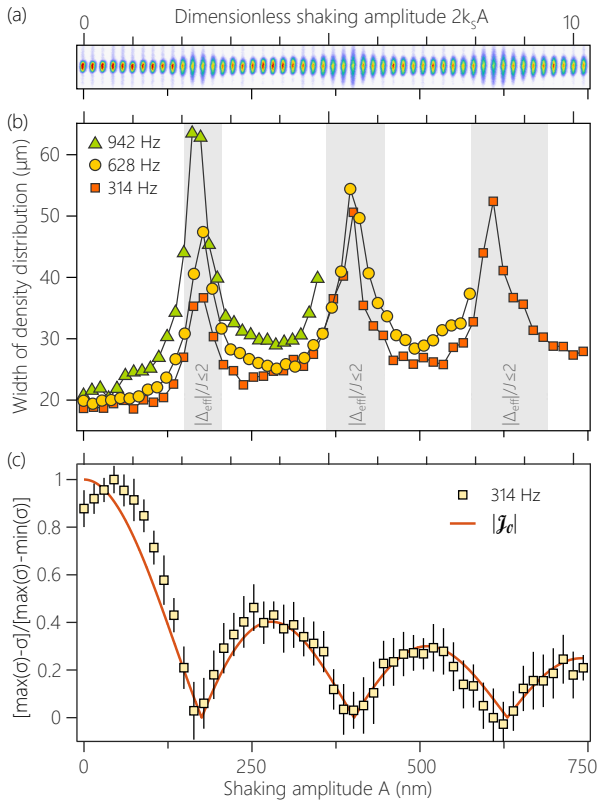

Figure 4.10: Phasonic modulation causes dynamic delocalization. **(a)** Absorption images of the atomic density distribution after 10s evolution for varying amplitudes of a 314Hz phason modulation, showing peaks in the late-time width at several drive amplitudes. **(b)** Width of the atomic density distribution after 10s evolution versus phason modulation amplitude, for three different driving frequencies. The delocalized regions are observed to be independent of drive frequency. The primary and secondary lattice depths are $10E_{R,p}$ and $0.5E_{R,p}$. Here $E_{R,p} = h^2/2m\lambda_p^2$ is the recoil energy, m is the atomic mass, and h is Planck's constant. Shaded areas show the regime of theoretically predicted delocalization described in the text. **(c)** Quasidisorder strength can be inferred from transport. Plot shows a normalized form of the late-time width σ versus phason modulation amplitude, for primar lattice depth $8.5E_{R,p}$ and secondary lattice depth $0.124E_{R,\mathrm{p}}$, corresponding to the delocalized regime. In this regime the expansion speed is approximately proportional to the quasidisorder strength, so the expected functional form is the absolute value of a Bessel function $|\mathcal{J}_0(2k_sA)|$, shown here as a solid line with no fit parameters. All of the panels share the same x-axis scaling, measured in the dimensionless shaking amplitude $2k_sA$ (panel top) and in the actual shaking amplitude A (panel bottom). *Reproduced from reference* [39].

Defining $\max(\sigma) = 2\alpha$, occurring at $\Delta_{\mathrm{eff}} = 0$, we should expect that

$$[\max(\sigma) - \sigma] = \alpha\Delta_{\mathrm{eff}}/J \propto \mathcal{J}_0(2k_sA)$$

and the form of this expression is observed to hold in the data shown in figure 4.10(c).

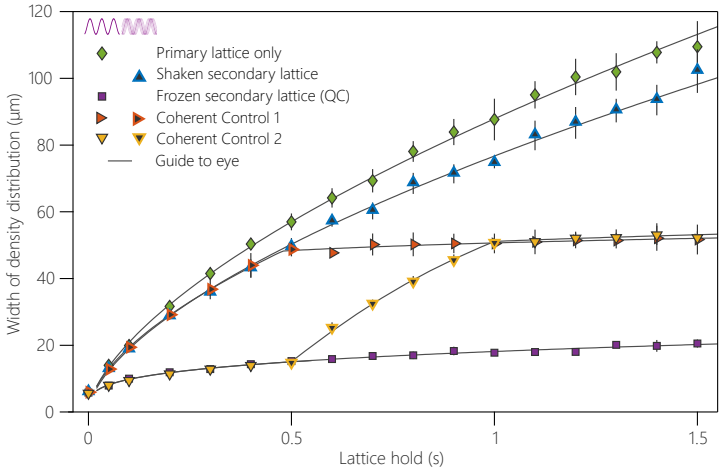

Figure 4.11: Reversible coherent control of localization. Symbols show measured late-time width of the density distribution versus hold time for five different experimental protocols: no secondary lattice (diamonds), continuous phasonic driving of secondary lattice (upward triangles), phasonic driving for the first 500ms (rightward triangles), phasonic driving only between 500 and 1000ms (downward triangles), and no driving of the secondary lattice (squares). For all protocols the primary lattice depth is $6E_{R,p}$, and for all but the first plot the secondary lattice depth is $0.5E_{R,p}$. At these values in the absence of driving the system is Aubry-André localized. Note especially that width evolution under the second "coherent control" protocol shows evidence of localization for times less than 0.5s and greater than 1s, and evidence of delocalization between those times, indicating reversible coherent control. Shaking frequency is 628Hz and phason amplitude is $2k_S A \approx 5.52$, near the second Bessel zero. *Reproduced from reference* [39].

Figure 4.11 shows a further feature of this drive protocol: using this phasonic drive gives coherent control of the localization. This is borne out in the data of figure 4.11 in that delocalization can be induced by application of the phasonic drive and returned to localization by removing the drive to observe some expansion (red triangles in figure 4.11). Alternatively, one can begin with the atoms localized before applying the drive to delocalize the atoms (yellow triangles in figure 4.11), and we observe the same amount of expansion as in the previous case. Thus, we find that the ordering of such a drive protocol is reversible.

Moreover, we argue from an analysis of the corresponding driven Hofstadter model that this transition between localization and delocalization is controlled coherently by the drive

amplitude A. This corresponding driven Hofstadter model can be constructed by adding time dependent phase factors to the terms in the Hofstadter Hamiltonian of equation (1.2) in the introduction to yield

$$H_{\text{Hof,Driven}-y} = -J \sum_{l,m} \Big[\; |l+1,m\rangle \langle l,m| \; + \; |l-1,m\rangle \langle l,m| \; + \\ \frac{\Delta}{2J} e^{-i2\pi\alpha l} e^{-i2k_s A\cos(\omega t)} \, |l,m+1\rangle \langle l,m| \; + \; \frac{\Delta}{2J} e^{i2\pi\alpha l} e^{i2k_s A\cos(\omega t)} \, |l,m-1\rangle \langle l,m| \; \Big] \tag{4.6}$$

In reference [39], this driven Hofstadter Hamiltonian is referred to as the "higher-dimensional superspace" for the dynamic quasiperiodic potential. Arguments almost identical to those presented in the introductory chapter 1 of this thesis map this to the set of driven AAH models given by

$$H_\nu = \sum_l -J\Big[\; |l+1;\nu\rangle \langle l;\nu| \; + \; |l-1;\nu\rangle \langle l;\nu| \; \Big] \; + \; \Delta\cos\left(2\pi(\alpha l - \nu) + 2k_s A\cos(\omega t)\right) \; |l;\nu\rangle \langle l;\nu|$$

The relationship between this H_ν and $H_{\text{Hof,Driven}-y}$ is given by

$$H_{\text{Hof,Driven}-y} = \int_{-1/2}^{1/2} \mathrm{d}\nu \, H_\nu$$

The added phase factors $\exp(\pm i2k_s A\cos(\omega t))$ in equation (4.6) can be mapped to an oscillating force (or electric field for charged particles) directed along the y-direction, and this mapping is accomplished with a standard unitary transformation (see for example reference [1], section III.B. titled Dynamic Localization for this unitary transformation in a 1D lattice.) Since the dynamic localization in this 2D model is coherent, we deduce that the localization transition in the corresponding set of AAH models (each one corresponding to a different phason offset ν) is also coherent.

In the experimental data shown in figure 4.11, this coherent localization transition is seen in ability to coherently "activate" transport by using a certain drive amplitude A that corresponds to $\Delta_{\text{eff}}/J < 2$ and to coherently "freeze" the transport by choosing an amplitude A that corresponds to $\Delta_{\text{eff}}/J > 2$. The coherence is evident in that the overall expansion is independent of the time ordering of the periods of activated transport and frozen transport, up to effects not considered in the model, such as interactions. Moreover, this demonstrates that the increased spreading is not due to heating.

Lastly, we consider sinusoidally translating the primary lattice alone, which will serve in part as a prelude for the work discussed in chapter 5. For this analysis we will be interested in the reference frame that is comoving with the primary lattice, where the translation of the primary lattice in the lab frame is experienced as an oscillating force. We will now discuss how translation of the primary lattice is achieved.

In this experiment, the primary lattice setup does not correspond to that shown in figure 4.9(a). The primary lattice is not produced by retro-reflection from a mirror, but is instead formed by two counter-propagating beams each of which has its frequency independently controlled by an AOM. As explained in more detail in chapter 5, the velocity of the primary lattice is given by equation (5.3) reproduced here:

$$v_p = \frac{\lambda_p}{2}\Delta\nu_p$$

where $\Delta\nu_p$ is the frequency difference between the two laser beams that form the primary lattice.

Moreover, we can express the strength of the drive in the reference frame that is comoving with the primary lattice with the parameter

$$K_0 = \frac{m\lambda_p^2}{4\hbar}\Delta\nu_{\text{max},p}$$

This is equivalent to the definitions for K_0 given in chapter 5 and in reference [39], where we have assumed the form

$$\Delta\nu_p = \Delta\nu_{\max,p}\sin(\omega t)$$

However, we must also account for the translation of the secondary lattice relative to the primary lattice. In this case, the amplitude A of the secondary lattice in the reference frame of the primary lattice will be given by

$$A = \frac{\lambda_p}{2\omega}\Delta\nu_{\max} = \frac{2\hbar}{m\lambda_p}\frac{K_0}{\omega} \tag{4.7}$$

In the high frequency limit, the effective Hamiltonian will take the form

$$H^F_{\mathrm{CC,DL}} = -J_{\mathrm{eff}}\sum_l\Big[\,|l+1\rangle\langle l| + |l\rangle\langle l+1|\,\Big] + \Delta_{\mathrm{eff}}\sum_l\cos(2\pi\beta(l-\delta))\,|l\rangle\langle l| \tag{4.8}$$

which is again the only differs from the AAH Hamiltonian by the substitutions of J and Δ by their effective counterparts, given in this case by

$$J_{\mathrm{eff}} = J\mathcal{J}_0(K_0) \qquad \text{and} \qquad \Delta_{\mathrm{eff}} = \Delta\,\mathcal{J}_0(2k_{\mathrm{s}}A)$$

Here, Δ_{eff} is the same as above and the explanation for the form of J_{eff} will be explained in detail in chapter 5. Thus, one would expect a transition between localization and delocalization to occur at $\Delta_{\mathrm{eff}}/J_{\mathrm{eff}} = 2$. Figure 4.12 depicts data that agrees with this model at several drive frequencies $f = \omega/(2\pi)$. Note that J_{eff} as a function of drive strength K_0 is independent of the drive frequency,[3] but that A does vary inversely with drive frequency as a function of drive strength according to equation (4.7). It is this dependence of $\mathcal{J}_0(2k_{\mathrm{s}}A)$ on ω and K_0 that gives rise to the peaks of delocalization that are observed in the lower three panels of figure 4.12.

[3]This is assuming that the drive frequency is sufficiently high (discussed further in chapter 5) but also not resonant with excitations to higher band that would lead to atom loss in our bichromatic lattice system.

These peaks are spaced according to the zeros of the bessel function.

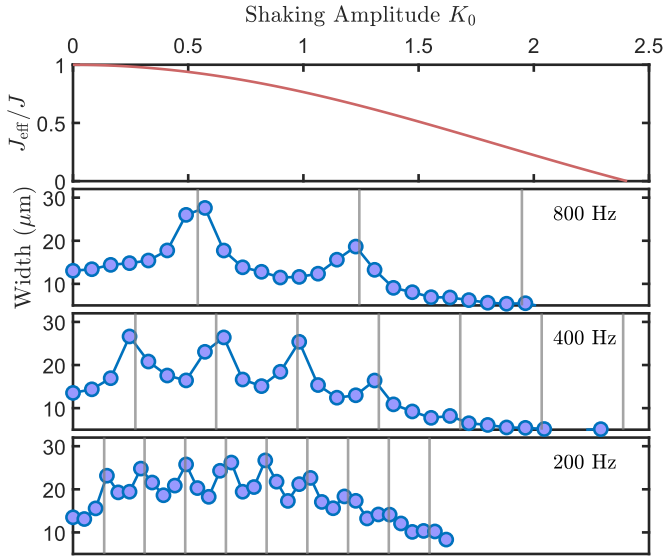

Figure 4.12: Interplay between dynamic localization and Aubry-André localization revealed by phase modulation of only the primary lattice. Top panel shows calculated effective tunneling strength as a function of modulation amplitude K_0. Lower panels show measured width of the density distribution after 1s expansion in a bichromatic lattice with only the primary lattice shaken, for various modulation frequencies as indicated. Gray lines indicate theoretically expected values of zero effective quasidisorder. *Reproduced from reference* [39].

Chapter 5

Simultaneous Dynamic Localization and Aubry-André Localization

5.1 Introduction

Due to the extended character of Bloch wavefunctions and associated energy structure, quantum lattice systems tend to be metals by default. That is to say, the quantum particles, usually electrons in solid state systems, diffuse readily in the lattice and can be motivated readily by the application of a force, such as an applied electric field in the case of electron systems. This behavior would be prevalent except for various localizing influences, which can take the form of interactions (Mott localization), disorder (Anderson localization), quantum statistics (band insulators), and periodic driving (dynamic localization). The interplay of various localizing phenomena is a deep topic which remains at the forefront of the study of condensed matter; a current example is the intense discussion of the many-body localized state which depends upon the interplay between interactions and disorder [40, 41].

As introduced in chapter 1, Anderson localization occurs when small scale disorder is superimposed with a lattice potential. The random change in potential on each lattice site

results in every eigenstate of the system being localized. Consequently, if a particle is placed in an initial state of a localized wavefunction then it will remain localized to the scale of the eigenstates. This localization has been observed in cold atom systems [42] and photonics systems [43].

Also introduced in chapter 1 is the related localization phenomenon that arises in the Aubry-André-Harper (AAH) model which is the tight-binding model description of a sinusoidal potential with period a_2 superimposed with a much stronger lattice potential of period a_1. Aubry-André localization occurs in this system provided that the sinusoidal potential is strong enough and that a_1/a_2 is irrational (excepting special values). As in Anderson localization, the eigenstate wavefunctions are exponentially localized, and so one can view the AAH potential in these cases as being "sufficiently disordered" to produce localization when the potential is strong enough, although there are important differences between the phenomena of the AAH model and Anderson localization to consider if one is being rigorous. In other words, the spatial quasiperiodicity of the Aubry-André-Harper (AAH) model can drive a metal-insulator transition [8, 44, 45]. This has been studied experimentally in photonic systems [46] and cold atom systems [47].

A temporally oscillating spatially uniform force applied to a lattice system can also give rise to localization by an entirely different mechanism, which can be viewed either as originating from a drive-induced flat Floquet band or from time-averaged Bloch oscillations [48]. In the academic literature, mechanism of localization is referred to as dynamic localization. In this experiment, our periodically driven realization of the AAH model provides an experimental study of the mutual enhancement and competition that exists between Aubry-André localization and dynamic localization.

Previous work has fruitfully examined driven AAH systems theoretically [49, 50] and the related topic of driven Anderson insulators theoretically [51, 52] and experimentally [53]. It is important to note that we focus on the regime in which the drive frequency that induces

dynamic localization is not necessarily large compared to the bandwidth. In this regime, commonly-used theoretical approximations of the high frequency effective Hamiltonian for the Floquet states break down, though numerical investigation has indicated (and we experimentally confirm) that localization can persist [49]. The experimental and numerical results we present here thus extend beyond previous work to reveal a richer and more complex phase diagram that arises when the drive frequency is near the spectral width of transitions within the lowest energy band. Our results demonstrate that even at these drive frequencies the high-frequency analytical model accurately predicts the basic structure of the phase diagram while also clearly revealing qualitative deviations from those predictions when the on-site potential in the driven AAH model is sufficiently strong.

5.2 Description of Experiment

The experiments we describe begin by loading a Bose-Einstein condensate of ^{84}Sr into a pair of superimposed coaxial 1D optical lattices with different spatial periods, aligned along an axis perpendicular to gravity. The deeper of these two lattices, which we refer to as the primary lattice, is generated by counterpropagating laser beams with wavelength $\lambda_p = 1064$ nm. The two primary lattice beams are derived from the same fiber amplifier (Toptica/Azurlight Model: ALS-IR-1064-50-A-CC-SF) seeded with a narrow linewidth laser (Coherent Model: Mephisto 200FC Laser System), but their frequency and amplitude can be tuned independently using acousto-optic modulators (AOMs). One of the primary lattice beams has a much higher intensity than any of the other beams (approximately 2 W) in order to support the atoms against gravity, as the atoms will be attracted via the optical dipole force discussed in section 3.2. The depth of the primary lattice V_p is controlled by adjusting the intensity and polarization of the weaker beam. The two laser beams that form the secondary lattice have wavelength $\lambda_s = 874.6$ nm and are derived from a continuous wave titanium sapphire laser (M Squared

Model: SolsTiS 18W PSF-XF) stabilized against slow drift by a wavemeter. The secondary lattice beams are of roughly equal intensity, adjusted together to control the depth of the secondary lattice V_s, and have independently AOM-tunable frequency offsets.

The key capability offered by this setup is full time-dependent tunability of the potential depths (V_p and V_s) and spatial offset of the primary and secondary optical lattices δ_p and δ_s, up to slow uncontrollable drift in the phases due to thermal changes in the light propagation media, thermal expansion of the optical table, and small drifts of opto-mechanical components. Thus, we will not know the absolute starting values of δ_p and δ_s for an experimental run, but we will be able to controllably change its position from this initial value. As we will show, this capability enables the simultaneous experimental realization of both dynamic and quasidisorder-induced localization, thereby allowing the direct investigation of their interplay.

The system is depicted schematically in figure 5.1(a) and described by the one-dimensional bichromatic lattice Hamiltonian[1]

$$H = -\frac{\hbar^2}{2m}\frac{\mathrm{d}^2}{\mathrm{d}x^2} + V_p \sin^2(k_p(x-\delta_p)) + V_s \sin^2(k_s(x-\delta_s)) \tag{5.1}$$

where V_p and V_s are the depths of the primary and secondary lattice, respectively. $k_{p(s)} = 2\pi/\lambda_{p(s)}$ and $\delta_{p(s)}$ denotes the possibly time-dependent spatial offset of the of the primary (secondary) lattice, which is determined by the phase difference $\Delta\varphi_{p(s)}$ between the counterpropagating laser beams according to the formula

$$\delta_{p(s)} = \frac{\Delta\varphi_{p(s)}}{2k_{p(s)}} \tag{5.2}$$

[1]This is identical to the generic time dependent bichromatic lattice Hamiltonian in equation (4.1) presented as an introduction to chapter 4, but we have dropped the explicit time dependence of the parameters V_p, V_s, δ_p, and δ_s.

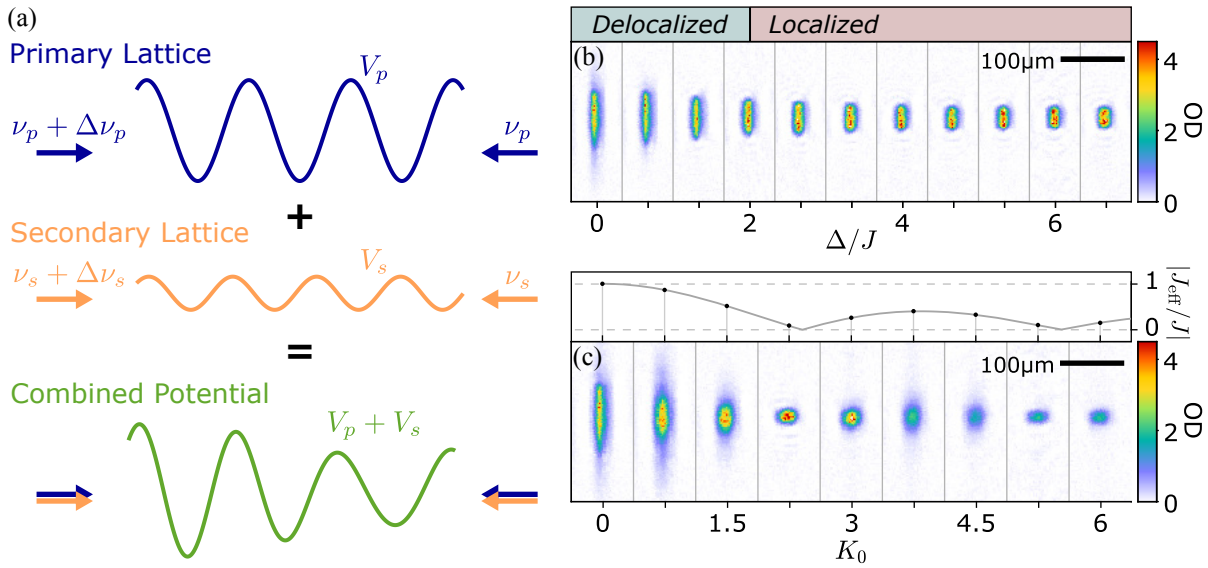

Figure 5.1: (a) A schematic of the 1D experiment model depicting primary (dark blue) and secondary (light orange) lattice, and resulting potential (green). (b) AAH localization observed in atomic clouds imaged after 500 ms of expansion. The localization-delocalization transition occurs at $\Delta/J = 2$ as indicated by the labeled bars above the panels. (c) Analogous cloud images for dynamic localization with sinusoidal drive strength K_0. Above each panel, a theoretical plot indicates the predicted $|J_{\mathrm{eff}}|$ for each cloud in the $\hbar\omega \gg 4J$ approximation. The parameter Δ/J in (b) and K_0 in (c) that describes the experimental conditions that produced the imaged cloud is indicated by the tick mark below each panel.

The velocity of each lattice is thus

$$v_{p(s)} = \frac{\mathrm{d}}{\mathrm{d}t}\delta_{p(s)} = \frac{\lambda_{p(s)}}{2}\Delta\nu_{p(s)} \tag{5.3}$$

where $\Delta\nu_{p(s)}$ is the frequency difference between the two laser beams forming the primary (secondary) lattice. We directly control $\Delta\nu_{p(s)}$ by adjusting the phase of the radio frequency (RF) drive to the AOM. All RF waveform generators share a clock signal so that the relative position of the two lattices is well controlled up to the aforementioned thermal drift in optical path lengths that are unimportant on the time scale of the collection of individual data points, but can change the relative positions of the lattices between runs. This drift effectively results in averaging over system realizations with different initial values of δ_p and δ_s in the experimental

data, but we note that a change in these initial values does not appear to measurably change the expansion dynamics in any case.

5.3 Theoretical Models of the Experiment

As discussed in chapter 1, the AAH model is simply a tight-binding approximation of Hamiltonian (5.1), which is well-justified if, as in our experiments, V_p and V_p/V_s are sufficiently large [54, 55]:

$$\begin{aligned} H_{\mathrm{AAH}} = & -J \sum_l \left[\, |l+1\rangle\langle l| + |l\rangle\langle l+1| \, \right] \\ & + \Delta \sum_l \cos(2\pi\beta(l-\delta)) \, |l\rangle\langle l| \end{aligned} \tag{5.4}$$

where J is the tunneling energy and Δ is the quasidisorder strength. Here $\delta = 2(\delta_s - \delta_p)/\lambda_p$, $\beta = \lambda_p/\lambda_s$, and $|l\rangle$ denotes the lowest band Wannier state of the primary lattice at site l corresponding to position $x_l = l\pi/k_p + \delta_p$. If β is chosen to be an appropriate irrational number[2], the Hamiltonian exhibits a localization-delocalization quantum phase transition at $\Delta/J = 2$. For finite-size systems, how sharply the localization properties vary as a function of Δ depends on the exact value of β and the system size (controlled in this case by a weak harmonic confinement along the lattice direction) [55]. Throughout this paper, J and Δ are calculated using numerically computed maximally localized Wannier states [56].

Figure 5.1(b) shows absorption images of atomic clouds that demonstrate the phase transition of the AAH model for $\beta = 1064/874.6$, presented in a format similar to Ref. [47]. Here the atoms are imaged *in situ* using absorption imaging after 500 ms of expansion in the combined lattice potential. $V_p = 9E_{R,p}$ across all the data shown, where $E_{R,p} = \hbar^2 k_p^2/2m$ is the recoil en-

[2]All but an infinitesimal fraction of irrational numbers are appropriate [11], so this is not a practical concern in an experiment.

ergy of the primary lattice. V_s was varied up to a maximum value of $0.592E_{R,p}$, still well within the regime described by the AAH Hamiltonian of equation (5.4), to realize the indicated values of Δ for the tight-binding approximation of the system. Images for various ratios Δ/J clearly indicate the phase transition, showing suppression of expansion for values of Δ/J greater than 2.

Dynamic localization also emerges in the special case of Hamiltonian (5.1) in which $V_s = 0$ and δ_p is periodically modulated [57, 58, 59, 60]. Considering the case $\delta_p = -A\cos(\omega t)$, a unitary transformation to the reference frame in which the lattice is stationary yields the Hamiltonian

$$H_{\mathrm{DL}} = -\frac{\hbar^2}{2m}\frac{\mathrm{d}^2}{\mathrm{d}x^2} + V_p \sin^2(k_p x) + m\frac{\mathrm{d}^2\delta_p}{\mathrm{d}t^2}x \tag{5.5}$$

describing a static lattice potential with an oscillating force. We define the drive strength K by

$$K\cos(\omega t)x = m\frac{\mathrm{d}^2\delta_p}{\mathrm{d}t^2}x = \frac{m\lambda_p\omega}{2}\Delta v_{\mathrm{max},p}\cos(\omega t)x \tag{5.6}$$

As in the AAH case, Hamiltonian (5.5) can be expressed in a tight-binding approximation [49]:

$$\begin{aligned} H_{\mathrm{DL,TB}} = & -J\sum_l \Big[\ |l+1\rangle\langle l| + |l\rangle\langle l+1|\ \Big] \\ & + K\cos(\omega t)\sum_l \frac{\lambda_p l}{2}\,|l\rangle\langle l| \end{aligned} \tag{5.7}$$

Further application of Floquet theory [2, 4] reveals that if one considers only single particle states and neglects exchange of energy with the drive in the high frequency limit $\hbar\omega \gg 4J$, then the system behaves according to the even simpler tight-binding effective Hamiltonian [57]

$$H^F_{\mathrm{DL,TB}} \approx -J_{\mathrm{eff}}\sum_l \Big[\ |l+1\rangle\langle l| + |l\rangle\langle l+1|\ \Big] \tag{5.8}$$

with $J_{\mathrm{eff}} = J\mathcal{J}_0(K_0)$, where $K_0 = K\lambda_p/2\hbar\omega$ is the dimensionless drive strength. Crucially,

hopping is entirely suppressed where the zeroth bessel function $\mathcal{J}_0$ has zeros, for example at $K_0 = 2.405$ and 5.520. Figure 5.1(c) shows absorption images taken after 500 ms of expansion in the presence of drives of various amplitude, for $V_p = 9E_{R,p}$ and drive frequency $\omega = 2\pi \times (300\text{ Hz}) = 5.9J/\hbar$. These data clearly demonstrate the effects of dynamic localization for K_0 close to the Bessel zeroes. We note that while $\hbar\omega = 5.9J$, which is not in the high-frequency limit, the results match well to features previously observed in the high frequency limit [60] and to numerical studies in this intermediate frequency regime [48].

Having demonstrated that the experimental system under investigation can clearly exhibit both quasidisorder-induced localization, figure 5.1(b), and drive-induced localization, figure 5.1(c), we proceed to investigate the main novel topic of this work, which is the interplay of these two phenomena. Specifically, we consider Hamiltonian (5.1) with primary lattice depth $V_p = 9E_{R,p}$ and variable secondary lattice depth V_s in the range $0E_{R,p}$ to $0.592E_{R,p}$. This corresponds to $J = 0.0242E_{R,p}$ and Δ ranging from 0 to $0.162E_{R,p}$ for tight-binding approximation (5.4). Moreover, we translate the superimposed lattices together according to $\delta_p = \delta_s + \delta_0 = -A\cos(\omega t)$, where δ_0 is a constant, to produce a sinusoidal force in the reference frame that is comoving with the lattice potentials. For these parameters, features of both AAH localization and dynamic localization are expected to be present [49, 50]. Making the unitary transformation to a frame in which the potential is static and then further making the tight-binding approximation, we have [49]

$$\begin{aligned} H_{\text{TB}} = & -J\sum_l \left[\, |l+1\rangle\langle l| + |l\rangle\langle l+1| \,\right] \\ & + \Delta\sum_l \cos(2\pi\beta l - \delta)\,|l\rangle\langle l| \\ & + K\cos(\omega t)\sum_l \frac{\lambda_p l}{2}\,|l\rangle\langle l| \end{aligned} \tag{5.9}$$

where all parameters are the same as those defined in equation (5.4) and equation (5.7). In the

high frequency driving limit of the tight-binding model $\hbar\omega \gg \max(4J, 2\Delta)$, an approximate effective Hamiltonian for (5.9) in the Floquet formalism is given by [49]

$$\begin{aligned} H^F_{\mathrm{TB}} \approx & -J_{\mathrm{eff}} \sum_l \Big[\, |l+1\rangle\langle l| + |l\rangle\langle l+1| \, \Big] \\ & + \Delta \sum_l \cos(2\pi\beta l - \delta) \, |l\rangle\langle l| \end{aligned} \tag{5.10}$$

where $J_{\mathrm{eff}} = J\mathcal{J}_0(K_0)$ is again the Bessel-renormalized hopping amplitude. This simply reproduces the AAH Hamiltonian (5.4) but with a drive dependent tunneling energy J_{eff}.

5.4 Main Results

We observe in experimental data that the effective Hamiltonian (5.10) captures the expansion dynamics of the system well for $\Delta/J \lesssim 2$ even when the drive frequency is $\hbar\omega = 5.9J$ for $\omega = 2\pi \times (300 \text{ Hz})$, where we are not in the high frequency regime $\hbar\omega \gg 4J$. To motivate the data presented in figure 5.2 that supports this claim, we note that the dynamics over many cycles is described by the time-evolution operator $U(t) = \exp(-iH^F_{\mathrm{TB}}t/\hbar)$ in this approximation if we ignore the micromotion that occurs on the time scale of the drive period [1]. In experiments with equivalent $\Delta/|J_{\mathrm{eff}}|$ but differing J_{eff}, the form of $U(t)$ implies equivalent evolution dynamics as a function of $t/(\hbar/|J_{\mathrm{eff}}|)$, provided the initial conditions are the same. In other words, the expansion should depend solely on $\Delta/|J_{\mathrm{eff}}|$ if we measure time in units of $\hbar/|J_{\mathrm{eff}}|$. Figure 5.2 presents σ of the atom density distribution as a function of the expansion time in units of $\hbar/|J_{\mathrm{eff}}|$. We observe that expansion is almost exclusively determined by the value of $\Delta/|J_{\mathrm{eff}}|$ for these values, matching what is predicted for the high frequency regime. The most notable deviation from the expected behavior is the accelerated expansion for $\Delta/|J_{\mathrm{eff}}| = 0$ and $K_0 = 3.7$ at later times, which was observed in the images to arise from a heated fraction of atoms that develops at the higher drive strength.

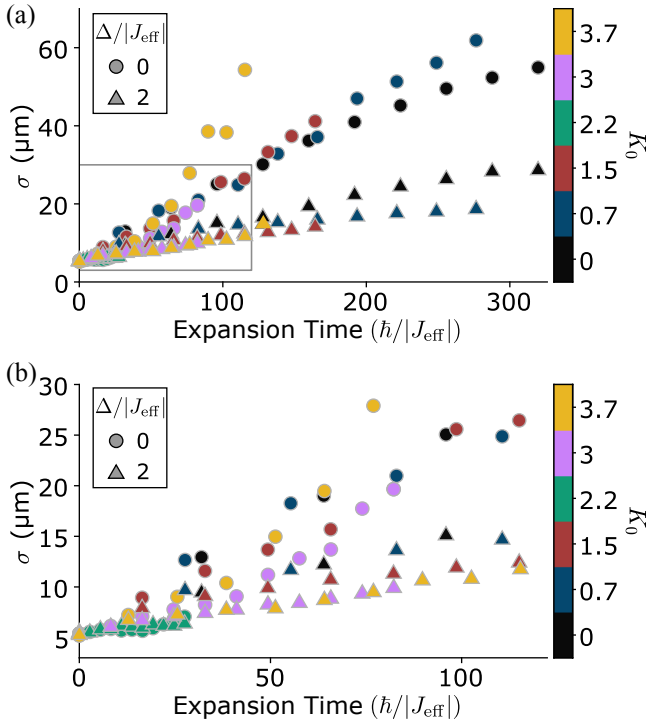

Figure 5.2: σ of the cloud as a function of expansion time for drive strengths indicated by data point color and for $\Delta/|J_{\text{eff}}|$ equal to 0, indicated by circular markers, or 2, indicated by triangular markers. (a) Cloud width presented as a function of expansion time given in units of the effective tunneling time $\hbar/|J_{\text{eff}}|$. (b) Same as (a), but with axis limits chosen to better show data for small values of $|J_{\text{eff}}|$. A gray box in figure (a) indicates the region shown in figure (b). We observe that the data trend in these units of time depends predominantly on whether $\Delta/|J_{\text{eff}}|$ is 0 or 2. Each data point value of σ is averaged from three experimental realizations.

Equation (5.10) further implies the localization phase diagram as a function of quasidisorder strength and drive amplitude to exhibit metallic Bessel lobes in which the critical quasidisorder strength varies as a $\mathcal{J}_0$ Bessel function, vanishing at the Bessel zeroes which define the boundary between lobes, i.e., a metallic phase should occur for $\Delta < 2J\mathcal{J}_0(K_0)$. To quantitatively visualize this expected localization phase diagram, we numerically calculate the inverse participation ration (IPR) of the Floquet eigenstates of Hamiltonian (5.9) calculated at the initial time in the micromotion. We found that the variation in IPR of the eigenstates due to micromotion over the course of one drive period was negligible regardless of the drive fre-

quencies considered in this paper, justifying our consideration of initial time. For the case $\hbar\omega = 50J$ in the high-frequency limit, we present the average IPR of the initial-time Floquet eigenstates, denoted $\langle \text{IPR} \rangle$, in figure 5.3(a). The results clearly display the delocalized lobes expected in this high-frequency regime.

To clarify the precise definition of $\langle \text{IPR} \rangle$, we note that the Floquet eigenstates, indexed by n, are of the form

$$|\Phi_n(t)\rangle = \sum_m e^{-im\omega t} \sum_l c_{n,m,l} |l\rangle$$

as is generically true for Floquet systems. We calculate the IPR of one of these Floquet eigenstates with the formula

$$\text{IPR}_n = \sum_l \left| \sum_m c_{n,m,l} \right|^4$$

which is the IPR of $|\Phi_n(t)\rangle$ at $t = 0$. The IPR will generally vary periodically in time with period $2\pi/\omega$, and one may be concerned by our defining IPR at a single time. However, we checked that these variations are insignificant in the cases considered here by randomly sampling the IPR calculated at several times, and observing that the IPR is not change by much. Lastly, the IPR averaged over all of the Floquet eigenstates is given by

$$\langle \text{IPR} \rangle = \frac{1}{N} \sum_{n=1}^{N} \text{IPR}_n$$

To experimentally explore this predicted phase structure, we measured the width of the atomic density distribution after allowing it to expand in the system for a fixed 500 ms, with system parameters of quasidisorder strength Δ and drive amplitude K_0 independently varied to map out a 2D parameter space. Figure 5.3(c) presents the resulting experimental data, for a drive frequency $\hbar\omega = 5.9J$.

However, it is worth noting that the width after expansion should not be exactly constant along the curve, since the actual expanded width depends on the effective tunneling time $\hbar/|J_{\text{eff}}|$,

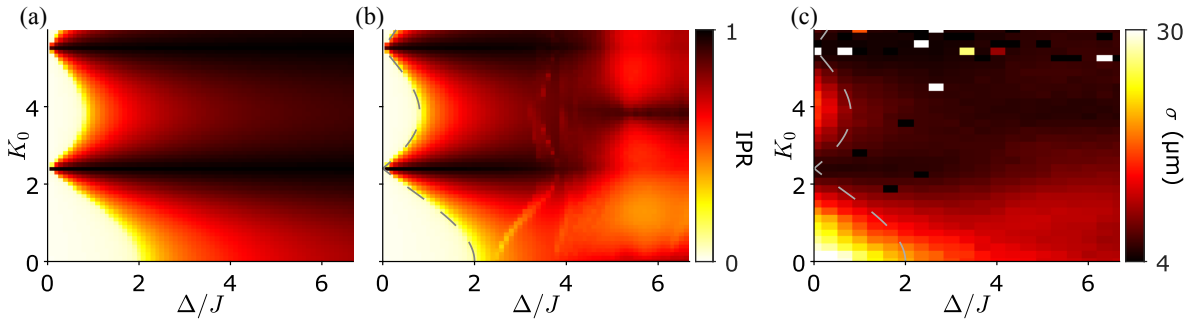

Figure 5.3: Interplay of dynamic localization and quasidisorder-induced localization. Numerically calculated Floquet state IPR for a $\boldsymbol{9.4E_{R,p}}$ primary lattice is shown in (a) for the high frequency drive limit $\hbar\omega = 50J$ and in (b) for intermediate drive frequency $\hbar\omega = 6.5J$ [will be $5.9J$ when redone at 9Er]. In (c), we present the fitted gaussian width σ of the transversely-integrated atomic density distribution after 500 ms of expansion, with $V_p = 9E_{R,p}$ and $\hbar\omega = 5.9J$. Each value is the average of three repeated measurements. In the region $\Delta/J > 2$, we observe clear differences between (a) and (b), suggesting differing Floquet eigenstate properties in these two frequency regimes. In the region $\Delta/J > 3$, the expansion behavior in (c) matches qualitatively with the Floquet eigenstate properties suggested by (b) while differing significantly from (a).

which varies with K_0. Nonetheless, this is a good indicator of the behavior.

The first main result of this experiment is the observation of the predicted delocalized lobes in the region with $\Delta/J < 2$, further supporting the observations of figure 5.2. The data clearly exhibit a drive-amplitude-dependent localization-delocalization phase transition and insulating states touching the y axis at the Bessel zeroes where $J_{\text{eff}} = 0$. The boundaries between localized and delocalized states at the edges of the lobes (shown as a dashed line) are in good agreement with the Bessel form predicted by Hamiltonian (5.10).

The second main result of this experiment is the observation of clear deviations from the structure predicted by the high-frequency approximation, which are especially pronounced in the region with $\Delta/J > 4$. We note in particular two features: a broad area of anomalously high expansion in the lower-right of the parameter space, and a narrow band of anomalously low expansion near the line $K_0 = 3.8$. We interpret these features as a signature of nontrivial phenomena not captured by the high-frequency approximation, and present both numerical and analytical support for this interpretation.

We note that the local suppression of expansion near $K_0 = 3.8$ for $\Delta/J > 4$ corresponds closely to the zero of the *first* Bessel function $\mathcal{J}_1$. To better understand this observation, we apply the Jacobi-Anger equation to Hamiltonian (5.1):

$$\begin{aligned} &2\sin^2(k_p(x-\delta_p)) = \\ &1 - \mathrm{Re}\left[\sum_{n=-\infty}^{\infty} \mathcal{J}_n(2k_pA)(-i)^n e^{i(k_p x - n\omega t)}\right] \end{aligned} \tag{5.11}$$

In the high frequency limit, one can consider the non-zero Bessel terms as averaging away over many cycles. However, when $\hbar\omega \approx 4J$, higher-order terms will contribute non-negligibly, with the $\mathcal{J}_1$ term dominating. We thus interpret the observed localized stripe near $K_0 = 3.8$ as the effect of a higher-order suppression of tunneling not captured in the commonly-used high-frequency approximation.

To provide numerical perspective on these features of the phase diagram, we plot in figure 5.3(b) the Floquet-eigenstate-averaged IPR derived in the same manner as for figure 5.3(a), but now for a drive frequency $\hbar\omega = 5.9J$, no longer in the limit of very small drive period. The resulting phase diagram clearly captures both of the the anomalous features of the experimental data noted above in the region $\Delta/J > 4$. Taken together, these numerical and analytical arguments demonstrate that the experimentally observed phase diagram of the interplay of dynamic and AAH localization not only quantitatively reproduces the expected metallic Bessel lobes, but also clearly displays features of anomalous localization and delocalization, which arise from higher-order terms typically neglected by high-frequency Floquet approximations.

5.5 Discussion

In summary, we have presented experimental and numerical investigation of the interplay of dynamic and Aubry-André localization in a regime where the drive frequency is not much

larger than the energy scale of the system. We identify localization behavior that depends intricately on system parameters in the strong secondary lattice regime that arise away from the high frequency drive limit. We further investigate expansion dynamics that support the notion that the high frequency model continues to match observation provided the secondary lattice depth is not so great. We have touched here on the rich structures that can arise when quantum systems are driven near the boundary of their natural response frequency. This and further study may prove insightful for future Floquet engineering applications where optimal system parameters may deviate from the simple high frequency model. This frequency regime is also potentially relevant to investigation of open quantum systems and of thermalization of quantum systems.

Chapter 6

Optical Lattices formed by Multiple Interfering Laser Beams

In this section, we will discuss optical lattices formed by multiple laser beams, first abstractly and then with a specific discussion of an active phase locking scheme. The active locking scheme that we will discuss has a fair bit of versatility, allowing the individual control of the intensity of each laser beam, complete control over the relative phases of the laser beams, and a couple classes of interesting geometries as applications.

6.1 Analysis of Multiple Interfering Laser Beams

As we saw in sections 3.2 and 3.3, the optical dipole trap is a flexible tool that enables rapid and controlled application of spatially varying potentials produced by the presence of laser beams. Of course, a famous feature of coherent laser light is interference, and interfering laser beams can produce interesting spatially varying potentials, such as the lattice potential. Such periodic potentials are referred to as optical lattices. We will consider here the mathematics of interfering laser beams and the potentials they create.

In section 3.3, we saw that the optical dipole trap potential felt by an atom in a laser beam depends on the complex electric field amplitude E and the polarization vector $\hat{\mathbf{u}}$ of the laser beam as defined in equation (3.2). In general, both the polarization and amplitude of the electric field will vary in space. For the ground state of strontium ^{84}Sr, we have the simplification that the potential depends only on the electric field amplitude, specifically, in proportion to $|E|^2$. However, even in this simple case, we must consider the light polarization as we sum the laser fields and so we ought to work with the complex vector representation $\mathbf{E} = E\hat{\mathbf{u}}$, with the notation and representations described in section 3.1.

6.1.1 General Case of Interfering Plane Waves

Let us consider N interfering plane waves of laser light, which we will enumerate with the index l. We assume they all have the same angular frequency ω, but allow them to have arbitrary wavenumber $\mathbf{k}_l$ and relative phaser ϕ_l. The superposition of these plane waves describes the total electric field $\mathbf{E}_{\text{tot}}$ and can be expressed as the sum

$$\mathbf{E}_{\text{tot}} \;=\; \sum_{l=1}^{N} \mathbf{E}_l \exp\Big(i(\mathbf{k}_l \cdot \mathbf{r} - \phi_l)\Big).$$

Note that to reduce visual clutter, we will use $\mathbf{E}_l$ in this section to represent what might more naturally be written as $\mathbf{E}_{l,0}$ following the definition of equation (3.1).

We can consider $|\mathbf{E}_{\text{tot}}|^2$ to gain some insight into the resulting total potential.

$$\begin{aligned}
|\mathbf{E}_{\text{tot}}|^2 &= \sum_l |E_l|^2 + \sum_{p\neq q} \Big(\mathbf{E}_p \cdot \mathbf{E}_q^*\Big) \exp\Big[i\Big((\mathbf{k}_p - \mathbf{k}_q)\cdot \mathbf{r} - (\phi_p - \phi_q)\Big)\Big] \\
&= \sum_l |E_l|^2 + \sum_{p>q} \Big(\mathbf{E}_p \cdot \mathbf{E}_q^*\Big) \exp\Big[i\Big((\mathbf{k}_p - \mathbf{k}_q)\cdot \mathbf{r} - (\phi_p - \phi_q)\Big)\Big] \\
&\qquad + \Big(\mathbf{E}_p^* \cdot \mathbf{E}_q\Big) \exp\Big[-i\Big((\mathbf{k}_p - \mathbf{k}_q)\cdot \mathbf{r} - (\phi_p - \phi_q)\Big)\Big]
\end{aligned} \tag{6.1}$$

We see that $|\mathbf{E}_{\text{tot}}|^2$ can be expressed as a sum of $\frac{1}{2}(N)(N-1)$ sinusoidal plane wave potentials, where each sinusoidal component is of the form

$$\text{Re}\left(A \exp\left[i\Big((\mathbf{k}_p - \mathbf{k}_q)\cdot \mathbf{r}\Big)\right]\right)$$

where

$$A = 2\mathbf{E}_p \cdot \mathbf{E}_q^* \exp\Big[-i\,(\phi_p - \phi_q)\Big]$$

In the case where there is solely a scalar light shift to consider as happens for the bosonic strontium ground states, the realized optical dipole potential is simply proportional to this $|\mathbf{E}_{\text{tot}}|^2$. In other cases however, the spatially varying polarization of $\mathbf{E}_{\text{tot}}$ needs to be considered.

6.1.2 Specializing to In-Plane Beams

Now let us assume that all of the $\mathbf{k}_l$ are in the same plane. Specifically, let $\mathbf{k}_l \cdot \hat{\mathbf{z}} = 0$. Then we can write

$$\mathbf{E}_l = E_{lz}\hat{\mathbf{z}} + E_{l\|}e^{-i\alpha_l}(\hat{\mathbf{k}}_l \times \hat{\mathbf{z}})$$

where $E_{lz}, E_{l\|}$ are real numbers.

In this case, we have

$$\mathbf{E}_p \cdot \mathbf{E}_q^* \;=\; E_{pz}E_{qz} + E_{p\|}E_{q\|}e^{-i(\alpha_p-\alpha_q)}(\hat{\mathbf{k}}_p \times \hat{\mathbf{z}})\cdot(\hat{\mathbf{k}}_q \times \hat{\mathbf{z}}) \;=\; E_{pz}E_{qz} + E_{p\|}E_{q\|}e^{-i(\alpha_p-\alpha_q)}\hat{\mathbf{k}}_p \cdot \hat{\mathbf{k}}_q$$

So, equation (6.1) becomes

$$\begin{aligned}|\mathbf{E}_{\text{tot}}|^2 = \sum_l |E_l|^2 + 2\sum_{p>q} E_{pz}E_{qz}\cos\Big((\mathbf{k}_p - \mathbf{k}_q)\cdot\mathbf{r} - (\phi_p - \phi_q)\Big) \\ + E_{p\|}E_{q\|}(\cos\theta_{pq})\cos\Big((\mathbf{k}_p - \mathbf{k}_q)\cdot\mathbf{r} - (\phi_p - \phi_q) - (\alpha_p - \alpha_q)\Big)\end{aligned} \tag{6.2}$$

where $\hat{\mathbf{k}}_p \cdot \hat{\mathbf{k}}_q = \cos\theta_{pq}$ and θ_{pq} is the angle between $\mathbf{k}_p$ and $\mathbf{k}_q$.

Of course, in the case of only linearly polarized beams (i.e. $\alpha_l = 0$) this simplifies a bit further to

$$|\mathbf{E}_{\text{tot}}|^2 = \sum_l |E_l|^2 + 2\sum_{p>q}\Big(E_{pz}E_{qz} + E_{p\|}E_{q\|}(\cos\theta_{pq})\Big)\cos\Big((\mathbf{k}_p - \mathbf{k}_q)\cdot\mathbf{r} - (\phi_p - \phi_q)\Big) \tag{6.3}$$

6.1.3 Four In-Plane Laser Beams with Out-of-Plane Polarizations

Let us consider a more concrete case of 4 "in-plane" laser beams, by which we mean their directions of propagation are all in the same plane, and let us further suppose that their polarizations are perpendicular to this plane. In other words, we will suppose that $\mathbf{k}_l \cdot \hat{\mathbf{z}} = 0$ and $\mathbf{E}_l = E_l\hat{\mathbf{z}}$.

Neglecting the overall energy offset term resulting from the sum over $|E_l|^2$, the potential of the optical lattice will be given by

$$\begin{aligned} V(\mathbf{r}) \propto\ & E_1E_2\cos\Big((\mathbf{k}_1 - \mathbf{k}_2)\cdot\mathbf{r} - (\phi_1 - \phi_2)\Big) + E_2E_3\cos\Big((\mathbf{k}_2 - \mathbf{k}_3)\cdot\mathbf{r} - (\phi_2 - \phi_3)\Big) \\ &+ E_3E_4\cos\Big((\mathbf{k}_3 - \mathbf{k}_4)\cdot\mathbf{r} - (\phi_3 - \phi_4)\Big) + E_4E_1\cos\Big((\mathbf{k}_4 - \mathbf{k}_1)\cdot\mathbf{r} - (\phi_4 - \phi_1)\Big) \\ &+ E_1E_3\cos\Big((\mathbf{k}_1 - \mathbf{k}_3)\cdot\mathbf{r} - (\phi_1 - \phi_3)\Big) + E_2E_4\cos\Big((\mathbf{k}_2 - \mathbf{k}_4)\cdot\mathbf{r} - (\phi_2 - \phi_4)\Big) \end{aligned} \tag{6.4}$$

In the case of bosonic isotopes of strontium in the ground state, the constant of proportionality is $\alpha^s_{n0}/4$, which follows from equation (3.20).

It is clear that even though equation (6.4) is expressed in terms of the 12 parameters E_l, $\mathbf{k}_l$, and ϕ_l for $l \in \{1, 2, 3, 4\}$, we do not in fact have 12 independently variably parameters to adjust $V(\mathbf{r})$. To make this more clear, let us define the following independent variables:

$$A_1 \equiv E_1E_2 \qquad A_2 \equiv E_2E_3 \qquad A_3 \equiv E_3E_4 \qquad A_X \equiv E_1E_3$$

$$\delta\mathbf{k}_1 \equiv (\mathbf{k}_1 - \mathbf{k}_2) \qquad \delta\mathbf{k}_2 \equiv (\mathbf{k}_2 - \mathbf{k}_3) \qquad \delta\mathbf{k}_3 \equiv (\mathbf{k}_3 - \mathbf{k}_4)$$

$$\delta\phi_1 \equiv (\phi_1 - \phi_2) \qquad \delta\phi_2 \equiv (\phi_2 - \phi_3) \qquad \delta\phi_3 \equiv (\phi_3 - \phi_4)$$

Expressing the potential in terms of these new variables, we have

$$\begin{aligned} V(\mathbf{r}) \propto\ & A_1 \cos\left(\delta\mathbf{k}_1 \cdot \mathbf{r} - \delta\phi_1\right) + A_2 \cos\left(\delta\mathbf{k}_2 \cdot \mathbf{r} - \delta\phi_2\right) \\ & + A_3 \cos\left(\delta\mathbf{k}_3 \cdot \mathbf{r} - \delta\phi_3\right) + \frac{A_1 A_3}{A_2} \cos\left((\delta\mathbf{k}_1 + \delta\mathbf{k}_2 + \delta\mathbf{k}_3) \cdot \mathbf{r} - (\delta\phi_1 + \delta\phi_2 + \delta\phi_3)\right) \\ & + A_X \cos\left((\delta\mathbf{k}_1 + \delta\mathbf{k}_2) \cdot \mathbf{r} - (\delta\phi_1 + \delta\phi_2)\right) + \frac{A_1 A_3}{A_X} \cos\left((\delta\mathbf{k}_2 + \delta\mathbf{k}_3) \cdot \mathbf{r} - (\delta\phi_2 + \delta\phi_3)\right) \end{aligned}$$

This suggests 10 free parameters, but in fact, once $\delta\mathbf{k}_1$ and $\delta\mathbf{k}_3$ are chosen, $\delta\mathbf{k}_2$ is not truly free,[1] as the restriction that each wavevector $|\mathbf{k}_l| = 2\pi/\lambda$ constrains the possible values for $\{\delta\mathbf{k}_1, \delta\mathbf{k}_2, \delta\mathbf{k}_3\}$. Nonetheless, $\delta\mathbf{k}_1$ and $\delta\mathbf{k}_3$ can independently be any vectors, so long as $|\delta\mathbf{k}_1|$, $|\delta\mathbf{k}_3| \leq 4\pi/\lambda$. This becomes quite clear in the following procedure for selecting values of $\delta\mathbf{k}_l$:

1. Choose $\delta\mathbf{k}_1$ and $\delta\mathbf{k}_3$.

2. Consider the possible set of $\{\mathbf{k}_1, \mathbf{k}_2, \mathbf{k}_3, \mathbf{k}_4\}$. Assuming $\delta\mathbf{k}_1 \neq 0$,[2] then there are at most 2 choices for $\mathbf{k}_1$ and $\mathbf{k}_2$. To see this, suppose the desired $\delta\mathbf{k}_1$ is achieved when $\mathbf{k}_1 = \mathbf{a}$ and $\mathbf{k}_2 = \mathbf{b}$, then we can alternatively choose $\mathbf{k}_1 = -\mathbf{b}$ and $\mathbf{k}_2 = -\mathbf{a}$. Similarly, setting $\delta\mathbf{k}_3$ gives at most two choices for $\mathbf{k}_3$ and $\mathbf{k}_4$.

3. Consider possible $\delta\mathbf{k}_2$, and it is clear that we are restricted to at most four choices of $\delta\mathbf{k}_2$. Figure 6.1 shows the graphical relationships between the vectors $\mathbf{k}_l$ and $\delta\mathbf{k}_l$, and one can consider this procedure geometrically as well by considering chords on the circle that correspond to the desired $\delta\mathbf{k}_1$ and $\delta\mathbf{k}_3$.

[1] See also grad school and the human condition.

[2] The case $\delta\mathbf{k}_1 = 0$ would mean that k_1 and k_2 are effectively part of a single plane wave, and you would get an interference pattern formed by only 3 waves.

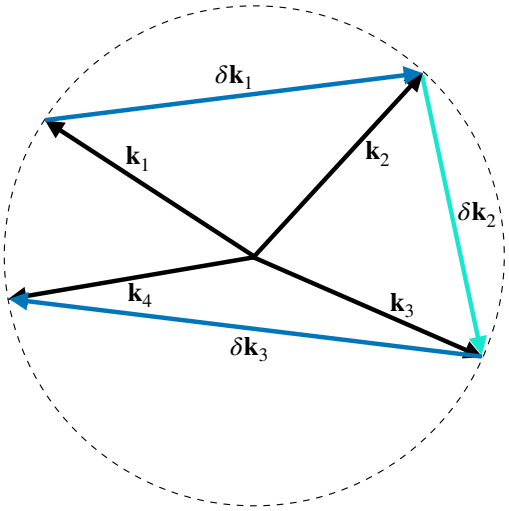

Figure 6.1: Diagram of the laser beam wave vectors $\mathbf{k}_l$ and the newly defined variables $\delta\mathbf{k}_l$. Notice that once $\delta\mathbf{k}_1$ and $\delta\mathbf{k}_3$ are chosen, there are few options for $\delta\mathbf{k}_2$.

6.1.4 Considerations of the Reciprocal Space

It is worth considering the fourier transformation $\tilde{V}(\boldsymbol{\xi})$ of the potential $V(\mathbf{r})$ in equation (6.1) in the general case or in equation (6.4) in the specialized planar case. One of course finds that the Fourier transform is only nonzero at $\boldsymbol{\xi} \in \{\, \mathbf{k}_i - \mathbf{k}_j \mid i, j = 1, ..., N \,\}$. This fourier transform can be considered to define a reciprocal space for an optical lattice if the nonzero values of $\boldsymbol{\xi}$ are coincident with a lattice of points. That is to say, the interference pattern forms an optical lattice if the set of points

$$S \equiv \left\{ \sum_{i,j} n_{ij} \left(\mathbf{k}_i - \mathbf{k}_j \right) \mid n_{ij} \in \mathbb{Z} \right\}$$

and the set defining some lattice

$$L = \left\{ \sum_{i=1,2,3} n_i \mathbf{b}_i \mid n_i \in \mathbb{Z} \right\}$$

are equivalent ($S = L$) for some appropriately chosen basis vectors $\mathbf{b}_1$, $\mathbf{b}_2$, and $\mathbf{b}_3$ of the reciprocal space lattice.[3]

In general, a set of N interfering laser beams will *not* form a lattice. However, for a d-dimensional lattice, you are guaranteed to form a lattice with $N = d + 1$ lattice beams [61]. We observe why this is necessarily true for the case of 3 interfering laser beams in 2 dimensions in subsection 6.1.6. The alternative to forming an optical lattice is to produce an "optical quasicrystal" from interfering laser beams as in [62].

6.1.5 Analysis of Laser Beam Phase Changes

Supposing that we are still in the situation that the potential is simply proportional to $|\mathbf{E}_{\text{tot}}|^2$ and considering the general expression for $|\mathbf{E}_{\text{tot}}|^2$ given in equation (6.1), the potential is of the form

$$V(\mathbf{r}) = \sum_{p,q} a_{p,q} \exp\left[i\Big((\mathbf{k}_p - \mathbf{k}_q) \cdot \mathbf{r} - (\phi_p - \phi_q)\Big)\right] \tag{6.5}$$

for coefficients $a_{p,q}$.

It is worthwhile to consider the ways in which the phases ϕ_l of the light affects the interference pattern. As is evident from equation (6.5), the potential only depends on these phases through the quantities $\phi_p - \phi_q$. We can consider the linear mapping from the set $\{\phi_l\}$ to the set of values $\{\phi_p - \phi_q\}$. To make this concrete, let us consider the case of 4 laser beams

$$\begin{bmatrix} (\phi_1 - \phi_2) \\ (\phi_2 - \phi_3) \\ (\phi_3 - \phi_4) \\ (\phi_4 - \phi_1) \\ (\phi_1 - \phi_3) \\ (\phi_2 - \phi_4) \end{bmatrix} = \begin{bmatrix} 1 & -1 & 0 & 0 \\ 0 & 1 & -1 & 0 \\ 0 & 0 & 1 & -1 \\ -1 & 0 & 0 & 1 \\ 1 & 0 & -1 & 0 \\ 0 & 1 & 0 & -1 \end{bmatrix} \begin{bmatrix} \phi_1 \\ \phi_2 \\ \phi_3 \\ \phi_4 \end{bmatrix} \equiv M \begin{bmatrix} \phi_1 \\ \phi_2 \\ \phi_3 \\ \phi_4 \end{bmatrix}$$

[3] Of course, it is possible that we only needs two basis vectors $\mathbf{b}_1$ and $\mathbf{b}_2$ to define the reciprocal space if it is a 2D lattice.

The null space of the matrix M is not empty, and we have

$$\text{null}(M) \;=\; \text{span}\left\{\begin{bmatrix} 1 \\ 1 \\ 1 \\ 1 \end{bmatrix}\right\} \;\equiv\; \text{span}\,\{\mathbf{v}_0\}$$

The existence of this null space can be argued on physical grounds: The A.C. Stark shift responsible for the optical lattice can be considered as arising from a time average of the energy over the laser frequency,[4] and advancing all of the phases by the same amount is equivalent to changing the initial time, and so is irrelevant to the time average.

Within the remaining 3-dimensional vector subspace given by $\mathbb{R}^4 \setminus \text{null}(M)$ of phase transformations, there is a 2-dimensional subspace that corresponds to spatial translations of the interference pattern and a 1-dimensional subspace corresponding to geometrical changes.

This realization leads to a convenient decomposition of the phase vector:

$$\begin{bmatrix} \phi_1 \\ \phi_2 \\ \phi_3 \\ \phi_4 \end{bmatrix} = c_0\mathbf{v}_0 + c_x\mathbf{v}_x + c_y\mathbf{v}_y + c_g\mathbf{v}_g$$

where variations of the c_0 coefficient causes no change to the optical potential, variations in c_x and c_y result in translations of the optical potential in the x and y direction respectively, and variations in c_g correspond to changes in the lattice geometry.

To identify the vectors $\mathbf{v}_x$ and $\mathbf{v}_y$, we can consider the translation brought about by changing

$$\mathbf{r} \longrightarrow \mathbf{r} - \boldsymbol{\delta}$$

[4] In the floquet formalism, this arises from calculating $\langle\!\langle \cdots \rangle\!\rangle$. One might also expect this given that we are disregarding the details of the "fast" laser cycle time dynamics when we considered the A.C. Stark shift as causing a "D.C." shift to the energy levels.

This corresponds to a shift in the arguments of the exponentials in equation (6.5) given by

$$i\Big((\mathbf{k}_p - \mathbf{k}_q)\cdot\mathbf{r} - (\phi_p - \phi_q)\Big) \;\longrightarrow\; i\Big((\mathbf{k}_p - \mathbf{k}_q)\cdot\mathbf{r} - (\mathbf{k}_p - \mathbf{k}_q)\cdot\boldsymbol{\delta} - (\phi_p - \phi_q)\Big)$$

A conclusion from the above is that if we change the phases so that

$$(\phi_p - \phi_q) \quad\rightarrow\quad (\phi_p - \phi_q) + (\mathbf{k}_p - \mathbf{k}_q)\cdot\boldsymbol{\delta} \tag{6.6}$$

for all p, q, then the result will be a translation of the interference pattern by the vector $\boldsymbol{\delta}$.

To determine $\mathbf{v}_x$, we can set $\boldsymbol{\delta} = \hat{\mathbf{x}}$ and identify the relevant changes in phase $\Delta\phi_l$ that give rise to the transformation expressed in (6.6). This process yields

$$\mathbf{v}_x = \begin{bmatrix} \Delta\phi_1 \\ \Delta\phi_2 \\ \Delta\phi_3 \\ \Delta\phi_4 \end{bmatrix}$$

Formally, $\mathbf{v}_x$ can be found by solving

$$\begin{bmatrix} (\mathbf{k}_1 - \mathbf{k}_2)\cdot\hat{\mathbf{x}} \\ (\mathbf{k}_2 - \mathbf{k}_3)\cdot\hat{\mathbf{x}} \\ (\mathbf{k}_3 - \mathbf{k}_4)\cdot\hat{\mathbf{x}} \\ (\mathbf{k}_4 - \mathbf{k}_1)\cdot\hat{\mathbf{x}} \\ (\mathbf{k}_1 - \mathbf{k}_3)\cdot\hat{\mathbf{x}} \\ (\mathbf{k}_2 - \mathbf{k}_4)\cdot\hat{\mathbf{x}} \end{bmatrix} = M\mathbf{v}_x$$

for $\mathbf{v}_x$. Likewise, $\mathbf{v}_y$ can be found by repeating the above procedure for $\boldsymbol{\delta} = \hat{\mathbf{y}}$. And finally, in the 4-beam case, $\mathbf{v}_g$ can be taken as a 4-D vector that is perpendicular to the vector space spanned by $\mathbf{v}_0$, $\mathbf{v}_x$, and $\mathbf{v}_y$.

One may wish to consider more the more general case of N interfering beams. This can

be done in the same way to identify $\mathbf{v}_0$, $\mathbf{v}_x$, and $\mathbf{v}_y$ in 2D, but the remaining orthogonal vector subspace given by $\mathbb{R}^N \setminus \text{span}\{\mathbf{v}_0, \mathbf{v}_x, \mathbf{v}_y\}$ will have dimension $N-3$. In reference [63], the authors consider potentials of a more general form given by

$$V(\mathbf{r}) = \sum_{l=1}^{N} a_l \exp\Big[i\Big(\mathbf{b}_l \cdot \mathbf{r} - \phi_l\Big)\Big] + a_l^* \exp\Big[-i\Big(\mathbf{b}_l \cdot \mathbf{r} - \phi_l\Big)\Big] \tag{6.7}$$

where the potential is generated in such a way that the ϕ_l's can be varied independently of each other. We can consider equation (6.5) as a special case of equation (6.7). As discussed in [63], potentials of this form can be quasiperiodic. In the theory of quasiperiodic systems, the lattice sites of the quasicrystal of this type in the physical d-dimensional space can be constructed by the cut-and-project (or projection) method as the projection of a set of points of a lattice in a d'-dimensional space onto the physical d-dimensional subspace, where $d' > d$ [35]. Thus, some of the vectors in $\mathbb{R}^N \setminus (\text{null}(M) \cup \text{span}\{\mathbf{v}_x, \mathbf{v}_y\})$ are associated with pure translations of the d-dimensional subspace through the higher d'-dimensional space. Such vectors are associated with the phasonic degrees of freedom of the quasicrystal. This allows us to choose a set of basis vectors in $\mathbb{R}^N$ for the changes in the phases ϕ_l of the laser beams (or of the sinusoidal potentials in equation (6.7)) so that each basis vector corresponds to a change of the lattice that is only one of the following types

1. No change to the potential
2. Pure spatial translation of the potential
3. Variation of a phasonic degree of freedom
4. Change of the geometry

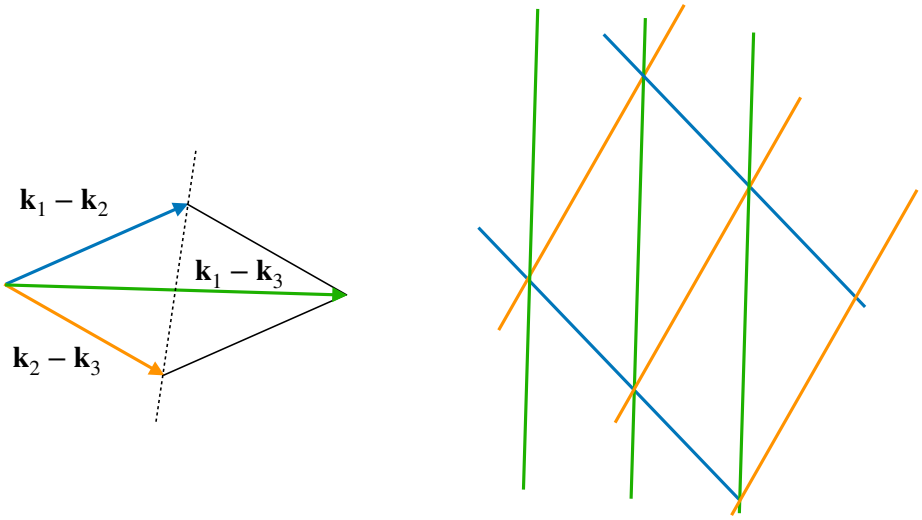

Figure 6.2: Left: Depiction of the vectors $(\mathbf{k}_1 - \mathbf{k}_2)$, $(\mathbf{k}_2 - \mathbf{k}_3)$, and $(\mathbf{k}_1 - \mathbf{k}_3)$, which can be considered as a subset of the reciprocal space for the lattice produced by the beam interference. Right: Lines of maximal value of the cosine terms that sum to make the potential, where colors corresponding to wavevectors in the left figure.

6.1.6 Special Case: 3-Beam Lattice in 2 Dimensions

Let us consider a 2D optical potential formed by 3 interfering beams that satisfy $\mathbf{k}_l \cdot \hat{\mathbf{z}} = 0$. We will see that indeed it produces an optical lattice as discussed in [62]. In this case, the potential is given by

$$\begin{aligned} V(\mathbf{r}) \propto\ & E_1 E_2 \cos\Big((\mathbf{k}_1 - \mathbf{k}_2)\cdot\mathbf{r} - (\phi_1 - \phi_2)\Big) + E_2 E_3 \cos\Big((\mathbf{k}_2 - \mathbf{k}_3)\cdot\mathbf{r} - (\phi_2 - \phi_3)\Big) \\ & + E_1 E_3 \cos\Big((\mathbf{k}_1 - \mathbf{k}_3)\cdot\mathbf{r} - (\phi_1 - \phi_3)\Big) \end{aligned} \tag{6.8}$$

The form of this potential implies the geometry depicted in the left side of figure 6.2. This results simply from the fact that $(\mathbf{k}_1 - \mathbf{k}_2) + (\mathbf{k}_2 - \mathbf{k}_3) = (\mathbf{k}_1 - \mathbf{k}_3)$. Clearly, the resulting potential will be a lattice with reciprocal lattice basis vectors $\mathbf{b}_1 = \mathbf{k}_1 - \mathbf{k}_2$ and $\mathbf{b}_2 = \mathbf{k}_2 - \mathbf{k}_3$. In the right side of figure 6.2, the resulting real space lattice is shown, where the lines indicate the maxima of the cosine plane waves, and the intersection of three lines corresponds to a lattice site. As

drawn, the maxima of the three waves always intersect in groups of three (in other words, there are no intersections of only two maxima). This is in fact mathematically inevitable regardless of the choice of phases ϕ_l in equation (6.8).

6.1.7 Considering Beams Along the $\hat{\mathbf{x}}$ and $\hat{\mathbf{y}}$ Axes

Let use consider how the analysis of phase shifts discussed in section 6.1.5 for the particular case of

$$\mathbf{k}_1 = k\hat{\mathbf{x}}, \quad \mathbf{k}_2 = k\hat{\mathbf{y}}, \quad \mathbf{k}_3 = k(-\hat{\mathbf{x}}), \quad \mathbf{k}_4 = k(-\hat{\mathbf{y}})$$

Then we find that we can take

$$\mathbf{v}_x = \begin{bmatrix} 1 \\ 0 \\ -1 \\ 0 \end{bmatrix}, \quad \mathbf{v}_y = \begin{bmatrix} 0 \\ 1 \\ 0 \\ -1 \end{bmatrix}, \quad \mathbf{v}_g = \begin{bmatrix} 1 \\ -1 \\ 1 \\ -1 \end{bmatrix}$$

This is of particular experimental relevance, in that it means that to preserve a lattice structure, it is critical to ensure that

$$\begin{bmatrix} \phi_1 \\ \phi_2 \\ \phi_3 \\ \phi_4 \end{bmatrix} \cdot \mathbf{v}_g = \text{const}$$

This condition can be equivalently be written as

$$\phi_1 + \phi_3 - \phi_2 - \phi_4 = \text{const}$$

or using subscripts to denote the beam direction

$$\phi_{\hat{\mathbf{x}}} + \phi_{-\hat{\mathbf{x}}} - \phi_{\hat{\mathbf{y}}} - \phi_{-\hat{\mathbf{y}}} = \text{const} \tag{6.9}$$

where $\phi_{\hat{\mathbf{x}}} = \phi_1$, $\phi_{-\hat{\mathbf{x}}} = \phi_3$, $\phi_{\hat{\mathbf{y}}} = \phi_2$, and $\phi_{-\hat{\mathbf{y}}} = \phi_4$.

Satisfying this condition in a real optical lattice can be challenging in practice, since the values of ϕ_l can drift as a result of practical reasons. from effective laser path length changes, which occur from mirror motion, thermal expansions, index of refraction changes of optics or air, laser frequency drift, etc. A system must be designed so that it maintains the value of $\phi_{\hat{\mathbf{x}}} + \phi_{-\hat{\mathbf{x}}} - \phi_{\hat{\mathbf{y}}} - \phi_{-\hat{\mathbf{y}}}$. Frequently, this is accomplished with feedback to control this phase, but this is not the only option. A discussion of some of the implementations for maintaining this condition are given in section 6.2.

6.1.8 Special Case: $\mathbf{k}_1 = -\mathbf{k}_2 = k\hat{\mathbf{x}}$ and $\mathbf{k}_3 = -\mathbf{k}_4 = k\hat{\mathbf{y}}$

In this case, we take $\mathbf{k}_1 = -\mathbf{k}_2 = k\hat{\mathbf{x}}$ and $\mathbf{k}_3 = -\mathbf{k}_4 = k\hat{\mathbf{y}}$. We also keep all polarizations in the $\hat{\mathbf{z}}$ direction. In this case, let us change to a slightly more natural notation by renaming the phases according to $\phi_1 \rightarrow \phi_{x,1}$, $\phi_2 \rightarrow \phi_{x,2}$, $\phi_3 \rightarrow \phi_{y,1}$, and $\phi_4 \rightarrow \phi_{y,2}$.[5]

Following the analysis in [64], if one ignores overall translations potential, the resulting potential can be expressed as

$$U = -\frac{1}{2}V_X \cos(2kx) - \frac{1}{2}V_Y \cos(2ky) - 2\sqrt{V_X V_Y}\cos(kx)\cos(ky)\cos(\phi)$$

where $\phi = \frac{1}{2}\left(\phi_{y,1} + \phi_{y,2} - \phi_{x,1} - \phi_{x,2}\right)$. In this case, we see that the parameter ϕ controls the geometry of the lattice. We will explore the effect of the laser beam phases on the lattice beam geometry further in section 6.2.

[5]This is slightly different notation than Greif uses. Specifically, he takes the counter propagating beams to be $\phi_2 \rightarrow \phi_{x,1} + \phi_{x,2}$ and $\phi_4 \rightarrow \phi_{y,1} + \phi_{y,2}$.

6.2 Four Beam Optical Lattice in 2D with Arbitrary Dynamic Laser Beam Parameters

In this section, we will present a new scheme for a lattice generated from the interference of four laser beams with wavevectors given by $\mathbf{k}_1 = -\mathbf{k}_2 = k\hat{\mathbf{x}}$ and $\mathbf{k}_3 = -\mathbf{k}_4 = k\hat{\mathbf{y}}$.

6.2.1 Previous Implementations

The practical problem of preserving the lattice geometry by maintaining the condition (6.9) has been solved in certain cases previously. The earliest that we are aware of was presented in [65]. Here, the lattice is formed by the interference of two arms of a Michelson interferometer as diagrammed schematically in Figure 6.3. The phase difference between the two arms corresponds to the quantity $(\phi_{\hat{\mathbf{x}}} + \phi_{-\hat{\mathbf{x}}} - (\phi_{\hat{\mathbf{y}}} + \phi_{-\hat{\mathbf{y}}}) + \text{const})$ so if one stabilizes the intensity of the light reaching the photodiode in Figure 6.3, then the lattice geometry will be preserved. In this case, instead of directly changing the phase of the laser beams, they change the overall frequency of the laser by small amounts such that the change in the magnitude of $\mathbf{k}_l$ induces phase changes of the beams, while negligibly changing the lattice constant constant of the optical lattice. In practice, this condition is easily satisfied since the wavelength of the laser λ is so small compared to an intentional or unintential centimeter scale difference in the path lengths of the two arms.

Another important and perhaps unintuitive feature of the scheme shown in figure 6.3 is that the lock preserves the geometry even if there are changes to the path lengths of the two arms, which are likely to arise if the mirrors drift, there is some thermal expansion of the optical table, or some change in the index of refraction of the air. That is to say, the constant in the expression $(\phi_{\hat{\mathbf{x}}} + \phi_{-\hat{\mathbf{x}}} - (\phi_{\hat{\mathbf{y}}} + \phi_{-\hat{\mathbf{y}}}) + \text{const})$ does not change in spite of these drifts, which can be shown by considering the phases of the for beams as a function of the optical path lengths

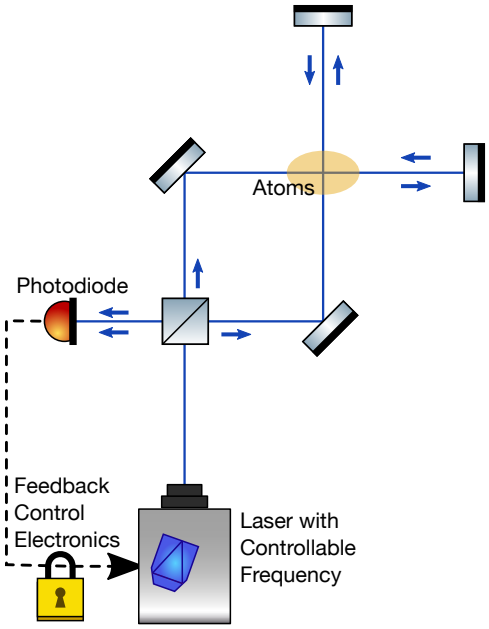

Figure 6.3: A schematic of the setup described in [65]

before and after the atoms. However, these drifts will induce a translation of the overall lattice. This is typically present on some level in optical lattice experiments, but the time scales are generally long enough that they are irrelevant to seconds scale experiments.

A very elegant approach is presented in [66]. In that work, the requisite condition in equation (6.9) is passively ensured by the geometry of the beam. That is to say, the constant in condition (6.9) is unchanged in spite of optical path length changes from mirror drift, etc. without the need for active feedback. Note again however that these drifts will cause translations of the lattice.

Another active stabilization approach is well presented in [64]. Here, an RF signal is generated from the interference of the lattice laser beams with a reference beam, and the phase difference relative to the reference beam is extracted. In this case, the system is such that the quantity $\phi_{\hat{\mathbf{x}}} + \phi_{-\hat{\mathbf{x}}}$ is held constant relative to the reference beam. Likewise, $\phi_{\hat{\mathbf{y}}} + \phi_{-\hat{\mathbf{y}}}$ is held constant. The net result is that condition (6.9) is satisfied. The scheme has as its technical precursor designs for fiber noise cancelation scheme initially presented in [67].

6.2.2 Related Implementations

We would also like to draw the reader's attention to a couple of other interesting works that are concerned with stabilizing the geometries of two dimensional optical lattices by controlling the relative phases of interfering laser beams.

The first is the Kagome lattice work conducted in the group of Dan Stamper-Kurn, where the hardware details are discussed in PhD theses from the group [68, 69, 70]. To produce a kagome lattice or trimerized-kagome lattice, two optical lattices are superimposed. Each of the two lattices is formed by three interfering laser beams, and the choice of in plane or out of plane polarization determines whether each will form a triangular lattice or a honeycomb lattice. One of the lattices is formed from the interference of 1064nm laser beams and the other 532nm laser beams. One challenge here is that the two superimposed lattices need to be spatially overlapped to within a small fraction of a lattice constant so that the desired kagome or trimerized-kagome lattice is produced. Relative phase changes of the individual laser beams would induce such a translation of the superimposed lattices relative to each other. To stabilize the relative position, good design of the geometry is utilized to maximize passive stability, while residually drift is managed with phase control of the individual beams using AOMs.

The second is a very different approach described in reference [63]. In this work, a hexagonal lattice was produced from the interference of frequency modulated laser beams. The modulated beam is equivalent to multiple copropagating laser beams of a discrete set of frequencies, said frequencies being the original laser frequency ν as well as $\nu + n\nu_M$ where $n \in \mathbb{Z}$ and ν_M is the frequency of the modulation. The laser beams with frequency $\nu + n\nu_M$ for $n \neq 0$ are referred to as sidebands. By choosing the frequency of each of the laser beams and the modulation frequency appropriately, it is possible to interfere the sideband of one modulated laser beam with the central frequency beam of another modulated beam. Doing so gives control of the phase of the resulting interference by changing the phase of the modulation. This

enables the creation of optical potentials where the geometry and position are fully controllable by varying the phase of the modulation, as was demonstrated for a hexagonal lattice in [63].

6.3 Polarization Encoded Retroreflection Phase-Lock

In this section, we will discuss a novel phase detection configuration that is well suited to active feedback and phase control. It has potentially fruitful applications the production dynamically driven bichromatic lattices, where each of the superimposed lattices can be independently phase controlled and modulated with a closed loop bandwidth ultimately limited by acousto-optic modulator (AOM) response times and and electronics. Unintended differential drift of the component lattices' positions is also passively avoided in this application. A separate application of the design is to produce a fully controllable optical lattice formed with four laser beams with wavevectors given by $\mathbf{k}_1 = -\mathbf{k}_2 = k\hat{\mathbf{x}}$ and $\mathbf{k}_3 = -\mathbf{k}_4 = k\hat{\mathbf{y}}$. By full control, we mean here that the intensities of each of the 4 beams can be independently controlled, that all of the phases can be independently controlled, and that these parameters can be independently changed at rates limited by the AOMs and electronics.

As with other phase detection schemes, the basic goal is to determine the difference in phase of a pair of beams by interfering them. Different from most schemes however, we will set one of the beams to have right-handed circular polarization and the other to have left-handed circular polarization. Assuming for simplicity for now that the two beams are of equal power, interfering the two beams will produce linearly polarized light, where the angle of linear polarization depends on the relative phase of the interfering beams.[6] In this way, the

[6]We refer to this overlap of oppositely circularly polarized light as "interference." Note however, that superimposing these beams does not actually cause a phase dependent intensity of the combined beam as is typically the case when one describes two beams as interfering. One could argue that a different term is more accurate, but we opt to refer to this as interference since ultimately the whole system will behave like an interferometer, and because interferometers formed with polarizing beam splitters frequently also "interfere" beams of orthogonal linear polarizations before a later polarizer produces a phase dependent beam intensity.

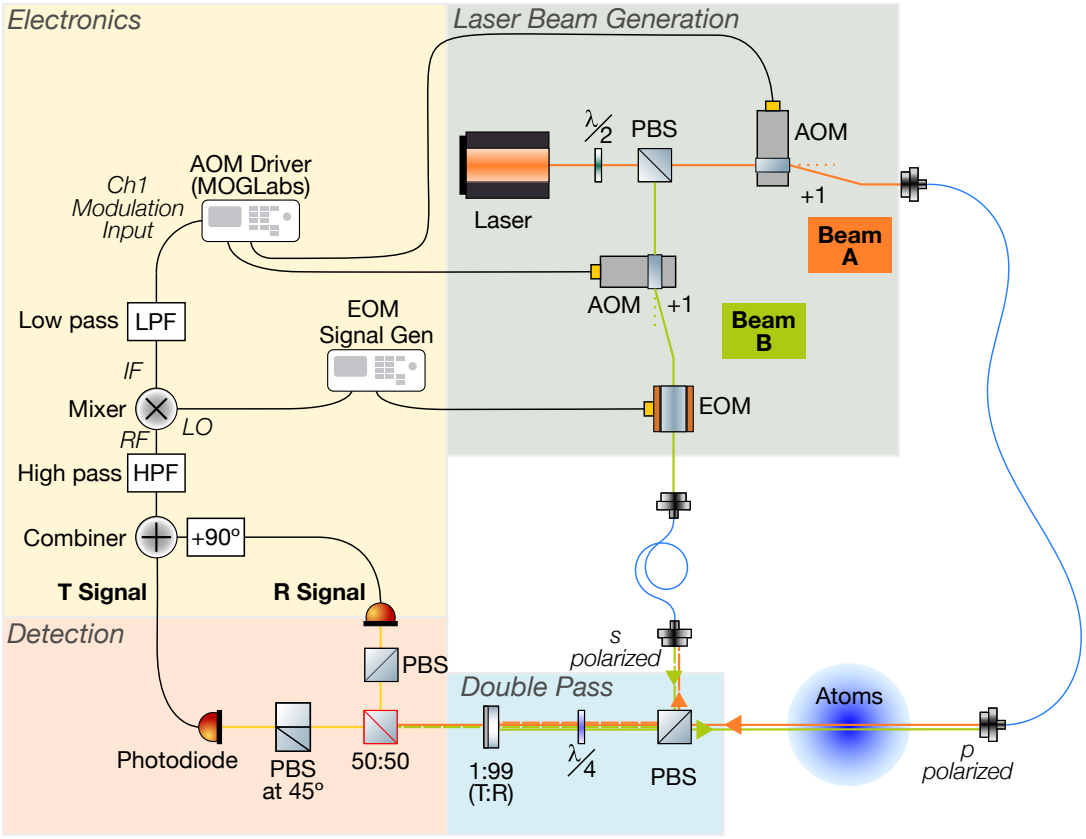

Figure 6.4: An overview schematic of a a polarization encoding retroreflection lock for a one dimensional lattice. Laser beams are shown as colored lines in orange, green, and yellow. Optical fibers are shown as blue curves. Electrical signal paths are shown as black lines. Background colors are used to roughly organize the diagram into the subsystems denoted Laser Beam Generation, Double Pass, Detection, and Electronics. The subsystems will be described in more detail in the subsequent sections. Only the components needed for the phase detection and lock are shown. In a full implementation, one must also include optics and electronics for beam power stabilization and control and lenses to focus the beams at the atoms, along with the many mirrors, etc. that were neglected for readability.

phase difference of the two beams is "encoded" onto the resulting linear polarization. We can then detect this phase by measuring the resulting polarization. To make the detection more robust to signal noise and more convenient to detect, we will modulate the phase of one of the beams at high frequency so that the polarization will also be modulated. We will see that this enables easy isolation and amplification of the generated signals that allows for robust phase detection and control using I/Q signal processing. A diagram of the most basic implementation

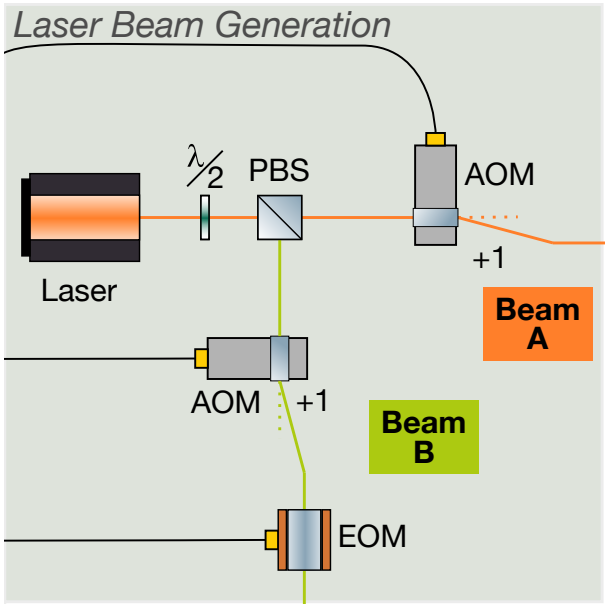

Figure 6.5: Optics to prepare the laser beams for the formed lattice. They are labeled as beam A (orange) and beam B (green). PBS denotes polarizing beam splitter. AOM denotes acousto-optic modulators. EOM denotes electro-optic modulator. $\lambda/2$ labels half waveplates.

of this polarization encoding for the case of a monochromatic 1D optical lattice is shown in figure 6.4. We would like to note that a similar phase lock configurations that was inspiring for this work is presented in the thesis of Tsz Him (Zephy) Leung [68].

6.3.1 Preparing the Lattice Beams

The optics to prepare the two laser beams that will interfere to form the 1D lattice are depicted in figure 6.5. Here we show a laser split into two beams using a polarizing beam splitter cube. We denote the two beams as A and B. Each beam is passed through an acousto-optic modulator (AOM). The AOMs provide control over the power and phase of each of the beams independently. In practice for a 1D lattice, one need only control the the phase of one of the beams (or equivalently control the frequency). The power of both of the beams needs to be controlled, which is typically best done by stabilizing with feedback using a power monitoring photodiode (power stabilization not shown in the diagrams.)

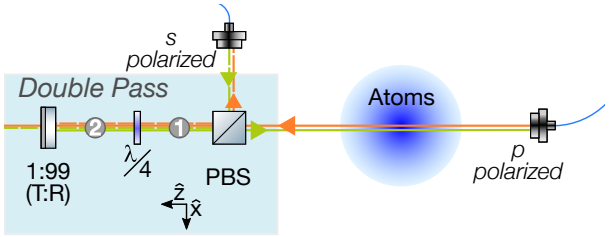

Figure 6.6: Diagram of the "Double Pass" configuration used to overlap the two beams and interfere them for later phase detection, while generating an optical lattice at the atomic cloud. $\lambda/4$ labels a quarter waveplate. Both beams are retroreflected at the far left of the diagram on the beam sampler labeled 1:99 (T:R) to indicate an order 1% transmission. The numbered gray circles indicate relevant points for analysis given in the text.

Beam B also passes through an electro-optic modulator (EOM) which adds a small ($\ll \pi/2$) high frequency modulation (order 10MHz) to the phase of one of the beams. When beams A and B are interfered on a photodiode, the resulting signal will have an A.C. component at the modulation frequency of the EOM. The A.C. component of the signal at this frequency can then be processed with a lock-in amplifier scheme to robustly determine the phase as compared to relying on a D.C. signal.

Beams A and B are then coupled into polarization maintaining optical fibers. As shown in figure 6.6, Beam A exits the optical fiber horizontally polarized relative to the optical table (p-polarized for reflecting optics whose surfaces are perpendicular to the table surface as is the case for most optics.) Beam B exits the optical fiber polarized vertical to the table (so that it is s-polarized for the relevant optics.) Beams A and B overlap to form a 1D optical lattice at the atoms after beam B has passed through the optics that have been labeled "double pass" because of similarity to the optics used in a double pass AOM setup.

6.3.2 Encoding Phase Difference onto Polarization

At the beam sampler on the far left of figure 6.6, a small amount of the superimposed beams is transmitted for detection. This light goes to the detection setup shown in figure 6.7. Let us analyze the polarization of the light that is transmitted through the beam sampler. To

do this, we will consider what happens to the beams as they traverse the double pass of figure 6.6. Beam A enters the double pass by transmitting through the PBS and beam B enters the double pass by reflecting off the PBS. After this happens, the two beams are propagating to the left in the $\hat{\mathbf{z}}$ direction at point 1 indicated in figure 6.6. At point 1, beam A is polarized in the $\hat{\mathbf{x}}$ direction, and we can represent its electric field using the conventions described in section 3.1 as[7]

$$\mathbf{E}_{A,1} = E_A \, e^{i(kz+\phi_A)}\hat{\mathbf{x}}$$

Likewise, the electric field for beam B is given by

$$\mathbf{E}_{B,1} = E_B \, e^{i(kz+\phi_B)}\hat{\mathbf{y}}$$

Here, $E_A, E_B \in \mathbb{R}$. At point 1 of figure 6.6, these two beams are superimposed to produce a beam of total electric field $\mathbf{E}_{\text{Tot},1}$ given by

$$\mathbf{E}_{\text{Tot},1} = \mathbf{E}_{A,1} + \mathbf{E}_{B,1}$$

Next, let us now consider the laser beams at point 2 in figure 6.6. In going from point 1 to point 2, the beams propagate through a quarter waveplate. The action of the waveplate is a linear transformation, so we can consider the waveplate as acting on beam A and beam B separately. The quarter waveplate is ideally set to transform each of the linear polarized beams to circularly polarized beams, but it does not matter whether beam A is transformed to right or left circular polarization. Let us make the choice to set the fast axis to be along the $\frac{1}{\sqrt{2}}(\hat{\mathbf{x}} - \hat{\mathbf{y}})$ direction and the slow axis to the $\frac{1}{\sqrt{2}}(\hat{\mathbf{x}} + \hat{\mathbf{y}})$ direction. The action of the waveplate will then

[7]Here, we implicitly model the laser beams as plane waves. If one wishes to have a more accurate model, we should consider E_A to be spatially dependent to produce a gaussian beam profile. In the case that the beam waist is large enough that the Rayleigh range is negligible compared to the propagation lengths, we can approximate it as a collimated beam and ignore the z dependence of E_A. Ignoring the spatial dependence of E_A is sufficient for our purposes here where we are only concerned with the polarizations and phases of the beams.

be to add $\pi/2$ phase to the $\frac{1}{\sqrt{2}}(\hat{\mathbf{x}}+\hat{\mathbf{y}})$ component of the electric field relative to the $\frac{1}{\sqrt{2}}(\hat{\mathbf{x}}-\hat{\mathbf{y}})$ component. We can represent this transformation mathematically as

$$\begin{aligned}
\mathbf{E}_2 \cdot \frac{1}{\sqrt{2}}(\hat{\mathbf{x}}-\hat{\mathbf{y}}) &= \mathbf{E}_1 \cdot \frac{1}{\sqrt{2}}(\hat{\mathbf{x}}-\hat{\mathbf{y}}) \\
\mathbf{E}_2 \cdot \frac{1}{\sqrt{2}}(\hat{\mathbf{x}}+\hat{\mathbf{y}}) &= e^{i\pi/2}\mathbf{E}_1 \cdot \frac{1}{\sqrt{2}}(\hat{\mathbf{x}}+\hat{\mathbf{y}}) \quad = \quad i\,\mathbf{E}_1 \cdot \frac{1}{\sqrt{2}}(\hat{\mathbf{x}}+\hat{\mathbf{y}})
\end{aligned}$$

where $\mathbf{E}_1$ represents the laser electric field before propagation through the waveplate and $\mathbf{E}_2$ after. In principle, the finite optical path length of the waveplate and between points 1 and 2 could imply an additional overall phase shift to both beams, but it is irrelevant to this analysis, since we will only be interested in the final polarization and relative phase shifts between beams A and B.

Using this transformation, and applying it to beams A and B individually, beams A and B at point 2 can be represented by

$$\begin{aligned}
\mathbf{E}_{A,2} &= \frac{1}{2}E_A\, e^{i(kz+\phi_A)}\Big[\,(\hat{\mathbf{x}}-\hat{\mathbf{y}}) + i\,(\hat{\mathbf{x}}+\hat{\mathbf{y}})\,\Big] \\
\mathbf{E}_{B,2} &= \frac{1}{2}E_B\, e^{i(kz+\phi_B)}\Big[\,(\hat{\mathbf{x}}-\hat{\mathbf{y}}) - i\,(\hat{\mathbf{x}}+\hat{\mathbf{y}})\,\Big]
\end{aligned} \tag{6.10}$$

and we see from each of their forms that $\mathbf{E}_{A,2}$ has left-handed circular polarization and $\mathbf{E}_{B,2}$ has right-handed circular polarization as desired.[8]

For a laser beam, polarization can be conveniently determined from the beam's Stokes parameters. Following [26] and using the complex notation of section 3.1, we can represent the laser beam by

$$\mathbf{E} = (\mathcal{E}_1\hat{\mathbf{e}}_1 + \mathcal{E}_2\hat{\mathbf{e}}_2)e^{i\mathbf{k}\cdot\mathbf{r}} \tag{6.11}$$

where $\hat{\mathbf{e}}_1$, $\hat{\mathbf{e}}_2$, and $\hat{\mathbf{k}} = \mathbf{k}/|\mathbf{k}|$ form a right handed orthonormal basis where $\hat{\mathbf{e}}_1 \times \hat{\mathbf{e}}_2 = \hat{\mathbf{k}}$. In our

[8] We follow the convention given in section 16 of [26] for right and left circular polarization. Here left-handed circular polarization is defined as a counterclockwise trace of the electric field vector as it evolves in time when the wavevector of the light wave is pointing at the viewer. It is not an intuitive convention in our opinion.

case, we have chosen $\hat{\mathbf{k}} = \hat{\mathbf{z}}$. Here, $\mathcal{E}_1$ and $\mathcal{E}_2$ are complex numbers. We can write

$$\mathcal{E}_1 = ae^{i\delta_1} \qquad \mathcal{E}_2 = be^{i\delta_2} \tag{6.12}$$

where $a, b, \delta_1, \delta_2 \in \mathbb{R}$. For this description, the Stokes parameters are defined by

$$\begin{aligned} s_0 &= a^2 + b^2 \\ s_1 &= a^2 - b^2 \\ s_2 &= 2ab\cos(\delta) \\ s_3 &= 2ab\sin(\delta) \end{aligned} \tag{6.13}$$

where $\delta \equiv \delta_2 - \delta_1$. Given knowledge of $\mathcal{E}_1$ and $\mathcal{E}_2$, we can calculate the Stokes parameters from

$$\begin{aligned} s_0 &= |\mathcal{E}_1|^2 + |\mathcal{E}_2|^2 \\ s_1 &= |\mathcal{E}_1|^2 - |\mathcal{E}_2|^2 \\ s_2 &= \mathrm{Re}\left(2\mathcal{E}_1^*\mathcal{E}_2\right) \\ s_3 &= \mathrm{Im}\left(2\mathcal{E}_1^*\mathcal{E}_2\right) \end{aligned} \tag{6.14}$$

as is readily confirmed by plugging in the expressions for $\mathcal{E}_1$ and $\mathcal{E}_2$ in equations (6.12) and confirming that one recovers equations (6.13).

It is also worth noting that the Stokes parameters have the property that [26]

$$s_1 = s_0\cos(2\gamma)\cos(2\alpha) \qquad s_2 = s_0\cos(2\gamma)\sin(2\alpha) \qquad s_3 = s_0\sin(2\gamma) \tag{6.15}$$

where α indicates the angle of the major axis of the polarization ellipse with the $\hat{\mathbf{e}}_1$-axis and γ is an angle that indicates the polarization.

Let us now consider the polarization of the combined laser beams at point 2 of figure 6.6

given by

$$\mathbf{E}_{\text{Tot},2} = \mathbf{E}_{A,2} + \mathbf{E}_{B,2} = \frac{1}{2}E_A\, e^{i(kz+\phi_A)}\Big[\,(\hat{\mathbf{x}} - \hat{\mathbf{y}}) + i\,(\hat{\mathbf{x}} + \hat{\mathbf{y}})\,\Big] + \frac{1}{2}E_B\, e^{i(kz+\phi_B)}\Big[\,(\hat{\mathbf{x}} - \hat{\mathbf{y}}) - i\,(\hat{\mathbf{x}} + \hat{\mathbf{y}})\,\Big]$$

Let us take $\hat{\mathbf{e}}_1 = \frac{1}{\sqrt{2}}(\hat{\mathbf{x}} - \hat{\mathbf{y}})$ and $\hat{\mathbf{e}}_2 = \frac{1}{\sqrt{2}}(\hat{\mathbf{x}} + \hat{\mathbf{y}})$, allowing us to identify

$$\begin{aligned}\mathcal{E}_1 =& \frac{1}{\sqrt{2}}E_A e^{i\phi_A} + \frac{1}{\sqrt{2}}E_B e^{i\phi_B} \\ \mathcal{E}_2 =& \frac{i}{\sqrt{2}}E_A e^{i\phi_A} - \frac{i}{\sqrt{2}}E_B e^{i\phi_B}\end{aligned} \tag{6.16}$$

and from this, we can readily calculate the Stokes parameters using equation (6.14) to find

$$\begin{aligned}s_0 &= E_A^2 + E_B^2 \\ s_1 &= 2E_A E_B \cos(\phi_B - \phi_A) \\ s_2 &= 2E_A E_B \sin(\phi_B - \phi_A) \\ s_3 &= E_A^2 - E_B^2\end{aligned} \tag{6.17}$$

Comparing this to equations (6.15), we can identify that $\alpha = (\phi_B - \phi_A)/2$. From this observation, we conclude that the phase difference between beams A and B is encoded onto the angle α of the polarization ellipse. This is what we mean when we say that the phase difference is encoded onto the polarization of the light.

To gain some intuition, it is helpful to consider the case that $E_A = E_B = E$. In this case, the combined beam has linear polarization, as can be identified from the stokes parameters by the fact that $s_3 = 0$ in this case. With a bit of algebraic manipulation, one can explicitly write

$$\mathbf{E}_{\text{Tot},2} = \mathbf{E}_{A,2} + \mathbf{E}_{B,2} = Ee^{i(kz+(\phi_A+\phi_B)/2)}\Big[\,\cos\big((\phi_B - \phi_A)/2\big)(\hat{\mathbf{x}} - \hat{\mathbf{y}}) \;+\; \sin\big((\phi_B - \phi_A)/2\big)(\hat{\mathbf{x}} + \hat{\mathbf{y}})\,\Big]$$

This expression reveals that the total field is in fact linearly polarized at the angle $(\phi_B - \phi_A)/2$

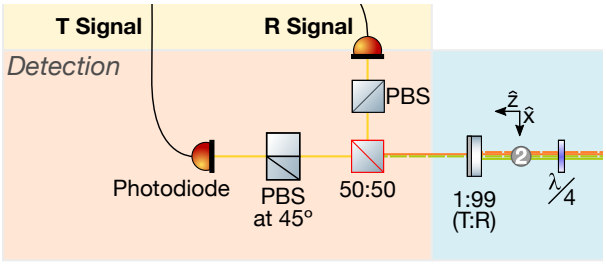

Figure 6.7: Optics for detection of the polarization and light phase.

to the $\frac{1}{\sqrt{2}}(\hat{\mathbf{x}} - \hat{\mathbf{y}})$ axis. In some sense, this is the ideal case since it will produce interferometric signals with the highest visibility, but we will see that deviating from the ideal is not a critical issue.

Now that we have demonstrated that the phase difference between beams A and B are encoded in the polarization of the combined beam, let us discuss how we can analyze the phase difference. The optics for the scheme that we will now describe is shown in figure 6.7. A sample of the superimposed beams are transmitted on the 1:99 beam sampler, which transmits 1% of the beam power as a sample and reflects the remainder. The sampled beam is then split with a non-polarizing beam splitter. We will now show that by polarizing these two samples along two different axes, we can unambiguously measure the phase $(\phi_B - \phi_A)/2$. These two polarizers are the polarizing beam splitters shown in figure 6.7.

The Mueller matrix for an ideal polarizer that polarizes at an angle θ relative to the $\hat{\mathbf{e}}_1$ axis, the $\frac{1}{\sqrt{2}}(\hat{\mathbf{x}} - \hat{\mathbf{y}})$ axis in our case, can be found to be [71][9]

$$P_\theta = \frac{1}{2}\begin{bmatrix} 1 & \cos(2\theta) & \sin(2\theta) & 0 \\ \cos(2\theta) & \cos^2(2\theta) & \sin(2\theta)\cos(2\theta) & 0 \\ \sin(2\theta) & \sin(2\theta)\cos(2\theta) & \sin^2(2\theta) & 0 \\ 0 & 0 & 0 & 0 \end{bmatrix}$$

[9]We note that the conventions of reference [71] differ somewhat from those that we adopt in this thesis. However, one can confirm with the methods described in section 4.3.4 of [71] on the Mueller calculus that the matrix is in fact the same for our convention as theirs.

We can calculate the effect of a polarizer on the sampled beams by applying this matrix to the Stokes vector defined by the parameters given in equation (6.17). In our case, we will measure the intensity of the polarized beam, which is proportional to the first element s_0 of the resulting vector. Thus, we find that

$$\begin{aligned} I(\theta) &\propto \frac{1}{2}E_A^2 + \frac{1}{2}E_B^2 + E_A E_B \cos(\phi_B - \phi_A)\cos(2\theta) + E_A E_B \sin(\phi_B - \phi_A)\sin(2\theta) \\ &= \frac{1}{2}E_A^2 + \frac{1}{2}E_B^2 + E_A E_B \cos\left((\phi_B - \phi_A) - 2\theta\right) \end{aligned} \tag{6.18}$$

We see that we can set $\theta = 0$ and $\theta = \pi/4$ to get

$$I(0) \propto \frac{1}{2}E_A^2 + \frac{1}{2}E_B^2 + E_A E_B \cos(\phi_B - \phi_A) \tag{6.19}$$

and

$$I(\pi/4) \propto \frac{1}{2}E_A^2 + \frac{1}{2}E_B^2 + E_A E_B \sin(\phi_B - \phi_A) \tag{6.20}$$

By detecting these two intensities on a photodiode, we can extract $\cos(\phi_B - \phi_A)$ and $\sin(\phi_B - \phi_A)$, which is sufficient to extract the value of $\phi_B - \phi_A$. Polarizing the sample beam onto these two axes as depicted in figure 6.7 is accomplished with the PBS and the PBS mounted at a 45 degree angle, but any polarizer will suffice. In this case, keeping in mind that we are working in the coordinate system with basis vectors $\frac{1}{\sqrt{2}}(\hat{\mathbf{x}} - \hat{\mathbf{y}})$ and $\frac{1}{\sqrt{2}}(\hat{\mathbf{x}} + \hat{\mathbf{y}})$, we have that the "T Signal" and "R Signal" denoted in figure 6.7 are proportional to $I(0)$ and $I(\pi/4)$, respectively.

In principle, detection of the signals given in equations (6.19) and (6.20) are sufficient to uniquely extract the phase difference $(\phi_B - \phi_A)$. However, doing so requires that one know the the ratio E_A/E_B, whose values could be intentionally or unintentionally changed over the course of an experiment. In the next section, we will discuss a way to relax this requirement substantially using phase modulation.

6.3.3 Error Signal Generation

Let us now discuss a scheme for setting $(\phi_B - \phi_A)$ to match a reference phase value ϕ_{ref}. More precisely, we will generate an error signal for the difference between $(\phi_B - \phi_A)$ and ϕ_{ref}, which can then be sent to a servo to maintain the condition $\phi_B - \phi_A = \phi_{\text{ref}}$.

As depicted in figure 6.5, beam B transmits through an EOM. We will use this EOM to apply a small phase modulation to beam B so that the phase of beam B will be time varying of the form

$$\phi_B + M \sin(\Omega_{\text{eo}} t + \phi_{\text{eo}})$$

where $M \ll 1$, and we assume that ϕ_B is slowly varying compared to Ω_{eo}. Making this assumption, the analysis of the previous section is the same, but with the replacement

$$\phi_B \quad \rightarrow \quad \phi_B + M \sin(\Omega_{\text{eo}} t + \phi_{\text{eo}})$$

Thus, the intensity of the beams that are detected by the photodiode are given by the updated forms of equations (6.19) and (6.20). The photodiodes in figure 6.5 will detect the "T Signal" denoted $V_{\text{T}} \propto I(0)$ and the "R Signal" denoted $V_{\text{R}} \propto I(\pi/4)$. Introducing an overall constant of proportionality K_{pd} between square of the electric field $|\mathbf{E}|^2$ and the photodiode voltage signals, we have that

$$\begin{aligned} V_{\text{T}} &= K_{\text{pd}} \left[\frac{1}{2} E_A^2 + \frac{1}{2} E_B^2 + E_A E_B \cos\left(\phi_B - \phi_A + M \sin(\Omega_{\text{eo}} t + \phi_{\text{eo}}) \right) \right] \\ V_{\text{R}} &= K_{\text{pd}} \left[\frac{1}{2} E_A^2 + \frac{1}{2} E_B^2 + E_A E_B \sin\left(\phi_B - \phi_A + M \sin(\Omega_{\text{eo}} t + \phi_{\text{eo}}) \right) \right] \end{aligned} \tag{6.21}$$

With the assumption that M is small, we can apply angle sum trigonometric identities for the cos and sin terms in equation (6.21). We can then further approximate $\cos(M) \approx 1$ and

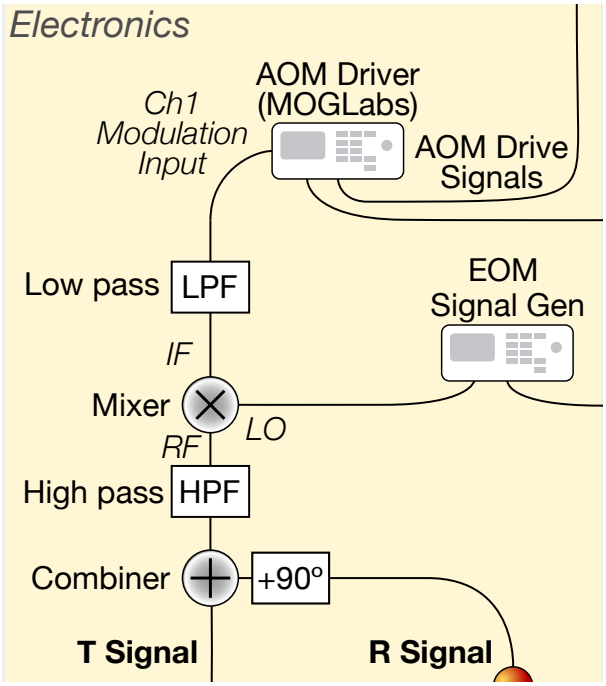

Figure 6.8:

$\sin(M) \approx M$ to write

$$V_{\mathrm{T}} = K_{\mathrm{pd}}\left[\frac{1}{2}E_A^2 \;+\; \frac{1}{2}E_B^2 \;+\; E_A E_B\cos(\phi_B-\phi_A) \;-\; M(E_A E_B)\sin(\phi_B-\phi_A)\sin(\Omega_{\mathrm{eo}}t+\phi_{\mathrm{eo}})\right]$$
$$V_{\mathrm{R}} = K_{\mathrm{pd}}\left[\frac{1}{2}E_A^2 \;+\; \frac{1}{2}E_B^2 \;+\; E_A E_B\sin(\phi_B-\phi_A) \;+\; M(E_A E_B)\cos(\phi_B-\phi_A)\sin(\Omega_{\mathrm{eo}}t+\phi_{\mathrm{eo}})\right] \tag{6.22}$$

The virtue of modulating with an EOM is now clear: the amplitudes of the AC components of V_{T} and V_{R} give $M(E_A E_B)\sin(\phi_B-\phi_A)$ and $M(E_A E_B)\cos(\phi_B-\phi_A)$, respectively. This signal is more immune to noise and also allows for convenient generation of an error signal using standard lock-in amplification techniques.

For reasons that will become clear in a moment, we will want to phase shift one of the signals by 90 degrees. Let us shift the phase the RF component of V_{R} as shown in figure 6.8.

This will convert V_{R} to

$$V_{\mathrm{R},+90^\circ} = K_{\mathrm{pd}}\left[\frac{1}{2}E_A^2 \;+\; \frac{1}{2}E_B^2 \;+\; E_A E_B \sin(\phi_B - \phi_A) \;+\; M(E_A E_B)\cos(\phi_B - \phi_A)\cos(\Omega_{\mathrm{eo}}t + \phi_{\mathrm{eo}})\right] \tag{6.23}$$

We can then sum the V_{T} and $V_{\mathrm{R},+90^\circ}$ signals to obtain

$$\begin{aligned} V_{\mathrm{T}} + V_{\mathrm{R},+90^\circ} = \; K_{\mathrm{pd}}\Big[&E_A^2 \;+\; E_B^2 \;+\; E_A E_B \cos(\phi_B - \phi_A) \;+\; E_A E_B \sin(\phi_B - \phi_A) \\ &- M(E_A E_B)\sin(\phi_B - \phi_A)\sin(\Omega_{\mathrm{eo}}t + \phi_{\mathrm{eo}}) + \; M(E_A E_B)\cos(\phi_B - \phi_A)\cos(\Omega_{\mathrm{eo}}t + \phi_{\mathrm{eo}})\Big] \end{aligned}$$

And one can easily confirm that

$$\begin{aligned} V_{\mathrm{T}} + V_{\mathrm{R},+90^\circ} = K_{\mathrm{pd}}\Big[&E_A^2 \;+\; E_B^2 \;+\; E_A E_B \cos(\phi_B - \phi_A) \;+\; E_A E_B \sin(\phi_B - \phi_A) \\ &+ M(E_A E_B)\cos(\phi_B - \phi_A + \phi_{\mathrm{eo}} + \Omega_{\mathrm{eo}}t)\Big] \end{aligned}$$

Lock-in amplifier techniques can then be used on this signal to create an error signal. Specifically, the signal is put through a high pass filter (HPF) and input to the RF input of a mixer (or phase detector) as shown in figure 6.8. It is mixed with a local oscillator (LO) input from the same driver as the EOM driver. The local oscillator signal is given by

$$V_{\mathrm{lo}} = A_{\mathrm{lo}} \sin(\Omega_{\mathrm{eo}}t + \phi_{\mathrm{lo}})$$

The ideal mixer output is then

$$\begin{aligned} V_{\mathrm{mix\ out}} &= A_{\mathrm{mo}} \cos(\phi_B - \phi_A + \phi_{\mathrm{eo}} + \Omega_{\mathrm{eo}}t)\sin(\Omega_{\mathrm{eo}}t + \phi_{\mathrm{lo}}) \\ &= \frac{A_{\mathrm{mo}}}{2}\Big[\sin(\phi_B - \phi_A + \phi_{\mathrm{eo}} - \phi_{\mathrm{lo}}) + \sin(2\Omega_{\mathrm{eo}}t + \phi_B - \phi_A + \phi_{\mathrm{eo}} + \phi_{\mathrm{lo}})\Big] \end{aligned}$$

where $A_{\mathrm{mo}} \equiv A_{\mathrm{lo}} K_{\mathrm{pd}} M(E_A E_B)$. Finally, we send the mixer output through a low pass filter

(LPF) resulting in the convenient error signal

$$V_{\mathrm{err}} = \frac{A_{\mathrm{mo}}}{2} \sin(\phi_B - \phi_A + \phi_{\mathrm{eo}} - \phi_{\mathrm{lo}}) \tag{6.24}$$

ϕ_{lo} and ϕ_{eo} are both easily controlled independently by using the two output channels of a signal generator, which is shown as the "EOM Signal Generator" in figure 6.8. We can instead consider these as defining the reference phase $\phi_{\mathrm{ref}} \equiv \phi_{\mathrm{lo}} - \phi_{\mathrm{eo}}$ so that

$$V_{\mathrm{err}} = \frac{A_{\mathrm{mo}}}{2} \sin(\phi_B - \phi_A - \phi_{\mathrm{ref}}) \tag{6.25}$$

Using this as an error signal for feedback on the beam A or beam B AOM driver to control the phase or frequency, one can impose a lock condition that implies $V_{\mathrm{err}} = 0$ and $\frac{dV_{\mathrm{err}}}{d\phi_B} = 0$. The resulting condition assuming $A_{\mathrm{mo}} > 0$ on the phase is that

$$\phi_B - \phi_A - \phi_{\mathrm{ref}} = 0 \qquad \Longrightarrow \qquad \phi_B - \phi_A = \phi_{\mathrm{ref}}$$

If a lock is implemented so that the above condition holds, one is able to directly control $\phi_B - \phi_A$ by changing ϕ_{ref}, which can be simply and robustly controlled with the phase of the local oscillator input ϕ_{lo} to the mixer. In the 1D case, this change in $\phi_B - \phi_A$ induces a translation of the optical lattice.

Note that in this idealized case we have the great benefit that the lock condition will be independent of E_A, E_B, M, A_{lo}, and K_{pd}. In practice however, one will typically be limited to some range of overall values of A_{mo}. This is because, unless extraordinary care is taken, a control servo such as a PID will not be stable for every slope of the error signal $\frac{dV_{\mathrm{err}}}{d\phi_B}$ near the lock point. Moreover, even in the stable range, how quickly one can vary ϕ_{ref} to control $\phi_B - \phi_A$ via the lock will potentially be limited due to the change in feedback response. Consequently, one must take care in confirming that the closed look behavior is sufficient for the parameters

(beam intensities, drive frequencies, etc.) one wishes to use in an experiment, but it is about the best one can hope for from an analog error signal.

6.3.4 Deviations from Ideal Optics Behavior

Imperfect Quarter Waveplate

One major practical concern is that the quarter waveplate of the "double pass" shown in figure 6.6 is imperfect. Specifically, if the quarter waveplate is imperfect, then part of beam A will transmit on the PBS cube after retro reflecting, instead of entirely reflecting as shown. This stray light will then interfere with beam A at the atoms to form a lattice even when beam B is not there. The nature of interference makes it so that the stray beam needs very little power to produce a significant lattice.

It maybe be possible to avoid this by not perfectly retroreflecting from the the beam sampler, and instead hitting the mirror at a very shallow angle. The sampled beams will not be perfectly overlapped when they reach the detection photodiodes, but assuming they are partly overlapped, a signal should be possible, albeit, with sacrificed visibility. We have not tried this in tests yet.

An alternative is to use multiple waveplates or use of some adjustable phase retarding element to that no stray beam reaches the atoms.

Note that this is much less of a concern for beam B because imperfect polarization does not send send stray light towards the atoms.

Imperfect Polarizations for Error Signal Detection

In our discussion of encoding the phase difference between beams A and B onto the polarization of the combined sampled beams in section 6.3.2, we assumed that the sampled beams had opposite circular polarizations. With this assumption, we need only make two intensity

measurements after passing the beam through linear polarizers with transmission axes at 45 degrees relative to each other to determine the phase difference between beams A and B. The setup to make this measurement was shown in figure 6.7. One would be justifiably concerned about the effect of imperfectly polarized sample beams. This could occur before the beams are combined, but we find less avoidably that nonpolarizing 50:50 beam splitters will change the polarization of the beams that pass through them, and the change will not necessarily be the same for the transmitted and reflected beam. We will show that a couple minor design changes remove this problem in practice.

The design changes are (1) make the polarizers (the PBS's in figure 6.7) rotatable and (2) add a variable attenuator in front of one of the photodiodes, such as a variable attenuator. The first change will allow one to ensure that the intensity of light reaching the "T Signal" photodiode varies like $\cos(\phi_B - \phi_A)$ and that reaching the "R Signal" photodiode varies like $\sin(\phi_B - \phi_A)$. The second change allows us to balance amplitudes of the sinusoidal signals on the photodiodes. In practical cases, one is able to vary the angle of the polarizers before the photodiode so that the signals look like $\cos(\phi_B - \phi_A)$ and $\sin(\phi_B - \phi_A)$, but the amplitudes of the signals might not exactly match. One can then use the variable attenuator to, such as a linear gradient filter on a tilt stage or a translation stage, to make the amplitudes of the two photodiode signal match.

This alternation to the designs is sufficient provided three conditions. Condition 1 is that all of the optical elements after the beam is sampled must be linear, in that their effect on the light polarization is a linear transformation. This is generally a safe assumption for the optical elements in the setup, as it allows for birefringent effects and partial polarizations. Condition 2 is that the polarizations are not changed "too dramatically" which we will state more quantitatively later, but which is typically not a concern for realistic optics. Finally, of greatest practical concern is condition 3 that there must be no stray beams present at the photodiode.

Conditions 1 and 3 are sufficient for the following analysis. Condition 3 simply ensures that are only two beams to analyze. Condition 1 allows us to consider the two sampled beams as being totally independent until we need to consider the intensity at the photodiodes. Let us specifically consider the situation right after the 50:50 beam splitter in figure 6.7. We can consider either the beams transmitted or the beams reflected from the 50:50 splitter, but in either case, we have two beams of some polarization that we wish to polarize and them measure on a photodiode. At this point, beam A and beam B may have started with some non-ideal polarizations and they have also had their polarizations changed by mathematically linear transformations. Let us consider the two beams represented as

$$\mathbf{E}_A = e^{i\phi/2}\begin{bmatrix} \cos(\rho/2) & -\sin(\rho/2) \\ \sin(\rho/2) & \cos(\rho/2) \end{bmatrix}\begin{bmatrix} \cos\theta_a \\ i\sin\theta_a \end{bmatrix} = e^{i\phi/2}\begin{bmatrix} \cos(\rho/2)\cos\theta_a - i\sin(\rho/2)\sin\theta_a \\ \sin(\rho/2)\cos\theta_a + i\cos(\rho/2)\sin\theta_a \end{bmatrix}$$

$$\mathbf{E}_B = e^{-i\phi/2}\begin{bmatrix} \cos(\rho/2) & \sin(\rho/2) \\ -\sin(\rho/2) & \cos(\rho/2) \end{bmatrix}\begin{bmatrix} \cos\theta_b \\ i\sin\theta_b \end{bmatrix} = e^{-i\phi/2}\begin{bmatrix} \cos(\rho/2)\cos\theta_b + i\sin(\rho/2)\sin\theta_b \\ -\sin(\rho/2)\cos\theta_b + i\cos(\rho/2)\sin\theta_b \end{bmatrix} \tag{6.26}$$

with the restriction $\theta_a, \theta_b \in [-\pi/4, \pi/4]$. These are not the most general electric fields, but let us now discuss what the parameters represent and why there is no loss of generality for our problem. ϕ represents the difference in phase between the two beams.[10] We have given up an irrelevant common phase factor $e^{i\phi_{\text{comm}}}$ on the two beams, since we are ultimately only concerned with a final measured intensity, which only depends on the phase difference between the beams. ρ represents the angle between the major axes of the two polarization ellipses of the beams. This parametrization does not allow for independently specifying the major axes of the polarization ellipses. However, this lost degree of freedom represents a change of coordinates, and it is unneeded since we will momentarily consider polarizing along an arbitrary axis.

[10] ϕ can be considered equivalent to $\phi_B - \phi_A$ for the beams considered in equations (6.10).

Let us now consider polarizing these combined beams along an arbitrary axis defined by the unit vector

$$\mathbf{u} = \begin{bmatrix} \cos\alpha \\ \sin\alpha \end{bmatrix}$$

The result will be an electric field of amplitude

$$E_u = \mathbf{u} \cdot \mathbf{E}_A + \mathbf{u} \cdot \mathbf{E}_B$$

The intensity of the beam after polarization will then be[11]

$$\begin{aligned} I \propto E_u^* \cdot E_u = 1 &+ \frac{1}{2}\cos(2\alpha - \rho)\cos(2\theta_a) + \frac{1}{2}\cos(2\alpha + \rho)\cos(2\theta_b) \\ &+ \Big[\cos(\rho)\cos(\theta_a - \theta_b) + \cos(2\alpha)\cos(\theta_a + \theta_b)\Big]\cos(\phi) \\ &+ \Big[\sin(\rho)\sin(\theta_a + \theta_b) - \sin(2\alpha)\sin(\theta_a - \theta_b)\Big]\sin(\phi) \end{aligned} \tag{6.27}$$

It would be great for our purposes if for some desired ϕ_0, we can always find some polarization axis α_0 such that

$$I = c_0 + b_0\cos(\phi - \phi_0)$$

where $b_0 \neq 0$. Theoretically, this is not always possible, but we will find a practically relevant sufficient condition that ensures that it is possible, given conditions on the ellipticity of polarization.

Before proving the sufficient condition, let us note the true minimum requirement for our purposes. Looking at figure 6.7, our goal is that the light intensity that reaches the "T" and

[11] We discourage the diligent reader from repeating the algebra to find this expression and to instead confirm it with the Mathematica by setting assumptions that all of the variables are real and then taking the difference between the initial and final expressions. We found it necessary to brace the expression for the difference with FullSimplify[TrigFactor[ExpToTrig[]]]. Mathematica does not otherwise readily generate this expression to our knowledge.

"R"' photodiodes be of the forms

$$I_T = c_t + b_t \cos(\phi - \phi_0) \quad \text{and} \quad I_R = c_r + b_r \sin(\phi - \phi_0)$$

respectively, where $b_t \neq 0$ and $b_r \neq 0$, but we have no requirement on ϕ_0. In other words, we need the intensity of the light that reaches photodiode "T" to vary as a cosine and the light that reaches photodiode "R" to vary as a sine. It follows from our analysis of the ideal case that everything will work out great if $b_t = b_r > 0$. However, when $b_t > 0$, $b_r > 0$, but $b_r \neq b_t$, we have the practical remedy of variably attenuating the light that reaches one of the photodiodes (or attenuating the electrical signal). Moreover, on the other ostensibly problematic case that $b_t > 0$ and $b_r < 0$, we can reverse roles of the electrical signals practically achieved by "swapping which bnc cable goes to which photodiode."

Even if we imagine that our 50:50 beam splitter in figure 6.7 outputs two perfect copies of the beams to the "T" and "R" photodiodes, and if we imagine polarizing them along axes at angles α_t and α_r, it is not theoretically possible to get intensities of the forms I_T and I_R above for all cases of polarizations of beams A and B. However, these theoretical cases require rather large changes in the polarization from the ideal right and left circularly polarized beams A and B, and so we have not seen them arise in practice.

THEOREM

Claim: Consider beam Σ defined as the beam formed by superimposing two arbitrary laser beams A and B represented by equations (6.26). We restrict to $\theta_a, \theta_b \in [-\pi/4, \pi/4]$ without loss of generality. If

$$|\theta_a + \theta_b| < \pi/4 \qquad \text{and} \qquad |\theta_a - \theta_b| > \pi/4. \tag{6.28}$$

then for any value ϕ_0 we can find a polarization axis α_0 such that the intensity of beam Σ becomes

$$I = c_0 + b_0 \cos(\phi - \phi_0)$$

for some $b_0 \neq 0$ after being polarized along this axis.

Proof: Consider that $\phi = (\phi - \phi_0) + \phi_0$ so that

$$\cos(\phi) = \cos(\phi_0)\cos(\phi - \phi_0) - \sin(\phi_0)\sin(\phi - \phi_0)$$

and

$$\sin(\phi) = \sin(\phi_0)\cos(\phi - \phi_0) + \cos(\phi_0)\sin(\phi - \phi_0)$$

Thus, we can write equation (6.27) for the intensity after polarization along axis α as

$$\begin{aligned} I \;\propto\; & 1 + \frac{1}{2}\cos(2\alpha - \rho)\cos(2\theta_a) + \frac{1}{2}\cos(2\alpha + \rho)\cos(2\theta_b) \\ & + \Big[\cos(\rho)\cos(\theta_a - \theta_b)\cos(\phi_0) + \sin(\rho)\sin(\theta_a + \theta_b)\sin(\phi_0) \\ & \quad + \cos(\theta_a + \theta_b)\cos(\phi_0)\cos(2\alpha) - \sin(\theta_a - \theta_b)\sin(\phi_0)\sin(2\alpha)\Big]\cos(\phi - \phi_0) \\ & + \Big[\sin(\rho)\sin(\theta_a + \theta_b)\cos(\phi_0) - \cos(\rho)\cos(\theta_a - \theta_b)\sin(\phi_0) \\ & \quad - \sin(\theta_a - \theta_b)\cos(\phi_0)\sin(2\alpha) - \cos(\theta_a + \theta_b)\sin(\phi_0)\cos(2\alpha)\Big]\sin(\phi - \phi_0) \end{aligned} \tag{6.29}$$

For equation (6.29) to take the desired form of $I = c_0 + b_0 \cos(\phi - \phi_0)$ where $b_0 \neq 0$, we need to find a value of α that satisfies the following two conditions:

Condition 1: The factor in front of $\sin(\phi - \phi_0)$ is 0

Condition 2: The factor in front of $\cos(\phi - \phi_0)$ is not also zero to ensure $b_0 \neq 0$

Satisfying condition 1 is equivalent to satisfying the equation

$$\begin{aligned}&\sin(\rho)\sin(\theta_a+\theta_b)\cos(\phi_0)-\cos(\rho)\cos(\theta_a-\theta_b)\sin(\phi_0)\\&-\ \sin(\theta_a-\theta_b)\cos(\phi_0)\sin(2\alpha)-\cos(\theta_a+\theta_b)\sin(\phi_0)\cos(2\alpha)=0\end{aligned}$$

for some value of α that we will denote α_0. This desired value α_0 will exist for a given choice of ϕ_0 if and only if[12]

$$\begin{aligned}&\Big(\sin(\rho)\sin(\theta_a+\theta_b)\cos(\phi_0)-\cos(\rho)\cos(\theta_a-\theta_b)\sin(\phi_0)\Big)^2\\&\leq\ \Big(\sin(\theta_a-\theta_b)\cos(\phi_0)\Big)^2+\Big(\cos(\theta_a+\theta_b)\sin(\phi_0)\Big)^2\end{aligned}\tag{6.30}$$

Let us now show that the inequality (6.30) indeed holds. To this end, let us first note that conditions (6.28) imply

$$\begin{aligned}&|\cos(\theta_a-\theta_b)|<\frac{1}{\sqrt{2}},\qquad|\sin(\theta_a-\theta_b)|>\frac{1}{\sqrt{2}},\\&\qquad\qquad\text{and}\\&|\cos(\theta_a+\theta_b)|>\frac{1}{\sqrt{2}},\qquad|\sin(\theta_a+\theta_b)|<\frac{1}{\sqrt{2}}\end{aligned}\tag{6.31}$$

Next, let us note that the following inequality holds for the left hand side (L.H.S.) of the inequality (6.30):

$$\begin{aligned}&\text{L.H.S of (6.30)}=\Big(\sin(\rho)\sin(\theta_a+\theta_b)\cos(\phi_0)-\cos(\rho)\cos(\theta_a-\theta_b)\sin(\phi_0)\Big)^2\\&<\ \frac{1}{2}\Big(|\sin(\rho|\,|\cos(\phi_0)|+|\cos(\rho)|\,|\sin(\phi_0)|\Big)^2=\frac{1}{2}\max\Big(\sin^2(\rho-\phi_0),\sin^2(\rho+\phi_0)\Big)\leq\frac{1}{2}\end{aligned}$$

where the first inequality follows from (6.31).

[12]Condition (6.30) follows from the fact that in general $c_1\cos(\alpha)+c_2\sin(\alpha)=\sqrt{c_1^2+c^2}\cos(\alpha-\delta)$ for $\tan(\delta)=c_2/c_1$ and that $\sqrt{c_1^2+c^2}\cos(\alpha-\delta)=L$ for some α if and only if $c_1^2+c^2\geq L^2$.

Then consider that the following holds for the right hand side (R.H.S.) of the inequality (6.30):

$$\begin{aligned}\frac{1}{2} &= \frac{1}{2}\cos^2(\phi_0) + \frac{1}{2}\sin^2(\phi_0) \\ &< \Big(\sin(\theta_a - \theta_b)\cos(\phi_0)\Big)^2 + \Big(\cos(\theta_a + \theta_b)\sin(\phi_0)\Big)^2 = \text{R.H.S of (6.30)}\end{aligned}$$

Comparing the previous two inequalities, we see that the inequality in (6.30) indeed holds. Thus, condition 1 can be satisfied for some $\alpha = \alpha_0$.

Now we turn our attention to condition 2. This condition is satisfied if for the value α_0 we have found, the intensity of beam Σ after polarization does not simply reduce to $I = c_0$ for some c_0 that is constant with respect to ϕ. Looking at equation (6.29), we see that this amounts to ensuring that the factor in front of $\cos(\phi - \phi_0)$ does not become zero for $\alpha = \alpha_0$. We will prove this by contradiction, by first assuming the opposite. That is, let us suppose that the factor on $\cos(\phi - \phi_0)$ in equation (6.29) is zero, i.e.,

$$\begin{aligned}&\cos(\rho)\cos(\theta_a - \theta_b)\cos(\phi_0) + \sin(\rho)\sin(\theta_a + \theta_b)\sin(\phi_0) \\ &+ \cos(\theta_a + \theta_b)\cos(\phi_0)\cos(2\alpha_0) - \sin(\theta_a - \theta_b)\sin(\phi_0)\sin(2\alpha_0) = 0\end{aligned} \tag{6.32}$$

At the same time, α_0 was chosen such that the factor on $\sin(\phi - \phi_0)$ in equation (6.29) is zero, i.e.,

$$\begin{aligned}&\sin(\rho)\sin(\theta_a + \theta_b)\cos(\phi_0) - \cos(\rho)\cos(\theta_a - \theta_b)\sin(\phi_0) \\ &- \sin(\theta_a - \theta_b)\cos(\phi_0)\sin(2\alpha_0) - \cos(\theta_a + \theta_b)\sin(\phi_0)\cos(2\alpha_0) = 0\end{aligned} \tag{6.33}$$

Let us consider 3 cases for the value of ϕ_0.

Case 1: $\sin(\phi_0) = 0$

In this case, equation (6.32) reduces to

$$\cos(2\alpha_0) = -\frac{\cos(\rho)\cos(\theta_a - \theta_b)}{\cos(\theta_a + \theta_b)} \tag{6.34}$$

which implies

$$|\cos(2\alpha_0)| = |\cos(\rho)|\,\frac{|\cos(\theta_a - \theta_b)|}{|\cos(\theta_a + \theta_b)|} < |\cos(\rho)| \qquad \text{or} \qquad \cos(2\alpha_0) = \cos(\rho) = 0$$

where the inequality follows from our assumptions on the values of $|\theta_a - \theta_b|$ and $|\theta_a + \theta_b|$.

Similarly, equation (6.33) reduces to

$$\sin(2\alpha_0) = \frac{\sin(\rho)\sin(\theta_a + \theta_b)}{\sin(\theta_a - \theta_b)} \tag{6.35}$$

which implies

$$|\sin(2\alpha_0)| \;=\; |\sin(\rho)|\,\frac{|\sin(\theta_a + \theta_b)|}{|\sin(\theta_a - \theta_b)|} < |\sin(\rho)| \qquad \text{or} \qquad \sin(2\alpha_0) = \sin(\rho) = 0$$

We see that equations (6.34) and (6.35) together imply a contradiction, since, if $\sin(\rho) \neq 0$ and $\cos(\rho) \neq 0$, we would need

$$|\cos(2\alpha_0)| < |\cos(\rho)| \qquad \text{and} \qquad |\sin(2\alpha_0)| < |\sin(\rho)|$$

which is impossible for any value of α_0. Likewise, if $\cos(\rho) = 0$, we would need

$$|\cos(2\alpha_0)| = 0 \qquad \text{and} \qquad |\sin(2\alpha_0)| < 1$$

which is impossible for any α_0, and if $\sin(\rho) = 0$, we would need

$$|\cos(2\alpha_0)| < 1 \qquad \text{and} \qquad |\sin(2\alpha_0)| = 0$$

which is also impossible for any α_0. If $\phi_0 = 0$, it is not possible that a value of α_0 will result in beam Σ having an intensity $I = c_0$ that is independent of ϕ as claimed.

Case 2: $\cos(\phi_0) = 0$

In this case, equation (6.32) reduces to equation (6.35) and equation (6.33) reduces to equation (6.34). So again, our assumption implies that equations (6.34) and (6.35) are simultaneously satisfied, which produces a contradiction as we saw in case 1.

Case 3: $\cos(\phi_0) \neq 0$ and $\sin(\phi_0) \neq 0$

In this final case, let us consider the following linear combinations of equation (6.32) and (6.33). First, we multiply equation (6.32) by $\cos(\phi_0)$, and we multiply equation (6.33) by $\sin(\phi_0)$. Then we can take the difference between the resulting equations to find

$$\cos(\rho)\cos(\theta_a - \theta_b)\Big(\cos^2(\phi_0) + \sin^2(\phi_0)\Big) \;+\; \cos(\theta_a + \theta_b)\cos(2\alpha_0)\Big(\cos^2(\phi_0) + \sin^2(\phi_0)\Big) \;=\; 0 \tag{6.36}$$

For second linear combination we will consider, we multiply equation (6.32) by $\sin(\phi_0)$, and we multiply equation (6.33) by $\cos(\phi_0)$. Then we can add the resulting equations to find

$$\sin(\rho)\sin(\theta_a + \theta_b)\Big(\cos^2(\phi_0) + \sin^2(\phi_0)\Big) \;-\; \sin(\theta_a - \theta_b)\sin(2\alpha_0)\Big(\cos^2(\phi_0) + \sin^2(\phi_0)\Big) \;=\; 0 \tag{6.37}$$

Of course, in both of the above two equations, we can make the replacement $\sin^2(\phi_0) + \cos^2(\phi_0) = 1$, and we readily see that equation (6.36) is the same as equation (6.34) and that equation (6.37) is the same as equation (6.35). Thus, we once again run into the contradiction of case 1.

After examining these three cases, we have ensured that the intensity can not be made independent of ϕ, which proves that condition 2 holds for all possible values of α_0. □

A Practical Corollary for Finding the Error Signal

The previous theorem is quite reassuring for our goal of creating an error signal in the setup of figure 6.7. We need only to ensure that the beams exiting the 50:50 beamsplitter have polarizations satisfying the conditions of the theorem, $|\theta_a + \theta_b| < \pi/4$ and $|\theta_a - \theta_b| > \pi/4$. Then the theorem guarantees that we can set the polarizers in front of the photodiodes at some angle so that the beam reaching photodiode "T" has the intensity $I_1 = c_1 + b_1 \cos(\phi - \phi_0)$ and the beam reaching photodiode "R" has the intensity $I_2 = c_2 + b_2 \sin(\phi - \phi_0) = c_2 + b_2 \cos(\phi - \phi_0 - \pi/2)$.

In fact, we can make the stronger statement that it is sufficient that only one of the outputs of the 50:50 beamsplitter to satisfy the conditions of the theorem assuming that the other photodiode has a signal that varies with phase.

An Edge Case of the Theorem

Finally, let us consider one practical case that is utilized in [68]. Here, a circularly polarized beam is interfered with a linearly polarized beam. Let the circularly polarized beam be beam A with $\theta_a = \pi/4$ and the linearly polarized beam be beam B with $\theta_b = 0$. This case does not satisfy the conditions of the theorem. In fact, there is one value of ϕ_0 for which there is no axis of polarization to get $I = c_0 + b_0 \cos(\phi - \phi_0)$ for $b_0 \neq 0$. In fact, it fails because $b_0 = 0$, and it corresponds to the axis of polarization that is perpendicular to the linear polarization.

Nonetheless, this is a practically useful setup, where one can use two polarization axes that are perpendicular to each other to find an error signal.

6.3.5 Deviations from Ideal Electronics Behavior

Non-ideal behavior of electrical components is also of practical concern. As can be seen from examining the ideal "T" and "R" electrical signals from the photodiodes given in equations (6.22), the difference in optical phase is encoded on the amplitudes of the the electrical signal.

We are dependent on a couple of things working properly. As already discussed, one need the factors of $M(E_A E_B)$ to actually be equal in equations (6.22), which can be addressed by variably attenuating the laser light that reaches the photodiodes. We bring this up again because one must be concerned with the possibility of the signal amplitudes being changed by the electronics. Also, one can consider attenuating the electrical signal rather than or in addition to the optical signal if one wishes.

More relevant is that the phase of the electrical signals must be correct. This cannot be fixed by changing the optical phases. Phase errors on the electrical systems can be induced by the summing element and the 90 degree phase adding element for the "R" signal. Manufacturers will typically provide these specifications. One can also induce phase error with cable delays.

We have considered making some variable phase shifting circuit. Commercial options are available, but not always with useful specifications or easy implementation. Active circuit designs can be readily found. Since in our case, we only need a very small phase shift range for correction of roughly 3 degrees or so, there seem to be plenty of options for small circuits made of resistors, capacitors, and trim potentiometers that allow some phase shift, but the design requires some consideration of impedance matching. One alternate approach is to have slightly varying RF cable lengths and tune the EOM frequency such that the cable phase delays perfectly compensate the imperfections in the electronics.

Let us calculate the consequence of a phase or amplitude difference from the ideal. We will denote the phase error by δ. With the plan of high passing the signals, we can simplify the

analysis by only considering the A.C. components of the signals. Further, let us assume that $\phi_{\text{eo}} = 0$. We can write this A.C. component of "T" signal as

$$V_{\text{T,ac}} \;=\; -a_t \sin(\phi_B - \phi_A)\sin(\Omega_{\text{eo}} t + \delta) \;=\; a_t \sin(\phi_A - \phi_B)\sin(\Omega_{\text{eo}} t + \delta)$$

and for the A.C. component of the "R" signal after 90 degree phase shift, we have

$$V_{\text{R,ac,+90°}} = a_r \cos(\phi_B - \phi_A)\cos(\Omega_{\text{eo}} t)$$

Both of the above equations follow simply from the V_T equality in equations (6.22) and equation (6.23).

These signals will be summed and fed into the mixer in figure 6.8. The mixer will be used to detect the phase ϕ_{meas} of this combined signal. Ideally, we want $\phi_{\text{meas}} = \phi_A - \phi_B$, but imperfections will cause a deviation between the measured phase and the true phase $\phi_A - \phi_B$.

The combined signal will be

$$\begin{aligned} V_{\text{mix in}} &= a_t \sin(\phi_A - \phi_B)\sin(\Omega_{\text{eo}} t + \delta) \;+\; a_r \cos(\phi_A - \phi_B)\cos(\Omega_{\text{eo}} t) \\ &= -a_t \sin(\phi_B - \phi_A)\cos(\delta)\sin(\Omega_{\text{eo}} t) \\ &\quad + \Big(a_r \cos(\phi_B - \phi_A) - a_t \sin(\phi_B - \phi_A)\sin(\delta)\Big)\cos(\Omega_{\text{eo}} t) \\ &= a_{\text{tot}} \cos(\Omega_{\text{eo}} t + \phi_{\text{meas}}) \end{aligned}$$

We see that

$$\phi_{\text{meas}} = \text{arctan2}\Big(\; a_r \cos(\phi_B - \phi_A) - a_t \sin(\phi_B - \phi_A)\sin(\delta),\;\; a_t \sin(\phi_B - \phi_A)\cos(\delta)\;\Big) \tag{6.38}$$

where arctan2 is the standard two-input arctangent function such that $\phi = \text{arctan2}(x, y)$ solves

for the angle ϕ that satisfies

$$\tan(\phi) = y/x, \quad \sin(\phi) = \frac{y}{\sqrt{x^2+y^2}}, \quad \text{and} \quad \cos(\phi) = \frac{x}{\sqrt{x^2+y^2}}$$

Generally, error of the measured phase given by $\phi_{\text{err}} = \phi_{\text{meas}} - (\phi_B - \phi_A)$ is not intuitively clear from equation (6.38). We will note that from plotting ϕ_{err} as a function of $(\phi_B - \phi_A)$, one can observe that a mismatch of the signal amplitudes by $a_t/a_r = 1.1$ at $\delta = 0$ causes a phase error that varies roughly sinusoidally with $(\phi_B - \phi_A)$, where the absolute value of the max error is roughly 2.5 degrees. If instead $a_t = a_r$, one can observe that there is no phase error for $(\phi_B - \phi_A) = 0$ or π, and a maximum phase error given by $\phi_{\text{err}} = \delta$ at $(\phi_B - \phi_A) = \pi/2$ or $3\pi/2$.[13]

[13]We sketch a reasonably clean geometric proof here. We can consider finding the output of arctan2 as equivalent to solving for the angle of the vector $x\hat{\mathbf{x}} + y\hat{\mathbf{y}}$. The vector whose angle we wish to find can be written as $\mathbf{v} = \cos(\phi_B - \phi_A)\hat{\mathbf{e}}_1 + \sin(\phi_B - \phi_A)\hat{\mathbf{e}}_2$. In the case of no error ($\phi_{\text{meas}} = \phi_B - \phi_A$), we have $\hat{\mathbf{e}}_1 = \hat{\mathbf{x}}$ and $\hat{\mathbf{e}}_2 = \hat{\mathbf{y}}$. For nonzero δ, ϕ_{meas} is found from getting the angle with $\hat{\mathbf{e}}_1 = \hat{\mathbf{x}}$ and $\hat{\mathbf{e}}_2 = -\sin(\delta)\hat{\mathbf{x}} + \cos(\delta)\hat{\mathbf{y}}$. And to get $\phi_{\text{err}} = \delta$, i.e. $\phi_{\text{meas}} = (\phi_B - \phi_A) + \delta$, we would have $\hat{\mathbf{e}}_1 = \cos(\delta)\hat{\mathbf{x}} + \sin(\delta)\hat{\mathbf{y}}$ and $\hat{\mathbf{e}}_2 = -\sin(\delta)\hat{\mathbf{x}} + \cos(\delta)\hat{\mathbf{y}}$. Since $|\hat{\mathbf{e}}_1| = 1$ and $|\hat{\mathbf{e}}_2| = 1$, we see that by constructing the vectors ϕ_{meas} for the case of interest will lie in the range $[(\phi_B - \phi_A), (\phi_B - \phi_A) + \delta]$, with the extreme values taken when $\sin(\phi_B - \phi_A) = 0$ or $\cos(\phi_B - \phi_A) = 0$.

Appendix A

Augmentation and Documentation to Maximally Localized Generalized Wannier States Code

A.1 Introduction

Walters et al. developed a valuable tool for MATLAB that enables straightforward determination of the Wannier states of optical lattices [72]. It is similar to Wannier90 used in the condensed matter physics and material science communities, but specialized for atomic physicists using optical lattices. The tool makes for convenient specification of an optical lattice in terms of its Fourier transform coefficients and generates as outputs the Wannier states and Hubbard model parameters for the lattice. We have found that this implementation works well for lattices with inversion symmetry, but we have also found that the correct Wannier states are often not found in cases where the lattice lacks inversion symmetry or has multiple sites per unit cell in many cases.

In this appendix, we will discuss edits made to the code implementation from [72]. The

code in this edited form works exclusively for 2D lattices and it enables calculation of Wannier states when there is no inversion symmetry and when there are multiple sites per unit cell. Similar straightforward edits could used to allow for analogous implementation in 3D and 1D if need be.

In the algorithm for finding the maximally localized Wannier states $|w_{n\mathbf{R}}\rangle$, a set of unitary matrices $\{U_{\mathbf{q}}\}$ with one matrix for each quasimomentum $\mathbf{q}$ is found by gradient descent methods [73, 74]. These $U_{\mathbf{q}}$ determine a change of basis for the set of bloch states $\{\psi_j^{\mathbf{q}}\}$ with band j and quasimomentum $\mathbf{q}$. The maximally localized Wannier states $|w_{n\mathbf{R}}\rangle$ are then given by[1]

$$|w_{n\mathbf{R}}\rangle = V \int_{\mathrm{BZ}} \frac{d\mathbf{q}}{(2\pi)^3} e^{-i\mathbf{q}\cdot\mathbf{R}} \sum_{j=1}^{J} |\psi_j^{\mathbf{q}}\rangle \, (U_{\mathbf{q}})_{jn} \tag{A.1}$$

The integral is over the quasimomentum vectors $\mathbf{q}$ in the brillouin zone and J is the number of bands. $|w_{n\mathbf{R}}\rangle$ denotes the Wannier state centered on site $\mathbf{R}$. The index n roughly indicates the Wannier states for band n, but technically n is a more general index in the case that multiple bands are close enough in energy that it is physically justified to combine states from multiple bands to generate Wannier states. Strictly speaking, n only indicates the Wannier states for band n in the case that each matrix $U_{\mathbf{q}}$ is diagonal, i.e., when there is no mixing between bands. In this special case that $U_{\mathbf{q}}$ is diagonal, it may also be helpful to note that we are simply redefining the bloch basis by adding a phase factor to each of the states in the bloch basis,

[1] A note here on a dissonant conventions set by the authors [72]. Here equation (A.1) is formally very similar to a Fourier transform using the convention

$$\psi(\mathbf{r}) = \frac{1}{(2\pi)^D} \int d\mathbf{k} \, \phi(\mathbf{k})$$

where $\psi(\mathbf{r})$ is the real space wavefunction, and $\phi(\mathbf{k})$ is its fourier transform. I believe this convention is used so that both $|w_{n\mathbf{R}}\rangle$ and $|\psi_j^{\mathbf{q}}\rangle$ are properly normalized. However, the actual fourier transform convention for wavefunctions used later by [72] opts for a differing fourier transform normalization convention given by

$$\psi(\mathbf{r}) = \frac{1}{(2\pi)^{D/2}} \int d\mathbf{k} \, \tilde{\phi}(\mathbf{k})$$

We just wanted to point this out

which are relevant for the integral over states in the brillouin zone.

The bulk of the change is to initialize the algorithm by providing an improved initial guess for $\{U_{\mathbf{q}}\}$ using the method described in [73] (Section IV, subsection D, under "1. Algorithm") and more recently in section 2.3 of [74]. We make a harmonic potential approximation of the lattice near each local minimum of the potential in a unit cell, and we construct a set of guess states $\{|g_l\rangle\}$ from the quantum harmonic oscillator states for each of the approximate harmonic potentials. The choice of guess state(s) to use to initialize each band (or set of mixed bands) is made by calculating the norms of the projections of each guess state onto the set of states in the band(s). We use the guess state with the largest norm after projection, with the caveat that a guess state $|g_l\rangle$ can only be used for initializing one Wannier state index n.

After the initial guess for $\{U_{\mathbf{q}}\}$ is made, the gradient descent algorithm is run almost exactly as written by Walters et al. save for the following key changes. Firstly, their algorithm was written with a step that initializes $\{U_{\mathbf{q}}\}$ assuming that the lattice has inversion symmetry. This step has been removed. Secondly, we removed a step where $\{U_{\mathbf{q}}\}$ was transformed so that an approximate Wannier state was translated back to a central site. Our understanding is that this line assumed that there was only one local minimum per unit cell, and it does not function properly when this is not the case. Lastly, we disabled the disentanglement algorithm based on [75]. We found that for the cases we tried, this algorithm seemed to take the Wannier state from an expected form with near minimal Ω values to states that were clearly incorrect with large Ω values. However, it is likely that this algorithm is vital in the type of lattices with entangled bands that we did not test.

In the following sections, we will describe in detail how the initialization steps were implemented.

A.2 Determination of Local Minima

Before initialization, we determine where the local minima of the lattice potential are within a unit cell. In code, this is done by the function `findPotentialLocalMinima`. This function finds the coordinates of each of the local minima and fits a small square grid of sample points to a general 2D quadratic function.

A.2.1 The Preferred Unit Cell

To search for local minima, the program will first sample the unit cell with a rectangular grid of points. It will then calculate a numerical approximation of the gradient of the potential at every point on the grid. Next, it checks the 100 points with the shallowest slope (smallest norm of the gradient vector) to see if they are the minimum among the neighboring points.

With this in mind, it would be ideal if the unit cell were a rectangle with sides parallel to the $\hat{\mathbf{x}}$ and $\hat{\mathbf{y}}$ direction so as to efficiently sample it with a rectangular grid of points. In 2D, one can always choose a rectangular unit cell, but in general, these rectangular unit cells do not have sides that are parallel to the $\hat{\mathbf{x}}$ and $\hat{\mathbf{y}}$ direction. One could rotate coordinates to take advantage of the rectangular unit cell, but we felt the benefit was not worth the effort of implementation. Without rotation, one can still choose the unit cell to be a parallelogram with one of the sides parallel to the $\hat{\mathbf{x}}$ or $\hat{\mathbf{y}}$ and the other not. In the case that one of the primitive lattice vectors is parallel to either the $\hat{\mathbf{x}}$ or $\hat{\mathbf{y}}$ direction, then the ideal rectangular unit cell can be found.

A.2.2 Case of Rectangular Primitive Cell

Let the two primitive vectors of the lattice be $\mathbf{a}_1$ and $\mathbf{a}_2$ and denote $\mathbf{a}_i = a_{i,x}\hat{\mathbf{x}} + a_{i,y}\hat{\mathbf{y}}$. In the case that one of the primitive lattice vectors is along the $\hat{\mathbf{x}}$ or $\hat{\mathbf{y}}$ direction, say $\mathbf{a}_i = a_i\hat{\mathbf{x}}$, we can

take the unit cell to be the rectangle with vertices

$$(0,0),\ \ (a_{i,x},0),\ \ (0,a_{(i+1),y}),\ \ \text{and}\ \ (a_{i,x},a_{(i+1),y})$$

and in the alternate case that $\mathbf{a}_i = a_i\hat{\mathbf{y}}$, we have

$$(0,0),\ \ (a_{(i+1),x},0),\ \ (0,a_{i,y}),\ \ \text{and}\ \ (a_{(i+1),x},a_{i,y})$$

Here and elsewhere, $\mathbf{a}_3 \equiv \mathbf{a}_1$.

In practice, we will opt to center the unit cell on the origin, and instead use the unit cell with vertices

$$\left(\frac{-a_{i,x}}{2},\frac{-a_{i+1,y}}{2}\right),\ \left(\frac{-a_{i,x}}{2},\frac{a_{i+1,y}}{2}\right),\ \left(\frac{a_{i,x}}{2},\frac{-a_{i+1,y}}{2}\right)\ \text{and}\ \left(\frac{a_{i,x}}{2},\frac{a_{i+1,y}}{2}\right)$$

and for $\mathbf{a}_i = a_i\hat{\mathbf{y}}$, we take

$$\left(\frac{-a_{(i+1),x}}{2},\frac{-a_{i,y}}{2}\right),\ \left(\frac{a_{(i+1),x}}{2},\frac{-a_{i,y}}{2}\right)\ \left(\frac{-a_{(i+1),x}}{2},\frac{a_{i,y}}{2}\right),\ \text{and}\ \left(\frac{a_{(i+1),x}}{2},\frac{a_{i,y}}{2}\right)$$

In the algorithm, an initial check is done to see if one of these rectangular unit cells is an option.

A.2.3 All Other Cases

In all other cases, there are four options of unit cell that have two sides parallel to $\hat{\mathbf{x}}$ or $\hat{\mathbf{y}}$:

1. Two sides parallel to $\mathbf{a}_1$ with magnitude $|\mathbf{a}_1|$. The remaining two sides parallel to $\hat{\mathbf{x}}$.

2. Two sides parallel to $\mathbf{a}_2$ with magnitude $|\mathbf{a}_2|$. The remaining two sides parallel to $\hat{\mathbf{x}}$.

3. Two sides parallel to $\mathbf{a}_1$ with magnitude $|\mathbf{a}_1|$. The remaining two sides parallel to $\hat{\mathbf{y}}$.

4. Two sides parallel to $\mathbf{a}_2$ with magnitude $|\mathbf{a}_2|$. The remaining two sides parallel to $\hat{\mathbf{y}}$.

In all cases, the length of the side parallel to $\hat{\mathbf{x}}$ or $\hat{\mathbf{y}}$ is such that the area of the unit cell is $|\mathbf{a}_1 \times \mathbf{a}_2|$.

For cases 1 and 2, the unit cell can be taken to be the parallelogram with vertices

$$(0,0),\ \ (a_{i,x}, a_{i,y}),\ \ (d_x, 0),\ \ \text{and}\ \ (d_x + a_{i,x}, a_{i,y})$$

where $\mathbf{a}_i$ is the primitive lattice vector that is parallel to two sides of the unit cell, and

$$d_x \equiv a_{(i+1),x} - \frac{a_{(i+1),y}}{a_{i,y}}\, a_{i,x}$$

Again, $\mathbf{a}_3 \equiv \mathbf{a}_1$.

However, we will instead translate the unit cell to be centered on the origin, giving a parallelogram with the vertices

$$\left(\frac{-d_x - a_{i,x}}{2}, \frac{-a_{i,y}}{2}\right),\ \left(\frac{-d_x + a_{i,x}}{2}, \frac{a_{i,y}}{2}\right),\ \left(\frac{d_x - a_{i,x}}{2}, \frac{-a_{i,y}}{2}\right),\ \text{and}\ \left(\frac{d_x + a_{i,x}}{2}, \frac{a_{i,y}}{2}\right)$$

Similarly, for options 3 and 4, we can define the unit cell by

$$(0,0),\ \ (a_{i,x}, a_{i,y}),\ \ (0, d_y),\ \ \text{and}\ \ (a_{i,x}, d_y + a_{i,y})$$

where

$$d_y \equiv a_{(i+1),y} - \frac{a_{(i+1),x}}{a_{i,x}}\, a_{i,y}$$

Translating the unit cell to be centered on the origin gives vertices

$$\left(\frac{-a_{i,x}}{2}, \frac{-d_y - a_{i,y}}{2}\right),\ \left(\frac{a_{i,x}}{2}, \frac{-d_y + a_{i,y}}{2}\right),\ \left(\frac{-a_{i,x}}{2}, \frac{d_y - a_{i,y}}{2}\right),\ \text{and}\ \left(\frac{a_{i,x}}{2}, \frac{d_y + a_{i,y}}{2}\right)$$

We would like to pick the unit cell option in light of the following considerations.

1. We will inscribe the unit cell with a rectangle of sample points that has sides parallel to $\hat{\mathbf{x}}$ and $\hat{\mathbf{y}}$ directions. We would like the rectangle to have the smallest area possible.

2. Secondarily, we would like the chosen unit cell to be "small" in the sense that the local minima in the unit cell as close as possible. (Otherwise, it will require translation by a lattice vector to make them adjacent.) To be concrete, we mean that we would like the longer diagonal of the unit cell to be as small as possible.

To satisfy the first preference, we will choose the vector $\mathbf{a}_i$ such that $\left|a_{i,x}a_{i,y}\right| \leq \left|a_{(i+1),x}a_{(i+1),y}\right|$

Two options then remain. If we take two of the sides to be parallel to the x axis, then the length of the long diagonal of the unit cell is given by

$$\sqrt{\left|a_{i,y}\right|^2 + \left(\left|a_{i,x}\right| + \left|d_x\right|\right)^2} = \sqrt{\left|a_{i,x}\right|^2 + \left|a_{i,y}\right|^2 + \frac{A}{\left|a_{i,y}\right|}\left(\frac{A}{\left|a_{i,y}\right|} + \left|a_{i,x}\right|\right)} \tag{A.2}$$

where $A = \left|d_x a_{i,y}\right|$ is the area of the unit cell.

If instead we take two of the sides to be parallel to the y axis, the length of the long diagonal of the unit cell is given by

$$\sqrt{\left|a_{i,x}\right|^2 + \left(\left|a_{i,y}\right| + \left|d_y\right|\right)^2} = \sqrt{\left|a_{i,x}\right|^2 + \left|a_{i,y}\right|^2 + \frac{A}{\left|a_{i,x}\right|}\left(\frac{A}{\left|a_{i,x}\right|} + \left|a_{i,y}\right|\right)} \tag{A.3}$$

where $A = \left|d_y a_{i,x}\right|$ is the area of the unit cell.

To satisfy the second preference we want to choose the unit cell with the shorter long diagonal. Comparing equation (A.2) and (A.3), we see that we can satisfy this by setting sides parallel to the x axis if $\left|a_{i,y}\right| > \left|a_{i,x}\right|$ and taking the sides parallel to the y axis if $\left|a_{i,y}\right| < \left|a_{i,x}\right|$.

A.2.4 Masking the Appropriate Region

Lastly, since we have sampled the rectangle that inscribes the unit cell, we will define a boolean mask to only check for local minima within the unit cell. This mask will basically "cut away" the excess sample points that are outside of the unit cell.

To do this, we will check 4 conditions. Let $\mathbf{v}_1$ and $\mathbf{v}_4$ represent opposite vertices of the parallelogram unit cell. Let $\mathbf{v}_2$ and $\mathbf{v}_3$ represent the other two vertices. We can define the directions parallel to each of the sides by the vectors

$$\mathbf{t}_1 = \mathbf{v}_2 - \mathbf{v}_1, \quad \mathbf{t}_2 = \mathbf{v}_3 - \mathbf{v}_1, \quad \mathbf{t}_3 = \mathbf{v}_2 - \mathbf{v}_4, \quad \text{and} \quad \mathbf{t}_4 = \mathbf{v}_3 - \mathbf{v}_4$$

Similarly, we can define a direction normal to each of the sides of the parallelograms by

$$\mathbf{n}_i = \begin{bmatrix} 0 & -1 \\ 1 & 0 \end{bmatrix} \mathbf{t}_i$$

Using the fact that $\mathbf{0}$ is on the interior of the unit cell parallelogram, we can determine that a point $\mathbf{r}$ is on the interior of the parallelogram, if and only if it satisfies all of the following conditions:

$$\text{sign}((\mathbf{r} - \mathbf{v}_1) \cdot \mathbf{n}_1) = \text{sign}((\mathbf{0} - \mathbf{v}_1) \cdot \mathbf{n}_1)$$

$$\text{sign}((\mathbf{r} - \mathbf{v}_1) \cdot \mathbf{n}_2) = \text{sign}((\mathbf{0} - \mathbf{v}_1) \cdot \mathbf{n}_2)$$

$$\text{sign}((\mathbf{r} - \mathbf{v}_4) \cdot \mathbf{n}_3) = \text{sign}((\mathbf{0} - \mathbf{v}_4) \cdot \mathbf{n}_3)$$

$$\text{sign}((\mathbf{r} - \mathbf{v}_4) \cdot \mathbf{n}_4) = \text{sign}((\mathbf{0} - \mathbf{v}_4) \cdot \mathbf{n}_4)$$

To check which points of the grid are in the unit cell, we require that it either satisfy the above conditions or be on one of two adjacent boundaries. We therefore change the condition

to be

$$\text{sign}((\mathbf{r}-\mathbf{v}_1)\cdot\mathbf{n}_1) = \Big(\text{sign}((\mathbf{0}-\mathbf{v}_1)\cdot\mathbf{n}_1) \text{ or } 0\Big)$$

$$\text{sign}((\mathbf{r}-\mathbf{v}_1)\cdot\mathbf{n}_2) = \Big(\text{sign}((\mathbf{0}-\mathbf{v}_1)\cdot\mathbf{n}_2) \text{ or } 0\Big)$$

$$\text{sign}((\mathbf{r}-\mathbf{v}_4)\cdot\mathbf{n}_3) = \text{sign}((\mathbf{0}-\mathbf{v}_4)\cdot\mathbf{n}_3)$$

$$\text{sign}((\mathbf{r}-\mathbf{v}_4)\cdot\mathbf{n}_4) = \text{sign}((\mathbf{0}-\mathbf{v}_4)\cdot\mathbf{n}_4)$$

As a code example, the first condition as an example will be implemented as

```
C1 = (sign((X-v1x)*n1x + (Y-v1y)*n1y) == sign(-v1x*n1x -v1y*n1y))
     | (sign((X-v1x)*n1x + (Y-v1y)*n1y) == 0)
```

where $\mathbf{v}_1 = (\texttt{v1x})\,\hat{\mathbf{x}} + (\texttt{v1y})\,\hat{\mathbf{y}}$ and $\mathbf{n}_1 = (\texttt{n1x})\,\hat{\mathbf{x}} + (\texttt{n1y})\,\hat{\mathbf{y}}$.

Likewise, generating similar conditions for the others, we can find the mask condition with the line

```
Mask = C1&C2&C3&C4
```

A.3 Quadratic Approximation of the Local Minima

This section will discuss how the local minima of the unit cell are determined and how they are fit to a quadratic approximation.

A.3.1 Gridding the Unit Cell

Having now identified a preferred unit cell that is centered on the origin we will describe how the grid of points chosen and how the gradient on those data points is calculated.

Let the rectangle that inscribes the unit cell have dimensions d_x by d_y. We would like to sample in this region on an approximately square grid with total points N. The number of points in each direction will be N_x and N_y, and we have $N_x N_y = N$. To get a roughly square grid, we want $d_x/d_y \approx N_x/N_y$. In the ideal case, we would have

$$\frac{N_x}{N_y} = \frac{N_x^2}{N} = \frac{d_x}{d_y} \qquad \Longrightarrow \qquad N_x = \sqrt{\frac{N d_x}{d_y}}$$

Since N_x and N_y must be integers, we will actually take

$$N_x = 2\,\mathrm{ceil}\left(\frac{1}{2}\sqrt{\frac{N d_x}{d_y}}\right) + 1$$

to ensure that N_x is an odd integer.

This will set the point spacing along the x direction to be $\delta_x = d_x/N_x$.

We will then set N_y using the formula

$$N_y = 2\,\mathrm{ceil}\left(\frac{1}{2}\frac{d_y}{d_x}N_x\right) + 1$$

to get a point spacing $\delta_y = d_y/N_y$.

Note that as an input we are providing N, but the output will give us N_x and N_y that satisfy $N_x N_y \gtrsim N$.

We can then set the sampled x points to be

$$\texttt{xpoints} = -\left(\frac{N_x+1}{2}\right)\delta_x : \delta_x : \left(\frac{N_x+1}{2}\right)\delta_x$$

This produces $N_x + 2$ data points. We do this to sample outside of the boundary by $\delta_x/2$ just to get an accurate gradient calculation at the edges. We will later then only consider the gradient at the points `xpoints(2:`N_x+1`)` corresponding to the points between $-\left(\frac{N_x-1}{2}\right)\delta_x$ and $\left(\frac{N_x-1}{2}\right)\delta_x$

spaced by δ_x.

We will use an almost identical setup for the y data points with

$$\texttt{ypoints} = -\left(\frac{N_y+1}{2}\right)\delta_y : \delta_y : \left(\frac{N_y+1}{2}\right)\delta_y$$

We can then use `meshgrid` in MATLAB to form the matrix grid of x and y values with

```
[X,Y] = meshgrid(xpoints,ypoints)
```

We will then further define a sampling of the potential `F` by

$$\texttt{F} = f\texttt{(X,Y)}$$

where $f(x, y)$ defines the lattice potential as a function of space.

We can then calculate the gradient of f on the sampling of points using

$$\texttt{[dFx,dFy] = gradient(F,}\delta_x\texttt{,}\delta_y\texttt{)}$$

We can then calculate the norm of the gradient at each of the points `normdF` which is simply identified with

```
normdF = sqrt(dFx.^2 + dFy.^2 )
```

A.3.2 Finding the Local Minima

To find the local minima we first get the 100 sampled points with the smallest values `normdF`. We check these points starting with the smallest `normdF` value and working up. To check if a point is a local minimum, we see if it has the minimum value of the potential among its 8 nearest neighbors on the rectangular grid. If it has the minimum value, we then at it to a

list of approximate local minima if it is not the neighbor of a point that is already on the list of approximate local minima (or a neighbor after translation by a lattice vector). We check the neighbors in case the sampling is such that multiple neighboring sample points have the same value.

A.3.3 Fitting the Local Minima to a Quadratic Approximation

To determine the quadratic approximation of the potential around each local minimum, a square grid of side length $\lambda/10$ of points around the approximate minimum is generated, where λ is the laser wavelength used to create the optical lattice. These points are fit by least squares to the quadratic model

$$V(x, y) = a_1 x^2 + a_2 xy + a_3 y^2 + a_4 x + a_5 y + a_6 \tag{A.4}$$

This is done in the usual fashion of least squares by writing

$$\mathbf{a} = \begin{bmatrix} a_1 \\ a_2 \\ a_3 \\ a_4 \\ a_5 \\ a_6 \end{bmatrix}, \qquad \mathbf{X} = \begin{bmatrix} \ddots & & \vdots & \vdots & & \\ x_i^2 & x_i y_i & y_i^2 & x_i & y_i & 1 \\ & & \vdots & \vdots & & \ddots \end{bmatrix}, \qquad \mathbf{v} = \begin{bmatrix} \vdots \\ V_i \\ \vdots \end{bmatrix}$$

Then each row would satisfy equation (A.4) if

$$\mathbf{v} = \mathbf{X}\mathbf{a}$$

and the minimum sum of the squared error is given by

$$\mathbf{X}^T\mathbf{X}\mathbf{a} = \mathbf{X}^T\mathbf{v}$$

In MATLAB, this is best solved by using the "\" operation:

$$\mathbf{a} = \mathbf{X}^T\mathbf{X}\backslash\mathbf{X}^T\mathbf{v}$$

The parameters a_i for each minimum location are returned as `quadFitParams`. The best fit minimum location is calculated by solving $\nabla V(x, y) = \mathbf{0}$ for $V(x, y)$ given in equation (A.4). It is a simple calculation to see that the minimum point (x_0, y_0) is determined by solving

$$\begin{bmatrix} 2a_1 & a_2 \\ a_2 & 2a_3 \end{bmatrix}\begin{bmatrix} x_0 \\ y_0 \end{bmatrix} = \begin{bmatrix} -a_4 \\ -a_5 \end{bmatrix}$$

which we have MATLAB solve for each local minimum. We return the set of found local minima in the matrix `potentialMinimaLocs`.

Lastly, we note that equation (A.4) can be rewritten in the form

$$V(x, y) = a_1(x - x_0)^2 + a_2(x - x_0)(y - y_0) + a_3(y - y_0)^2 + V_0 \tag{A.5}$$

where the values a_1, a_2, and a_3 are the same as in equation (A.4), x_0 and y_0 are the calculated coordinates of the minima, and

$$V_0 = a_6 - a_1x_0^2 - a_2x_0y_0 - a_3y_0^2$$

A.4 Approximate Wannier Function Guess States

Having found a quadratic form approximation to the wells in the the previous section, we will now use the eigenstates of those approximate wells for our initialization state. These eigenstates are simple harmonic oscillator states. We will express these states in fourier space because this will make the initialization calculations simpler computationally.

A.4.1 Harmonic Oscillator States in k-space

As is the common convention for optical lattices, the program considers the Hamiltonian in units of the recoil energy $E_R = \frac{h^2}{2\mu\lambda^2}$ where the position is in units of the laser wavelength λ and μ is the mass of the atom. The Hamiltonian is thus

$$H = -\frac{1}{(2\pi)^2}\frac{\partial^2}{\partial x^2} - \frac{1}{(2\pi)^2}\frac{\partial^2}{\partial y^2} + V(x,y) = \frac{\mathbf{k}^2}{(2\pi)^2} + V(x,y)$$

where the operator $\mathbf{k} = k_x\hat{\mathbf{x}} + k_y\hat{\mathbf{y}}$ satisfies $k_x = -i\frac{\partial}{\partial x}$ and $k_y = -i\frac{\partial}{\partial y}$. $\mathbf{k}$ is in units of $1/\lambda$.[2]

We will suppose that we have chosen the coordinates x and y such that $V(x,y)$ can be expanded as

$$V(x,y) \approx V_0 + b_1x^2 + b_3y^2 = V_0 - b_1\frac{\partial^2}{\partial k_x^2} - b_3\frac{\partial^2}{\partial k_y^2} \tag{A.6}$$

In this approximation,

$$H = -b_1\frac{\partial^2}{\partial k_x^2} - b_3\frac{\partial^2}{\partial k_y^2} + \frac{\mathbf{k}^2}{(2\pi)^2} + V_0$$

However, let us consider the Hamiltonian H' that differs from H by the energy minimum V_0. This will not change the eigenstates, and we will easily get the eigenvalues of H from those

[2]Take heed that this differs from the other common convention in which $\mathbf{k}$ is given in units of $2\pi/\lambda$ and x, y are given in units of $\lambda/2\pi$. The forms are similar but factors of 2π appear in various locations.

of H' by adding back the energy V_0.

$$H' \equiv H - V_0 = -b_1 \frac{\partial^2}{\partial k_x^2} - b_3 \frac{\partial^2}{\partial k_y^2} + \frac{\mathbf{k}^2}{(2\pi)^2}$$

We can easily apply separation of variables to H' to get the eigenstates. That is, we will solve for

$$H' \Phi_x(x)\Phi_y(y) = E\Phi_x(x)\Phi_y(y)$$

Considering just the k_x equation

$$\left(-b_1 \frac{\partial^2}{\partial k_x^2} + \frac{k_x^2}{(2\pi)^2}\right)\Phi_x = E_x \Phi_x$$

We will do one more change of variables using $k_x = \sqrt{(2\pi)}\, b_1^{1/4}\, \xi$ to get

$$\left(-\frac{\sqrt{b_1}}{2\pi}\frac{\partial^2}{\partial \xi^2} + \frac{\sqrt{b_1}}{2\pi}\xi^2\right)\Phi_x = E_x \Phi_x$$

so that we can write the eigenstate problem as

$$\left(-\frac{\partial^2}{\partial \xi^2} + \xi^2\right)\Phi_x = \frac{2\pi E_x}{\sqrt{b_1}}\Phi_x$$

This is the equation found for the 1D harmonic oscillator equation and the solution is easily found in and introductory quantum textbook, e.g., [76] equation [2.72]. The solutions are

$$\Phi_{x,m}(\xi) = \left(\frac{1}{\pi}\right)^{1/4} \frac{1}{\sqrt{2^m\, m!}} H_m(\xi) e^{-\xi^2/2}$$

normalized to

$$\int_{-\infty}^{\infty} \Phi^*_{x,m}(\xi)\Phi_{x,m}(\xi)\, d\xi = 1$$

with energies

$$\frac{2\pi E_{x,m}}{\sqrt{b_1}} = 2m + 1 \qquad \Longrightarrow \qquad E_{x,m} = \frac{\sqrt{b_1}}{2\pi}(2m + 1)$$

for $m \in \{0, 1, 2, 3, \dots\}$.

And finally, we can change the variable back k_x to get[3]

$$\Phi_{x,m}(k_x) \;=\; h_{m,b_1}(k_x) \;\equiv\; \left(\frac{1}{2\pi^2\sqrt{b_1}}\right)^{1/4} \frac{1}{\sqrt{2^m\, m!}} H_m\left(\frac{k_x}{\sqrt{2\pi}\, b_1^{1/4}}\right) e^{-k_x^2/(4\pi\sqrt{b_1})} \tag{A.7}$$

The full solution is thus

$$\Phi_{m,p}(k_x, k_y) = \Phi_{x,m}(k_x)\Phi_{y,p}(k_y) = h_{m,b_1}(k_x)\, h_{p,b_3}(k_y) \tag{A.8}$$

with energy

$$E_{m,p} = \frac{\sqrt{b_1}}{2\pi}\Big(2n + 1\Big) + \frac{\sqrt{b_3}}{2\pi}\Big(2p + 1\Big) + V_0 \tag{A.9}$$

for $m, p \in \{0, 1, 2, 3, \dots\}$.

A.4.2 Constructing Guess States in k-space

As we found in section A.3, we will have an approximate local potential of the form of equation (A.5):

$$V(x, y) = a_1(x - x_0)^2 + a_2(x - x_0)(y - y_0) + a_3(y - y_0)^2 + V_0$$

Defining $x' \equiv x - x_0$ and $y' \equiv y - y_0$, we have

$$V(x', y') = a_1 x'^2 + a_2 x' y' + a_3 y'^2 + V_0$$

[3]Note that we abuse notation here in the usual way: $\Phi_{x,n}(\xi)$ is technically a different function than $\Phi_{x,n}(k_x)$, but we still use $\Phi_{x,n}$ to represent the function in both case because it is describing the same physical wavefunction.

This differs from the approximation in equation (A.6) by the cross term $a_2 x' y'$, so to use the results of section A.4.1, we will want to make a change of variables.

We can consider the first three terms as a quadratic form and solve an eigenvalue problem to allow for separation of variables:

$$\mathbf{r}'^T A \mathbf{r}' = \begin{bmatrix} x' & y' \end{bmatrix} \begin{bmatrix} a_1 & a_2/2 \\ a_2/2 & a_3 \end{bmatrix} \begin{bmatrix} x' \\ y' \end{bmatrix} = \begin{bmatrix} x' & y' \end{bmatrix} R \begin{bmatrix} \lambda_1 & 0 \\ 0 & \lambda_2 \end{bmatrix} R^T \begin{bmatrix} x' \\ y' \end{bmatrix}$$

where R is a rotation matrix that satisfies $R^T R = I = R R^T$, and we have

$$R = \begin{bmatrix} \hat{\mathbf{v}}_1 & \hat{\mathbf{v}}_2 \end{bmatrix}$$

where $\mathbf{v}_i$ are the eigenvectors satisfying $A\hat{\mathbf{v}}_i = \lambda_i \hat{\mathbf{v}}_i$ and $\hat{\mathbf{v}}_i \cdot \hat{\mathbf{v}}_i = 1$.

Doing one more change of variables, we can write

$$\begin{bmatrix} \bar{x} \\ \bar{y} \end{bmatrix} = R^T \begin{bmatrix} x' \\ y' \end{bmatrix} \tag{A.10}$$

or equivalently, $\bar{x} = \hat{\mathbf{v}}_1 \cdot \mathbf{r}'$ and $\bar{y} = \hat{\mathbf{v}}_2 \cdot \mathbf{r}'$. And finally, we can write

$$V(\bar{x}, \bar{y}) = \lambda_1 \bar{x}^2 + \lambda_2 \bar{y}^2 + V_0$$

and we can write $b_1 \equiv \lambda_1$ and $b_3 \equiv \lambda_2$ which matches the desired form of equation (A.6).

We now turn to fourier space. From the considerations in section A.4.1, we know that the eigenstates in $(\bar{x}, \bar{y})$ coordinates can be taken to be product states. These product states are given by equations (A.8) and (A.7) using. Specifically, we can write the position space wave function as

$$\bar{\Psi}_{m,p}(\bar{x}, \bar{y}) = \frac{1}{2\pi} \iint h_{m,b_1}(\bar{k}_x) h_{p,b_3}(\bar{k}_y)\, e^{i\bar{\mathbf{k}}\cdot\bar{\mathbf{r}}}\, d\bar{k}_x\, d\bar{k}_y \tag{A.11}$$

where

$$\bar{\mathbf{k}} \equiv \begin{bmatrix} \bar{k}_x \\ \\ \bar{k}_y \end{bmatrix} \qquad \bar{\mathbf{r}} \equiv \begin{bmatrix} \bar{x} \\ \\ \bar{y} \end{bmatrix}$$

The energy of the eigenstate in (A.11) is given by

$$E_{m,p} = \frac{\sqrt{b_1}}{2\pi}\Big(2n+1\Big) + \frac{\sqrt{b_3}}{2\pi}\Big(2p+1\Big) + V_0$$

We can then transform to the $\mathbf{r}'$ coordinates by replacing $\bar{\mathbf{r}}$ with $R^T\mathbf{r}'$ using equation (A.10), and carry out a change of variables on the integral in equation (A.11). This gives

$$\begin{aligned}
\bar{\Psi}_{m,p}(\bar{x},\bar{y}) &= \frac{1}{2\pi}\iint h_{m,b_1}(\bar{k}_x) h_{p,b_3}(\bar{k}_y)\; e^{i\bar{\mathbf{k}}\cdot\bar{\mathbf{r}}}\, d\bar{k}_x\, d\bar{k}_y \\
&= \frac{1}{2\pi}\iint h_{m,b_1}(\bar{k}_x(\mathbf{k}')) h_{p,b_3}(\bar{k}_y(\mathbf{k}'))\; e^{i\mathbf{k}'\cdot\mathbf{r}'}\; \left|R^T\right| dk'_x\, dk'_y \\
&= \frac{1}{2\pi}\iint h_{m,b_1}(\bar{k}_x(\mathbf{k}')) h_{p,b_3}(\bar{k}_y(\mathbf{k}'))\; e^{i\mathbf{k}'\cdot\mathbf{r}'}\, dk'_x\, dk'_y \\
&= \Psi'_{m,p}(x',y')
\end{aligned} \tag{A.12}$$

where we have used

$$\bar{\mathbf{k}}\cdot\bar{\mathbf{r}} = \bar{\mathbf{k}}^T\bar{\mathbf{r}} = \Big(\mathbf{k}'^T R\Big) R^T\mathbf{r}' = \mathbf{k}'^T\mathbf{r}' = \mathbf{k}'\cdot\mathbf{r}'$$

and $\left|R^T\right| = 1$. Lastly, we note that, since

$$\bar{\mathbf{k}} = R^T\mathbf{k}' = \begin{bmatrix} \hat{\mathbf{v}}_1^T \\ \\ \hat{\mathbf{v}}_2^T \end{bmatrix}\mathbf{k}'$$

we can read off

$$\bar{k}_x(\mathbf{k}') = \hat{\mathbf{v}}_1\cdot\mathbf{k}' \qquad \text{and} \qquad \bar{k}_y(\mathbf{k}') = \hat{\mathbf{v}}_2\cdot\mathbf{k}'$$

We see from the construction of equation (A.12) that

$$\mathscr{F}\left[\Psi'_{m,p}(x',y')\right] \;=\; h_{m,b_1}(\bar{k}_x(\mathbf{k}'))h_{p,b_3}(\bar{k}_y(\mathbf{k}')) \;=\; h_{m,b_1}(\hat{\mathbf{v}}_1\cdot\mathbf{k}')h_{p,b_3}(\hat{\mathbf{v}}_2\cdot\mathbf{k}')$$

Finally, we can get the wavefunction in the the original $\mathbf{r}$ coordinates and its fourier transform by considering

$$\begin{aligned}\Psi_{m,p}(x,y)=\Psi'_{m,p}(x-x_0,y-y_0) &= \iint h_{m,b_1}(\hat{\mathbf{v}}_1\cdot\mathbf{k}')h_{p,b_3}(\hat{\mathbf{v}}_2\cdot\mathbf{k}')\; e^{i\mathbf{k}'\cdot(\mathbf{r}-\mathbf{r}_0)}\,dk'_x\,dk'_y \\ &= \iint e^{-i\mathbf{k}'\cdot\mathbf{r}_0}h_{m,b_1}(\hat{\mathbf{v}}_1\cdot\mathbf{k}')h_{p,b_3}(\hat{\mathbf{v}}_2\cdot\mathbf{k}')\; e^{i\mathbf{k}'\cdot\mathbf{r}}\,dk'_x\,dk'_y \qquad \text{(A.13)} \\ &= \iint e^{-i\mathbf{k}\cdot\mathbf{r}_0}h_{m,b_1}(\hat{\mathbf{v}}_1\cdot\mathbf{k})h_{p,b_3}(\hat{\mathbf{v}}_2\cdot\mathbf{k})\; e^{i\mathbf{k}\cdot\mathbf{r}}\,dk_x\,dk_y\end{aligned}$$

In the last equality above, we made a trivial "change of variables" with $\mathbf{k}=\mathbf{k}'$ to maintain notational consistency.

From equation (A.13), we identify the eigenstate function in momentum space as

$$\Phi_{m,p}(k_x,k_y) \;=\; \mathscr{F}\left[\Psi_{m,p}(x,y)\right] \;=\; e^{-i\mathbf{k}\cdot\mathbf{r}_0}h_{m,b_1}(\hat{\mathbf{v}}_1\cdot\mathbf{k})h_{p,b_3}(\hat{\mathbf{v}}_2\cdot\mathbf{k}) \qquad \text{(A.14)}$$

A.5 Bloch Function in k-Space

Next, let us consider the bloch wavefunctions in momentum space, since this is how the program stores these wavefunctions. Denoting the bloch function in band j with quasimomentum $\mathbf{q}$ by

$$\psi_j^{\mathbf{q}}(\mathbf{r}) = e^{i\mathbf{q}\cdot\mathbf{r}}\; u_j^{(\mathbf{q})}(\mathbf{r})$$

We consider the fourier series coefficients of $u_j^{\mathbf{q}}(\mathbf{r})$ which are defined by

$$c_j^{(\mathbf{q},\mathbf{G})} = \frac{1}{\sqrt{\Gamma}} \int_{\mathrm{PC}} d\mathbf{r}\; u_j^{(\mathbf{q})}(\mathbf{r})\; e^{-i\mathbf{G}\cdot\mathbf{r}} \tag{A.15}$$

where the integral is over a primitive lattice cell ("PC") with volume (area) Γ and $\mathbf{G}$ are the reciprocal lattice vectors. Conversely, it is also true that

$$u_j^{(\mathbf{q})}(\mathbf{r}) = \frac{1}{\sqrt{\Gamma}} \sum_{\mathbf{G}} c_j^{(\mathbf{q},\mathbf{G})} e^{i\mathbf{G}\cdot\mathbf{r}} \tag{A.16}$$

The program stores these coefficients $c_j^{(\mathbf{q},\mathbf{G})}$ with the following MATLAB variables

- $c_j^{(\mathbf{q}_n,\mathbf{G}_m)}$ = `bloch.State`(m, n, j) (Size = $M \times N^2 \times J$)
- $\mathbf{q}_n$ = `bloch.Q.Mesh`$(1, n)\hat{\mathbf{x}}$ + `bloch.Q.Mesh`$(2, n)\hat{\mathbf{y}}$ Size = $2 \times N^2$
- $\mathbf{G}_m$ = `recip.Gk(1,m)`$\hat{\mathbf{x}}$ + `recip.Gk(2,m)`$\hat{\mathbf{y}}$

We start with the bloch state using the expression in (A.16)

$$\psi_j^{\mathbf{q}}(\mathbf{r}) = e^{i\mathbf{q}\cdot\mathbf{r}} u_j^{(\mathbf{q})}(\mathbf{r}) = \frac{1}{\sqrt{\Gamma}} \sum_{\mathbf{G}} c_j^{(\mathbf{q},\mathbf{G})} e^{i(\mathbf{G}+\mathbf{q})\cdot\mathbf{r}} \tag{A.17}$$

Note that in the program is normalized so that

$$\sum_{\mathbf{G}} \left| c_j^{(\mathbf{q},\mathbf{G})} \right|^2 = 1$$

or equivalently

$$\int_{\mathrm{PC}} \psi_j^{\mathbf{q}\,*}(\mathbf{r})\; \psi_j^{\mathbf{q}}(\mathbf{r})\; d\mathbf{r} = 1 \tag{A.18}$$

where the integral is over a primitive cell of area Γ.

Taking the fourier transform of equation (A.17), we get

$$\tilde{\psi}_j^{\mathbf{q}}(\mathbf{k}) \;=\; \frac{1}{2\pi}\int_{\mathbb{R}^2} \psi_j^{\mathbf{q}}(\mathbf{r}) e^{-i\mathbf{k}\cdot\mathbf{r}}\, d\mathbf{r} \;=\; \frac{1}{2\pi\sqrt{\Gamma}} \sum_{\mathbf{G}} c_j^{(\mathbf{q},\mathbf{G})} \delta(\mathbf{G}+\mathbf{q}-\mathbf{k}) \tag{A.19}$$

A.6 Algorithm Initialization

Firstly, the definition of Wannier states in 2D can be found by considering equation (2) from reference [74] and replacing the $(2\pi)^3$ factor by $(2\pi)^2$ for our 2D case:

$$|w_{n\mathbf{R}}\rangle = \Gamma \int_{\mathrm{BZ}} \frac{d\mathbf{q}}{(2\pi)^2} e^{-i\mathbf{q}\cdot\mathbf{R}} \sum_{j=1}^{J} |\psi_j^{\mathbf{q}}\rangle \, (U_{\mathbf{q}})_{jn} \tag{A.20}$$

Γ is the real space primitive cell area. J is the number of bands being consider.[4] $|\psi_j^{\mathbf{q}}\rangle$ are the bloch states. $U_{\mathbf{q}}$ is a unitary matrix for each value of $\mathbf{q}$ which we wish to find using the program. $U_{\mathbf{q}}$ represents a choice of gauge for the set of bloch states, and you can consider it as redefining the original bloch basis $\{|\psi_j^{\mathbf{q}}\rangle\}$ to provide a new set of basis states $\{|\tilde{\psi}_j^{\mathbf{q}}\rangle\}$given by

$$|\tilde{\psi}_n^{\mathbf{q}}\rangle = \sum_{j=1}^{J} |\psi_j^{\mathbf{q}}\rangle \left(U_{\mathbf{q}}\right)_{jn} \tag{A.21}$$

in which case, the more standard definition of Wannier states is recovered

$$|w_{n\mathbf{R}}\rangle = V \int_{\mathrm{BZ}} \frac{d\mathbf{q}}{(2\pi)^2} e^{-i\mathbf{q}\cdot\mathbf{R}} \, |\tilde{\psi}_n^{\mathbf{q}}\rangle$$

It should be noted that for the program $U^{\mathbf{q}}$ is effectively a matrix that is being multiplied

[4]Note that if there are entangled bands the sum over the first J bands is changed to a sum over the bands j in the set $\mathcal{J}_{\mathbf{q}}$, and in general this set will be different at different qausimomentum values $\mathbf{q}$ in the brillouin zone.

on the right hand side of row vectors. That is to say, whereas by typical convention

$$(U\mathbf{v})_m = \sum_n U_{mn} v_n$$

the convention chosen in equation (A.20) and elsewhere is more like

$$(\mathbf{v}^{\mathrm{t}} U^{\mathrm{t}})_n = \sum_m v_m U_{mn}$$

The consequence of this is that subsequent transformations of $U_{\mathbf{q}}$ are done by right multiplication of matrices.

In equation (26) of reference [74], initialization is described as a redefinition of the basis states with the formula

$$|\tilde{\psi}_n^{\mathbf{q}}\rangle = \sum_{j=1}^{J} |\psi_j^{\mathbf{q}}\rangle \left(A_{\mathbf{q}} S_{\mathbf{q}}^{-1/2}\right)_{jn}$$

This is equivalent to setting the initial guess for $U_{\mathbf{q}}$ in equation (A.20) to be

$$U_{\mathbf{q},\mathrm{init}} \equiv A_{\mathbf{q}} S_{\mathbf{q}}^{-1/2}$$

The matrix $A_{\mathbf{q}}$ is defined by a block diagonal matrix

$$\left(A_{\mathbf{q}}\right)_{jn} = \begin{cases} \langle \psi_j^{\mathbf{q}} | g_n \rangle & \text{if band } j \text{ and band } n \text{ are in the same set of composite bands} \\ 0 & \text{otherwise} \end{cases} \tag{A.22}$$

where $\{|g_n\rangle\}$ are the initialization guess Wannier states. $S_{\mathbf{q}}$ is then defined by

$$S_{\mathbf{q}} = A_{\mathbf{q}}^{\dagger} A_{\mathbf{q}} \tag{A.23}$$

In the program, the composite bands are specified in the elements of the cell array `groups`.

If two band indices are in the same element of `groups` they are considered composite. So, as an example, if `groups = {1,[2.3]}` then bands 2 and 3 are composite, so the nonzero elements of $A_{\mathbf{q}}$ are $(A_{\mathbf{q}})_{1,1}$, $(A_{\mathbf{q}})_{2,2}$, $(A_{\mathbf{q}})_{2,3}$, $(A_{\mathbf{q}})_{3,2}$, and $(A_{\mathbf{q}})_{3,3}$. The nonzero elements are the same for $U_{\mathbf{q}}$ as well.

Heuristically, one can think of this as "trying to express the guess state $|g_n\rangle$ in terms of the available bloch states, with the restriction that $U_{\mathbf{q}}$ be unitary." If one were so fortunate that the guess state $|g_n\rangle$ is the Wannier state, one would find that

$$|w_{n\mathbf{R}}\rangle = |g_n\rangle = \Gamma \int_{\mathrm{BZ}} \frac{d\mathbf{q}}{(2\pi)^2} e^{-i\mathbf{q}\cdot\mathbf{R}} \sum_{j=1}^{J} |\psi_j^{\mathbf{q}}\rangle \left(A_{\mathbf{q}} S_{\mathbf{q}}^{-1/2}\right)_{jn}$$

so that

$$U_{\mathbf{q}} = A_{\mathbf{q}} S_{\mathbf{q}}^{-1/2}$$

In the program, we implement this in the initialization method of the `Wannier90` class. It sets the matrices $U_{\mathbf{q}}$ defined in the property `Wannier90.U` to the initial value based on the guess states and simultaneously updates the overlap matrices stored in `Wannier90.Mmn`. To encode the guess states, we define a class called `InitializationHOStates` that contains information about the harmonic oscillator states that will be used as $|g_n\rangle$, and we provide an object of this class as an input to the initialization method of the `Wannier90` class.

A.6.1 Calculating Elements of $U_{\mathbf{q},\mathbf{init}}$

We will calculate the elements of $A_{\mathbf{q}}$ from equation (A.22) in k-space.

For us, we will set our guess states to harmonic oscillator states from equation (A.14) of section A.4.2

$$|g_n\rangle = |\Phi_{m,p}^{\mathbf{r}_0}\rangle$$

where we use the superscript $\mathbf{r}_0$ to indicate that it is the harmonic oscillator for the approximate

potential centered on the point $\mathbf{r}_0$.

We will calculate the inner products in k-space, since it is relatively simple and less computationally intensive. Using equations (A.14) and (A.19), we see that

$$\begin{aligned}\langle \psi_j^{\mathbf{q}} | \Phi_{m,p}^{\mathbf{r}_0} \rangle &= \iint \left[\frac{1}{2\pi\sqrt{\Gamma}} \sum_{\mathbf{G}} \left(c_j^{(\mathbf{q},\mathbf{G})} \right)^* \delta(\mathbf{G}+\mathbf{q}-\mathbf{k}) \right] \left[e^{-i\mathbf{k}\cdot\mathbf{r}_0} h_{m,b_1}(\hat{\mathbf{v}}_1 \cdot \mathbf{k})\; h_{p,b_3}(\hat{\mathbf{v}}_2 \cdot \mathbf{k}) \right] dk_x\, dk_y \\ &= \frac{1}{2\pi\sqrt{\Gamma}} \sum_{\mathbf{G}} \left(c_j^{(\mathbf{q},\mathbf{G})} \right)^* \left[\iint \delta(\mathbf{G}+\mathbf{q}-\mathbf{k})\, e^{-i\mathbf{k}\cdot\mathbf{r}_0}\, h_{m,b_1}(\hat{\mathbf{v}}_1 \cdot \mathbf{k})\; h_{p,b_3}(\hat{\mathbf{v}}_2 \cdot \mathbf{k})\; dk_x\, dk_y \right] \\ &= \frac{1}{2\pi\sqrt{\Gamma}} \sum_{\mathbf{G}} \left(c_j^{(\mathbf{q},\mathbf{G})} \right)^* e^{-i(\mathbf{G}+\mathbf{q})\cdot\mathbf{r}_0}\, h_{m,b_1}(\hat{\mathbf{v}}_1 \cdot (\mathbf{G}+\mathbf{q}))\; h_{p,b_3}(\hat{\mathbf{v}}_2 \cdot (\mathbf{G}+\mathbf{q}))\end{aligned} \tag{A.24}$$

Note here that the integrals are over all of space whereas the bloch states are normalized for integration over a primitive cell per equation (A.18). Consequently, this overlap integral can take on values of magnitude greater than 1 and $\langle \psi_j^{\mathbf{q}} | \psi_j^{\mathbf{q}} \rangle \neq 1$ usually. Fortunately, this does not matter for our calculation of $U_{\mathbf{q},\text{init}}$ since it is made unitary by its construction.

The method `InitializationHOState.HOkSpaceFunctions(n,kx,ky)` returns the values of a guess state n according to equation (A.14) where different values of n will indicate different values of m and p as well as different local minima positions $\mathbf{r}_0$. During the program, the guess states in `InitializationHOState` will be sorted so that state n in of the `InitializationHOState` object does correspond to the $|g_n\rangle$ used in equation (A.22) to calculate $A_{\mathbf{q}}$. This sorting will be explained in section A.7.

In the program, the bloch states are encoded in the class `Bloch` with the following properties being relevant to our calculation

- $c_j^{(\mathbf{q}_n,\mathbf{G}_m)}$ = `bloch.State`(m,n,j) Size = $M \times N^2 \times J$
- $\mathbf{q}_n$ = `bloch.Q.Mesh`$(1,n)\hat{\mathbf{x}}$ + `bloch.Q.Mesh`$(2,n)\hat{\mathbf{y}}$ Size = $2 \times N^2$

- $\mathbf{G}_m$ = `recip.Gk(1,m)`$\hat{\mathbf{x}}$ + `recip.Gk(2,m)`$\hat{\mathbf{y}}$

With these conventions, we can implement equation (A.24) in MATLAB with the following line of code

$$
\begin{aligned}
(A_{\mathbf{q}_n})_{ji} &= \texttt{A(j,i,n)} \\
&= \texttt{transpose(bloch.State(:,n,j))} \\
&\quad * \texttt{transpose(} \\
&\qquad \texttt{initHOState.HOkSpaceFunction(i,G(1,:)+q(1,n),G(2,:)+q(2,n))} \\
&\quad \texttt{)}
\end{aligned}
\tag{A.25}
$$

where

$$\texttt{G(r,:)} = \texttt{recip.Gk(r,:)} \quad \text{and} \quad \texttt{q(r,n)} = \texttt{bloch.Q.Mesh(r,n)}$$

and `initHOState` is an object of class `InitializationHOState`. We drop the $1/\sqrt{\Gamma}$ factor because $A_{\mathbf{q}}$ only needs to be specified up to a normalization factor.

Note that the harmonic oscillator states are normalized as defined. That is to say

$$\int_{-\infty}^{\infty}\int_{-\infty}^{\infty}\left|\texttt{initHOState.HOkSpaceFunction(i,}k_x\texttt{,}k_y\texttt{)}\right|^2 dk_x\, dk_y = 1$$

for all `i`. However, harmonic states on different sites are not orthogonal.

A.7 Choosing Best Guess State

In the limit of a deep lattice the Wannier states are very well approximated by the guess state based on the harmonic oscillator approximation. Moreover, comparing the average band energy and approximate guess state energies will make it clear which guess state will be used

for which band. However, when bands are close in energy or the lattice is shallow, which guess states are good for which band is not immediately obvious.

Finding the best guess state(s) for a given band (set of composite bands) can be done by checking which guess state has the largest norm after being projected onto the set of bloch states under consideration. Mathematically, we see that this is found by considering the projection operator[5]

$$\hat{P}_n = \sum_{j \in J_n} \sum_{\mathbf{q}} |\psi_j^{\mathbf{q}}\rangle\langle\psi_j^{\mathbf{q}}|$$

where J_n is the set of composite bands that will be considered for the n^{th} guess state. Then as our metric for how good a guess state is the expectation value of the projection operator for state $|g_n\rangle$

$$\langle g_n|\hat{P}|g_n\rangle = \sum_{j \in J_n} \sum_{\mathbf{q}} \left|\langle\psi_j^{\mathbf{q}}|g_n\rangle\right|^2$$

Notably, the term in the sum is closely related to the elements of $A_{\mathbf{q}}$ since

$$\left|\left(A_{\mathbf{q}}\right)_{m,n}\right|^2 = \left|\langle\psi_{\mathbf{q}}^m|g_n\rangle\right|^2$$

so we are able to save some calculation time by saving the elements for the best projection expectation value as the program runs.

In the program, we start with the first band, calculate the expectation value of the projection of the possible guess states onto the first band (along with any higher bands that are considered composite with the first band), and we set guess state $|g_1\rangle$ to be the guess state with the best projection value. We then remove that guess state $|g_1\rangle$ from consideration for higher bands. We then repeat the procedure with the remaining guess states for the second band (and all other composite bands with band 2) and set that as $|g_2\rangle$ and so forth.

This concludes the initialization procedure, and the remaining gradient descent methods

[5]One might wish to replace the sum over $\mathbf{q}$ with an integral of $\mathbf{q}$ over the brillouin zone. In the program, we have assumed periodic boundary conditions, so the sum is more relevant.

are carried out using the procedures implemented by Walters et al. [72] with the exception of the minor changes described in section A.1.

A.8 Some Notes on the Inputs and Outputs

Here we provide a short summary of some of the relevant inputs and outputs of the program by Walters et al. as a small supplement the information provided in their documentation.

A.8.1 Reciprocal Lattice Inputs

The reciprocal lattice points of the optical lattice are given by

$$\mathbf{G}_n = h_n \mathbf{b}_1 + k_n \mathbf{b}_2$$

The reciprocal lattice basis vectors are defined in the program with the variable `G` by

$$\mathtt{G} = [\ [\mathtt{b}_{1,1}; \mathtt{b}_{2,1}]\ \ [\mathtt{b}_{1,2}; \mathtt{b}_{2,2}]\ ]$$

where $\mathbf{b}_1$ and $\mathbf{b}_2$ the primitive reciprocal lattice vectors given in units of $1/\lambda$ so that

$$\mathbf{b}_n = \frac{1}{\lambda}\left(\mathtt{b}_{1,n}\,\hat{\mathbf{x}} + \mathtt{b}_{2,n}\,\hat{\mathbf{y}}\right)$$

As a simple example, for a simple 2D square lattice, formed with a laser of wavelength λ, we would have

$$\mathbf{b}_1 = \frac{4\pi}{\lambda}\hat{\mathbf{x}} \quad \text{and} \quad \mathbf{b}_2 = \frac{4\pi}{\lambda}\hat{\mathbf{y}}$$

In the code, this would be defined by

$$\texttt{G} = 4\pi \; [\; [1; 0] \;\; [0; 1] \;]$$

In theory, there are an infinite number of points $\mathbf{G}_n$ in reciprocal space, but for computational purposes, we limit ourselves to a finite number of them. We set a cutoff $G_{\max}$, so that only the set

$$\{\mathbf{G}_n : \; |\mathbf{G}_n| < G_{\max}\}$$

is used.

$G_{\max}$ is specified by the program in units of $1/\lambda$ with the variable `Gmax`. Specifically

$$G_{\max} = \frac{\texttt{Gmax}}{\lambda}$$

Note that $G_{\max}$ specifies the spatial resolution of the wavefunctions and bloch waves, so one must make sure that these functions do not vary significantly on the length scale of $2\pi/G_{\max}$.

A.8.2 Setting Model System Size

We must also set the size of our system, which is taken the have periodic boundary conditions. This is determined by specifying a pair of primitive vectors in fourier space that will generate a lattice of discrete points in fourier space. This lattice of points will have the same geometry as the optical lattice potential in reciprocal space, but the points spacing will be smaller than the reciprocal lattice. Let us denote these primitive vectors in fourier space as $\mathbf{k}_{\min,1}$ and $\mathbf{k}_{\min,2}$. These are set with the input `N`, which is an integer that determines these vectors by the formula

$$\mathbf{k}_{\min,1} = \frac{\mathbf{b}_1}{\texttt{N}} \quad \text{and} \quad \mathbf{k}_{\min,2} = \frac{\mathbf{b}_2}{\texttt{N}}$$

The primary practical requirement for `N` is that it needs to be large enough to avoid the periodic boundary conditions affecting the Wannier states.

A.8.3 Lattice Potential Inputs

The potential $V(\mathbf{r})$ is given to the code with a reciprocal space representation with the values v_n, where the relationship between the two is given by the following equation

$$v_n = \frac{1}{\sqrt{\Gamma}} \int_{\mathrm{PC}} d\mathbf{r}\ V(\mathbf{r}) e^{-i\mathbf{G}_n \cdot \mathbf{r}}$$

where the integral is over a primitive cell (PC) in real space and Γ is the area of the primitive cell. Likewise, we have that

$$V(\mathbf{r}) = \frac{1}{\sqrt{\Gamma}} \sum_n v_n\, e^{i\mathbf{G}_n \cdot \mathbf{r}}$$

In optical lattices, $v_n \neq 0$ for only a few values of n. To take advantage of this, the inputs that specify the lattice potential in the program are the $\mathbf{G}_n$ values for which v_n is nonzero. These values of $\mathbf{G}_n$ are given in the form

$$\mathbf{G}_n = h_n \mathbf{b}_1 + k_n \mathbf{b}_2$$

where we input the relevant h_n and k_n values using

$$\texttt{hkl} = [\ [h_1;\ k_1]\ [h_2;\ k_2]\ \ \cdots\ \ [h_N;\ k_N]\ ]$$

and the corresponding reciprocal lattice weights v_n are given by with two variables, `vi` and `v0`. Most of the information is proved in

$$\texttt{vi} = [\alpha v_1\ \ \alpha v_2\ \ \cdots\ \ \alpha v_N]$$

where the user is free to use any factor α that is convenient. The value `v0` then specifies the total lattice depth in recoil energies of the laser $E_R = h^2/2\mu\lambda^2$ where μ is the mass of the atom. Mathematically,

$$\texttt{v0} = (\max\ V(\mathbf{r}) - \min\ V(\mathbf{r}))/E_R$$

A.8.4 A Small Glossary of Symbols

- D – the dimension $D = 2$ for our purposes
- N – as described at the end of the inputs section, sets the minimum values of $\mathbf{k}$ in fourier space.
- M – the number of non-discarded reciprocal lattice vectors $\mathbf{G}$. These are the reciprocal lattice vectors that satisfy $\mathbf{G} \leq G_{\max}$
- J – the number of bands
- B – the number of neighbors considered

A.8.5 Bloch State and Energy Info

The bloch state and energy information are stored in the object `bloch` (of class `Bloch`).

Let us denote the energy associated with band j and quasimomentum $\mathbf{q}$ as $E_{j,\mathbf{q}}$. This value is stored in

- $E_{j,\mathbf{q}_n} = \texttt{bloch.Energy}(m,n)$ Size $= J \times N^D$
- $\mathbf{q}_n = \texttt{bloch.Q.Mesh}(1,n)\hat{\mathbf{x}} + \texttt{bloch.Q.Mesh}(2,n)\hat{\mathbf{y}}$ Size $= D \times N^D$

Denoting the Bloch function in band j with quasimomentum $\mathbf{q}$ by

$$\psi_j^{\mathbf{q}}(\mathbf{r}) = e^{i\mathbf{q}\cdot\mathbf{r}}\ u_j^{(\mathbf{q})}(\mathbf{r})$$

Recall that the fourier coefficients of $u_j^{\mathbf{q}}(\mathbf{r})$ which are defined by

$$c_j^{(\mathbf{q},\mathbf{G})} = \frac{1}{\sqrt{\Gamma}} \int_{\mathrm{PC}} d\mathbf{r}\; u_j^{(\mathbf{q})}(\mathbf{r})\; e^{-i\mathbf{G}\cdot\mathbf{r}} \tag{A.26}$$

where the integral is over a primitive cell ("PC") with volume (area) Γ and $\mathbf{G}$ are the reciprocal lattice vectors. This was previously defined in equation (A.15), and we have copied it here for convenience. We also have that

$$u_j^{(\mathbf{q})}(\mathbf{r}) = \frac{1}{\sqrt{\Gamma}} \sum_{\mathbf{G}} c_j^{(\mathbf{q},\mathbf{G})} e^{i\mathbf{G}\cdot\mathbf{r}} \tag{A.27}$$

This was also previously defined in equation (A.16).

The code stores these coefficients $c_j^{(\mathbf{q},\mathbf{G})}$ with the following

- $c_j^{(\mathbf{q}_n,\mathbf{G}_m)} = \texttt{bloch.State}(m,n,j)$ Size $= M \times N^D \times J$
- $\mathbf{q}_n = \texttt{bloch.Q.Mesh}(1,n)\hat{\mathbf{x}} + \texttt{bloch.Q.Mesh}(2,n)\hat{\mathbf{y}}$ Size $= D \times N^D$
- $\mathbf{G}_m = \texttt{recip.Gk(1,m)}\hat{\mathbf{x}} + \texttt{recip.Gk(2,m)}\hat{\mathbf{y}}$

`bloch.Hv` is the potential expressed in fourier space. It has size $M \times M$ and it is hermitian.

A.9 Hubbard Parameters

As a supplement for understanding the Bose-Hubbard model, we recommend section 3 of reference [77]. The Bose-Hubbard (BH) hamiltonian that we are calculating parameters for is

$$H_{\mathrm{BH}} = \sum_{\substack{m,n,o,p \\ \mathbf{R},\mathbf{R}',\mathbf{R}'',\mathbf{R}'''}} \Big[-t^{mn}_{\mathbf{R}\mathbf{R}'}\; b^{m\dagger}_{\mathbf{R}} b^{n}_{\mathbf{R}'} + \frac{U^{mnop}_{\mathbf{R}\mathbf{R}'\mathbf{R}''\mathbf{R}'''}}{2} b^{m\dagger}_{\mathbf{R}} b^{n\dagger}_{\mathbf{R}'} b^{o}_{\mathbf{R}''} b^{p}_{\mathbf{R}'''} \Big]$$

where $b^{m\dagger}_{\mathbf{R}}$ and $b^{m}_{\mathbf{R}}$ are the bosonic creation and annihilation operators.

Note here that in the expression for H_{BH}, we allow for the possibility that $\mathbf{R} = \mathbf{R}'$ and $n = m$ which is more accurately described as a chemical potential term even though we use the "hopping parameter" t to denote this chemical potential term. In other words, the chemical potentials are the terms of the form $t^{mm}_{\mathbf{RR}} = t^{mm}_{\mathbf{00}}$. These terms are important typically.

This program calculates the following parameters.

$$t^{mn}_{\mathbf{R0}}, \quad U^{mmnn}_{\mathbf{00RR}}, \quad U^{mmnn}_{\mathbf{000R}}, \quad U^{mmmn}_{\mathbf{000R}}, \quad U^{mmmn}_{\mathbf{00R0}}, \quad \text{and} \quad U^{mmnn}_{\mathbf{R0R0}}$$

The t parameters are calculated in units of E_R. The U parameters are calculated in units of $g/\lambda^D = gE_R/\tilde{g}$ where g is the interaction coupling constant of the Gross-Pitaevskii equation and $\tilde{g} \equiv \lambda^D E_R$.

Note that for lattices with multiple sites per unit cell, hopping from one site in the unit cell to another site in the unit cell will be a value $t^{mn}_{\mathbf{00}}$ (occurring for $\mathbf{R} = 0$), where n and m correspond to the different Wannier states in the same unit cell.

The values of the BH parameters are saved in the object `ManyBody`. The notation seems very inconsistent across the board, but the documentation is clear enough. In total, we have that

- $t^{mn}_{\mathbf{R}_i\mathbf{0}}$ =`ManyBody.J(m,n,i)`
- $U^{mmnn}_{\mathbf{00R}_i\mathbf{R}_i}$ = `ManyBody.Ujjnn(m,n,i)`
- $U^{mmnn}_{\mathbf{000R}_i}$ = `ManyBody.U0jnn(m,n,i)`
- $U^{mmmn}_{\mathbf{000R}_i}$ = `ManyBody.U0jmn(m,n,i)`
- $U^{mmmn}_{\mathbf{00R}_i\mathbf{0}}$ = `ManyBody.Uj0mn(m,n,i)`
- $U^{mmnn}_{\mathbf{R}_i\mathbf{0R}_i\mathbf{0}}$ = `ManyBody.Uj0j0(m,n,i)`

Where $\mathbf{R}_i$ correspond to translations of the Wannier states by the lattice vectors specified in `manyBody.Sites` which are given in units of the primitive lattice vectors $\mathbf{a}_1$ and $\mathbf{a}_2$, so that

$$\mathbf{R}_i = \texttt{manyBody.Sites(1,i)}\ \mathbf{a}_1 + \texttt{manyBody.Sites(2,i)}\ \mathbf{a}_2$$

If one wishes the check, the lattice vectors are stored in the variable lattice, specifically,

$$\mathbf{a}_i = \lambda\left(\texttt{lattice.R(1,i)}\hat{\mathbf{x}} + \texttt{lattice.R(2,i)}\hat{\mathbf{y}}\right)$$

The primitive translation vectors $\mathbf{a}_i$ of the generated lattice are defined in the code by

$$\mathbf{a}_1 = \frac{2\pi}{\hat{\mathbf{z}}\cdot(\mathbf{b}_1\times\mathbf{b}_2)}(\mathbf{b}_2\times\hat{\mathbf{z}}) = \frac{\lambda}{\sqrt{2}}\hat{\mathbf{x}} \qquad \mathbf{a}_2 = \frac{2\pi}{\hat{\mathbf{z}}\cdot(\mathbf{b}_1\times\mathbf{b}_2)}(\hat{\mathbf{z}}\times\mathbf{b}_1) = \frac{\lambda}{\sqrt{2}}\hat{\mathbf{y}}$$

Note that the t and U values will depend on where the calculated Wannier states are located.

A.10 An Adjustment to the Potential Object Initialization

We also made some minor and performance improving changes to the `Potential` class. For one, we changed the initialization input `vi` to `viOverRootArea` where

$$\texttt{viOverRootArea} = \frac{v_i}{\sqrt{\Gamma}}$$

and where Γ is the unit cell area. Previously, `viOverRootArea` was named as `vi` and then renormalized, so this change was primarily to minimize ambiguity and confusion in the code.

Also, we changed the `Potential` class so that it more precisely finds the maximum and minimum of an initially incorrectly scaled version of the lattice potential. The found maximum and minimum are then used to determine the fourier coefficients of the correctly scaled lattice

that has the desired depth of `v0`. Previously, a grid of points on a unit cell of the lattice was sampled and found the maximum and minimum of the sample points. We keep this step, increasing the density of points in the sample grid of a unit cell, now using 700^2 points, and we extend the procedure to find the max and min using the extremum of a least squares quadratic fit to a square grid of sampled points that is 0.01λ by 0.01λ. This added step is procedurally the same as that used to identify of the local minima on the potential for the harmonic guess states. We believe this should be quite accurate given that features cannot be too much smaller than a wavelength. Before this change, there were small errors in the depth, but the tunneling parameters in the bose-hubbard model would vary by about 1% as a result at `v0` $= 10E_R$.

Appendix B

Spectroscopy Setup to Lock to 461 nm Laser Frequency

As already mentioned in section 2.1, the 461 nm laser is locked using a spectroscopy cell. The signal is made free of doppler broading by use of a standard pump-probe method (see for example [78].) We specifically use modulation transfer spectroscopy [79, 80], implemented with a resonant home-built EOM, driven with a sine wave from a RIGOL DG1022Z signal generator at frequency 20.2 MHz. The error signal is generated using a lock-in amplifier built from components purchased from Mini-Circuits. The spectroscopy cell setup and a picture of the spectroscopy cell are shown in figure B.1. A schematic of the electronics for the lock-in is shown in figure B.2 and a picture of the actual box containing most of the electronics is shown in figure B.3

We will briefly go over some points of the spectroscopy setup. The total laser light picked off from the full 461 nm laser output by the beam splitter is about 6 mW. This light's frequency is then adjusted using two AOMs. The first AOM is a single pass that lowers the beam's frequency by 212.5 MHz. The second AOM is used in a double pass configuration that raises the laser beam's frequency back up by either 845.8 MHz (for ^{84}Sr) or 575 MHz (for ^{88}Sr)

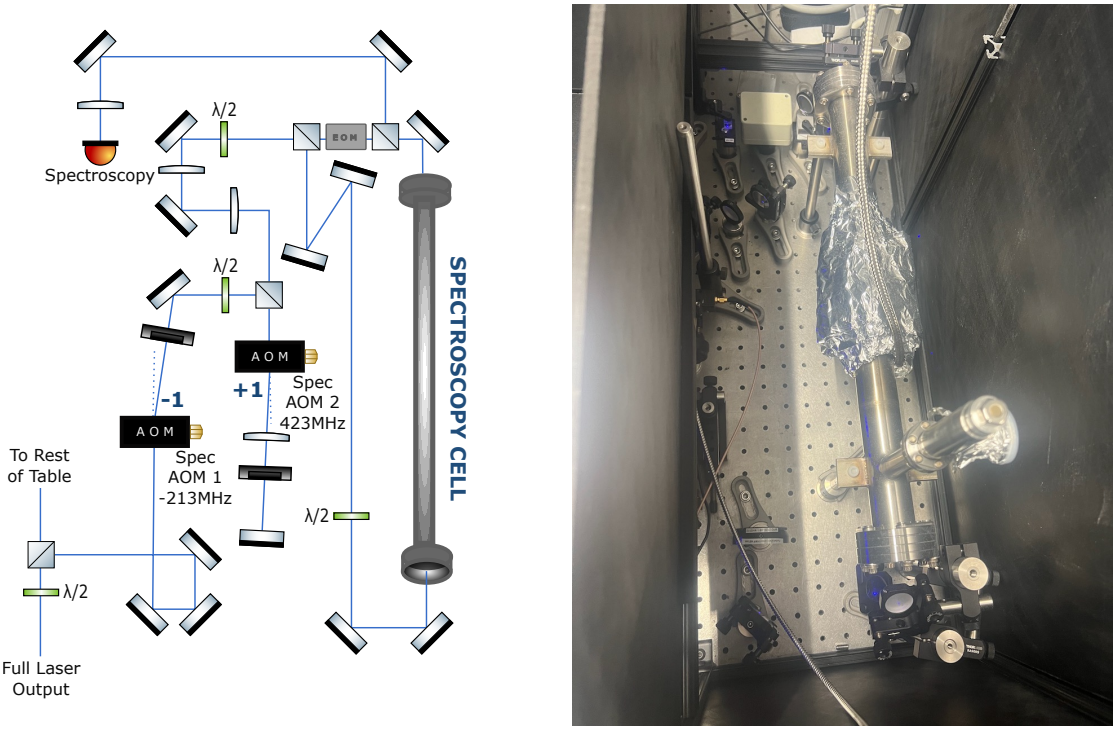

Figure B.1: Left: A diagram of the optics used for the blue spectroscopy cell. This is a subset of the optics shown in figure 2.1 of the entire laser diagram. See figure 2.1 for the meanings of the symbols for the optical elements. Right: An image of the spectroscopy cell on the laser table.
Diagram Credit: Anna Dardia

after both passes. This adjustment of the AOM frequency changes the output frequency of the 461 nm laser via the laser lock. After the double pass AOM, there is about 2.2 mW of laser power. The final power in the pump beam is about 1mW and the final power in the probe beam is about 0.3 mW.

The error signal and the DC (technically low frequency) component of spectroscopy photodiode intensity are sent using two separate cables to the Digilock 110 module of our 461 nm Toptica laser. The module then communicates with a lab computer and Toptica's Digilock application displays both the DC component of the spectroscopy photodiode along with the error signal. The amplitude of the error signal is typically 120 mV peak to trough and its maximum limits set by the input to the modules are ±1 V. The DC signal of the probe beam is useful to

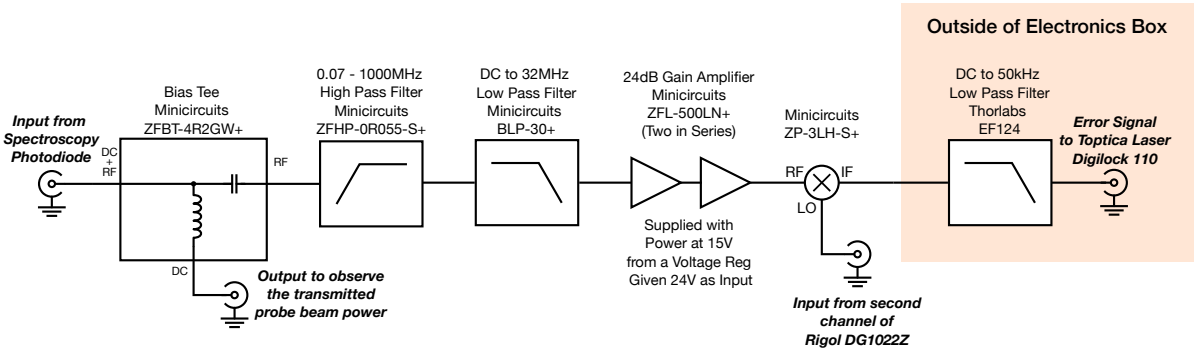

Figure B.2: Electronics diagram for the lock-in amplifier that we built to generate an error signal for the stabilization of our 461 nm laser.

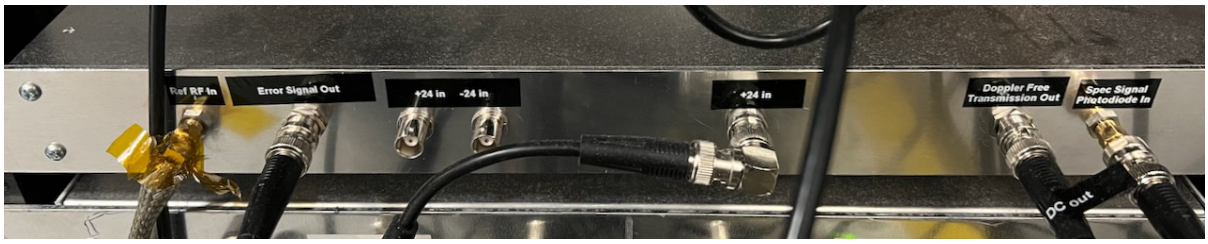

Figure B.3: An image of the front panel of the server rack mounted electronics box for the 461 nm spectroscopy electronics. Note that the inputs and outputs are horizontally flipped compared to the diagram in figure B.2 and that the two unconnected "+24 in" and "-24 in" BNCs were not used in the end. To clarify some of the labeling differences between the front panel and figure B.2: "Spec Signal Photodiode In" is the input from the spectroscopy photodiode; "Doppler Free Transmission Out" is the DC output of the bias tee; "Error Signal Out" is the IF output of the mixer; and "Ref RF In" is the LO input to the mixer

observe the broad doppler limited absorption as the laser scans in that one can tune the laser towards where the probe is most attenuated as it passes through the spectroscopy cell to find the small doppler free peak near the bottom of this minimum. The doppler free peak in the DC signal is visible but very small compared to the noise at our operating beam powers and spectroscopy cell vapor pressures, so it is better to use the error signal to identify the desired laser frequency lock point the scan range is near this point. Images of these signals on the Digilock 110 software are shown in figure B.5.

Lastly, we note that if desirable one can observe the error signal and DC signal directly on an oscilloscope, but typically this information is better displayed on the Digilock 110 software.

The displayed signals will look similar to what is shown in figure B.4.

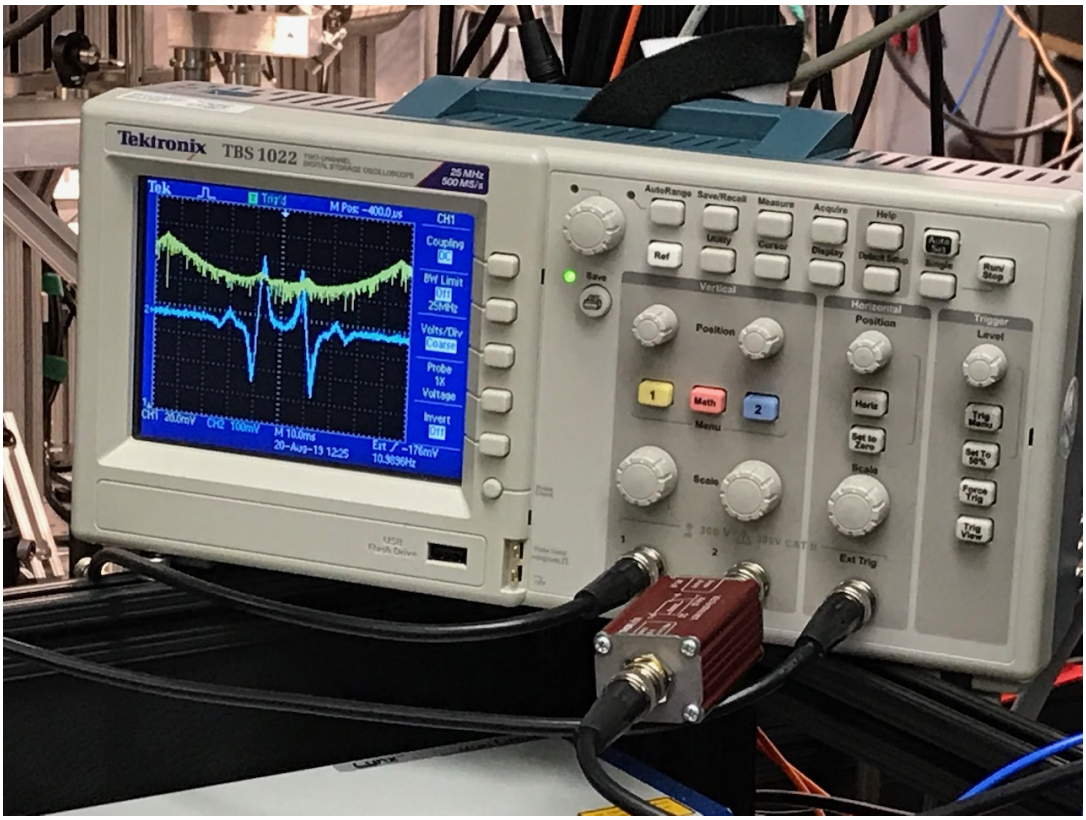

Figure B.4: An image of the oscilloscope viewing the DC signal from the spectroscopy photodiode on channel 1 and the error signal on channel 2. The laser is scanning the 922nm frequency with a triangle waveform, and here we see one full cycle of this scan (up then down).

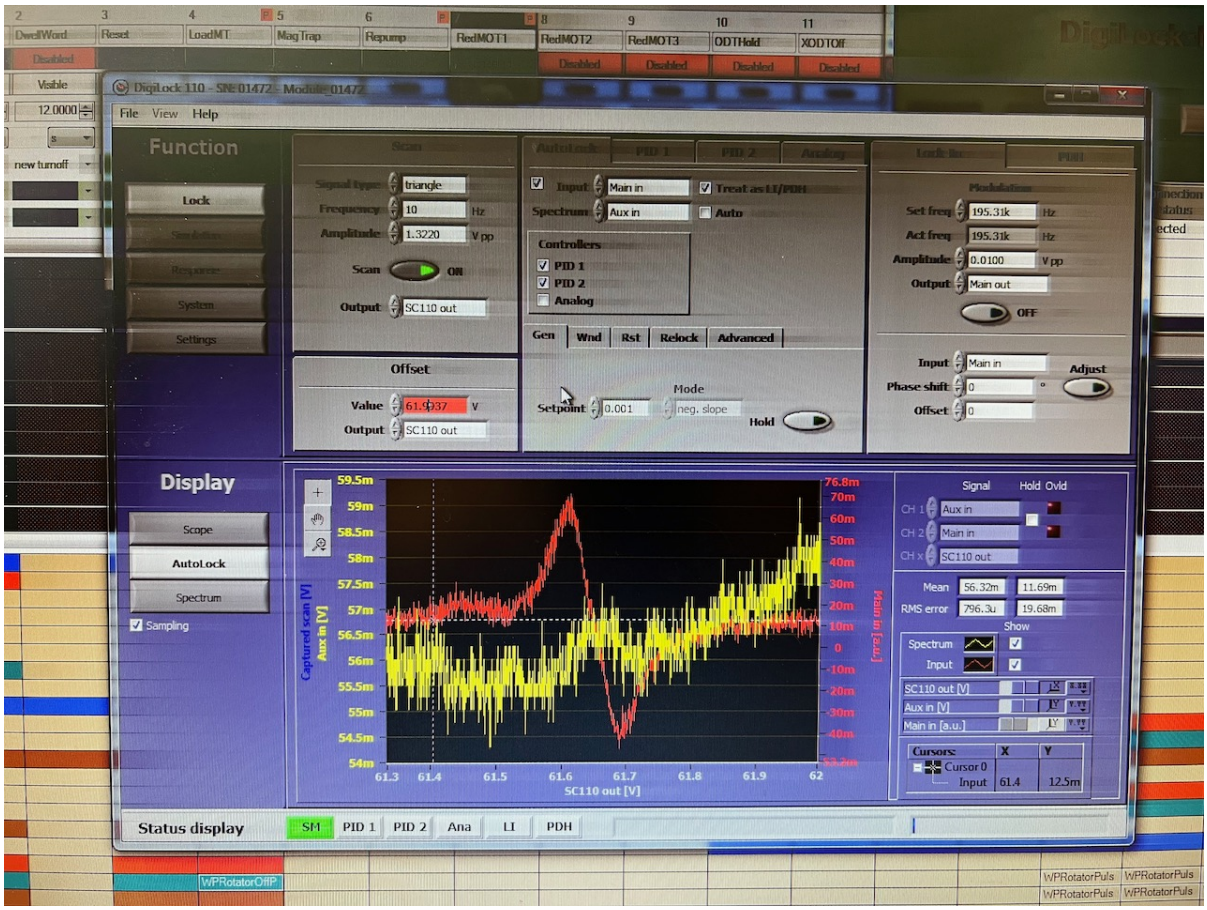

Figure B.5: An image of the digilock software with the 461 nm laser set to scan. We see here the error signal centered in red, indicating that the spectroscopy cell's probe beam is being scanned across the atomic resonance. The yellow trace depicts the low frequency component of the spectroscopy photodiode, and one sees the very small doppler free peak about where the error signal crosses 0.

Appendix C

689 nm Spectroscopy for Laser Stabilization

Here we will discuss the spectroscopy setup used for the stabilization of the 689 nm laser. The optics for the spectroscopy setup are shown in figure C.1. It utilizes the exact same method of modulation transfer spectroscopy [79, 80] that is used for the 461 nm laser as discussed in appendix B. The primary difference of note in the optics used for the 689 nm laser spectroscopy setup is that the pump beam's frequency is modulated using a double pass AOM rather than an EOM.

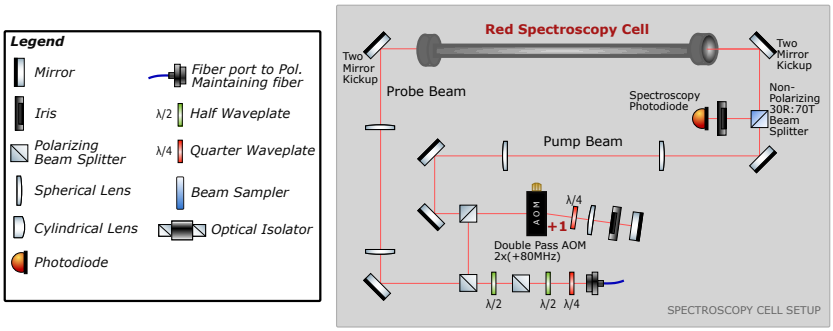

Figure C.1: Diagram of the spectroscopy optics used for the 689 nm laser.
Diagram Credit: Anna Dardia.

Because the linewidth of the 689 nm transition is only 7.4 kHz, the optimal modulation frequency is much lower than that used in the generation of the 461 nm spectroscopy signal. This is the reason that generation of modulation with a double pass AOM is preferable. Moreover, the low modulation frequency allows us to utilize the digital lock-in that comes with the control software of the TOPTICA DL pro laser that we use (TOPTICA, Product ID: DL pro 020098.)

To drive the AOM, we use a commercial signal generator (RF-Consultant Robert Yarbrough, Model: TPI-1002-A) whose output is amplified by an RF amplifier from Mini-Circuits (Model: ZHL-3A.) The modulation signal from our 689 nm laser controller is sent to the modulation input of the TPI-1002-A signal generator. However, we find that we get the best error signal in our experiment when the TPI-1002-A is maximally modulated, and the voltage range of the modulation signal from the laser controller is insufficient to achieve this. To fix this, we incorporated a simple op amp circuit composed of a buffer and an inverting amplifier with a gain of approximately 1.8 at the modulation frequency that serves to amplify the modulation input signal of the TPI-1002-A. A diagram of this circuit is shown figure C.2.

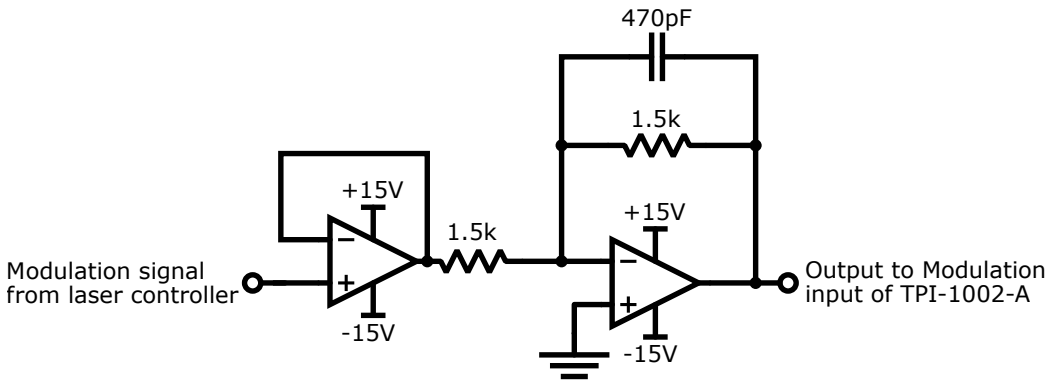

Figure C.2: Diagram of the amplifier circuit for the red spectroscopy modulation signal.

Appendix D

Spectroscopy Cell Drawings from ANCORP

Presented in this appendix are technical drawings of the red spectroscopy cell that were provided by ANCORP during the finalizing and approval process for the custom order. If one is interested in ordering the same or a similar design from ANCORP, these drawings can be referenced as drawing number 8002365 revision A. We reproduce these drawings with permission from ANCORP.

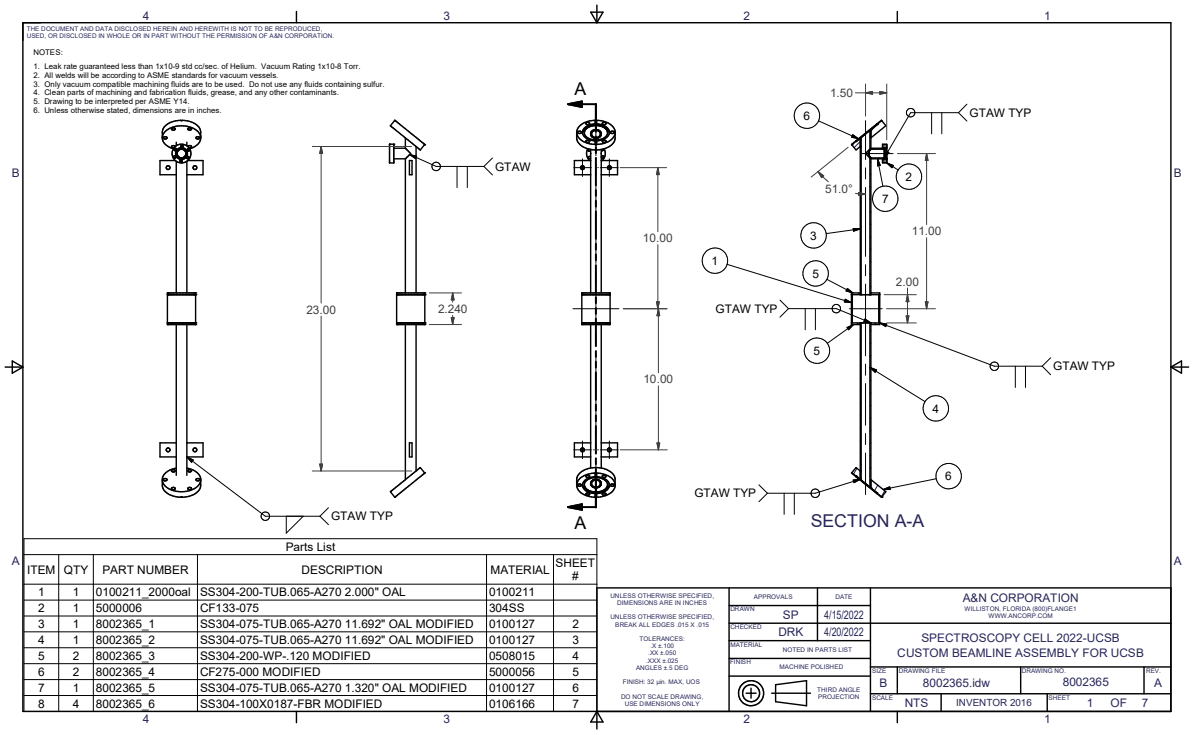

Figure D.1: ANCORP Drawing 8002365 Rev A, Page 1

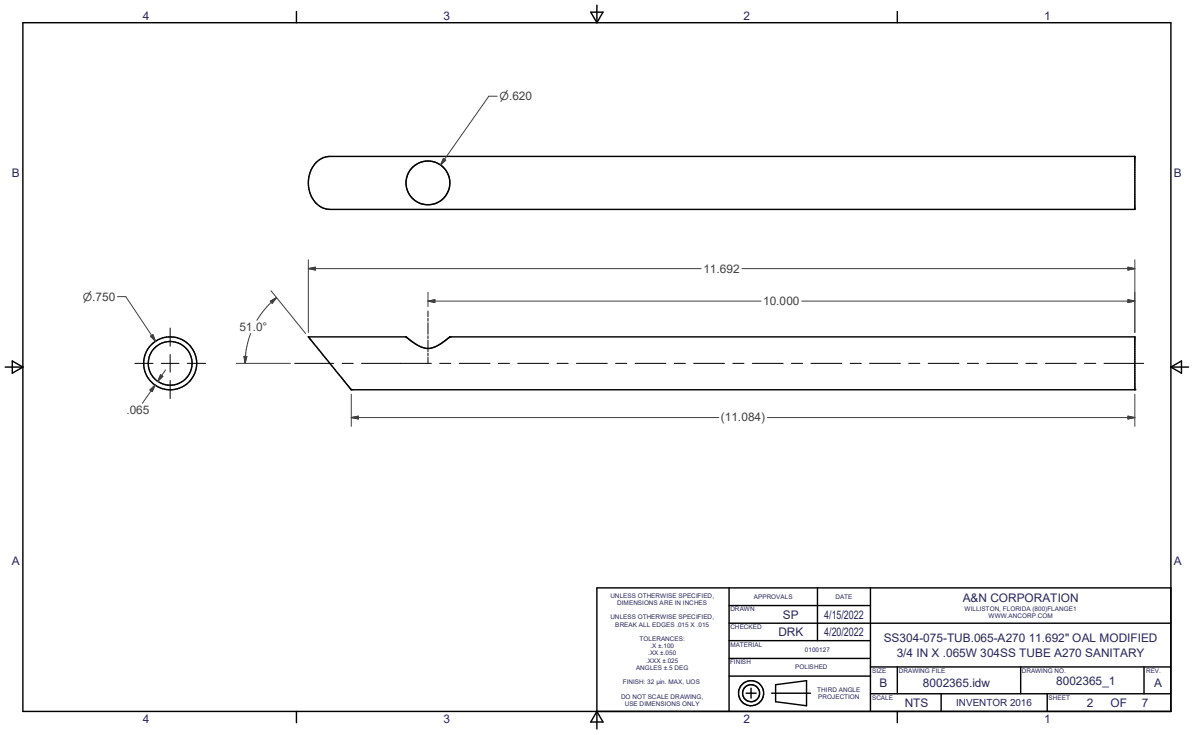

Figure D.2: ANCORP Drawing 8002365 Rev A, Page 2

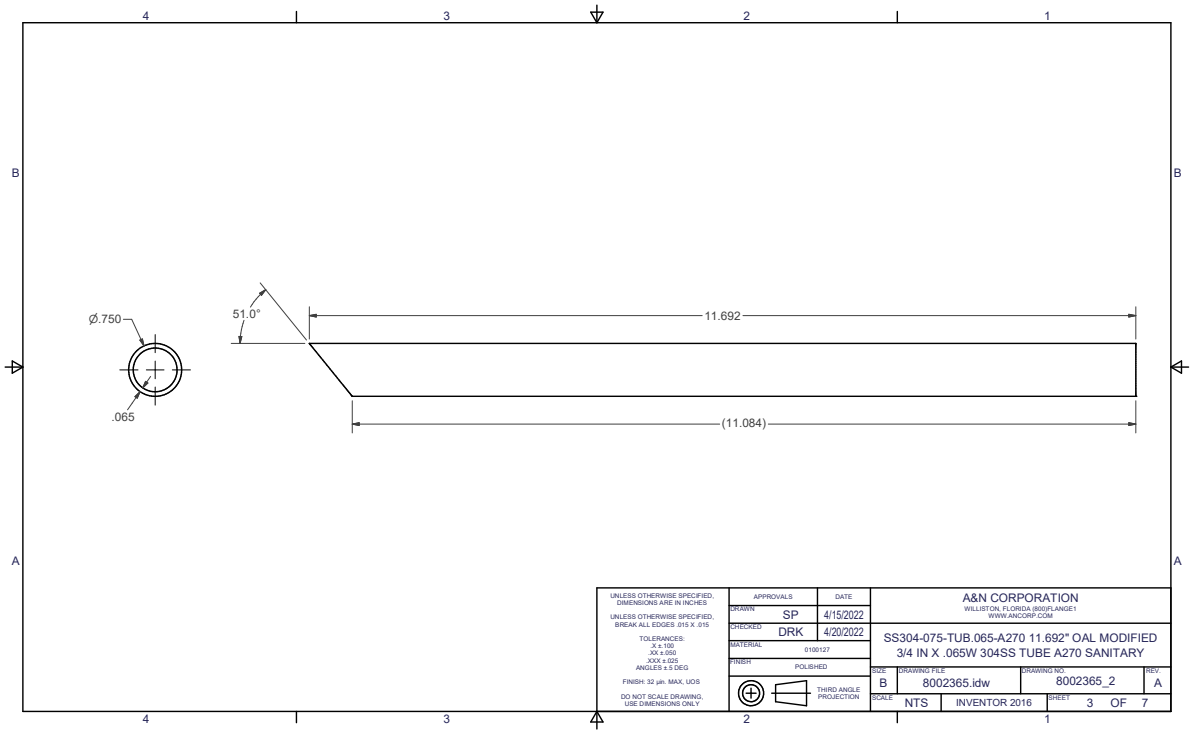

Figure D.3: ANCORP Drawing 8002365 Rev A, Page 3

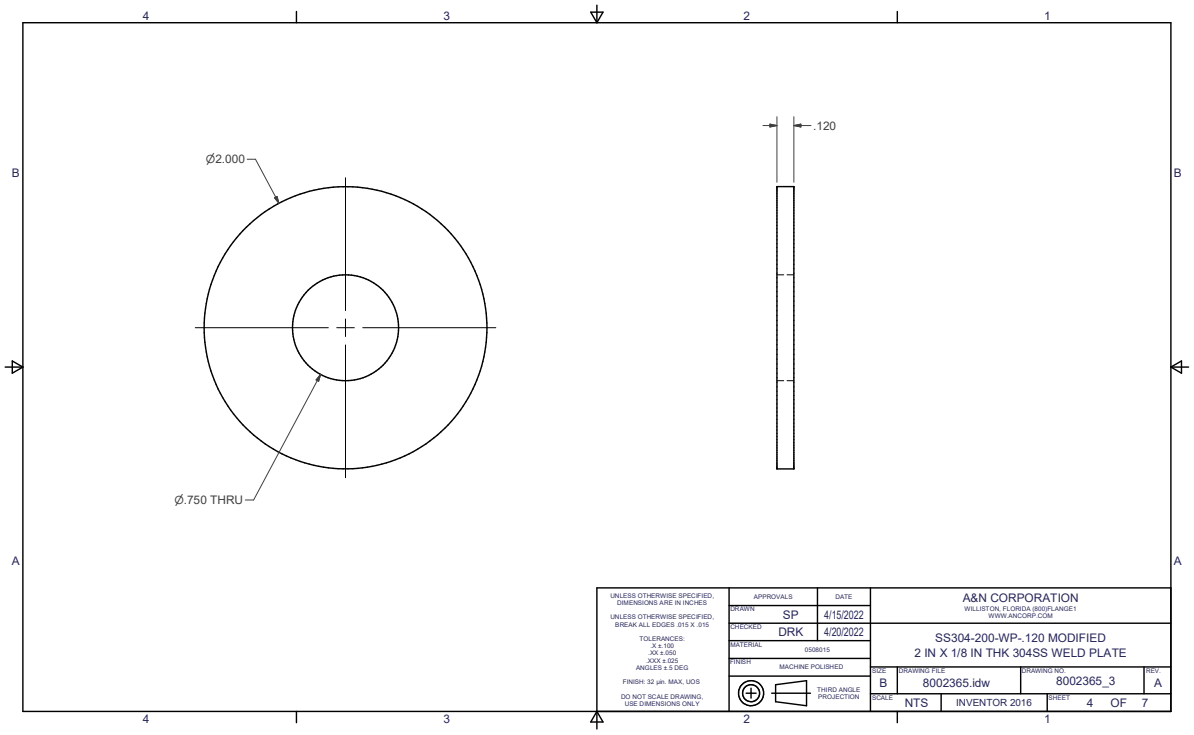

Figure D.4: ANCORP Drawing 8002365 Rev A, Page 4

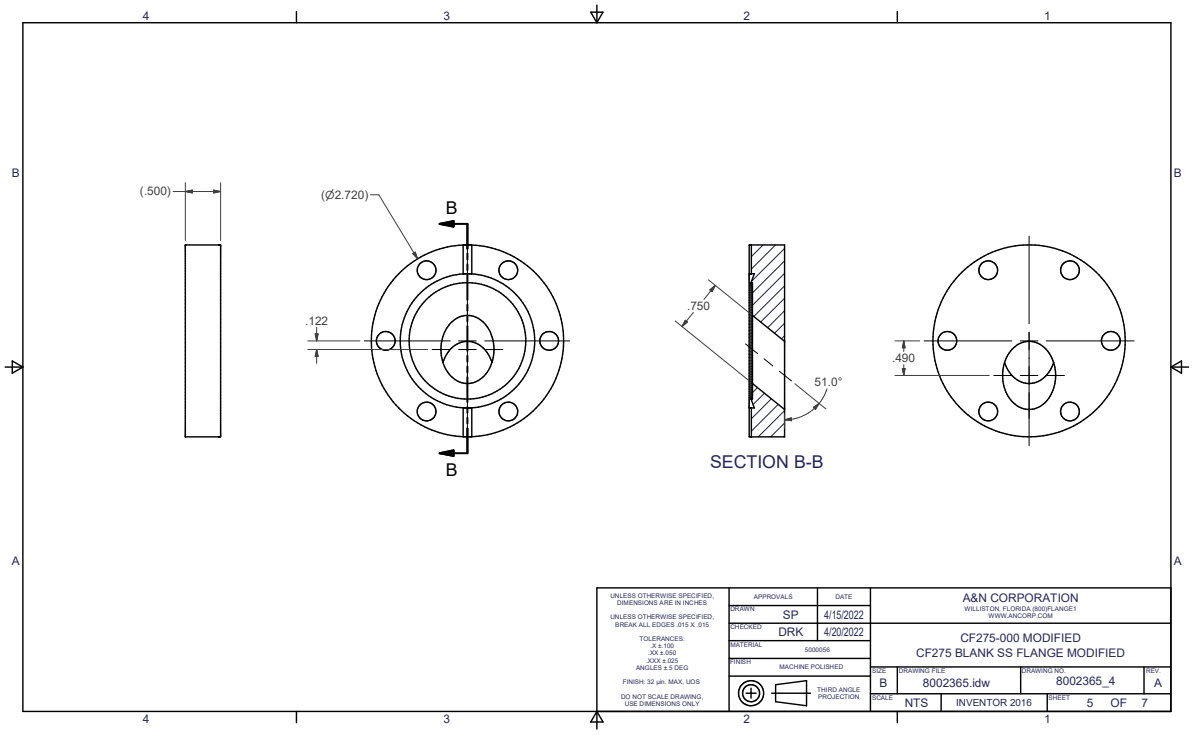

Figure D.5: ANCORP Drawing 8002365 Rev A, Page 5

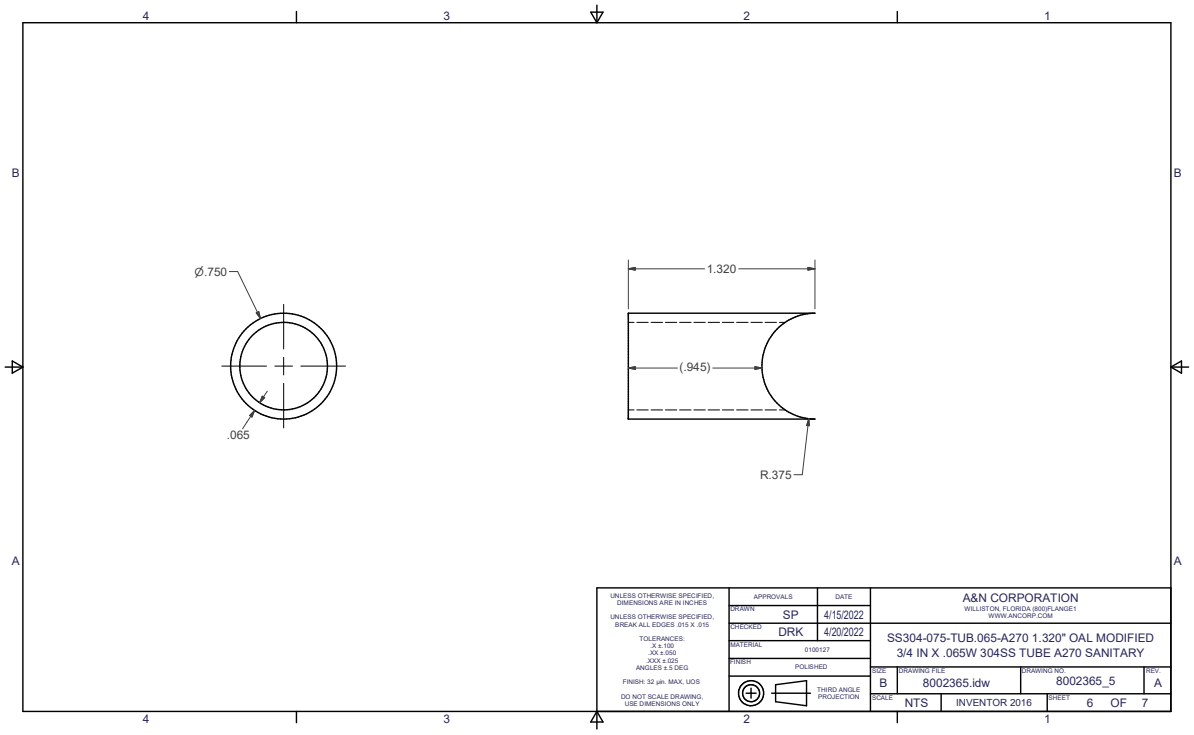

Figure D.6: ANCORP Drawing 8002365 Rev A, Page 6

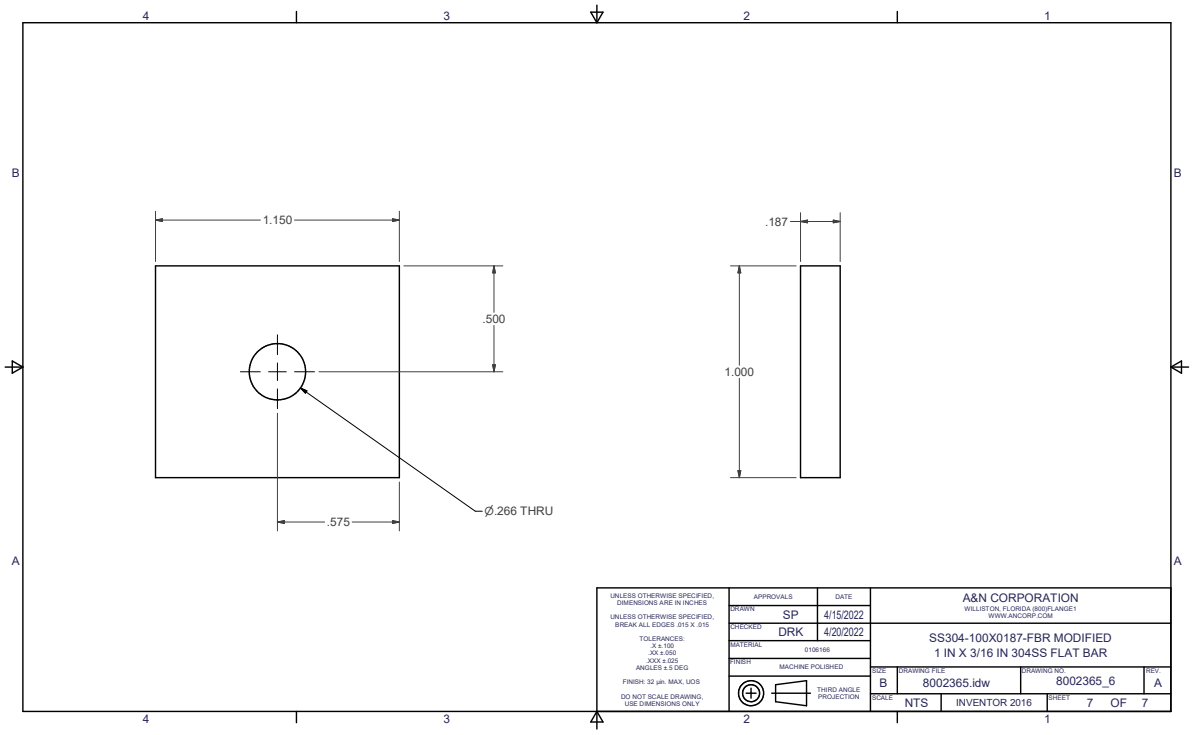

Figure D.7: ANCORP Drawing 8002365 Rev A, Page 7

Appendix E

Technical Drawings and Extra Details for Multiple Piece Nozzle Design

Here are the technical drawings for the nozzle designs discussed in subsection 2.6.2.

The microcapillaries used in the nozzle were ordered from MicroGroup® and made of 304 stainless steel. The OD of the microcapillaries is nominally 0.0083" (min: 0.0080, max: 0.0085). The ID is nominally 0.0043 (min: 0.0035, max: 0.0050). The cut length was specified as 0.197" ± 0.001".

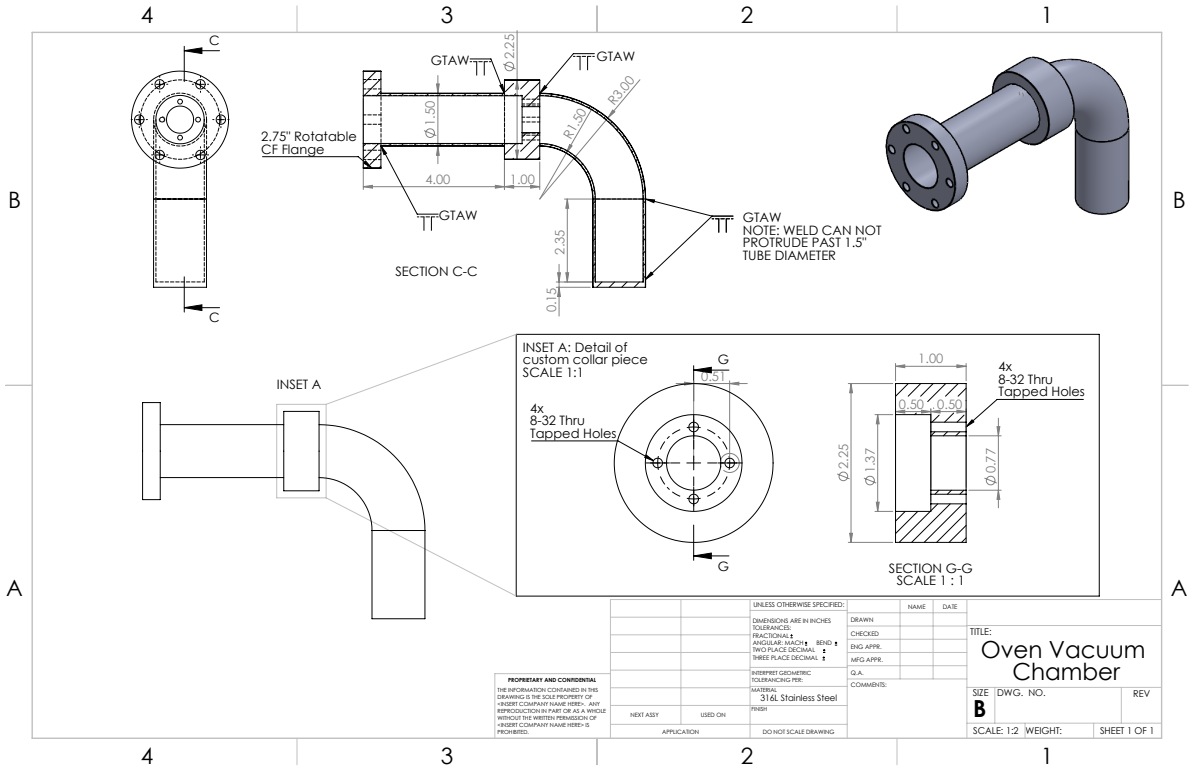

Figure E.1: This was shown in section 2.6.2, and we reproduce it hear for ease of comparison with the other components.

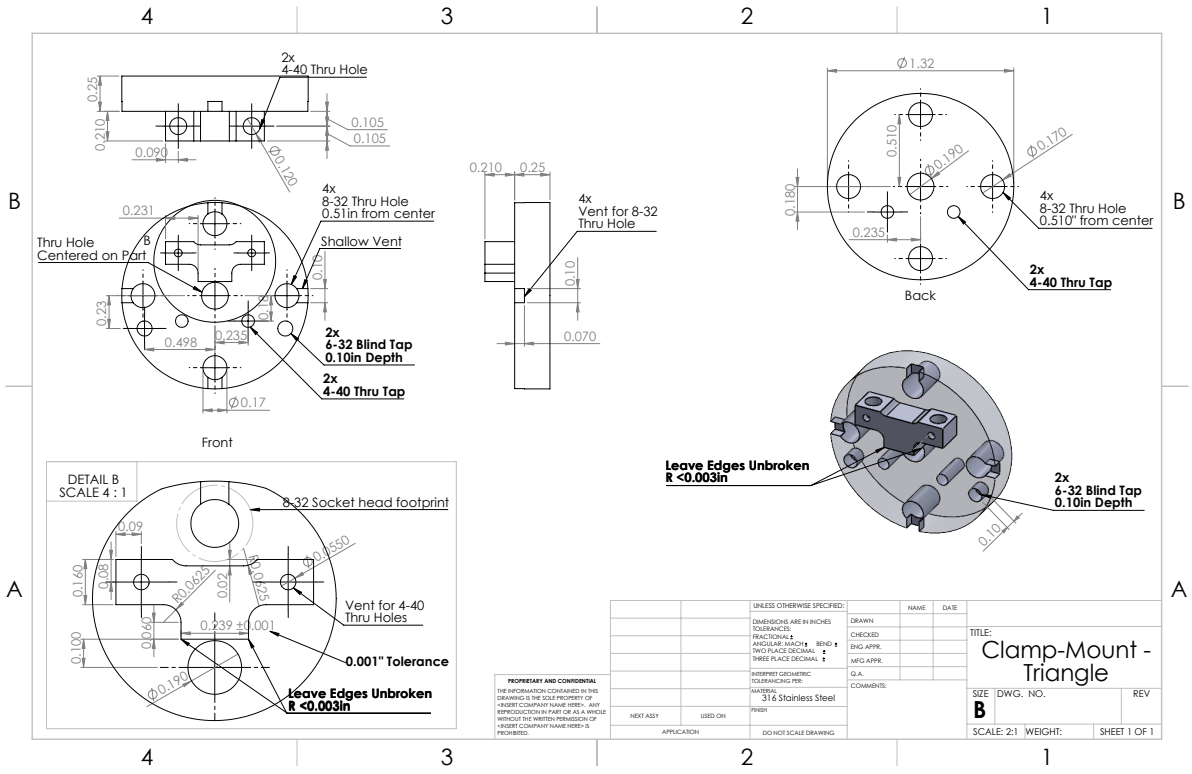

Figure E.2: The base piece to which the channel piece (shown in figure E.3) is to be clamped and tightened when the microcapillaries are in place. Once the nozzle is assembled, it is attached to the interior collar piece shown in "Inset A" of figure E.1.

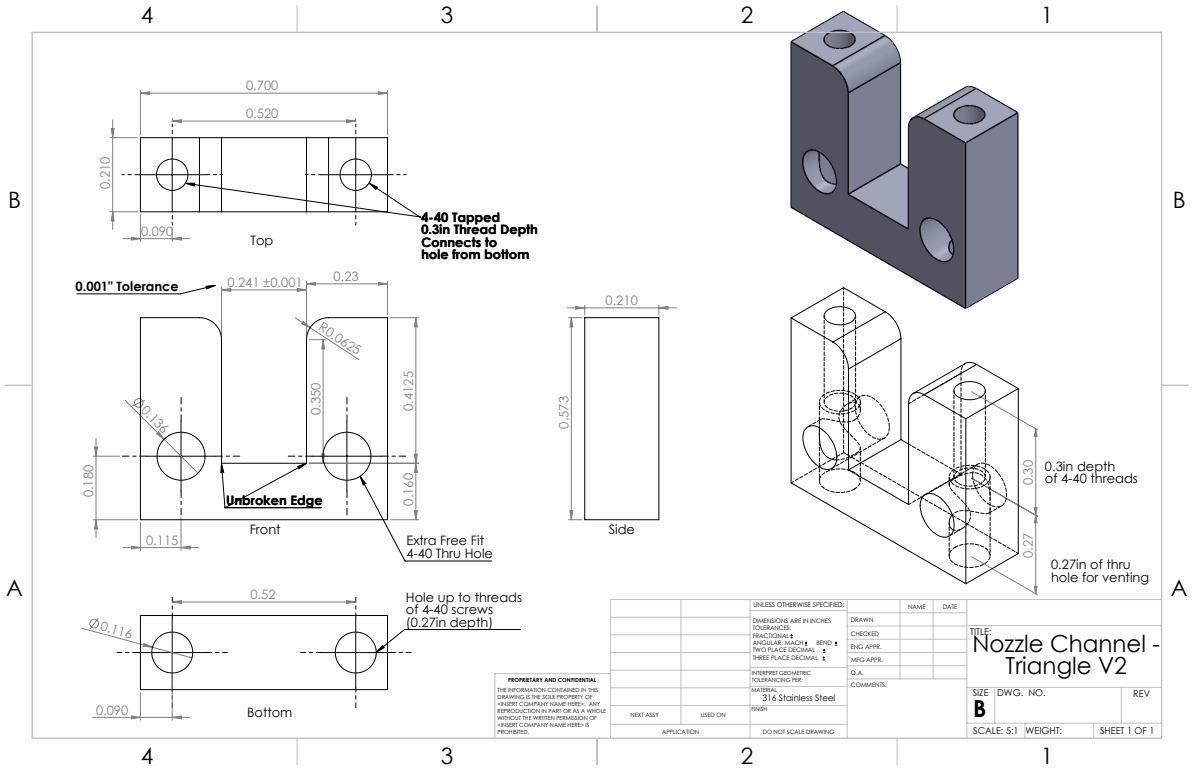

Figure E.3: The U-shaped channel piece into which two wedge pieces of the form shown in figure E.4 are to be loaded, followed by the loading of the stacked array of microcapillaries.

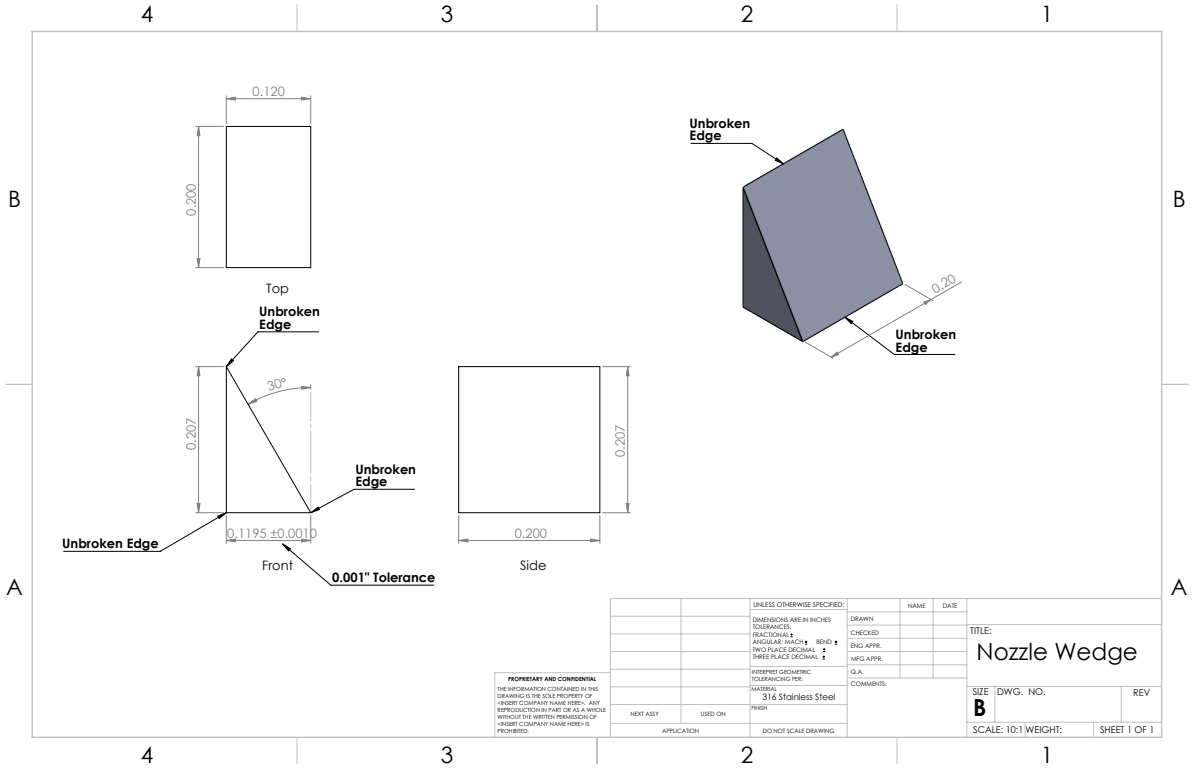

Figure E.4: Sharp cornered wedges to be placed in the channel of the piece shown in figure E.3.

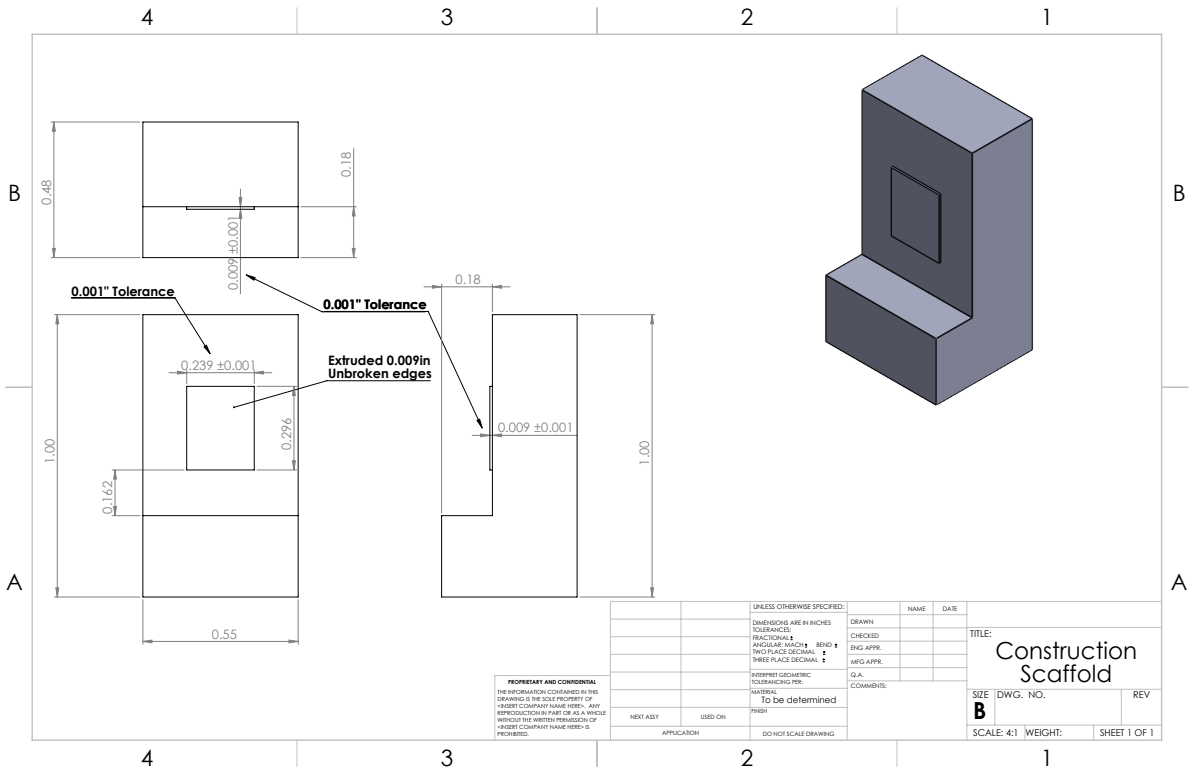

Figure E.5: A scaffold to aid in assembly of the nozzle. As noted in subsection 2.6.2, I recommend that the height of the extrusion be increased from 0.296” to 0.318” to accommodate 3 extra rows

Appendix F

Interlock to Close Gate Valve in the Event of Elevated Pressure

As a precaution against elevated pressures in the main chamber, we designed and installed an interlock circuit to close one of the gate valves, thereby separating the main vacuum chamber section of our machine from the middle and oven sections. In the event of a leak in the oven or middle sections, the interlock is designed to trigger the closure of one of the gate valves and to keep it closed until all fault conditions are eliminated and a manual reset button is pressed.

Pressure increase in our main chamber from a leak in our chamber is of major concern. In general, background gas pressure is a limiting factor for the maximum duration of ultracold atom experiments because the trapped atoms will collide with the hot background gases and be expelled from the trap. In the worst scenarios, enough air could enter the main chamber so as to deposit a layer of water adsorbed to the surface of the chamber. If not addressed, the slow release of atoms from this layer would enormously limit the pressure in the chamber with an unacceptably long outgas time on the scale of years. Those with experience with ultrahigh vacuum experiments know that this is the reason why a water bake is conducted when the chamber is assembled. During said bake, the chamber itself is heated to above 150°C for a

few days while a turbomolecular pump removes gases (especially water) from the chamber. The increased temperature dramatically accelerates the rate at which water and other volatile compounds are released from the surfaces of chamber walls so that at the end of the process the compounds present on the surface have either been removed or are so strongly adhered to the surface that they are of no consequence. Needing to conduct such a bake would be a very disruptive process for a mature experiment, requiring the dismantling of the optical setups from around the chamber. In our case, the magnet coils would be practically impossible to remove from around the chamber and so would need to be baked with the chamber, and the cooling water would need to be flushed out of the magnets in the process.

The pressure in the middle and oven section are of much less concern as long as they are not so high as to cause an increase in the main chamber. The pressures in these region are predominantly limited by the flux of strontium atoms out of the oven and collisions with the background gases are of much less concern for cooling with the Zeeman slower.

The gatevalves were purchased from MDC vacuum with a Kalrez elastomer seal (MDC Model: GV-1500M-P-1, Kalrez Pneumatic). More details of their use in the machine design are discussed in Shankari Rajagopol's thesis in section 5.1.1 on the strontium oven [13]. The gate valves are opened and closed by a pneumatical actuator. The pneumatic is controlled by a solenoid that is energized by application of 120V AC power. When energized with 120V AC power, the gate valve opens and when de-energized, the gate valve closes. The interlock acts to apply or remove the 120V AC control power so that when a fault is detected the solenoid is de-energized with a relay and the gate valve is closed.

To detect a fault, an analog signal from the ion gauges is used. This signal is carried over a firewire cable. Since a BNC connector is more convenient for us, we cut a firewire cable and connected the relevant analog signal wire to a BNC connector. The output analog signal

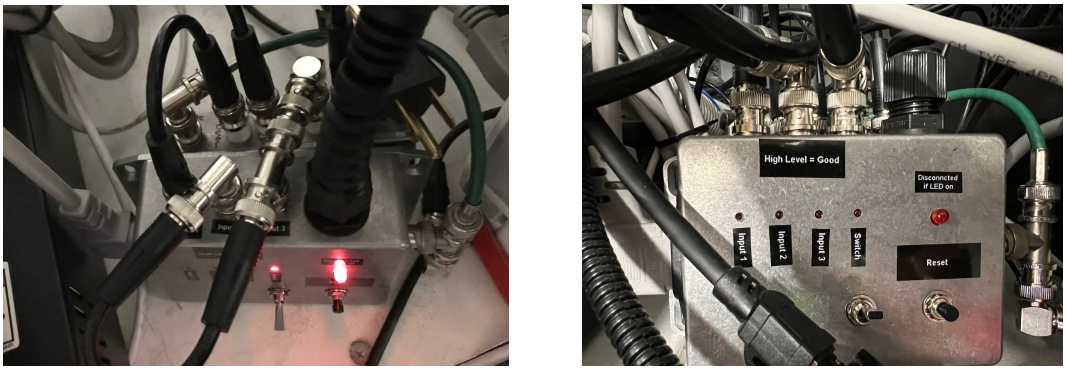

Figure F.1: Left: An image of the two pressure interlock electronics boxes. The box nearer the bottom of the image with the LEDs is the Relay Box. It indicates the fault status and applies or removes power from the pneumatic control solenoid to actuate the gate valve. The smaller partially obstructed box behind is the Fault Determination Box. It takes as input the ion gauge analog voltage signal (V_{IG}) and based on its value determines if a fault has occurred. Right: A front view of the Relay Box.

voltage V_{IG} from the ion gauge for a given gauge pressure reading P is designed to be

$$V_{\mathrm{IG}} = 11 + \log_{10}\left(\frac{P}{1\ \mathrm{Torr}}\right)$$

The interlock circuitry is divided between two electronics boxes. These two boxes with their interconnect BNCs as finally installed above the strontium machine are depicted in figure F.1. We will refer to them as the "Relay Box" and the "Fault Determination Box."

Let us first discuss the designs of the Relay Box. It takes in three digital signals that signify whether or not a fault has occurred. A digital "low" level indicates a present fault. A digital "high" level indicates a good pressure signal status. This convention was chosen so a disconnected BNC or signal loss would cause a fault. If a fault signal is present on one of the three BNC inputs, the corresponding LED will light. If a fault occurs or the manual switch is flipped, the control circuitry will latch into the fault state, indicated by the larger red LED. When latched in the fault state, relays remove 120V AC power to de-energize the gate valve control solenoid, causing the gate valve to close. To reset the latch and open the gate valve, all fault signals and the manual switch must be set to open, and then the reset button must be

pressed.

A schematic of the Relay Box circuitry is shown in Figure F.2 with a description of the components and their function in the caption.

Now let us discuss the Fault Determination Box. As inputs, it takes the analog signals (V_{IG}) from the oven ion gauge and the middle section ion gauge. Each of these signals is sent to a pair of comparators. The first comparator for each signal determines if the pressure is too high by comparing to signal to a reference voltage. The reference voltage for the oven section is set so that the comparator output goes low when the pressure in the oven is below 1×10^{-6} Torr. Likewise, the reference voltage for the middle section is set to give a low comparator output when the pressure in the middle section goes below 5.6×10^{-8} Torr. The second comparator for each signal checks if the ion gauge voltage goes below 147 mV, which is taken as an indication that the pressure signal was lost, in which case, the comparator output goes low. The outputs of the comparators for each signal are sent to an AND gate so that if either fault condition is present (high pressure or lost signal) the output of the AND gate, which is the output of the box, will be low.

A schematic of the Fault Determination Box is shown in Figure F.3.

Because we only have two fault signals out of the Fault Determination Box and three inputs to the Relay Box, we send one of the fault signals to two of the inputs of the Relay Box. Potentially, a third fault condition could be sent to the Relay Box if desired.

We add one final note that we initially set the high pressure threshold for the middle section higher, but we found that when the gate valve opened, it causes a small transient pressure spike which would trip the interlock if the setting was too low.

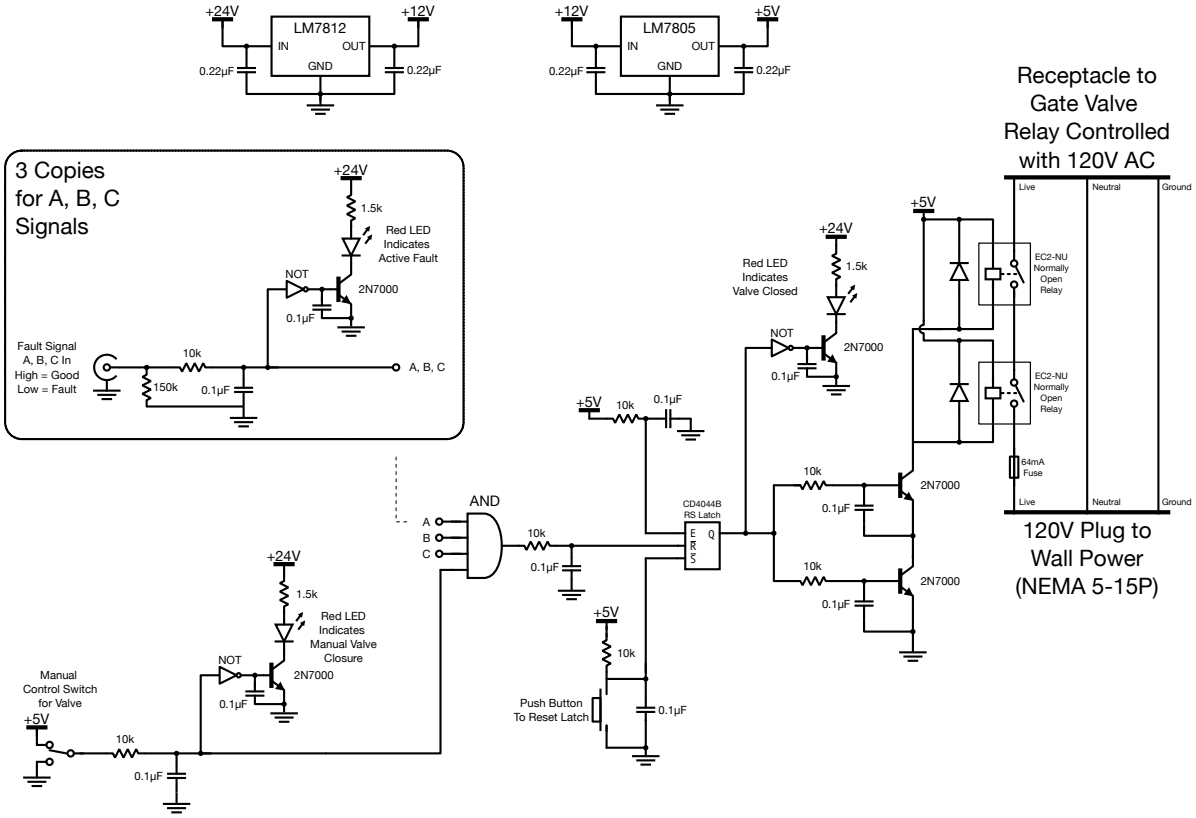

Figure F.2: A circuit diagram showing the contents of the Relay Box. The LM78xx regulators are used to convert the supplied 24V DC to the 5V used for the high logic level. A 5V supply could be used instead, but a convenient 24V supply was already available in lab. The circuit section inscribed by the box depicts the wiring for the three incoming fault signals. It contains a 150 kΩ pulldown resistor and an aggressive low pass made with the 10 kΩ and 1.0 µF serves to mitigate the effect of transient noise or signals that might cause an inconvenient trip. This lowpass is used defensively in various other places for the same reason. The circuitry for the LED control is also shown. A similar circuit is shown below the box for the manual control switch. If any of these signals go low, they will reach the AND gate whose low output trips the latch (CD4044B) causing its output Q to go low. When Q is low, it stops current from flowing through the two transistors. The second transistor is redundant to help reduce the chance of failure. In turn, the cessation of current through the reed relays' control solenoids causes it to go into its normally open position, thereby cutting power to the gate valve. The second relay is again for redundancy to reduce the risk of one failing.

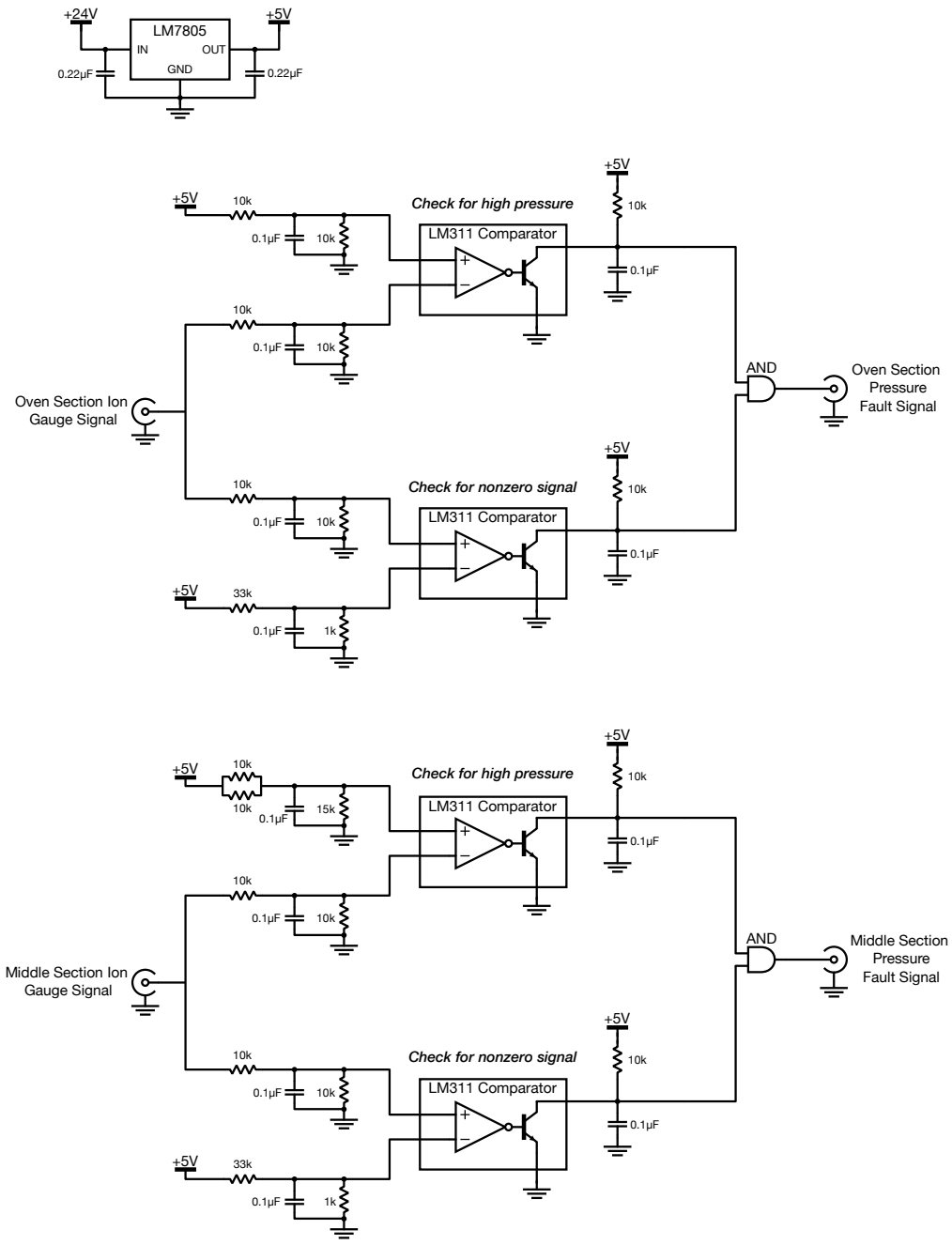

Figure F.3: A circuit diagram showing the contents of the Fault Determination Box. A description of most of the components is given in the text. The LM7805 uses the 24V input voltage and converts it to the 5V logic high level. Voltage dividers are used to set reference voltages and 0.1 μF are used to low pass signals to make the signals less susceptible to transient signal spikes.

Appendix G

Pneumatic Atomic Beam Shutter

In this appendix, we document a minor modification to the mechanical atomic beam shutter made partly in Fall 2022 and partly in Spring 2022. A picture of the beam shutter setup is shown in figure G.1. The basic idea of the beam shutter is the same as previously. A rod extends into the atomic beam right after the oven nozzle to block the stream of atoms. The rod is mounted to the machine on a flexible hydroformed bellows so that by bending the bellows, the rod is moved out of the beam path.

Previously, we used a solenoid actuator to pull the rod out of the beam path. We found over time that this actuator failed to work consistently and that the solenoids we used were deteriorating rapidly each time we replaced them. We believe that the original bellows had work hardened over time due to repeated bending, and so to overcome the increased stiffness of the bellows, we replaced the solenoid actuator with a pneumatic actuator. Not long after this, a small leak opened in the bellows, which we believe resulted from its deterioration after too many cycles. We think that a solenoid actuator could have in principle worked adequately for a long time with infrequent replacement of the solenoid actuator, as has been the case on the lithium machine. However, the bellows that was on the strontium machine seems to have been custom manufactured to be slightly shorter than the one used on the lithium machine, resulting

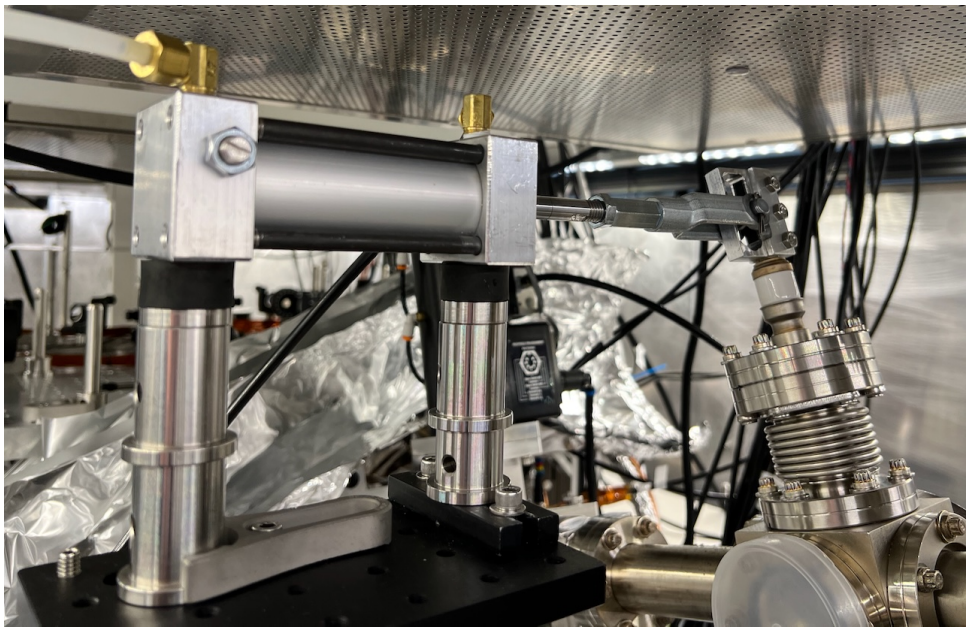

Figure G.1: An overview image of the pneumatic actuator,

in more strain within the material on each actuation cycle of the shutter. In our replacement, we used a longer bellows, that we believe is the same model as used on the lithium machine. We continue to use the pneumatic shutter because it seems to reliably and repeatably actuate the beam shutter since installation, but we believe that use of a solenoid would again suffice since the replacement of the work hardened bellows.

Mechanical Components

The physical object that currently blocks the atomic beam is a modified rod shaped feedthrough (Kurt J. Lesker Co. Model: EFT0313373) that is set in the path of the atomic beam leaving from the nozzle. The rod is modified with the addition of an affixed aluminum piece that is visible in figure G.2. To create this, we internally threaded a short distance into a tube shaped piece of aluminum using a tap and externally threaded the tip of the feedthrough from Lesker. We then tightened the threaded piece of aluminum onto the copper rod so that the resulting assembly was a longer rod with a wider diameter near where the beam is blocked.

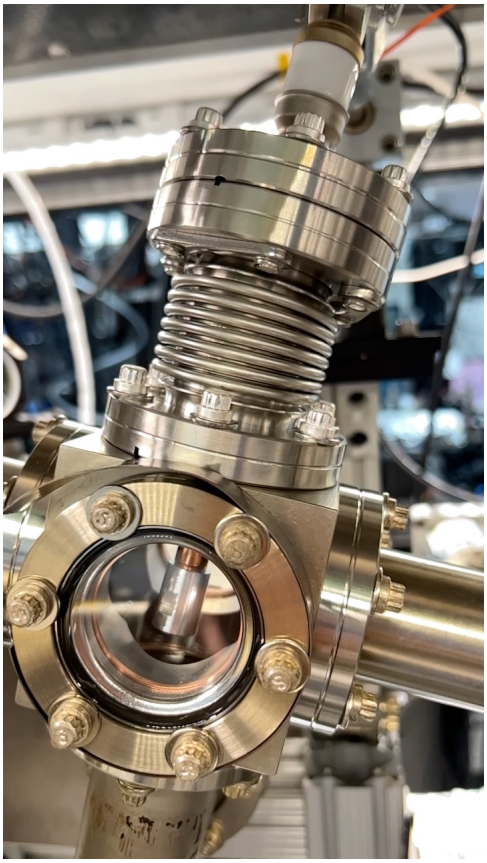

Figure G.2: An image of the modified feedthrough in the vacuum chamber that serves as an atomic beam shutter. One can see the flattened part of the aluminum piece for use with a spanner wrench.

On the aluminum piece, it was helpful to cut small parallel flat edges that a spanner wrench can go across to tighten on the rod. As a precaution against breaking the vacuum seal of the feedthrough, we made sure to clamp only on the rod of the feedthrough (rather than the CF flange) during the tightening process.

The bellows that connects the feedthrough to the vacuum chamber was purchased from Lesker (Model: MHT-CF-03.) Before installation, it is 3 inches long from end to end measured from the outward faces of the CF flanges. When under vacuum, it compresses to a length of approximately 2.625 inches, which is an important parameter for design of the feedthrough.

To pull the feedthrough with a linear pneumatic actuator, we use a rendition of the scotch

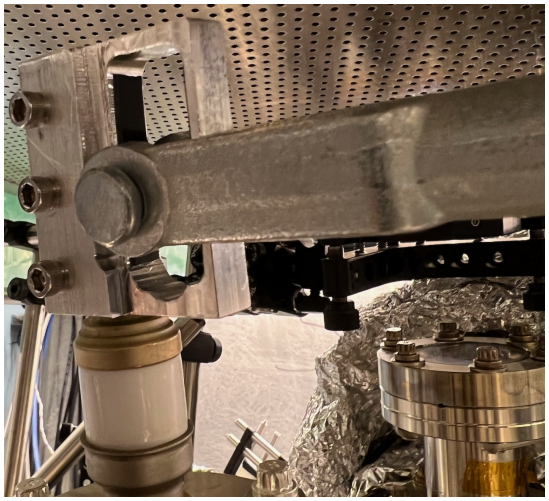

Figure G.3: An image of the scotch yoke type linkage between the feedthrough and the pneumatic actuator. A thin layer of cushioning material was adhered to the interior of the aluminum channel to help with cushioning, but we believe it is not significantly improving functionality.

yoke in which an aluminum piece with a channel cut into it is clamped around the part of the feedthrough that extends out of the chamber. An image of this linkage is shown in figure G.3. To fasten this channel to the pneumatic actuator, we use a clevis rod end (McMaster-Carr Model: 1583K24.) Because the 1 inch length of travel of the pneumatic actuator is more than it ideally would be, we effectively reduce the motion by cutting the channel wider ($\approx 7/8$ inch) than the clevis pin (diameter $5/8$ inch) that fits into it. Thus, as the actuator pulls the beam shutter out of the atomic beam, it moves freely ($\approx 1/4$ inch) before making contact with the edge of the channel to pull the shutter.

The end of the pneumatic actuator that we use is threaded with $5/8$"-11 threads. In principle the clevis rod end could be directly threaded onto this. A nut can be placed on the actuator rod first before attaching the clevis rod end, and then the clevis rod end can be screwed on and locked into place by tightening the nut against it. However, in practice, the location of the pneumatic actuator mount is too far from the beam shutter for this, and we must effectively extend the rod. To accomplish this, we use a coupling nut, also known as an extension nut

(e.g., McMaster-Carr, Model: 90264A460) and a threaded rod (e.g., McMaster-Carr, Model: 98750A056) that we attach between the pneumatic actuator and the clevis rod end.

I recommend the use of a pneumatic actuator that has a pneumatic cushion on both ends of the cylinder. We currently use one that is only cushion when the rod is withdrawn into the cylinder, but a cushion when the rod is extend as well is preferred to minimize mechanical shocks. This version can be ordered from McMaster-Carr, but must be ordered custom from the manufacturer. The model number we were given on a quote was 6491K999, but we believe this is a generic number for a custom pneumatic shutter of this type. The type we are using now is similar to model number 6491K221, but we cannot confirm if we used McMaster-Carr as the supplier when it was purchased, or if this is the exact one in use.

As can be seen in figure G.1, the pneumatic actuator is mounted on a breadboard that is then mounted to 80/20 aluminum extrusion supports. The connection to the bread board includes vibration damping mounts (McMaster Model: 9213K19) as well as pillar posts (Thorlabs Model: RS2P.) Not much special consideration need be given to the mounting, as long as there is some freedom in the placement of the actuator and the mechanical forces are not transferred towards delicately aligned elements of the machine.

Pneumatics

For the pneumatic control, we use a meter-out configuration. In this configuration, we controllably restrict the flow of the exhausted air from the pneumatic cylinder. A pneumatic circuit diagram is shown in figure G.4. First, the air supply from the building is regulated down to a lower pressure which helps to control the speed of actuation. This air is then split and directed through two solenoid controlled 2-position, 3-way direction control valves that are synchronized electronically so that only one of them passes pressurized air through at a time, while the other one is set to vent air back through a muffler. Thus, one of the directional control valves applies pressurized air to one side of the piston in the pneumatic actuator, while

the other is set to vent air from the opposite side of the piston.

Between the directional control valves and the pneumatic actuator are flow control valves (McMaster-Carr Model: 3019N128.) These flow control valves are arranged to allow air to freely flow towards the pneumatic actuator through a check valve, while flow is restricted through an adjustable needle valve for air flowing out of the actuator. This arrangement of restricted flow *out* of the actuator is the reason for the term "meter-out." By adjusting the needle valves, one can control the speed at which the pneumatic actuator moves.

Lastly, we note that this implementation could be simplified with the use of a 2-position, 4-way directional control valve that replaces the function of the two separate control valves in figure G.4. Such an alternative is shown in figure G.5

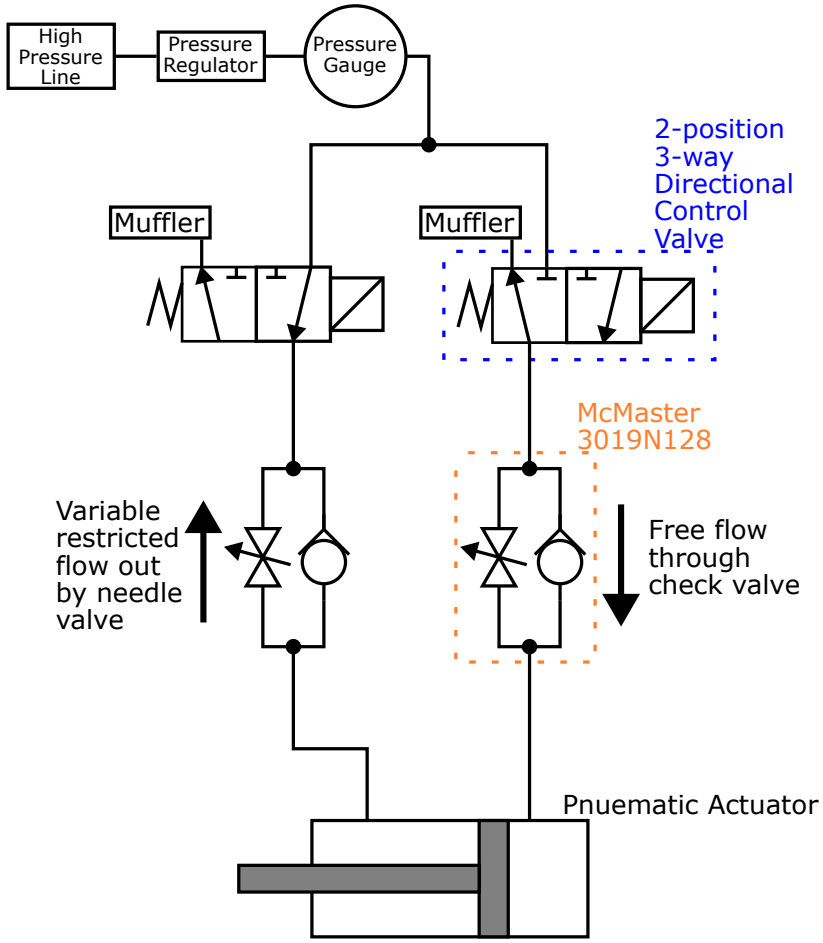

Figure G.4: A schematic diagram of the control components that are used to realize the meter-out c the pneumatic actuator. The 2-position, 3-way valves are set to flow pressurized air into the actuator when the solenoid, indicated by the box with line through it, is energized and set to vent air out of the actuator through a muffler when the solenoid is not energized. The directional control valve solenoids are controlled by relays that apply or remove 120V power.

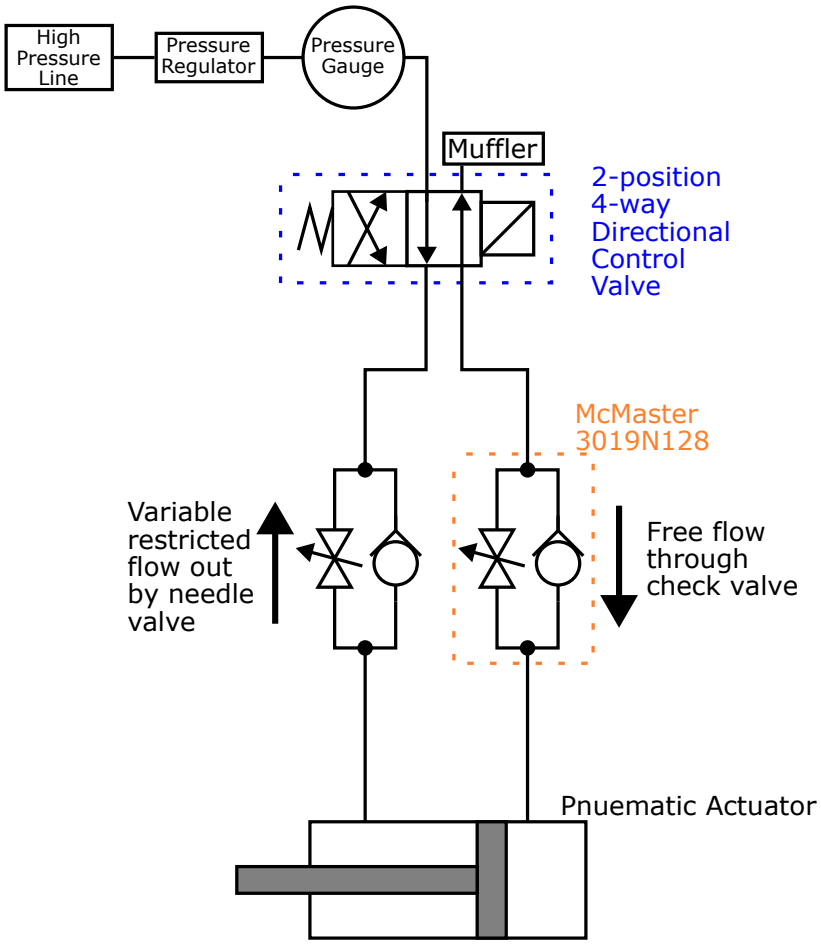

Figure G.5: A schematic diagram of an alternative pneumatic control system.

Appendix H

New Mexico Shutter Circuit Diagram

We will use this appendix simply to document a small circuit that we made recently to aid in the control of a commercial beam shutter (NM Laser Products Model: LST-5VDC). This shutter is actuated by application or removal of 5V power from a solenoid controlled actuator. To suppress the inductive load of the solenoid, per the recommendations of the manufacturer, we designed the circuit depicted in figure H.1. This snub circuit must handle the inductive load when the shutter goes from open (high TTL) to closed (low TTL).

We found that this circuit sufficiently suppresses the transient voltage spike across the solenoid. An oscilloscope trace of the voltage across solenoid is shown in figure H.2.

Finally, in figure H.3, we present images of the box that the circuit is in to show the connections and indicator lights on the box.

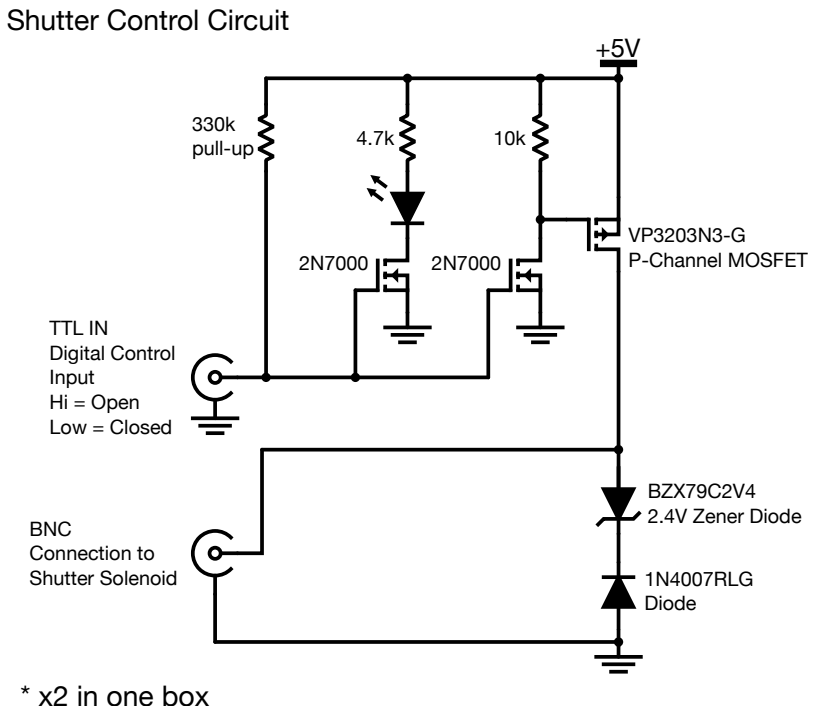

Figure H.1: Schematic of the control circuit.

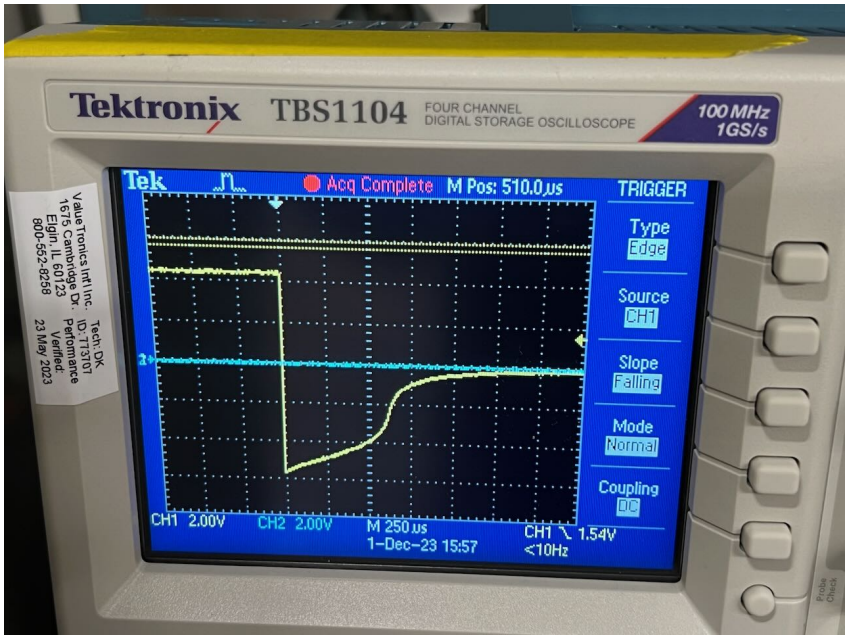

Figure H.2: An oscilloscope trace triggered at the switch from open to close of the voltage across the solenoid, which is equal to the voltage across the diodes.

Figure H.3: The box with the circuit in it.

Bibliography

[1] André Eckardt. Colloquium: Atomic quantum gases in periodically driven optical lattices. *Reviews of Modern Physics*, 89:011004, Mar 2017.

[2] Martin Holthaus. Floquet engineering with quasienergy bands of periodically driven optical lattices. *Journal of Physics B*, 49(1):013001, January 2016.

[3] André Eckardt and Egidijus Anisimovas. High-frequency approximation for periodically driven quantum systems from a floquet-space perspective. *New Journal of Physics*, 17(9):093039, sep 2015.

[4] Cristian M. Le, Ryosuke Akashi, and Shinji Tsuneyuki. Missing quantum number of floquet states. *Physical Review A*, 105:052213, May 2022.

[5] Hideo Sambe. Steady states and quasienergies of a quantum-mechanical system in an oscillating field. *Physical Review A*, 7:2203–2213, Jun 1973.

[6] P G Harper. Single Band Motion of Conduction Electrons in a Uniform Magnetic Field. *Proceedings of the Physical Society. Section A*, 68(10):874–878, October 1955.

[7] Douglas R. Hofstadter. Energy levels and wave functions of Bloch electrons in rational and irrational magnetic fields. *Physical Review B*, 14(6):2239–2249, September 1976.

[8] Serge Aubry and Gilles André. Analyticity breaking and Anderson localization in incommensurate lattices. *Annals of the Israel Physical Society*, 3(133):18, 1980.

[9] Attila Szabó and Ulrich Schneider. Non-power-law universality in one-dimensional quasicrystals. *Physical Review B*, 98:134201, Oct 2018.

[10] Douglas R. Hofstadter. *The Energy Levels of Bloch Electrons in a Magnetic Field*. PhD thesis, 1975.

[11] Svetlana Ya. Jitomirskaya. Metal-insulator transition for the almost Mathieu operator. *Annals of Mathematics*, 150(3):1159–1175, 1999.

[12] P. W. Anderson. Absence of diffusion in certain random lattices. *Physical Review*, 109:1492–1505, Mar 1958.

[13] Shankari Vani Rajagopal. *Realizing and probing driven quantum systems with ultracold gases*. PhD thesis, University of California, Santa Barbara, June 2019.

[14] Ruwan Senaratne. *Quantum Simulation of Strongly-Driven Systems Using Ultracold Lithium and Strontium*. PhD thesis, University of California, Santa Barbara, June 2018.

[15] William D. Phillips and Harold Metcalf. Laser deceleration of an atomic beam. *Physical Review Letters*, 48:596–599, Mar 1982.

[16] John Prodan, Alan Migdall, William D. Phillips, Ivan So, Harold Metcalf, and Jean Dalibard. Stopping atoms with laser light. *Physical Review Letters*, 54:992–995, Mar 1985.

[17] Ruwan Senaratnea, Shankari V. Rajagopal, Zachary A. Geiger, Kurt M. Fujiwara, Vyacheslav Lebedevb, and David M. Weld. Effusive atomic oven nozzle design using an aligned microcapillary array. *Review of Scientific Instruments*, 86:023105, January 2015.

[18] Matthieu Vangeleyn, Paul F. Griffin, Erling Riis, and Aidan S. Arnold. Single-laser, one beam, tetrahedral magneto-optical trap. *Optics Express*, 17(16):13601–13608, Aug 2009.

[19] Simon Stellmer. *Degenerate quantum gases of strontium*. PhD thesis, January 2013.

[20] Jonatan Höschele, Sandra Buob, Antonio Rubio-Abadal, Vasiliy Makhalov, and Leticia Tarruell. Atom-number enhancement by shielding atoms from losses in strontium magneto-optical traps. *Phys. Rev. Appl.*, 19:064011, Jun 2023.

[21] John F. Barry. *Laser Cooling and Slowing of a Diatomic Molecule*. PhD thesis, December 2013.

[22] CORNING SAS Specialty Glass. *Alkali Borosilicate Code 7056*, 2020. Available at `https://www.corning.com/media/worldwide/csm/documents/fiches%20Verre%20pour%20poudre%207056.pdf`.

[23] Werner Espe, Max Knoll, and Marshall P. Wilder. Getter materials for electronic tubes. *Electronics*, October 1950. Available at `http://www.tubebooks.org/file_downloads/Getter_Material.pdf`.

[24] Karl Jousten, editor. *Handbook of Vacuum Technology*. Wiley-VCH Verlag GmbH & Co. KGaA, 2008.

[25] J. P. Gordon and A. Ashkin. Buffer-gas-induced collision shift for the ^{88}Sr $^1S_0$-$^3P_1$ clock transition. *Physical Review A*, 80:030501(R), September 2009.

[26] Andrew Zangwill. *Modern Electrodynamics*. Cambridge University Press, Cambridge, 2012.

[27] Rudolf Grimm, Matthias Weidemüller, and Yurii B. Ovchinnikov. Optical dipole traps for neutral atoms. volume 42 of *Advances In Atomic, Molecular, and Optical Physics*, pages 95–170. Academic Press, 2000.

[28] F. Le Kien, P. Schneeweiss, and A. Rauschenbeutel. Dynamical polarizability of atoms in arbitrary light fields: general theory and application to cesium. *The European Physical Journal D*, 67(92), 2013.

[29] N.L. Manakov, V.D. Ovsiannikov, and L.P. Rapoport. Atoms in a laser field. *Physics Reports*, 141(6):320–433, 1986.

[30] Ivan H. Deutsch and Poul S. Jessen. Quantum control and measurement of atomic spins in polarization spectroscopy. *Optics Communications*, 283(5):681–694, 2010. Quo vadis Quantum Optics?

[31] Robert Littlejohn. Lecture notes for Physics 221AB quantum mechanics, 2020-2021.

[32] Martin M. Boyd. *High Precision Spectroscopy of Strontium in an Optical Lattice: Towards a New Standard for Frequency and Time*. PhD thesis, October 2007.

[33] Ivan H. Deutsch and Poul S. Jessen. Quantum-state control in optical lattices. *Physical Review A*, 57:1972–1986, Mar 1998.

[34] Marc de Boissieu. Phonons, phasons and atomic dynamics in quasicrystals. *Chemical Society Reviews*, 41:6778–6786, 2012.

[35] F. Gahler and J. Rhyner. Equivalence of the generalised grid and projection methods for the construction of quasiperiodic tilings. *Journal of Physics A: Mathematical and General*, 19(2):267, feb 1986.

[36] Shankari V. Rajagopal, Toshihiko Shimasaki, Peter Dotti, Mantas Račiūnas, Ruwan Senaratne, Egidijus Anisimovas, André Eckardt, and David M. Weld. Phasonic spectroscopy of a quantum gas in a quasicrystalline lattice. *Physical Review Letters*, 123:223201, Nov 2019.

[37] Yaacov E. Kraus and Oded Zilberberg. Topological Equivalence between the Fibonacci Quasicrystal and the Harper Model. *Physical Review Letters*, 109(11):116404, September 2012.

[38] Toshihiko Shimasaki, Max Prichard, H. Esat Kondakci, Jared E. Pagett, Yifei Bai, Peter Dotti, Alec Cao, Anna R. Dardia, Tsung-Cheng Lu, Tarun Grover, and David M. Weld. Anomalous localization in a kicked quasicrystal. *Nature Physics*, January 2024.

[39] Toshihiko Shimasaki, Yifei Bai, H. Esat Kondakci, Peter Dotti, Jared E. Pagett, Anna R. Dardia, Max Prichard, André Eckardt, and David M. Weld. Reversible phasonic control of a quantum phase transition in a quasicrystal, 2023.

[40] Fabien Alet and Nicolas Laflorencie. Many-body localization: An introduction and selected topics. *Comptes Rendus Physique*, 19(6):498–525, September 2018.

[41] R. Moessner and S. L. Sondhi. Equilibration and order in quantum Floquet matter. *Nature Physics*, 13(5):424–428, May 2017.

[42] Juliette Billy, Vincent Josse, Zhanchun Zuo, Alain Bernard, Ben Hambrecht, Pierre Lugan, David Clément, Laurent Sanchez-Palencia, Philippe Bouyer, and Alain Aspect. Direct observation of Anderson localization of matter waves in a controlled disorder. *Nature*, 453(7197):891–894, June 2008.

[43] Diego Guzman-Silva, Matthias Heinrich, Tobias Biesenthal, Yaroslav V. Kartashov, and Alexander Szameit. Experimental study of the interplay between dynamic localization and anderson localization. *Optics Letters*, 45(2):415–418, Jan 2020.

[44] Kristian Rayanov, Günter Radons, and Sergej Flach. Decohering localized waves. *Physical Review E*, 88(1):012901, July 2013.

[45] Yaacov E. Kraus, Yoav Lahini, Zohar Ringel, Mor Verbin, and Oded Zilberberg. Topological states and adiabatic pumping in quasicrystals. *Physical Review Letters*, 109(10):106402, September 2012.

[46] Y. Lahini, R. Pugatch, F. Pozzi, M. Sorel, R. Morandotti, N. Davidson, and Y. Silberberg. Observation of a Localization Transition in Quasiperiodic Photonic Lattices. *Physical Review Letters*, 103(1):013901, June 2009.

[47] Giacomo Roati, Chiara D'Errico, Leonardo Fallani, Marco Fattori, Chiara Fort, Matteo Zaccanti, Giovanni Modugno, Michele Modugno, and Massimo Inguscio. Anderson localization of a non-interacting Bose-Einstein condensate. *Nature*, 453(7197):895–898, June 2008.

[48] Martin Holthaus. Collapse of minibands in far-infrared irradiated superlattices. *Physical Review Letters*, 69:351–354, Jul 1992.

[49] Klaus Drese and Martin Holthaus. Exploring a metal-insulator transition with ultracold atoms in standing light waves? *Physical Review Letters*, 78:2932–2935, Apr 1997.

[50] Stephan Arlinghaus, Matthias Langemeyer, and Martin Holthaus. Dynamic localization in optical lattices. In S. Keshavamurthy and P. Schlagheck, editors, *Dynamical Tunneling: Theory and Experiment*, chapter 12. CRC Press, 1st ed. edition, 2011.

[51] Martin Holthaus, Gerald H. Ristow, and Daniel W. Hone. ac-field-controlled anderson localization in disordered semiconductor superlattices. *Physical Review Letters*, 75:3914–3917, Nov 1995.

[52] Martin Holthaus and Daniel W. Hone. Localization effects in ac-driven tight-binding lattices. *Philosophical Magazine B*, 74(2):105–137, 1996.

[53] Diego Guzman-Silva, Matthias Heinrich, Tobias Biesenthal, Yaroslav V. Kartashov, and Alexander Szameit. Experimental study of the interplay between dynamic localization and anderson localization. *Optics Letters*, 45(2):415–418, Jan 2020.

[54] Xiao Li, Xiaopeng Li, and S. Das Sarma. Mobility edges in one-dimensional bichromatic incommensurate potentials. *Physical Review B*, 96:085119, Aug 2017.

[55] Michele Modugno. Exponential localization in one-dimensional quasi-periodic optical lattices. *New Journal of Physics*, 11(3):033023, mar 2009.

[56] R. Walters, G. Cotugno, T. H. Johnson, S. R. Clark, and D. Jaksch. Ab initio derivation of hubbard models for cold atoms in optical lattices. *Physical Review A*, 87:043613, Apr 2013.

[57] André Eckardt, Christoph Weiss, and Martin Holthaus. Superfluid-insulator transition in a periodically driven optical lattice. *Physical Review Letters*, 95:260404, Dec 2005.

[58] R. Graham, M. Schlautmann, and P. Zoller. Dynamical localization of atomic-beam deflection by a modulated standing light wave. *Physical Review A*, 45:R19–R22, Jan 1992.

[59] K. W. Madison, M. C. Fischer, R. B. Diener, Qian Niu, and M. G. Raizen. Dynamical bloch band suppression in an optical lattice. *Physical Review Letters*, 81:5093–5096, Dec 1998.

[60] H. Lignier, C. Sias, D. Ciampini, Y. Singh, A. Zenesini, O. Morsch, and E. Arimondo. Dynamical control of matter-wave tunneling in periodic potentials. *Physical Review Letters*, 99(22):220403, Nov 2007.

[61] K. I. Petsas, A. B. Coates, and G. Grynberg. Crystallography of optical lattices. *Physical Review A*, 50:5173–5189, Dec 1994.

[62] Konrad Viebahn, Matteo Sbroscia, Edward Carter, Jr-Chiun Yu, and Ulrich Schneider. Matter-wave diffraction from a quasicrystalline optical lattice. *Physical Review Letters*, 122:110404, Mar 2019.

[63] M. N. Kosch, L. Asteria, H. P. Zahn, K. Sengstock, and C. Weitenberg. Multifrequency optical lattice for dynamic lattice-geometry control. *Physical Review Research*, 4:043083, Nov 2022.

[64] Daniel Günther Greif. *Quantum magnetism with ultracold fermions in an optical lattice*. PhD thesis, ETH Zurich, 2013.

[65] A. Hemmerich and T. W. Hänsch. Two-dimesional atomic crystal bound by light. *Physical Review Letters*, 70:410–413, Jan 1993.

[66] J. Sebby-Strabley, M. Anderlini, P. S. Jessen, and J. V. Porto. Lattice of double wells for manipulating pairs of cold atoms. *Physical Review A*, 73:033605, Mar 2006.

[67] Long-Sheng Ma, Peter Jungner, Jun Ye, and John L. Hall. Delivering the same optical frequency at two places: accurate cancellation of phase noise introduced by an optical fiber or other time-varying path. *Optics Letters*, 19(21):1777–1779, Nov 1994.

[68] Tsz Him Leung. *Interacting Ultracold Bosonic Atoms in Geometrically Frustrated Lattices*. PhD thesis, University of California, Berkeley, 2020.

[69] Thomas Hamish Barter. *Quantum Simulation of the Bose-Hubbard Model with Ultracold Atoms in Triangular Optical Superlattices*. PhD thesis, University of California, Berkeley, 2018.

[70] Claire K. Thomas. *Quantum Simulation of Triangular, Honeycomb and Kagome Crystal Structures using Ultracold Atoms in Lattices of Laser Light*. PhD thesis, University of California, Berkeley, 2017.

[71] Pericles S. Theocaris and Emmanuel E. Gdoutos. *Matrix Theory of Photoelasticity*. Springer Berlin, Heidelberg, 1 edition, 1979.

[72] Richard Walters, Giovanni Cotugno, Tomi H. Johnson, Stephen R. Clark, and Dieter Jaksch. Ab initio derivation of hubbard models for cold atoms in optical lattices. *Physical Review A*, 87:043613, April 2013.

[73] Nicola Marzari and David Vanderbilt. Maximally localized generalized wannier functions for composite energy bands. *Physical Review B*, 56(20):12847, July 1997.

[74] Giovanni Pizzi, Valerio Vitale, Ryotaro Arita, Stefan Blügel, Frank Freimuth, Guillaume Géranton, Marco Gibertini, Dominik Gresch, Charles Johnson, and Takashi Koretsune. Wannier90 as a community code: new features and applications. *Journal of Physics: Condensed Matter*, 32:165902, 2020.

[75] Ivo Souza, Nicola Marzari, and David Vanderbilt. Maximally localized wannier functions for entangled energy bands. *Physical Review B*, 65:035109, 2001.

[76] David J. Griffiths. *Introduction to Quantum Mechanics*. Pearson Education, Inc., 2nd edition, 2005.

[77] Dieter Jaksch and Peter Zoller. The cold atom hubbard toolbox. *arXiv:cond-mat/0410614*, 2004. https://doi.org/10.48550/arXiv.cond-mat/0410614.

[78] Christopher J. Foot. *Atomic Physics*. Oxford University Press Inc., New York, Great Clarendon Street, Oxford OX2 6DP, first edition, 2005.

[79] D. J. McCarron, S. A. King, and S. L. Cornish. Modulation transfer spectroscopy in atomic rubidium. *Measurement Science and Technology*, 19(10):105601, August 2008.

[80] Jon H. Shirley. Modulation transfer processes in optical heterodyne saturation spectroscopy. *Optics Letters*, 7:537–539, 1982.